

# **Cross-Section Measurement of $t\bar{t}\gamma$ Production in $pp$ Collisions at $\sqrt{s} = 8$ and 13 TeV with the ATLAS Experiment**

Dissertation  
zur Erlangung des Grades eines Doktors  
der Naturwissenschaften

vorgelegt von  
Sara Ghasemi  
geb. in Tehran, Iran

eingereicht bei der Naturwissenschaftlich-Technischen Fakultät  
der Universität Siegen  
Siegen 2019



# Abstract

---

The cross-section measurement of top-quark pair production in association with a photon ( $t\bar{t}\gamma$ ) probes the electromagnetic coupling of the top quark. The inclusive and differential fiducial cross sections of  $t\bar{t}\gamma$  are measured with the data collected by the ATLAS detector from proton-proton collisions at the Large Hadron Collider, at the centre-of-mass energy of  $\sqrt{s} = 8$  TeV, with a corresponding integrated luminosity of  $20.2 \text{ fb}^{-1}$ , and at the centre-of-mass energy of  $\sqrt{s} = 13$  TeV, with a corresponding integrated luminosity of  $36.1 \text{ fb}^{-1}$ . The measurements are performed in the single-lepton final state. Signal events in the  $\sqrt{s} = 8$  (13) TeV measurement are selected by requiring one photon with a transverse momentum of  $p_T > 15$  (20) GeV, one isolated electron or muon, and at least four jets where at least one of them is originated from a  $b$ -quark. The fiducial region is defined to be close to the selection requirements. The inclusive cross-sections in  $\sqrt{s} = 8$  and 13 TeV are measured to be  $139 \pm 7$  (stat.)  $\pm 17$  (syst.) fb and  $521 \pm 9$  (stat.)  $\pm 41$  (sys.) fb, respectively, in agreement with the corresponding next-to-leading-order theoretical predictions of  $151 \pm 24$  fb and  $495 \pm 99$  fb. The differential cross-sections are measured as a function of transverse momentum and absolute pseudorapidity of the photon, in both  $\sqrt{s} = 8$  and 13 TeV data-sets, and as a function of the distance between the photon and the lepton in  $\sqrt{s} = 13$  TeV data-set. All differential measurements are in agreement with the theoretical predictions at next-to-leading-order accuracy.



# Zusammenfassung

---

Durch die Messung des Wirkungsquerschnitts eines Top-Quark-Paars in Verbindung mit einem Photon ( $t\bar{t}\gamma$ ) kann das elektromagnetische Kopplung eines Top-Quarks erforscht werden. Die Messung des inklusiven und differenziellen Fiduzialquerschnitts wird anhand von Daten, die durch eine Proton-Proton-Kollision produziert und im ATLAS-Detektor erhoben werden durchgeführt. Die Massenschwerpunktenergie beträgt  $\sqrt{s} = 8$  TeV mit einer integrierten Luminosität von  $20.2 \text{ fb}^{-1}$  beziehungsweise  $\sqrt{s} = 13$  TeV mit einer integrierten Luminosität von  $36.1 \text{ fb}^{-1}$ . Die Messungen wurden im Single-Lepton Final-State durchgeführt. Die Signaleignisse in den  $\sqrt{s} = 8$  (13) TeV Messungen wurden so selektiert, dass ein Photon mit einer Querdynamik (transverse momentum) von  $p_T > 15$  (20) GeV, ein isoliertes Elektron oder Muon und mindestens vier Jets vorhanden sind. Mindestens einer dieser Jets muss von einem  $b$ -quark entstanden sein. Die Fiduzialregion ist durch die Selektionsanforderungen definiert. Der inklusive Wirkungsquerschnitt wurde bei der  $\sqrt{s} = 8$  und der 13 TeV Messungen mit  $139 \pm 7$  (stat.)  $\pm 17$  (syst.) fb beziehungsweise  $521 \pm 9$  (stat.)  $\pm 41$  (syst.) fb gemessen. Die gemessenen Werte sind in guter Übereinstimmung mit theoretischen Vorhersagen von  $151 \pm 24$  fb beziehungsweise  $495 \pm 99$  fb. Die differenziellen Wirkungsquerschnitte werden in beiden Messungen ( $\sqrt{s} = 8$  und 13 TeV) als Funktion des Transversalimpulses beziehungsweise der absoluten Pseudorapidität des Photons und für  $\sqrt{s} = 13$  TeV zusätzlich als die Funktion des Abstands zwischen dem Photon und dem Lepton gemessen. Die Messungen sind in guter Übereinstimmung mit theoretischen Vorhersagen mit einer Genauigkeit in der nächsthöheren Reihenfolge.



# Acknowledgements

---

First and foremost, I would like to express the deepest appreciation to my supervisor Prof. Dr. Ivor Fleck, for his continuous support and patience, and for giving me the opportunity to work in a world-class experiment. I learnt so much during my time in Siegen and in CERN and by participating in various conferences and workshops, all of which would have not been possible without the support of my supervisor. I am also very grateful to Priv.-Doz. Dr. Markus Cristinziani for accepting to be the second reviewer of this dissertation, and to the other members of my Ph.D. committee, Prof. Dr. Markus Risse and Prof. Dr. Wolfgang Kilian.

I would like to thank all my colleagues in the analysis team, from university of Siegen, university of Bonn, university of Göttingen and CERN, without their contribution this work would have not been completed. It has been a great privilege to spend several years working with you and learning from you. I am eternally grateful for your efforts and commitments to our success. I would like to specially thank Dr. Yichen Li and Dr. Carmen Diez Pardos for all the fruitful discussions and feedbacks.

My deepest gratitude goes to my parents for their endless support and love, and for teaching me to be a free thinker not a follower. It is needless to say, none of this would have been possible without you. My dear sister, Saba, thank you for always showing me that ray of hope in life, and for trying to keep me in the real world. Finally, Shahram, words will never be enough. Thank you for letting me get absorbed, and waiting for me to come out again. I can not wait to share more and more adventures with you.



# Contents

---

<b>1</b>	<b>Introduction</b>	<b>1</b>
<b>2</b>	<b>Theoretical Context</b>	<b>3</b>
2.1	The Standard Model of Particle Physics . . . . .	3
2.1.1	Particle Content and the Forces . . . . .	4
2.1.2	Quantum Electrodynamics . . . . .	6
2.1.3	Quantum Chromodynamics . . . . .	8
2.1.4	Electroweak Theory . . . . .	11
2.1.5	The Electroweak Symmetry Breaking and the Higgs-Englert-Brout Mechanisms . . . . .	15
2.2	Proton-Proton Interactions . . . . .	17
2.2.1	Parton Density Functions . . . . .	18
2.2.2	Overview of a Proton-Proton Collision . . . . .	19
2.2.3	Cross Sections in Proton-Proton Collisions . . . . .	21
2.3	Top Quark . . . . .	23
2.3.1	Top Quark Production in Proton-Proton Collisions . . . . .	24
2.3.2	Top Quark Decay . . . . .	24
2.4	Top Quark Pair Production in Association with a Photon . . . . .	26
<b>3</b>	<b>Experimental Setup</b>	<b>29</b>
3.1	The Large Hadron Collider . . . . .	29
3.1.1	The Collider Setup . . . . .	30
3.1.2	The Experiments . . . . .	30
3.1.3	Luminosity . . . . .	31
3.2	The ATLAS Detector . . . . .	32
3.2.1	Coordinate System and Useful Kinematic Variables . . . . .	33
3.2.2	Magnets . . . . .	34
3.2.3	Inner Detector . . . . .	35
3.2.4	Calorimeters . . . . .	38
3.2.5	Muon Spectrometer . . . . .	41
3.2.6	Trigger System . . . . .	43
<b>4</b>	<b>From Detector to Physics: Event Reconstruction</b>	<b>45</b>
4.1	Tracks and Vertices . . . . .	45
4.2	Electron . . . . .	47
4.3	Muon . . . . .	49
4.4	Jet . . . . .	51
4.5	Photon . . . . .	53
4.6	Missing Transverse Momentum . . . . .	57

<b>5 Data and Simulated Samples</b>	<b>59</b>
5.1 Collision Data . . . . .	59
5.2 Monte Carlo Simulated Samples . . . . .	59
5.2.1 Simulation of Signal Events . . . . .	61
5.2.2 Simulation of Background Events . . . . .	62
5.2.3 Removal of the Event Double Counting between Samples . . . . .	64
<b>6 Cross-Section Definitions and Likelihood Description</b>	<b>65</b>
6.1 Total Cross Section . . . . .	65
6.2 Fiducial Cross Section . . . . .	66
6.3 Differential Cross Section . . . . .	68
6.4 Likelihood Function . . . . .	69
6.4.1 General Description . . . . .	69
6.4.2 Likelihood Function for $\sigma_{t\bar{t}\gamma}$ Measurement . . . . .	71
<b>7 Cross-Section Measurement of <math>t\bar{t}\gamma</math> at 8 TeV</b>	<b>73</b>
7.1 Signal Region Selection . . . . .	73
7.1.1 Selection at Object-level . . . . .	74
7.1.2 Selection at Event-level . . . . .	75
7.1.3 Events with More Than One Photon . . . . .	76
7.2 Analysis Strategy . . . . .	79
7.2.1 Utilisation of Template Fit Method . . . . .	79
7.2.2 Definition of the Fiducial Region . . . . .	81
7.2.3 Fit Strategy . . . . .	82
7.2.4 Theoretical Prediction . . . . .	83
7.3 Extraction of Templates . . . . .	83
7.3.1 Prompt-Photon Template . . . . .	83
7.3.2 Hadronic-fake Template . . . . .	84
7.3.3 Electron-fake Template . . . . .	98
7.4 Background Estimation . . . . .	99
7.4.1 Hadronic-fake Background . . . . .	99
7.4.2 Electron-fake Background . . . . .	99
7.4.3 Backgrounds with Prompt Photons . . . . .	100
7.5 Systematic Uncertainties . . . . .	105
7.5.1 Modelling Uncertainties . . . . .	105
7.5.2 Experimental Uncertainties . . . . .	106
7.5.3 Template Uncertainties . . . . .	108
7.6 Results . . . . .	110
<b>8 Cross-Section Measurement of <math>t\bar{t}\gamma</math> at 13 TeV</b>	<b>113</b>
8.1 Signal Region Selection . . . . .	114
8.1.1 Selection at Object-level . . . . .	114
8.1.2 Selection at Event-level . . . . .	115
8.2 Analysis Strategy . . . . .	116
8.2.1 Neural Networks . . . . .	116
8.2.2 Definition of the Fiducial Region . . . . .	118
8.2.3 Strategy of Inclusive Cross-Section Measurement . . . . .	118

8.2.4	Strategy of Differential Cross-Section Measurement . . . . .	119
8.2.5	Theoretical Prediction . . . . .	120
8.3	Estimation of Hadronic-fake Background . . . . .	121
8.3.1	The ABCD Method . . . . .	121
8.3.2	Treatment of the Photon Isolation–Identification Correlation . . . . .	128
8.3.3	Extraction of Hadronic-fake Scale Factor . . . . .	131
8.4	Estimation of other Backgrounds . . . . .	132
8.4.1	Electron-fake Background . . . . .	133
8.4.2	Fake-Lepton Background . . . . .	133
8.4.3	Backgrounds with Prompt Photons . . . . .	134
8.4.4	Summary of Background Yields . . . . .	134
8.5	Systematic Uncertainties . . . . .	135
8.5.1	Modelling Uncertainties . . . . .	135
8.5.2	Experimental Uncertainties . . . . .	136
8.6	Results . . . . .	137
<b>9</b>	<b>Summary and Conclusion</b>	<b>141</b>
<b>Bibliography</b>		<b>145</b>
<b>Appendix</b>		<b>153</b>
<b>A Extra Material for the 8 TeV Analysis</b>		<b>153</b>
A.1	Hadronic-fake Template . . . . .	153
A.1.1	Hadronic-fake Template and the Jet Multiplicity . . . . .	153
A.1.2	Hadronic-fake Template Re-weighting Using More $\eta$ Bins . . . . .	154
<b>B Extra Material for the 13 TeV Analysis</b>		<b>157</b>
B.1	Hadronic-fake Background Estimation . . . . .	157
B.1.1	Origin of Hadronic-fake Photons . . . . .	157
B.1.2	More Control Plots . . . . .	159
B.1.3	More on MC-based Double Ratio . . . . .	172
B.1.4	Data-Driven Double Ratio . . . . .	174
<b>C List of Monte Carlo Samples</b>		<b>181</b>
C.1	Monte Carlo Samples Used in the 8 TeV Analysis . . . . .	181
C.1.1	Nominal Samples . . . . .	181
C.1.2	Samples for Estimation of Systematic Uncertainties . . . . .	182
C.1.3	Other Samples . . . . .	183
C.2	Monte Carlo Samples Used in the 13 TeV Analysis . . . . .	183
C.2.1	Nominal Samples . . . . .	183
C.2.2	Samples for Estimation of Systematic Uncertainties . . . . .	188
<b>List of Abbreviations</b>		<b>189</b>



# CHAPTER 1

---

## Introduction

---

Particle physics tries to answer the question of what the fundamental constituents of matter are and how they interact. The *Standard Model* has been so far the most successful theory of particle physics. It classifies all the known elementary particles and describes their interactions via three of the four fundamental forces, the electromagnetic, weak and strong. The tremendous success of the Standard Model to provide remarkable predictions and describe a large amount of experimental data, has secured its place as the most accepted theory among the particle physicists. Yet, it leaves behind some unanswered questions and unexplained phenomena, strengthening the belief that it is only an approximation to a more complete theory. Thus, it is important to experimentally test the predictions of the Standard Model to the best possible accuracy and search for deviations hinting to the *Beyond the Standard Model* theories.

Among the most intriguing particles in the Standard Model is the top quark. It is the heaviest of all known elementary particles. Its large mass implies a strong coupling to the Higgs boson. Its mass is very close to the electroweak symmetry breaking scale, which has raised speculations about its role in the mechanism of electroweak symmetry breaking. Due to its very short lifetime, the top quark is the only quark that decays before it has a chance to form a hadron. All these unique features make the top quark an interesting subject of scientific research. More specially, top quark physics plays an important role in the search for new physics beyond the Standard Model.

In the past 24 years since the discovery of top quark [1, 2], considerable advances have been made in understanding its properties. Nevertheless, there are still some of the top quark properties that are not experimentally determined. In particular, the electroweak coupling of the top quark to the photon has not yet been directly measured. At the Large Hadron Collider, the top-photon coupling can be probed through studying the production of a top-quark pair in association with a photon ( $t\bar{t}\gamma$ ). Any deviation from the Standard Model predicted top-photon coupling manifests itself in the deviations in the measured cross section or kinematic distributions of the  $t\bar{t}\gamma$  process. The cross-section measurement of the  $t\bar{t}\gamma$  process is sensitive to several new physics models, such as anomalous dipole moments of the top quark [3–5], composite top quarks [6], and some of the Wilson coefficients in top-quark effective field theories [7].

This thesis presents two  $t\bar{t}\gamma$  measurements, both using the data collected by the ATLAS detector from proton-proton collisions in the Large Hadron Collider. The first measurement is performed with the data collected in 2012 in run-1 of data taking, at a centre-of-mass energy of  $\sqrt{s} = 8$  TeV, corresponding to an integrated luminosity of  $20.2 \text{ fb}^{-1}$ . The second measurement uses the data collected in 2015 and 2016 in run-2 of data taking, at a centre-of-mass energy of  $\sqrt{s} = 13$  TeV, with a corresponding  $36.1 \text{ fb}^{-1}$  integrated luminosity. Both measurements are performed in the single-lepton decay channel of  $t\bar{t}\gamma$ , where one of the  $W$  bosons resulting from the decay of top quark decays into a lepton (electron

or muon) and a neutrino and the other  $W$  boson into two quarks. In both analyses, the inclusive and differential cross sections of  $t\bar{t}\gamma$  are measured in fiducial phase spaces within the detector acceptance, chosen to be as close as possible to the phase spaces defined by the selection requirements.

For short, throughout the thesis the two measurements are referred to by the centre-of-mass energy of the data-set they used.

The thesis is structured as follows. Chapters 2 to 6 provide material which are relevant for both of the analyses. In Chapter 2, the theoretical context is introduced. This includes an overview on the Standard Model of particle physics, the proton-proton interactions, the top quark, and the  $t\bar{t}\gamma$  process. The Large Hadron Collider and the ATLAS detector are described in Chapter 3. Chapter 4 reviews the reconstruction procedure and definitions of the used physical objects. The experimental data and simulated samples are described in Chapter 5. In Chapter 6, the definitions of cross sections, together with a description of the likelihood function are given. Chapters 7 and 8 are devoted to the  $t\bar{t}\gamma$  cross-section measurement in 8 TeV and in 13 TeV, respectively. Finally, Chapter 9 provides a summary of the two analyses and conclusions.

The results of the two analyses presented in Chapters 7 and 8 have been published by the ATLAS Collaboration in Refs. [8, 9]. The key contributions of the author of the thesis in each of the analyses are explicitly mentioned at the beginning of Chapters 7 and 8. For any results that are not originally performed or repeated by the author, citations are made. The author has also contributed in the development of photon reconstruction in ATLAS for run-2 of data taking, the detail of which can be found in Section 4.5.

Throughout this thesis the natural units ( $\hbar = c = 1$ ) are used.

# CHAPTER 2

---

## Theoretical Context

---

This chapter introduces the theoretical framework of the analyses presented in this thesis. The theoretical aspects underlying this thesis can all be described by the standard model of particle physics, a theory that describes the dynamics of subatomic world. Throughout Section 2.1, the basic concepts of the standard model are outlined. In Section 2.2, general features of the high energy proton-proton collisions occurring at the Large Hadron Collider (LHC) are explained. Physics of the top quark is the cornerstone of this thesis. In this regard, Section 2.3 gives a brief overview on the top quark. Finally, the theoretical aspects of the main focus of this thesis, the  $t\bar{t}\gamma$  production, are given in Section 2.4.

### 2.1 The Standard Model of Particle Physics

The Standard Model (SM) of particle physics is a renormalisable Quantum Field Theory (QFT) that categorises all known elementary particles<sup>1</sup> and describes the interactions among them. Since its development in the 1960's, the SM has been thoroughly tested and has been very successful in describing a large variety of phenomena in particle physics, with high precision.

Each elementary particle in the SM is described by a field extending through space. The SM provides a description of three of the four fundamental forces - strong, electromagnetic and weak - which govern the dynamics of the elementary particles. The particle content of the SM and some description of the three forces are outlined in Section 2.1.1.

The SM is a gauge theory based on the invariance under the symmetry group:

$$G = SU(3)_C \otimes SU(2)_L \otimes U(1)_Y, \quad (2.1)$$

where  $SU(3)_C$  is the symmetry group of the strong interaction and  $SU(2)_L \otimes U(1)_Y$  corresponds to the electroweak interaction, a unification of the electromagnetic and the weak interactions. On the requirement that the system remains unchanged under the local gauge transformations above, all three interactions are derived. This is discussed in Sections 2.1.2, 2.1.3, and 2.1.4, while Section 2.1.5 discusses how breaking the symmetry provides mass for the particles.

The symmetry principles postulated in the SM imply existence of associated conserved charges, according to Noether's theorem. The conserved charge associated with the  $SU(3)_C$  symmetry is called *colour*. The  $SU(2)_L \otimes U(1)_Y$  symmetry is associated to conservation of *weak isospin*,  $I$ , and *weak hypercharge*,  $Y$ , which are related to the electric charge,  $Q$ , by  $Q = I_3 + \frac{Y}{2}$ , where  $I_3$  is the third component

---

<sup>1</sup> Elementary particle refers to a point-like particle with no internal structure, characterised by a unique set of quantum numbers.

of the weak isospin. In the symmetry group of Equation 2.1, the subscripts  $C$  and  $Y$  refer to colour and hypercharge, respectively, while  $L$  indicates "left-handed-ness" as weak isospin acts only on left-handed fields.

This Section cannot attempt to give a full review of the SM. There are many textbooks and reviews that cover this subject thoroughly, such as Refs. [10–14] on which this Section is based.

### 2.1.1 Particle Content and the Forces

According to the SM, matter is composed of *fermions* (half-integer spin particles). For each fermion there also exists an antiparticle with the same mass and spin, but opposite sign electric charge and additive quantum numbers. The gauge fields corresponding to the strong and electroweak interactions represent *bosons* (integer spin particles). Interactions between the fermions are mediated by exchanging gauge bosons.

There are twelve *flavours* (or types) of fermions, classified into six *quarks* and six *leptons*. This classification is according to the transformation properties of the fermions under the  $SU(3)_C$  group. Quarks are the triplets of the  $SU(3)_C$  group and carry colour charges. The six quark flavours are: *up* ( $u$ ), *charm* ( $c$ ) and *top* ( $t$ ) which are referred to as *up-type* quarks and have an electric charge of<sup>2</sup>  $Q = +2/3$ , *down* ( $d$ ), *strange* ( $s$ ) and *bottom* ( $b$ ) which form the so-called *down-type* quarks and carry an electric charge of  $Q = -1/3$ . Leptons are the singlets of the  $SU(3)_C$  group and are colourless. They consist of *electron* ( $e$ ), *muon* ( $\mu$ ) and *tau-lepton* ( $\tau$ ), all carrying an electric charge of  $Q = -1$ , and three corresponding *neutrinos* ( $\nu_e, \nu_\mu, \nu_\tau$ ) that are electrically neutral. Figure 2.1 summarises the approximate masses and some quantum numbers of the quarks and leptons.

Quarks and leptons can furthermore be organised into three *generations* or *families*. Each lepton generation forms a doublet of an electrically charged lepton and its corresponding neutrino, and each quark generation is a doublet of an up-type and a corresponding down-type quark. They can be seen in Figure 2.1 as well. Going from the first to the third generation, the particle masses increase, except for the neutrinos which are (almost) massless in all generations. All visible stable matter is in fact only made up of the first generation of fermions, in form of the  $u$ - and  $d$ -quarks that constitute protons and neutrons in the atomic nuclei, and the electrons that are bound to the nuclei. The particles in higher generations are not stable and decay into lighter particles.

Each quark flavour comes in three colour charges, labeled as *red* (R), *green* (G), and *blue* (B), and each antiquark carry an anti-colour ( $\bar{R}, \bar{G}, \bar{B}$ ). But experiments suggest that all free particles are colourless. Therefore, quarks and antiquarks can only exist in colourless bound states called *hadrons*. This is known as the *colour confinement*, explained more in Section 2.1.3. Hadrons are distinguished into two categories: *mesons* which are bound states formed from a quark and an antiquark that respectively carry a colour and its corresponding anti-colour, and *baryons* which consist of three quarks or three antiquarks carrying three different (anti-)colours. This introduces an additive and conserved quantum number in the SM, called the *baryon number* ( $B$ ). Its value is  $1/3$  for quarks and  $-1/3$  for antiquarks, resulting to  $B = 1$  for baryons,  $B = -1$  for antibaryons, and  $B = 0$  for mesons.

Leptons are also assigned an additive quantum number, the *lepton number* ( $L$ ). It has a value of  $L = 1$  for leptons,  $L = -1$  for antileptons, and  $L = 0$  for the rest of the fundamental particles. In addition, each lepton generation is assigned with a *lepton family number* ( $L_e, L_\mu$  and  $L_\tau$ ) which is equal to 1 and  $-1$  for the charged lepton and neutrino of that family, respectively, and 0 for any particle outside of that family. In the SM, both overall and family lepton numbers are conserved<sup>3</sup>. This means that in any interaction,

<sup>2</sup> The electric charges are all stated in units of the elementary charge  $e$ .

<sup>3</sup> While the lepton number is absolutely conserved, neutrino oscillations violates the lepton family number conservation. The neutrino oscillations, which is a phenomenon beyond the SM, is the only known cross-generation mixing among the leptons.

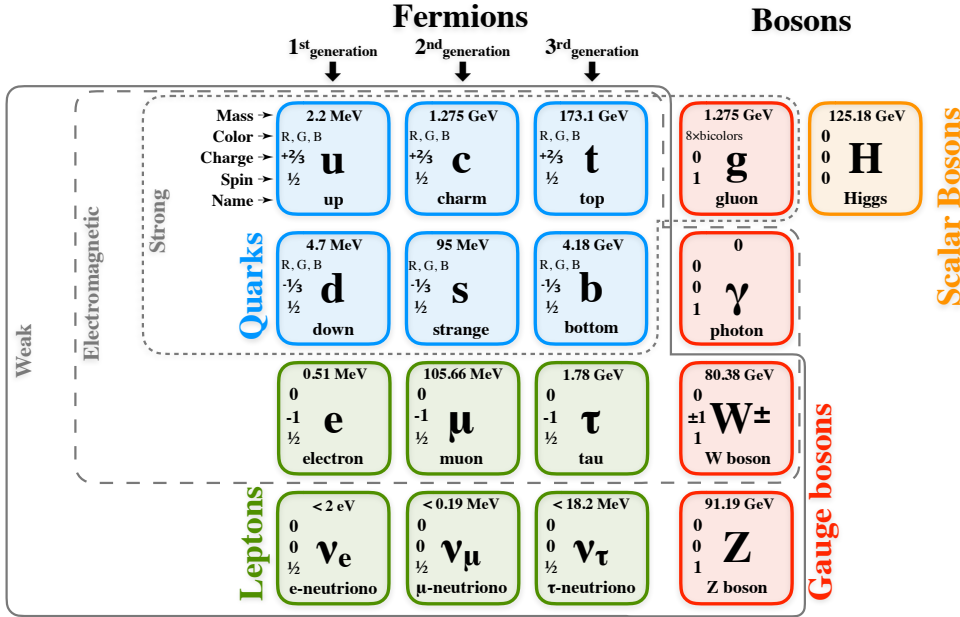


Figure 2.1: Particle content of the SM. The masses are taken from Ref. [15] and are subject to reevaluation. They are rounded to fit in the figure. The particles that participate in or mediate each of the three interactions are marked.

the number of leptons from a same family remains the same.

The electromagnetic force is responsible for attracting the electrons to atomic nuclei and holding the atoms together. All particles that carry an electric charge can participate in electromagnetic interactions. Therefore, neutrinos are the only fermions that do not interact electromagnetically. *Photon* is the gauge boson that mediates the electromagnetic interaction. It is massless and electrically neutral. The fact that the photon is massless accounts for the long range of the electromagnetic force.

The strong force is responsible for binding the quarks together into hadrons and forming the atomic nuclei. Only the particles that carry colour can participate in the strong interactions, and among fermions that is only quarks. The corresponding gauge bosons of the strong force are eight massless and electrically neutral *gluons*. Gluons themselves carry colour charge, therefore they interact strongly also among themselves. Since the colour charge must be conserved in a gluon exchange, gluons are bicoloured, carrying one unit of a colour and one unit of a different anti-colour. Although gluons are massless, but the long distance behaviour of the strong force is different than the electromagnetic force, due to the gluon self-interactions. This is explained in Section 2.1.3.

The weak force is responsible for the radioactive decay of atoms. All fermions feel the weak interaction. The weak interaction is mediated by two charged gauge bosons,  $W^+$  and  $W^-$  bosons with  $Q = +1$  and  $-1$  respectively, and the neutral Z boson. Unlike photon and gluons, the gauge bosons of

Nevertheless it indicates that the conservation of lepton family number is not absolute.

the weak interaction are massive. This makes the range of weak force limited to the subatomic distances ( $\sim 10^{-18}$  m). The *charged current* weak interactions are mediated by the  $W^\pm$  bosons and involved in transitioning the flavours between up-type quarks and down-type quarks or between charged leptons and neutrinos. The *neutral current* weak interaction is mediated by the  $Z$  boson and conserves the flavour. Since  $W^\pm$  carry electric charge, they can couple to a photon, but the electrically neutral  $Z$  boson can not. Similar to gluons, the  $W^\pm$  and  $Z$  bosons interact among each other.

The  $SU(2)_L$  group, which is related to the weak interaction, represents a chiral symmetry. The weak interaction violates parity, since only left-handed fermions (or right-handed antifermions)<sup>4</sup> take part in the charged current weak interactions. This arranges the fermions into left-handed doublets, carrying a weak isospin of  $I = 1/2$ , and right-handed singlets, corresponding to  $I = 0$  value. The left- and right-handed representations of fermions are summarised in Table 2.1, alongside some of their quantum numbers. The lepton and quark doublets in each generations from a left-handed representation, where the third component of weak isospin for the charged leptons is  $I_3 = -1/2$  and for the neutrinos is  $I_3 = +1/2$ , and up- and down-type quarks take  $I_3$  values of  $+1/2$  and  $-1/2$  respectively. However, in the left-handed quark doublets, the weak eigenstates of the down-type quarks ( $d'$ ,  $s'$ , and  $b'$ ) are linear combinations of their mass eigenstates ( $d$ ,  $s$ , and  $b$ ). This is explained in Section 2.1.4. There are no right-handed neutrinos (or left-handed antineutrinos) in the SM.

				$I$	$I_3$	$Y$	$Q$
Leptons	$\begin{pmatrix} \nu_e \\ e \end{pmatrix}_L$	$\begin{pmatrix} \nu_\mu \\ \mu \end{pmatrix}_L$	$\begin{pmatrix} \nu_\tau \\ \tau \end{pmatrix}_L$	1	$+1/2$	-1	0
	$e_R$	$\mu_R$	$\tau_R$	0	$-1/2$	-1	-1
Quarks	$\begin{pmatrix} u \\ d' \end{pmatrix}_L$	$\begin{pmatrix} c \\ s' \end{pmatrix}_L$	$\begin{pmatrix} t \\ b' \end{pmatrix}_L$	1	$+1/2$	$+1/3$	$+2/3$
	$u_R$	$c_R$	$t_R$	0	$-1/2$	$+1/3$	$-1/3$
	$d_R$	$s_R$	$b_R$		0	$-2/3$	$-1/3$

Table 2.1: The left-handed and right-handed representations of leptons and quarks, and their electroweak quantum numbers.

In addition to the mentioned gauge bosons, which are vector gauge fields (spin 1), the SM also includes a massive neutral scalar boson (spin 0), the *Higgs* boson. Higgs boson delivers mass to the elementary particles through a mechanism involving spontaneous symmetry breaking. Thus, the Higgs boson couples to all particles that have mass, including itself.

## 2.1.2 Quantum Electrodynamics

The first piece of the SM to reach a mature form was the Quantum Electrodynamics (QED), which describes interactions of photons with charged fermions.

A free fermion of mass  $m$  is described by the Dirac Lagrangian:

$$\mathcal{L}_{\text{Dirac}} = \bar{\psi}(x)(i\gamma^\mu \partial_\mu - m)\psi(x), \quad (2.2)$$

<sup>4</sup> Fermions can be divided into left- and right-handed chirality eigenstates. The momentum of a left-handed particle is anti-parallel to its spin, and for a right-handed particle it is parallel to its spin.

where  $\psi(x)$  is the 4-component spinor representing the fermion field,  $\bar{\psi}(x) = \psi^\dagger(x)\gamma^0$  is its adjoint, and  $\gamma^\mu$  ( $\mu = 0, 1, 2, 3$ ) are the  $\gamma$ -matrices. The Dirac Lagrangian is invariant under the global  $U(1)$  transformation<sup>5</sup>:

$$\begin{aligned}\psi(x) &\rightarrow \psi'(x) \equiv e^{i\theta}\psi(x); \quad \theta \in \mathbb{R} \\ \mathcal{L}_{\text{Dirac}} &\rightarrow \mathcal{L}_{\text{Dirac}}.\end{aligned}\quad (2.3)$$

But it is not invariant under the local  $U(1)$  transformation, where the phase factor  $\theta$  depends on the space-time coordinate ( $\theta = \theta(x)$ ):

$$\begin{aligned}\psi(x) &\rightarrow \psi'(x) \equiv e^{i\theta(x)}\psi(x) \\ \mathcal{L}_{\text{Dirac}} &\rightarrow \mathcal{L}_{\text{Dirac}} - \bar{\psi}(x)\gamma^\mu \partial_\mu \theta(x)\psi(x).\end{aligned}\quad (2.4)$$

A local gauge invariance can be established by adding a new spin-1 field  $A_\mu(x)$  to the Lagrangian, to cancel out the unwanted extra term in Equation 2.4. This new vector field transforms as:

$$A_\mu(x) \rightarrow A'_\mu(x) \equiv A_\mu(x) + \frac{1}{e}\partial_\mu \theta(x). \quad (2.5)$$

By defining the *covariant derivative* based on the vector field  $A_\mu(x)$ :

$$D_\mu \equiv \partial_\mu - ieA_\mu(x), \quad (2.6)$$

which has the desired transformation property of:

$$D_\mu \psi(x) \rightarrow (D_\mu \psi)'(x) \equiv e^{i\theta(x)}D_\mu \psi(x), \quad (2.7)$$

and then replacing  $\partial_\mu$  in Equation 2.2 with  $D_\mu$ , the Lagrangian turns into:

$$\begin{aligned}\mathcal{L} &= i\bar{\psi}(x)\gamma^\mu D_\mu \psi(x) - m\bar{\psi}(x)\psi(x) \\ &= \mathcal{L}_{\text{Dirac}} - e\bar{\psi}(x)\gamma^\mu A_\mu(x)\psi(x)\end{aligned}\quad (2.8)$$

which is now invariant under local  $U(1)$  transformation. Requiring the local gauge invariance added an interaction term to the Lagrangian between a fermion with charge  $e$  and an external electromagnetic four-potential  $A_\mu$ . The external potential field can be regarded as a true propagator field (a physical particle) if a proper gauge-invariant kinematic term for it will be added to the Lagrangian. The required term is:

$$\mathcal{L}_{\text{Kin}} \equiv -\frac{1}{4}F_{\mu\nu}(x)F^{\mu\nu}(x), \quad (2.9)$$

where

$$F_{\mu\nu}(x) \equiv \partial_\mu A_\nu(x) - \partial_\nu A_\mu(x) \quad (2.10)$$

---

<sup>5</sup> The family of phase transformations  $U(\theta) = e^{i\theta}$  form a unitary abelian group  $U(1)$ . The phase factor  $\theta$  can run continuously over real numbers. It is unmeasurable, has no physical meaning, and can be chosen completely arbitrarily. But once it is fixed, the value is for all space-time; hence the name *global*.

is the electromagnetic field strength tensor. The  $\mathcal{L}_{\text{Kin}}$  is invariant under local  $U(1)$  transformation, but a mass term for the vector field (like  $\frac{1}{2}m^2 A_\mu(x)A^\mu(x)$ ) violates the invariance and is prohibited. Thus, the photon, being the corresponding gauge boson to  $A_\mu(x)$  field, is massless.

Adding Equation 2.9 to Equation 2.8, the full Lagrangian of QED can be written:

$$\begin{aligned}\mathcal{L}_{\text{QED}} = & \underbrace{i\bar{\psi}(x)\gamma^\mu\partial_\mu\psi(x) - m\bar{\psi}(x)\psi(x)}_{\text{free fermion}} \\ & - \underbrace{e\bar{\psi}(x)\gamma^\mu\psi(x)A_\mu(x)}_{\text{photon-fermion interaction}} \\ & - \underbrace{\frac{1}{4}F_{\mu\nu}(x)F^{\mu\nu}(x)}_{\text{free photon}}.\end{aligned}\quad (2.11)$$

Additional fermions can be added to the theory simply by adding their corresponding Dirac and interaction terms to the Lagrangian.

The QED Lagrangian gives rise to the well-known Maxwell equations:

$$\partial_\mu F_{\mu\nu} = J^\nu, \quad (2.12)$$

where  $J^\nu \equiv e\bar{\psi}(x)\gamma^\nu\psi(x)$  is the conserved electromagnetic current, and  $Q \equiv \int d^3x J^0(x)$  is the corresponding conserved charge. This is a remarkable result, simply achieved by requiring a local gauge invariance.

The interaction term in  $\mathcal{L}_{\text{QED}}$  is illustrated by the Feynman diagram in Figure 2.2. The charge  $e$  which characterises the strength of the interaction is an arbitrary constant in this theory. The associated electromagnetic coupling, or fine structure constant  $\alpha = \frac{e^2}{4\pi}$ , is determined experimentally. Its value is  $\alpha \approx \frac{1}{137}$  with  $e$  being the charge of an electron (i.e. elementary charge). The smallness of the electromagnetic coupling strength allows to perform perturbative QED calculations.

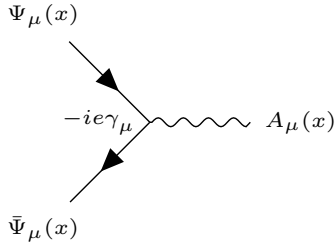


Figure 2.2: Feynman diagram for the QED vertex.

### 2.1.3 Quantum Chromodynamics

The Quantum Chromodynamics (QCD) is the theoretical description of the strong interactions among quarks and gluons. Following the successful QED prescription (Section 2.1.2), the Lagrangian of QCD is obtained by requiring symmetry under local  $SU(3)_C$  gauge transformations.

In the following, the quark fields are denoted by  $q_f^\alpha$  with  $\alpha = 1, 2, 3$  being the colour index and  $f = 1, \dots, 6$  the flavour index. For simplicity, the vector representation of the quark fields in the colour

space is used:

$$q_f = \begin{pmatrix} q_f^1 \\ q_f^2 \\ q_f^3 \end{pmatrix}. \quad (2.13)$$

The Lagrangian that describes a free quark of flavour  $f$  with the mass  $m_f$  has a similar structure to Equation 2.2:

$$\mathcal{L}_0 = \bar{q}_f(x)(i\gamma^\mu \partial_\mu - m_f)q_f(x). \quad (2.14)$$

The  $SU(3)$  transformation in colour space can be written as:

$$q_f^\alpha(x) \rightarrow (q_f^\alpha(x))' \equiv U_\beta^\alpha q_f^\beta(x), \quad (2.15)$$

with  $U$  denoting the unitary  $3 \times 3$  matrices of the form:

$$U = e^{i\theta_a \frac{\lambda_a}{2}}, \quad (2.16)$$

where a sum over repeated colour indices is applied. The  $\lambda_a$  ( $a = 1, \dots, 8$ ) are the eight generators of the  $SU(3)$  group<sup>6</sup>, known as Gell-Mann matrices. They are traceless and satisfy the commutation relation  $[\lambda_a, \lambda_b] = if_{abc}\lambda_c$ , where the structure constants  $f_{abc}$  are real and fully antisymmetric under interchange of any pair of indices. This manifests the non-abelian nature of the QCD theory.

The Lagrangian  $\mathcal{L}_0$  is invariant under the global  $SU(3)$  transformation, i.e. when the eight phase parameters are arbitrary real constants ( $\theta_a \in \mathbb{R}$ ). In analogy to QED, to impose an invariance under the local  $SU(3)_C$  gauge transformation, i.e. when  $\theta_a = \theta_a(x)$ , new vector gauge fields  $G_\mu^a(x)$  and covariant derivation  $D_\mu$  are needed:

$$D_\mu \equiv \partial_\mu - ig_s \frac{\lambda_a}{2} G_\mu^a(x), \quad (2.17)$$

where  $g_s$  is the strong coupling constant. Note that since there are eight independent gauge parameters, eight different gauge fields are needed. The  $G_\mu^a(x)$  gauge fields represent the eight gluons. They transform as:

$$G_\mu^a(x) \rightarrow (G_\mu^a)'(x) \equiv G_\mu^a(x) + \frac{1}{g_s} \partial_\mu \theta(x) - f_{abc} \theta(x) G_\mu^b(x). \quad (2.18)$$

The last term that involves the gluon field itself was not present for the photon field in Equation 2.5. This comes from the non-abelian structure of the  $SU(3)$  group, in contrast to the abelian structure of  $U(1)$ . Replacing  $\partial_\mu$  in Equation 2.14 by  $D_\mu$ , and adding a kinematic term for gluons based on the gluon field strength tensor of the form:

$$G_{\mu\nu}^a(x) = \partial_\mu G_\nu^a(x) - \partial_\nu G_\mu^a(x) - g_s f_{abc} G_\nu^b(x) G_\nu^c(x), \quad (2.19)$$

one gets the QCD Lagrangian:

---

<sup>6</sup> A  $U(N)$  group is formed of unitary  $N \times N$  matrices and has  $N^2$  generators. The  $SU(N)$  denotes a special unitary group where the group is restricted by fixing the determinant of the unitary  $N \times N$  matrices to one, and therefore has  $N^2 - 1$  generators.

$$\begin{aligned}
 \mathcal{L}_{\text{QCD}} = & \underbrace{\sum_f [i\bar{q}_f(x)\gamma^\mu \partial_\mu q_f(x) - m_f \bar{q}_f(x)q_f(x)]}_{\text{free quark}} \\
 & - \underbrace{g_s \sum_f \bar{q}_f(x)\gamma^\mu \frac{\lambda_a}{2} q_f(x) G_\mu^a(x)}_{\text{quark-gluon interaction}} \\
 & - \underbrace{\frac{1}{4} G_{\mu\nu}^a(x) G_a^{\mu\nu}(x)}_{\text{gluon-gluon interaction}} .
 \end{aligned} \tag{2.20}$$

Similar to photons, mass terms for gluons are forbidden as they violate the invariance. The second part of the Lagrangian represents the colour interaction between quarks and gluons, illustrated by the Feynman diagram in Figure 2.3(a). The last term of the Lagrangian is not purely kinematic, unlike the similar term for photons in Equation 2.11. Owing to the non-abelian character of the theory, this term contains orders of  $g_s G^3$  and  $g_s^2 G^4$ . This indicates gluon self-interactions of 3- and 4-gluon vertices, as shown in Figures 2.3(b) and 2.3(c) respectively. Gluon self-interaction reflects the fact that gluons themselves carry colour charge.

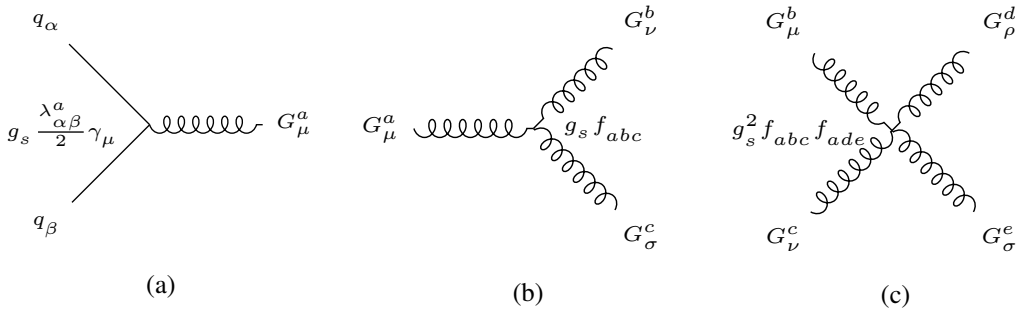


Figure 2.3: Feynman diagrams for the QCD vertices.

All interactions in Equation 2.20 are given in terms of a single universal coupling constant  $g_s$ , while in QED it was possible to assign arbitrary electromagnetic charge to each different fermion. All colour-triplet quark flavours couple to the gluons with exactly the same strength. This is also a result of the non-abelian structure of QCD.

### Asymptotic freedom, quark confinement, and the running coupling constants

The important consequences of gluons self-interactions are the *asymptotic freedom* and *colour confinement*, which can be understood in terms of *running coupling constant*. Despite the name, the coupling constants in the SM depend on the separation distance between the interacting particles, or equivalently, on the energy scale  $Q^2$ . They are said to 'run' with energy.

In QED, the effective coupling gets weaker in larger distances (lower energies), due to the vacuum polarisation which screens each charge. Its aforementioned value  $\sim \frac{1}{137}$  is in fact a measure at  $Q^2 = 0$  (far distance, fully screened charge). At an energy scale around  $W$  boson mass ( $Q^2 \approx m_W^2$ ) the value is  $\sim \frac{1}{128}$  [15]. Since the QED coupling variation over the accessible energy range is small, the value

$\alpha(0) = \frac{1}{137}$  is fine enough for most purposes.

In QCD, however, the strong coupling ( $\alpha_s = \frac{g_s^2}{4\pi}$ ) has an opposite behaviour. The virtual quark-antiquark pair productions act similar as the vacuum polarisation in QED, screening the colour charge. But there are more contributions in QCD because of the gluons self-interaction. The gluon contributions work in the other direction and have an anti-screening effect<sup>7</sup>. The anti-screening effect is in fact dominant, therefore the strong coupling constant decreases with increasing energy (decreasing distances).

As a result, at very short distances (large energy scale) the effective strong coupling becomes quite small and vanishes asymptotically. This makes the quarks to behave almost like free particles within the hadrons. The phenomena is known as asymptotic freedom.

On the other hand, if two quarks are pulled apart (decreasing energy),  $\alpha_s(Q^2)$  becomes larger and larger as they separate further. Eventually, the energy needed to pull them further apart is enough to create a quark-antiquark pair from the vacuum. Therefore, the quarks are pulled into confined states. This is known as colour confinement, and is the reason that particles which carry colour charge (quarks and gluons) do not appear as free particles.

Unlike the QED coupling, the variation of  $\alpha_s$  over the accessible energy range is substantial. Its value at the scale of  $Z$  boson mass ( $Q^2 = m_Z^2$ ) is  $\alpha_s \approx 0.1181(11)$  [15]. This is small enough to allow a perturbative treatment of QCD. In low energy scales though, QCD is non-perturbative, as the perturbation expansions in  $\alpha_s$  do not converge.

### 2.1.4 Electroweak Theory

The weak interaction is substantially weaker than both strong and electromagnetic interactions. While the lifetimes of the particles decaying through strong and electromagnetic interactions are in the order of  $\sim 10^{-23}$  s and  $\sim 10^{-16}$  s respectively, particles that decay by weak interaction last much longer. For example, the muon decay ( $\mu^- \rightarrow e^- \bar{\nu}_e \nu_\mu$ ) has a lifetime of the order of  $10^{-6}$  s.

The weak interaction was interpreted by Fermi in 1930's as a four-fermion interaction with a strength given by the Fermi constant  $G_F$ . Today it is better understood in terms of the electroweak theory. The electroweak theory unifies the electromagnetic and weak interactions. It was first proposed by Glashow [17] in 1961 and completed by Weinberg [18] and Salam [19] in 1967. The electroweak theory considers the electromagnetic and weak forces the results of a spontaneous symmetry breaking.

As mentioned in Section 2.1.1, experiments have shown that the weak interaction violates parity, as only left-handed fermions (or right-handed antifermions) couple to  $W^\pm$  bosons. The left-handed fermions appear in doublets and the right-handed ones in singlet. The  $SU(2)$  group is the simplest choice for a symmetric group with doublet representation. To include the electromagnetic interactions, an additional  $U(1)$  group is also needed (see Section 2.1.2). Thus, the symmetry group of the electroweak theory is  $SU(2) \otimes U(1)$ .

The spinor field  $\psi(x)$  that describes a fermion can be separated into left- and right-handed components, using the projection operators  $P_L$  and  $P_R$ :

$$P_{L/R}\psi(x) = \frac{1}{2}(1 \mp \gamma_5)\psi(x) = \psi_{L/R}(x), \quad (2.21)$$

where the subscripts L and R always denote the left- and right-handed, respectively, and  $\gamma_5 = i\gamma_0\gamma_1\gamma_2\gamma_3$ . Considering only one family of quarks for simplicity, the following notation is used:

$$\psi_1(x) = \begin{pmatrix} q_u \\ q_d \end{pmatrix}_L, \quad \psi_2(x) = q_{uR}, \quad \psi_3(x) = q_{dR}, \quad (2.22)$$

---

<sup>7</sup> A nice illustration can be found in Ref. [16].

where  $q_u(x)$  and  $q_d(x)$  represent the spinor fields of the up- and down-type quarks, respectively. All the following discussions are valid for the lepton sector as well; one just have to replace in the notation of Equation 2.22 the  $q_d(x)$  with a charged lepton spinor field ( $l(x)$ ) and the  $q_u(x)$  with its corresponding neutrino ( $\nu_l(x)$ ).

The free Lagrangian is written as:

$$\mathcal{L}_0 = \sum_{j=1}^3 i\bar{\psi}_j(x)\gamma^\mu\partial_\mu\psi_j(x), \quad (2.23)$$

and is invariant under the global gauge transformations of the  $SU(2)_L \otimes U(1)_Y$  group. The fermion mass terms are not included in the Lagrangian as they would mix the left- and right-handed fields and spoil the invariance. The gauge transformations of the  $SU(2)_L \otimes U(1)_Y$  group acts as:

$$\begin{aligned} \psi_1(x) &\rightarrow \psi'_1(x) \equiv e^{iy_1\beta}U_L\psi_1(x), \\ \psi_2(x) &\rightarrow \psi'_2(x) \equiv e^{iy_2\beta}\psi_2(x), \\ \psi_3(x) &\rightarrow \psi'_3(x) \equiv e^{iy_3\beta}\psi_3(x). \end{aligned} \quad (2.24)$$

The  $SU(2)_L$  transformation acts only on the doublet field  $\psi_1(x)$  through the  $2 \times 2$  unitary matrices  $U_L$ :

$$U_L = e^{i\alpha_a \frac{\sigma_a}{2}}, \quad (2.25)$$

where  $\sigma_a$  ( $a = 1, 2, 3$ ) are the three generators of the  $SU(2)$  group, known as Pauli matrices. Same as QCD, this is a non-abelian gauge symmetry since  $\sigma_a$  are non-commutative:  $[\sigma_a, \sigma_b] = 2i\epsilon_{abc}\sigma_c$ . The  $U(1)_Y$  transformation is a simple phase transformation as in QED (Equation 2.3) and in analogy, the parameters  $y_i$  are called hypercharges.

Requiring the Lagrangian to hold its invariance locally, i.e. when  $\alpha_a = \alpha_a(x)$  ( $a = 1, 2, 3$ ) and  $\beta = \beta(x)$ , introduces four new vector gauge fields  $W_\mu^a(x)$  ( $a = 1, 2, 3$ ) and  $B_\mu(x)$ , and covariant derivation  $D_\mu$  that acts on the fields as:

$$\begin{aligned} D_\mu\psi_1(x) &\equiv [\partial_\mu + ig\frac{\sigma_a}{2}W_\mu^a(x) + ig'y_1B_\mu(x)]\psi_1(x), \\ D_\mu\psi_2(x) &\equiv [\partial_\mu + ig'y_2B_\mu(x)]\psi_2(x), \\ D_\mu\psi_3(x) &\equiv [\partial_\mu + ig'y_3B_\mu(x)]\psi_3(x), \end{aligned} \quad (2.26)$$

where  $g$  and  $g'$  are the coupling constants of  $SU(2)_L$  and  $U(1)_Y$  respectively. Similar as in QED, the hypercharges are arbitrary parameters and  $g'$  is a free parameter. This does not hold for  $g$ , as it is unique due to the non-abelian structure of the  $SU(2)_L$ , similar as in QCD. After replacing  $\partial_\mu$  in Equation 2.23 with  $D_\mu$ , the last step is adding kinematic terms for the gauge fields, using the strength tensors:

$$B_{\mu\nu}(x) \equiv \partial_\mu B_\nu(x) - \partial_\nu B_\mu(x), \quad (2.27)$$

$$W_{\mu\nu}^a(x) = \partial_\mu W_\nu^a(x) - \partial_\nu W_\mu^a(x) - g\epsilon_{abc}W_\nu^b(x)W_\nu^c(x). \quad (2.28)$$

Then, the Lagrangian of the electroweak theory is written as:

$$\begin{aligned}
 \mathcal{L}_{\text{EW}} = & \underbrace{\sum_{j=1}^3 i\bar{\psi}_j(x)\gamma^\mu\partial_\mu\psi_j(x)}_{\text{free massless fermion}} \\
 & \underbrace{-g\bar{\psi}_1(x)\gamma^\mu\frac{\sigma_a}{2}\psi_1(x)W_\mu^a(x) - g' \sum_{j=1}^3 y_i\bar{\psi}_j(x)\gamma^\mu\psi_j(x)B_\mu}_{\text{fermion-boson interaction}} \\
 & \underbrace{-\frac{1}{4}B_{\mu\nu}B^{\mu\nu} - \frac{1}{4}W_{\mu\nu}^a(x)W_a^{\mu\nu}(x)}_{\text{boson-boson interaction}} .
 \end{aligned} \tag{2.29}$$

The interaction terms between fermion fields and the gauge bosons contain charged-current and neutral-current interactions. The charged-current interactions are mediated by the gauge fields:

$$W_\mu^\pm = \frac{1}{\sqrt{2}}(W_\mu^1 \pm iW_\mu^2), \tag{2.30}$$

and transition the flavour between the components of the doublet field  $\psi_1(x)$ , as shown in Figure 2.4. The current term in the charged-current interactions has the form of  $\bar{\psi}\gamma^\mu(1 - \gamma_5)\psi$ , which is a vector minus axial vector (V-A) structure. This is different from the current terms  $\bar{\psi}\gamma^\mu\psi$  with a pure vector structure, seen before in QED and QCD Lagrangians (Equations 2.11 and 2.20). This V-A structure manifests the parity violation nature of the weak interaction, taking into account Equation 2.21.

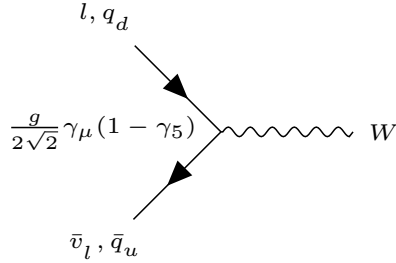


Figure 2.4: Feynman diagrams for charged-current weak interaction vertex.

The neutral-currents conserve the fermion flavour. They are mediated by the gauge fields:

$$\begin{aligned}
 Z_\mu &= \cos\theta_W W_\mu^3 - \sin\theta_W B_\mu, \\
 A_\mu &= \sin\theta_W W_\mu^3 + \cos\theta_W B_\mu,
 \end{aligned} \tag{2.31}$$

where  $\theta_W$  is called the *weak mixing angle* and defined as:

$$\sin\theta_W = \frac{g'}{\sqrt{g^2 + g'^2}}, \quad \cos\theta_W = \frac{g}{\sqrt{g^2 + g'^2}}. \tag{2.32}$$

In order for the  $A_\mu$  in Equation 2.31 to be identical to the photon of QED theory, these conditions

must be hold:

$$g \sin \theta_W = g' \cos \theta_W = e, \quad \frac{Y}{2} = Q - I_3, \quad (2.33)$$

where  $e$  is the elementary charge,  $Q$  is the electric charge that is the conserved quantity in QED (see Section 2.1.2),  $I_3 = \frac{\sigma_3}{2}$  is the third component of the weak isospin  $I$  that is the conserved quantity in  $SU(2)_L$ , and  $Y$  is the hypercharge that is the conserved quantity in  $U(1)_Y$ . In the neutral-current interaction terms, the coupling of fermions to  $Z$  boson also appears with a V-A structure, but with more complexity since it follows a form of  $\gamma^\mu(c_A - c_V\gamma_5)$  where  $c_A \neq c_V \neq 1$ .

Same as for the gluons, due to the non-abelian structure of the  $SU(2)$  group the kinematic terms of the gauge bosons in Equation 2.29 are not purely kinematics and they contain cubic and quadratic self-interactions among the gauge bosons, as shown in Figure 2.5.

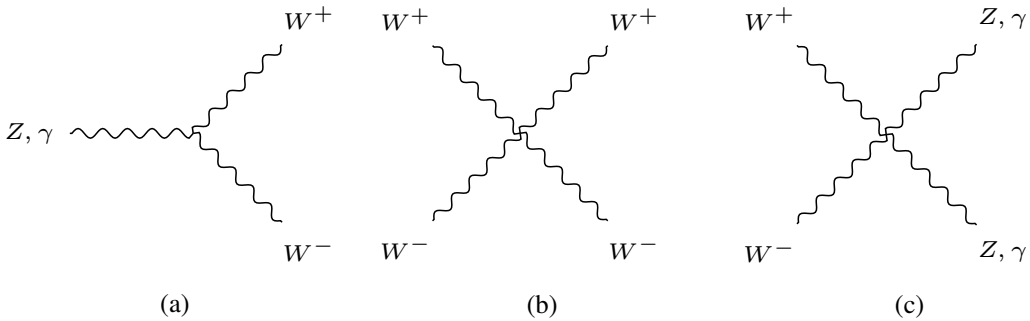


Figure 2.5: Feynman diagrams for Electroweak gauge bosons self-interaction.

The local gauge symmetry forbids to add mass terms for the gauge bosons to Equation 2.29. This was not a problem for photon and gluons, but experiments have shown that the  $W$  and  $Z$  bosons are massive. Also, as mentioned earlier there are no mass terms for the fermions in Equation 2.29, because they would communicate the left- and right-handed fields which have different transformation properties (Equation 2.24) and breaks the gauge symmetry. In Section 2.1.5 it is explained how the masses of weak bosons and fermions enter the theory.

## CKM matrix

As mentioned in Section 2.1.1, the weak eigenstates of the quarks are not equal to their flavour eigenstates. A unitary  $3 \times 3$  matrix had to be introduced in order to translate the flavour eigenstates (denoted by  $d'$ ,  $s'$ , and  $b'$ ) to the mass eigenstates (denoted by  $d$ ,  $s$ , and  $b$ ):

$$\begin{pmatrix} d' \\ s' \\ b' \end{pmatrix} = \begin{pmatrix} V_{ud} & V_{us} & V_{ub} \\ V_{cd} & V_{cs} & V_{cb} \\ V_{td} & V_{ts} & V_{tb} \end{pmatrix} \begin{pmatrix} d \\ s \\ b \end{pmatrix}. \quad (2.34)$$

This matrix is known as the *CKM matrix*, taken its name from Cabibbo, Kobayashi, and Maskawa who developed it. The CKM matrix in fact describes the strength of flavour-changing weak decays, mediated by  $W^\pm$  bosons. The transition probability for a quark of flavour  $q_1$  to a quark of flavour  $q_2$  is proportional to  $|V_{q_1 q_2}|^2$ .

### 2.1.5 The Electroweak Symmetry Breaking and the Higgs-Englert-Brout Mechanisms

Unlike photon and gluons, the  $Z$  and  $W^\pm$  bosons are massive. But as seen in Section 2.1.4 the gauge symmetry prevents to add mass terms for them to the Lagrangian. To generate the masses, the gauge symmetry must be broken in some way, but a fully symmetric Lagrangian is still needed in order to preserve the renormalisability of the theory. This is solved by a process known as *spontaneous symmetry breaking (SSB)*, and the Higgs-Englert-Brout mechanisms [20, 21]. The symmetry is broken as  $SU(2)_L \otimes U(1)_Y \rightarrow U(1)_{em}$ , where  $em$  stands for electromagnetic.

To achieve SSB in the framework of SM, an additional  $I = 1/2$  doublet of complex scalar fields is introduced:

$$\Phi(x) = \begin{pmatrix} \phi^+(x) \\ \phi^0(x) \end{pmatrix}, \quad (2.35)$$

where:

$$\begin{aligned} \phi^+(x) &= \frac{1}{\sqrt{2}}(\phi_1(x) + i\phi_2(x)), \\ \phi^0(x) &= \frac{1}{\sqrt{2}}(\phi_3(x) + i\phi_4(x)). \end{aligned} \quad (2.36)$$

This is called the Higgs field, with four real components in total. The contribution of the Higgs sector to the Lagrangian of SM is:

$$\mathcal{L}_{\text{Higgs}} = (D_\mu \Phi(x))^\dagger (D_\mu \Phi(x)) \underbrace{-\mu^2 \Phi^\dagger(x) \Phi(x) - \lambda (\Phi^\dagger(x) \Phi(x))^2}_{-V(\Phi)}, \quad (2.37)$$

where  $D_\mu$  is the covariant derivative defined in Equation 2.26, with the hypercharge parameters being fixed to  $y_\Phi = 1/2$ . The value is fixed by requiring the correct couplings between  $\Phi(x)$  and  $A_\mu(x)$ ; i.e. photon does not couple to the neutral  $\phi^0$ , and the  $\phi^+$  has the right electric charge ( $Q = +1$ ). The Lagrangian is invariant under local  $SU(2)_L \otimes U(1)_Y$  transformation. The last two terms form the potential  $V(\Phi)$ , where  $\mu, \lambda \in \mathbb{R}$ ,  $\lambda > 0$  and  $\mu^2 < 0$ . The constant  $\lambda$  must be greater than zero in order to bound the potential from below. The constant  $\mu^2$  is chosen to be negative because this leads to a non-vanishing  $\Phi$  field at the minimum of the potential, corresponding to a scenario in which the gauge symmetry is broken in the expected vacuum state. In a QFT, the ground state (the lowest energy state) is the vacuum; thus the SSB mechanism will appear when there is a symmetric Lagrangian but a non-symmetric vacuum.

Minimising the potential  $V(\Phi)$  with respect to  $\Phi \Phi^\dagger$  yields:

$$\Phi_{\text{vac}} \Phi_{\text{vac}}^\dagger = |\Phi_{\text{vac}}|^2 = \phi_{1,\text{vac}}^2 + \phi_{2,\text{vac}}^2 + \phi_{3,\text{vac}}^2 + \phi_{4,\text{vac}}^2 = \frac{v^2}{2}, \quad v \equiv \sqrt{\frac{-\mu^2}{\lambda}}, \quad (2.38)$$

where the quantity  $v$  is called the *vacuum expectation value*. Thus, there is a set of equivalent minima lying around a circle of radius  $v$ , instead of a unique vacuum state. Choosing one of them breaks the  $SU(2)_L \otimes U(1)_Y$  gauge symmetry spontaneously, but preserves the invariance under a residual  $U(1)$  symmetry that can be identified with electromagnetism.

From all the possible solutions of Equation 2.38, without loosing generality one can choose

$$\phi_{1,\text{vac}} = \phi_{2,\text{vac}} = \phi_{4,\text{vac}} = 0, \quad \phi_{3,\text{vac}} = v, \quad (2.39)$$

and expand the perturbations around the chosen vacuum as:

$$\Phi(x) = \frac{1}{\sqrt{2}} \begin{pmatrix} 0 \\ v + H(x) \end{pmatrix}. \quad (2.40)$$

Substituting Equation 2.40 in Equation 2.37, expanding the covariant derivatives, and using the expressions in Equations 2.30 and 2.31, gives rise to the following points<sup>8</sup>: The scalar field  $H(x)$ , representing the Higgs boson, has a mass term with

$$m_H^2 = -2\mu^2 > 0. \quad (2.41)$$

The mass terms for the weak gauge bosons also appear now in the Lagrangian with

$$\begin{aligned} m_W &= \frac{gv}{2}, \\ m_Z &= \frac{v}{2} \sqrt{g^2 + g'^2}, \end{aligned} \quad (2.42)$$

while the photon remains massless ( $m_A = 0$ ). Using Equation 2.33, it can be seen than the masses of  $W^\pm$  and  $Z$  bosons are related to each other through the weak mixing angel:

$$\cos \theta_W = \frac{m_W}{m_Z}. \quad (2.43)$$

The Lagrangian also includes interaction terms between the Higgs boson and the massive gauge bosons, with the coupling constants determined in terms of  $m_Z$ ,  $m_W$ , and  $v$ , and self-interaction terms of the Higgs boson, with the coupling constants in terms of  $m_H$  and  $v$ . The interaction vertices are shown in Figure 2.6.

The Higgs-Englert-Brout mechanisms also generates mass for all the fermions. This is done by including the interaction terms between the Higgs doublet and the fermions in the theory. These couplings are referred to as *Yukawa couplings*. The corresponding Lagrangian sector for one family of the quarks and the leptons is written as:

$$\mathcal{L}_{\text{Yukawa}} = -G_d (\bar{q}_u, \bar{q}_d)_L \begin{pmatrix} \phi^+ \\ \phi^0 \end{pmatrix} q_{dR} - G_u (\bar{q}_u, \bar{q}_d)_L \begin{pmatrix} \phi^{0*} \\ -\phi^- \end{pmatrix} q_{uR} - G_l (\bar{\nu}_l, \bar{l})_L \begin{pmatrix} \phi^+ \\ \phi^0 \end{pmatrix} l_R + \text{h.c.}, \quad (2.44)$$

where "h.c." indicates hermitian conjugate, and the second term involves the charge conjugated Higgs doublet  $\Phi^C \equiv i\sigma_2 \Phi^*$ . Additional fermion families can be included in the theory simply by adding their corresponding terms to the Lagrangian. This Lagrangian is invariant under  $SU(2)_L \otimes U(1)_Y$ . By substituting Equation 2.40, i.e. breaking the symmetry spontaneously,  $\mathcal{L}_{\text{Yukawa}}$  reduces to:

$$\mathcal{L}_{\text{Yukawa}} = -(1 + \frac{H}{v}) (m_d \bar{q}_d q_d + m_u \bar{q}_u q_u + m_l \bar{l} l), \quad (2.45)$$

where  $\bar{f} \equiv (\bar{f}_R, \bar{f}_L)$  and  $f \equiv (f_L, f_R)^T$  for  $f = l, q_u, q_d$ , and

---

<sup>8</sup> See the expanded  $\mathcal{L}_{\text{Higgs}}$  in Ref. [14].

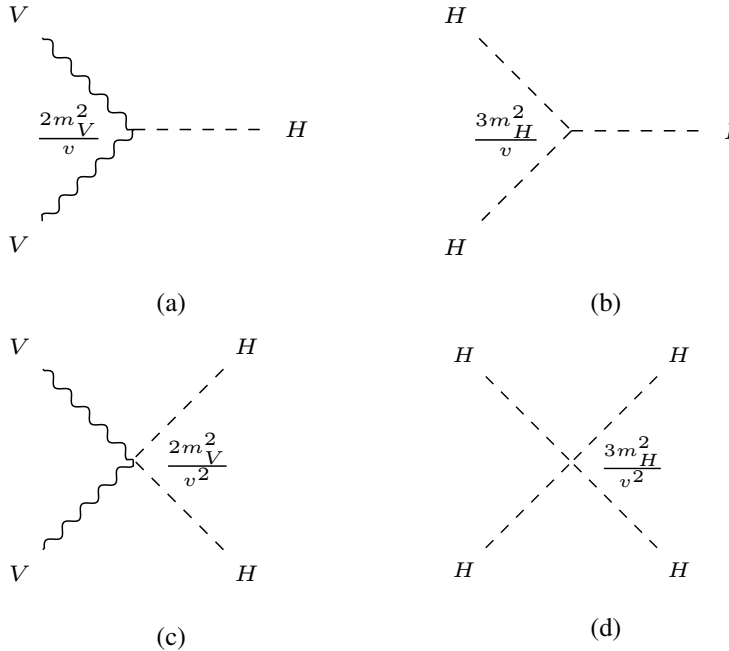


Figure 2.6: Feynman diagrams for Higgs interaction vertices, where  $V$  stands for the massive vector bosons ( $Z$ ,  $W^+$  and  $W^-$ ).

$$m_d = \frac{vG_d}{\sqrt{2}}, \quad m_u = \frac{vG_u}{\sqrt{2}}, \quad m_l = \frac{vG_l}{\sqrt{2}} \quad (2.46)$$

are the masses of the fermions. In the SM neutrinos are massless, since no right-handed neutrino exists. The neutrino oscillation phenomenon that requires massive neutrinos is beyond the SM.

## 2.2 Proton-Proton Interactions

As discussed in Section 2.1.1, hadrons consist of two or three (anti)quarks, bound together by exchanging gluons. These are called the *valence (anti)quarks*. However, the quantum fluctuations can cause a gluon to split into a pair of virtual quark-antiquark which then annihilates back into a gluon. The gluons themselves can interact and produce more gluons. Therefore, a hadron does not only consist of valence (anti)quarks, but also a *sea* of quarks, antiquarks and gluons.

The proton is the lightest baryon. It is a composite of three valence quarks, two  $u$ -quarks and one  $d$ -quark ( $uud$ ), giving it a net electric charge of +1. The other baryon that makes up the ordinary matter, the neutron, has a  $udd$  composition and is neutral. The neutron is slightly heavier than the proton, therefore a free neutron decays into a proton via the conversion of a  $d$ -quark to a  $u$ -quarks in a weak interaction mediated by  $W$  bosons, as shown in Figure 2.8. Baryon number conservation, however, keeps the proton stable.

A high-energy proton-proton ( $pp$ ) collision, such as those occurring in the LHC, can not be described as an interaction of point-like protons. Rather, these are the constituents of the protons that interact: valence quarks, sea quark and antiquarks, and gluons, collectively referred to as *partons*. In the following, the relevant aspects of the physics of  $pp$  collisions at the LHC are briefly introduced, based on Refs. [23–26].

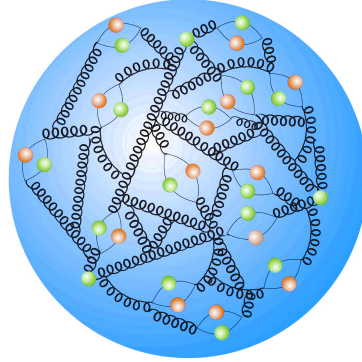


Figure 2.7: A schematic illustration of proton composition of partons, where quarks are represented by green circles, antiquarks by orange circles, and gluons by springs. Image taken from [22].

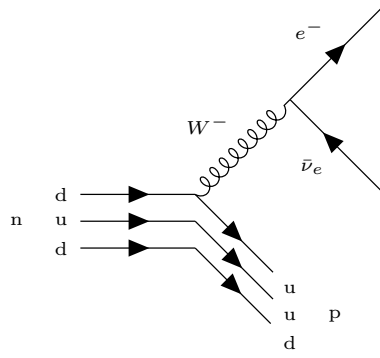


Figure 2.8: A Feynman diagram of the decay of a neutron into a proton

### 2.2.1 Parton Density Functions

When a proton is accelerated, its momentum is distributed among its constituents, each carrying a fraction of the total momentum. The Parton Distribution Function (PDF)  $f_i(x)$  describes the probability of a given parton of type  $i$  to carry a given fraction  $x$  of the proton momentum. One can stipulate:

$$\sum_i \int_0^1 x f_i(x) dx = 1, \quad (2.47)$$

where  $i$  runs over all parton types.

The internal structure of a proton can not be described in a perturbative QCD approach, since it involves low momentum transfers, hence high  $\alpha_s$  (see Section 2.1.3). Therefore, PDFs need to be determined experimentally.

The determination of PDFs typically involves global fits to data-sets from several experiments. They are mainly extracted from deep inelastic scattering experiments, e.g. electron-proton collisions in HERA. Additional constraints can be added from experimental data of Drell-Yan and jet production processes. The level of structure revealed increases with the energy scale at which the proton is probed, i.e. the energy transfer  $Q^2$  in the collision. Although the PDFs are of non-perturbative origin, their evolution with  $Q^2$  can be calculated from DGLAP equations [27–30] that are derived from perturbative QCD. Once the PDF at a given scale  $Q_0^2$  is fixed from the fit to experimental data, its evolution at any given

scale  $Q^2 > Q_0^2$  can be described by DGLAP equations at leading order (LO), next-to-leading order (NLO), or next-to-next-to-leading order (NNLO) in the perturbative development in the strong coupling constant,  $\alpha_s(Q^2)$ .

There are several collaborations that provide PDFs, with semi-regular updates when new data and/or theoretical developments become available, such as MSTW [31], CTEQ [32], and NNPDF [33]. Examples of PDFs provided by MSTW collaboration at two different  $Q^2$  values are shown in Figure 2.9. It can be seen that the sea-quark distributions are mainly concentrated at small  $x$  values while the valence-quark distributions are extended to moderate and high  $x$  values, showing that the valence quarks carry higher fractions of the proton momentum than sea quarks. The gluon distribution increases more steeply towards low  $x$  than the valence- or the sea-quark distributions, and they are dominant at low  $x$  range. Going to a higher energy scale enhances the contributions of soft gluons and sea quarks.,

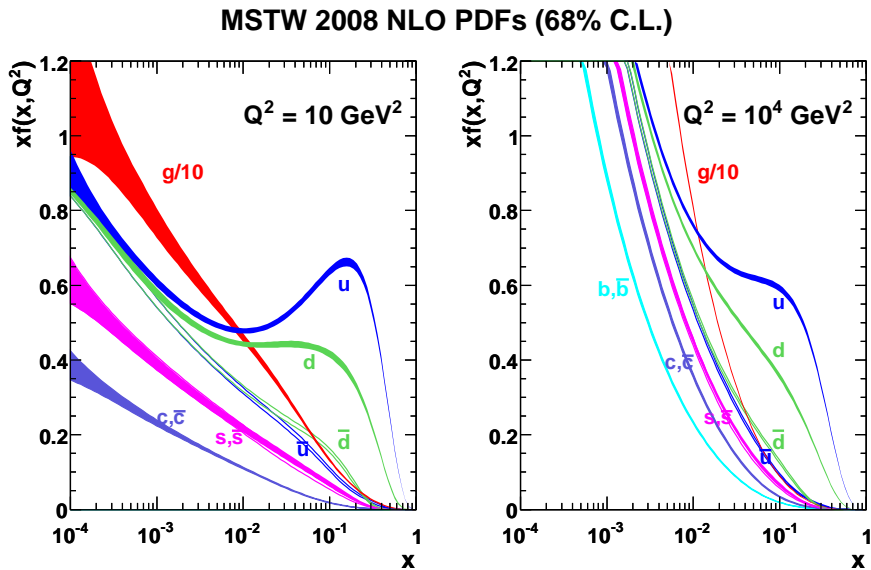


Figure 2.9: The PDFs provided by MSTW group using NLO predictions at  $Q^2 = 10 \text{ GeV}^2$  (left) and  $Q^2 = 10^4 \text{ GeV}^2$  (right) [31]. The estimations for gluons are divided by 10.

## 2.2.2 Overview of a Proton-Proton Collision

A  $p\bar{p}$  collision that leads to production of new particles is a rather complex process, but it can be separated into the following parts, which are also summarised in Figure 2.10.

### Hard Scattering Process

When two partons, one from each of the colliding protons, interact with a sufficiently large momentum transfer, the energy is enough to break the partons confinement and produce new particles. This is the *hard scattering process* of interest.

### Initial and Final State Radiations

The accelerated colour and electrical charges can radiate gluons (QCD radiation) and photons (QED radiation) through bremsstrahlung process. Emissions from the incoming partons of a hard process are

referred to as *initial state radiations (ISR)* and the radiations made by the outgoing particles are called *final state radiations (FSR)*.

### Parton Shower

When accelerated coloured particles radiate gluons, the emitted gluons themselves can further emit QCD radiations since they carry colour, or produce quark-antiquark pairs. Then the newly emitted gluons, quarks and antiquarks continue the same behaviour, leading to a cascade of particles referred to as *parton showers*.

### Hadronisation

As explained in the previous Section, due to colour confinement quarks and gluons can not be observed individually. As the outgoing quarks and gluons (scattered partons and proton remnants) separate further, or equivalently as the interaction scale falls during the parton showering, the strong coupling of the colour charges rises. It rises to the point that the neutralising colour charges get created out of vacuum. The initial quarks and gluons join with these newly created colour-charged particles and form colour-neutral hadrons. This process is known as *hadronisation*.

Hadronisation is a non-perturbative process, as it involves interactions with small momentum transfer, hence large coupling constant. It is therefore only described by phenomenological models. Two commonly used models are the Lund (String) Model [34] and the Cluster Model [35].

When a quark or a gluon goes through parton showering and hadronisation, it originates a *jet*. A jet is a collimated spray of energetic hadrons that emerges approximately in the direction of the parton that has originated it.

### Decay

The hadrons formed in the hadronisation stage, or any other unstable particles that are produced within the hard scattering process decay into more stable particles.

### Underlying Events

The remaining partons of each proton may continue to travel in the original direction of the proton beams, forming the beam remnants that go through hadronisation, or can also interact. These interactions are typically soft and involve low momentum transfer, and referred to as the *underlying events*.

### Pile-up

In the LHC the  $pp$  collisions are performed by colliding bunches of protons rather than single protons, to increase the chance of collision (see Section 3.1 for detail). In a single bunch crossing multiple  $pp$  collisions can occur, a phenomenon known as *pile-up* (not included in Figure 2.10). Besides the underlying events, pile-up is another source of soft QCD interactions. Pile-up could be *in-time*, which are the additional  $pp$  collisions occur during the same bunch crossing that includes the hard process of interest, or *out-of-time* that refers to the additional  $pp$  collisions from the bunch crossing just before or after of it.

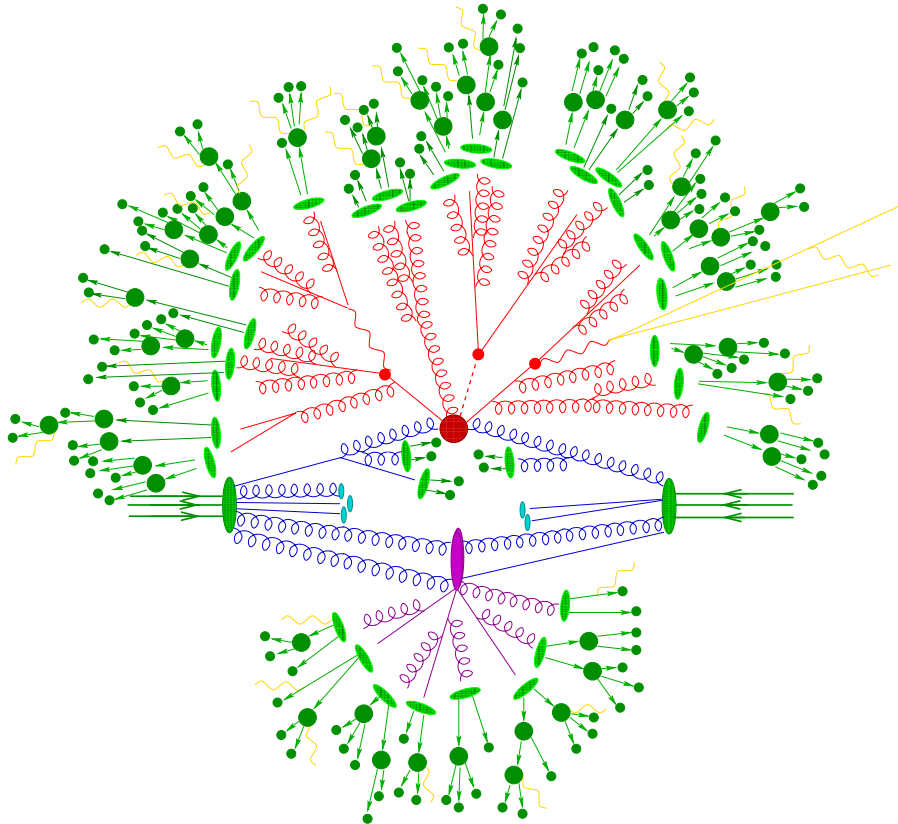


Figure 2.10: Pictorial representation of an example for a  $pp$  collision leading to new particles production, here  $t\bar{t}H$  production. The hard scattering process is shown with the big red bulb in the middle. It is followed by the decay of both top quarks and the Higgs boson, shown with small red bulbs. Additional QCD radiations are shown in red, while the initial state radiations coming out of the incoming partons are shown in blue. Secondary interactions shown by big purple bulb happens, forming the underlying events. Hadronisation of the colour-charged particles are shown with light green bulbs, and the decay of hadrons with dark green bulbs. The QED radiations happen in form of photons, shown in yellow waves. [36]

### 2.2.3 Cross Sections in Proton-Proton Collisions

*Cross section* is a measure of the probability that under a given initial and final state conditions, a specific scattering process happens. The cross section of the process of interest in  $pp$  collisions is often the quantity that its theory prediction is being experimentally verified in a physics analysis. Predicted cross sections of some relevant processes at the Tevatron collider ( $p\bar{p}$  collisions) and at the LHC ( $pp$  collisions) are shown in Figure 2.12 as an example.

In high energy  $pp$  collisions, the hard scattering processes can be described by the perturbative QCD, as they involve large momentum transfer and therefore a small coupling constant ( $\alpha_s \ll 1$ ). On the other hand, the energy available for the process depends on the PDFs, which as explained before are non-perturbative. The *factorisation theorem* allows to treat these domains separately. According to the factorisation theorem, the cross section of hadron collisions can be separated into two parts: a hard scattering partonic cross section which is calculated from perturbative QCD, and the soft non-perturbative terms which are factored into universal PDFs and are independent from the hard scatter process. The  $Q^2$  scale that separates these two domains is called the *factorisation scale*.

Assuming the hard scatterings that occur between partons  $a$  and  $b$  from protons  $A$  and  $B$ , and result

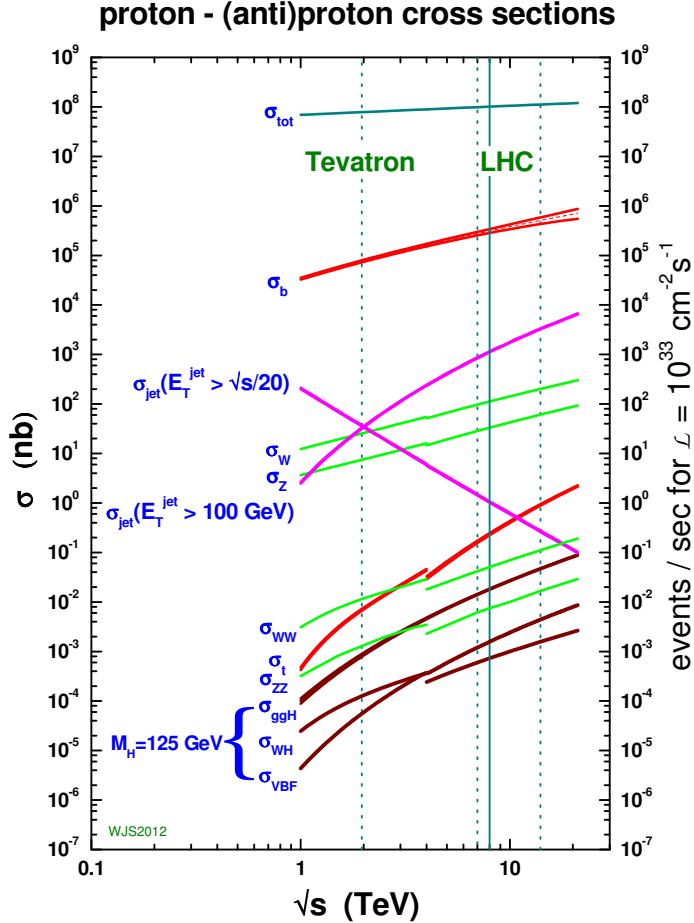


Figure 2.11: SM predictions for hard-scattering cross sections in  $p\bar{p}(pp)$  collisions at the Tevatron(LHC) collider as a function of centre-of-mass energy [37].

into the final state  $X$  ( $ab \rightarrow X$ ), the total cross section of two colliding protons can be written as:

$$\sigma_{AB} = \sum_{a,b} \int_0^1 \int_0^1 dx_a dx_b f_a(x_a, \mu_F^2) f_b(x_b, \mu_F^2) \times \hat{\sigma}^{ab \rightarrow X}(\sqrt{\hat{s}}, \mu_F^2, \mu_R^2), \quad (2.48)$$

where the sum runs over all possible combinations of initial state partons  $a$  and  $b$  that result a final state  $X$ ,  $\mu_F$  is the factorisation scale, and  $\hat{\sigma}$  is the hard scattering partonic cross section. The effective centre-of-mass energy for the partonic process is

$$\sqrt{\hat{s}} = \sqrt{x_a x_b s}, \quad (2.49)$$

where  $\sqrt{s}$  is the centre-of-mass energy of the  $pp$  collision. The PDFs  $f_{a/b}(x_{a/b}, \mu_F^2)$  are evaluated at the scale  $\mu_F^2$  as explained in Section 2.2.1.

Partonic cross sections are calculated from scattering amplitudes. In calculation of the amplitudes, all

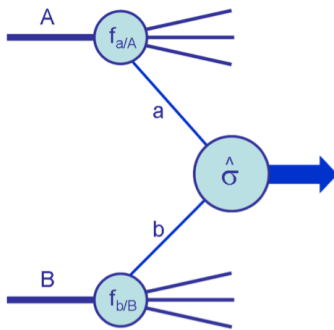


Figure 2.12: Schematic diagram of the structure of a hard scattering process in a  $pp$  collision. Taken from [24].

possibilities have to be integrated over. In higher order calculations infinities such as ultraviolet<sup>9</sup> divergences in loop diagrams appear, due to the momenta in the denominator. The divergences are removed by the renormalisation procedure, where the singularities are absorbed by parametrising the coupling constant. This enters another scale called *renormalisation scale*, denoted by  $\mu_R$ , into Equation 2.48 through the renormalised coupling  $\alpha_s(\mu_R^2)$ .

In the frame work of perturbative QCD the partonic cross section can be expanded in terms of the strong coupling  $\alpha_s$ :

$$\hat{\sigma}^{ij \rightarrow X} = \sum_{n=1} \alpha_s^n(\mu_R^2) \hat{\sigma}_n \quad (2.50)$$

The lowest order of the precision (LO,  $n = 1$ ), corresponds to the amplitude, or the Matrix Element (ME), calculated from the tree-level Feynman diagrams. The higher orders (NLO, NNLO, ...) involve more complex Feynman diagrams including radiation of gluons, loops and boxes.

Both factorisation and renormalisation scales are arbitrary. Typically the momentum transfer of the hard process is a good choice for these scales.

The cross section calculated to all orders in perturbative theory is invariant under changes in  $\mu_F$  and  $\mu_R$  scales. However, if calculated in a fix order of precision, the cross section has dependency on these unphysical scales. By varying the choices of the two scales, one gets a handle on the theoretical uncertainties. Including higher order of terms in the perturbative expansion makes the dependency weaker. Thus, LO calculations suffer from a larger uncertainty. For most processes the results obtain at NLO or NNLO are sufficiently significant.

## 2.3 Top Quark

This section briefly discusses the top quark; a more thorough treatment can be found in Refs. [15, 38], and a review on the status of the top-quark physics in Ref. [39].

The existence of a third generation of quarks was first postulated by Kobayashi and Maskawa in 1973 [40]. Once the existence of the bottom quark was inferred from the observation of upsilon-meson resonances in 1977 [41, 42], the search for its weak isospin partner, the top quark, was launched. However, it took nearly two decades of intensive experimental efforts until finally the top quark was discovered. Due to the heavy mass of the top quark, its discovery was only made possible by the tech-

<sup>9</sup> High momentum transfer regime is referred to as ultraviolet, and the low momentum transfer regime as infrared.

nological progresses in high energy physics. The discovery of the top quark was announced in 1995 by CDF [1] and DØ [2] experiments at the Tevatron collider, using the data collected from proton-antiproton ( $p\bar{p}$ ) collisions at the centre-of-mass energy of 1.8 TeV. This confirmed the three-generation structure of the SM.

Top quark has many properties that make it an interesting particle to study. It is the heaviest of all known elementary particles. With a mass of  $173.34 \pm 0.76$  GeV [43], it is significantly heavier than the next heaviest quark, the bottom quark. Given its large mass, it has a very short lifetime ( $\approx 5 \times 10^{-25}$  s [15]) which is one order of magnitude shorter than the characteristic hadronisation time of QCD. This means that top quarks decay before forming a hadron; contrary to the other five quarks which are confined in hadrons. This peculiarity offers an unique opportunity to study a bare quark that passes on its properties, such as its spin information, directly to its decay products. In addition, the large mass of top quark implies a large coupling to the Higgs boson, as the Yukawa coupling constant is proportional to the mass of fermion (see Equation 2.46). Top quark is the only fermion that has a Yukawa coupling very close to unity, making it a relevant place to look for the signatures of new physics scenarios. With a mass close to the electroweak symmetry breaking scale, the top quark is speculated to play an important role in the understanding of the electroweak symmetry breaking mechanism.

### 2.3.1 Top Quark Production in Proton-Proton Collisions

In  $pp$  collisions, top quarks can be produced singly or as a pair of top and antitop ( $t\bar{t}$ ). While the single top can only be produced via electroweak interactions, the pair production occurs dominantly via strong interaction. Hence, the  $t\bar{t}$  production cross section is around two to three times larger than the single-top production cross section, due to the different couplings strengths of weak and strong interactions.

The strong  $t\bar{t}$  production in LO has contributions from the gluon-gluon fusion ( $gg \rightarrow t\bar{t}$ ) and the quark-antiquark annihilation ( $q\bar{q} \rightarrow t\bar{t}$ ) processes. Figure 2.13 shows the corresponding Feynman diagrams. In  $pp$  collisions, antiquarks only appear as sea quarks. Therefore, the quark-antiquark annihilation takes place between valance or sea quarks and sea antiquarks. The required partonic centre-of-mass energy for the  $t\bar{t}$  production according to Equation 2.49 is  $\sqrt{x_a x_b s} \geq 2m_{\text{top}}$ , with  $m_{\text{top}}$  being the mass of the top quark. For large  $\sqrt{s}$  values, as in the LHC, small  $x_{a/b}$  values and large  $Q^2$  scales are relevant. As explained in Section 2.2.1, this corresponds to a range significantly dominated by gluons. For these two reasons, the gluon-gluon fusion is the dominant process for the  $t\bar{t}$  production at the LHC ( $\sim 90\%$  for  $\sqrt{s} = 13$  TeV [39]). At NLO,  $t\bar{t}$  production processes include higher-order corrections to the LO, like additional real emission of gluon and loops. The processes with  $qg$  and  $\bar{q}g$  initial states appear first in the NLO.

The production of single-top quark takes place via electroweak charged-current interactions. Some Feynman diagrams of the LO processes contributing in single-top production are shown in Figure 2.14. Based on the virtuality of the  $W$  boson involved in the interaction, they are categorised into the  $t$ -channel ( $ub \rightarrow tb$  or  $db \rightarrow t\bar{u}$ , Figure 2.14(a)), the  $s$ -channel ( $u\bar{d} \rightarrow t\bar{b}$ , Figure 2.14(b)), and the  $Wt$ -channel ( $gb \rightarrow Wt$ , Figure 2.14(c)). In the later case, a top quark is produced in association with a  $W$  boson. At the LHC, the dominant single-top production process is the  $t$ -channel, followed by the  $Wt$ -channel.

### 2.3.2 Top Quark Decay

Since top quarks decay very quickly, the distance between its production and decay vertices is shorter than the spatial resolution of any detector, by many orders of magnitude. Therefore, top quarks can only be detected via their decay products.

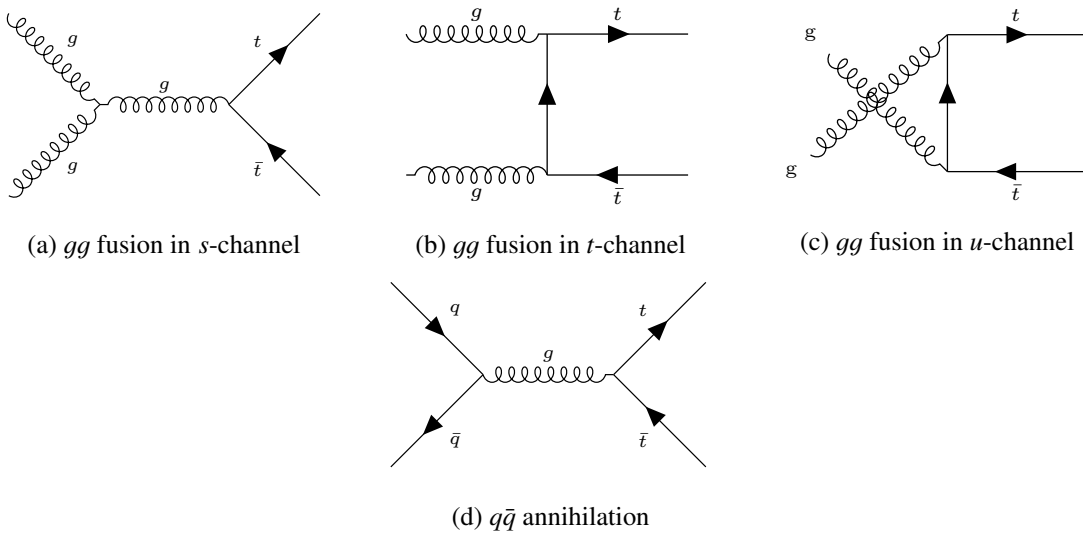


Figure 2.13: Leading-order Feynman diagrams contributing to top-quark pair production via strong interactions.

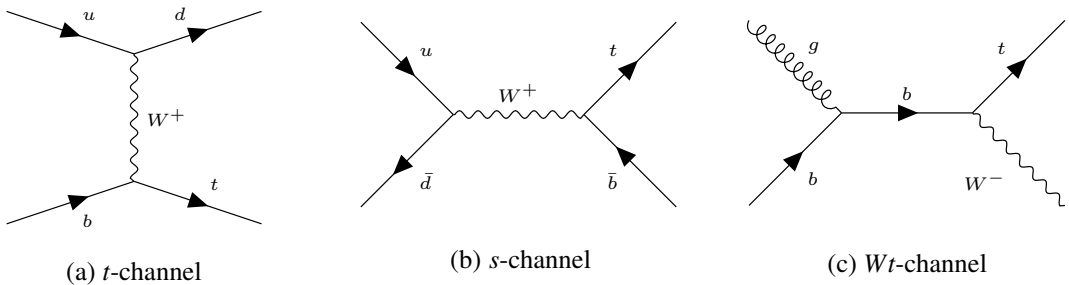


Figure 2.14: Leading-order Feynman diagrams contributing to the single-top production via electroweak interactions.

Top quark is the only quark heavier than the  $W$  boson, therefore it can directly decay through  $t \rightarrow Wq$ . The large mass difference allows for a large decay phase-space, resulting to the short lifetime of the top quark. Considering that the value of  $V_{tb}$  element of the CKM matrix (see Section 2.1.4) is very close to one, top quark decays almost inclusively into a  $W$  boson and a  $b$ -quark. The decay of top quark to a  $Wd$  or  $Ws$  final state are suppressed by the far smaller CKM off-diagonal elements ( $|V_{tb}| \gg |V_{ts}|, |V_{td}|$ ). The top-quark decay width for a value of  $m_{\text{top}} = 173.3$  GeV is predicted to be 1.35 GeV, corresponding to a mean lifetime of  $\approx 5 \times 10^{-25}$  s [15].

The  $W$  boson further decays, either leptonically – into a charged lepton and its corresponding neutrino ( $W^+ \rightarrow l^+ \nu_l$ ,  $W^- \rightarrow l^- \bar{\nu}_l$ ,  $l = e, \mu, \tau$ ), or hadronically – into a quark and antiquark of the first two families ( $W^+ \rightarrow q_1 \bar{q}_2$ ,  $W^- \rightarrow \bar{q}_1 q_2$ ,  $q_1 = u, c$ ,  $q_2 = d, s$ ). Considering that each of the hadronic decays has three possible colour combinations, and neglecting the lepton and quark masses, one expects two third of the  $W$  bosons to decay hadronically.

The decay mode of the  $W$  boson defines the final state of a top quark production process. In the case of  $t\bar{t}$  production, there are three possible final states: The *dilepton channel* where both  $W$  bosons decay leptonically, the *single-lepton channel* where one  $W$  boson decay leptonically and the other one into quarks, and the *all-hadronic channel* where both  $W$  boson decay into quarks. The respective branching fractions are shown in Figure 2.15(a). The final state relevant to this thesis is the single-lepton channel,

shown in Figure 2.15(b). It has a higher production rate than the dilepton channel and a better signal-to-background ratio than the all-hadronic channel.

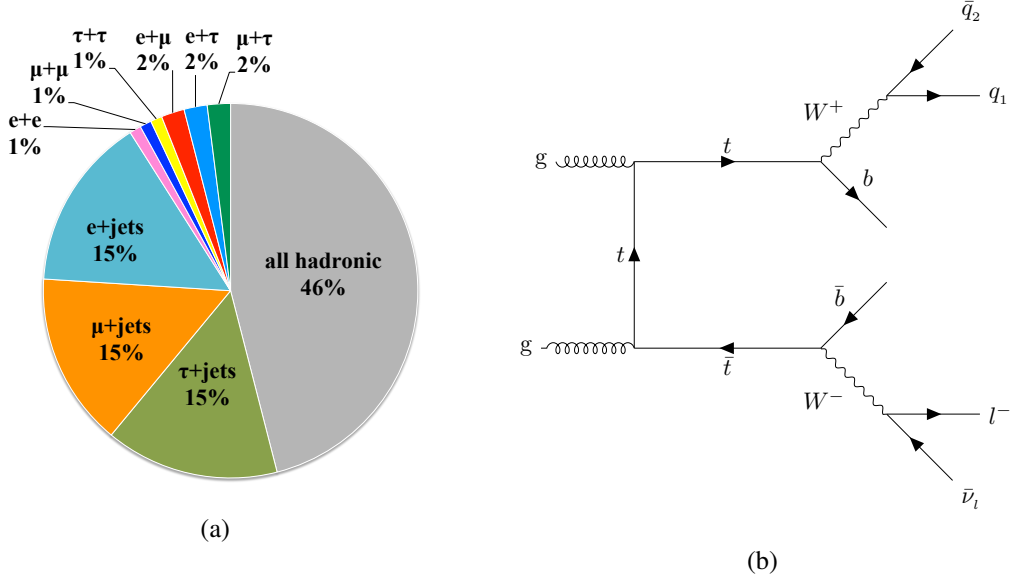


Figure 2.15: (a) Branching ratios of  $t\bar{t}$  decay. (b) A Feynman diagram for the single-lepton decay channel of  $t\bar{t}$ .

## 2.4 Top Quark Pair Production in Association with a Photon

Among those properties of the top quarks which yet need to be experimentally determined and are sensitive to new physics, are its electroweak couplings. These coupling strengths are well predicted by the SM and can be studied through different observables. For example, the polarisation of the  $W$  bosons decayed from the top quarks is a result of V-A structure (see Section 2.1.4) of the  $W-t-b$  vertex; the cross-section of single-top production directly depends on the strength of the coupling to the  $W$  bosons; and the cross-section and dynamics of the associated production of the top quarks and an electroweak gauge boson (for example  $t\bar{t} + V$ ,  $V = W, Z, \gamma$ ) can probe the coupling to such boson.

The production of a top quark pair in association with a photon ( $t\bar{t}\gamma$ ) is the target study of this thesis. Through the measurement of  $t\bar{t}\gamma$  process, the top-photon coupling is probed. Any deviation from the SM predicted top-photon coupling manifests in a deviated cross section or kinematic distributions. For instance, a deviation in the distribution of the transverse momentum of the photon could hint to new physics through anomalous dipole moments of the top quark [3–5]. Also, precise measurements of  $t\bar{t}\gamma$  process can constrain new physics models containing composite top quarks [6]. In addition, the result of measurement can be interpreted in the framework of effective field theories, to constrain some of the Wilson coefficients in top-quark effective field theories [7]. According to the SM, the coupling of the top quark to a photon is completely vectorial and depends exclusively on the electric charge of the top quark. Therefore, the cross-section measurement of  $t\bar{t}\gamma$  can be used to directly determine the top quark charge as well.

In the analyses presented in this thesis, the  $t\bar{t}\gamma$  process is studied in the single-lepton final state. During the production and decay of the top-antitop pair, the massless photon can be emitted from any electrically charged particle, and not just the top quark. The  $t\bar{t}\gamma$  production can be classified into two

types of processes:

- *Radiative top production*: The photon is radiated from an incoming charged parton (ISR) or an off-shell top quark, as shown in Figure 2.16.

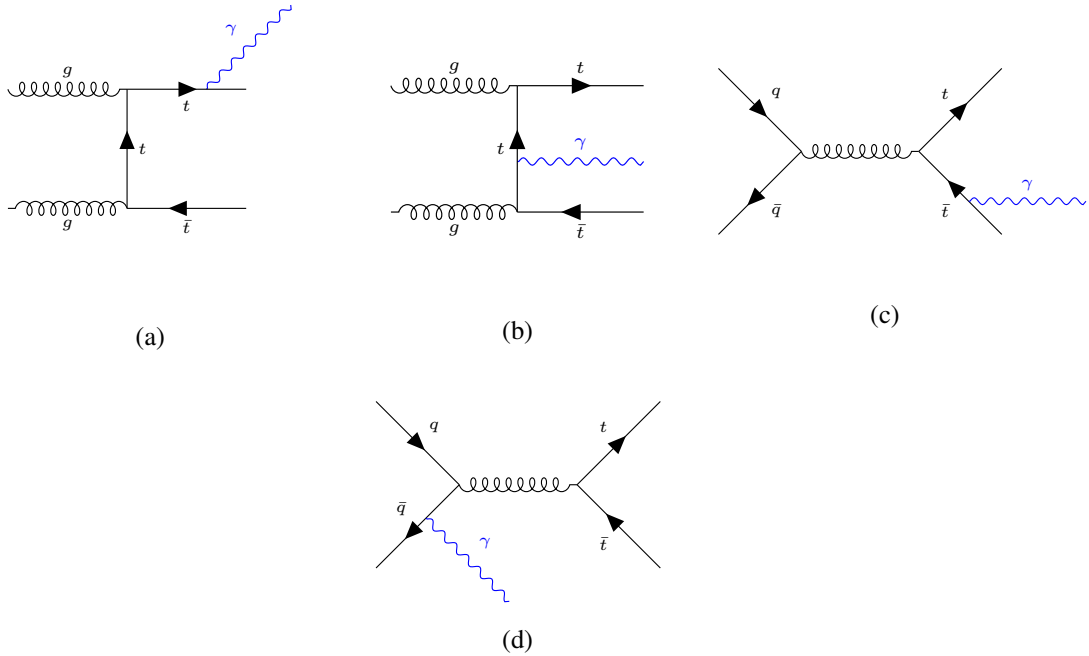


Figure 2.16: Examples of leading-order Feynman diagrams for the  $t\bar{t}\gamma$  processes classified as radiative top production, where the photon is emitted from (a)(b)(c) an off-shell top quark, or from (d) incoming quarks.

- *Radiative top decay*: The photon is radiated from an on-shell top quark or any of the charged particles within the decay chain (FSR), as illustrated in Figure 2.17.

In order to probe the top-photon coupling, only the cross section of  $t\bar{t}\gamma$  processes where the photon is emitted from a top quark (either in radiative top production or in radiative top decay) should be considered. However, it is not experimentally possible to distinguish these processes. But it is possible to constrain the measured phase space to a region more sensitive to the top-photon coupling by exploiting the kinematic properties of the events. What is done in practice is to place requirements on the angular distance between the photon and the lepton, and the photon and the jets. These requirements efficiently reduce the contribution from the FSR, but are not so effective on reduction the ISR contribution. However this is tolerable, since as mentioned in Section 2.3 the contribution from quark-antiquark annihilation initial state is only in the order of 10%.

The first evidence for the  $t\bar{t}\gamma$  production with a significance of  $3.0\sigma$  was reported by the CDF experiment at the Tevatron collider in  $p\bar{p}$  collisions at  $\sqrt{s} = 1.96$  TeV, in a data-set with total luminosity of  $6.0 \text{ fb}^{-1}$  [44]. The observation of  $t\bar{t}\gamma$  production with  $5.3\sigma$  significance was achieved by the ATLAS experiment at the LHC in  $pp$  collisions at  $\sqrt{s} = 7$  TeV, using a data-set corresponding to a total luminosity of  $4.59 \text{ fb}^{-1}$  [45]. This was followed by more measurements in the LHC in higher centre-of-mass energies. Both CMS and ATLAS experiments performed fiducial cross-section measurement at  $\sqrt{s} = 8$  TeV, using  $19.7 \text{ fb}^{-1}$  and  $20.2 \text{ fb}^{-1}$  of data, respectively [8, 46]. The ATLAS measurement included the first  $t\bar{t}\gamma$  differential cross-section measurement, while in the CMS measurement the ratio of

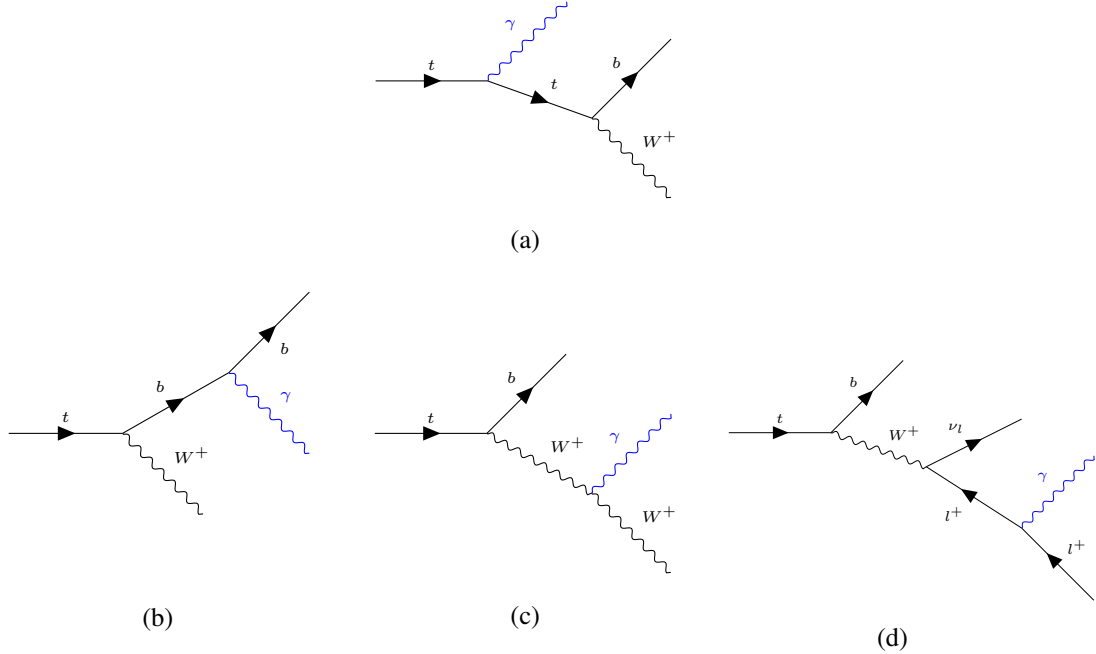


Figure 2.17: Examples of leading-order Feynman diagrams for the  $t\bar{t}\gamma$  processes classified as radiative top decay, where the photon is radiated from (a) an on-shell top quark or (b)(c)(d) one of the charged particles in the decay chain.

the  $t\bar{t}\gamma$  fiducial cross-section to the  $t\bar{t}$  total cross section was reported. The most recent  $t\bar{t}\gamma$  measurement is done by ATLAS, using a data-set of the size  $36.1 \text{ fb}^{-1}$  from  $pp$  collisions at  $\sqrt{s} = 13 \text{ TeV}$ , measuring the fiducial and the differential cross sections [9]. All the measurements before this were performed only in the single-lepton decay channel of  $t\bar{t}\gamma$ , while in this measurement the dilepton decay channel was included as well. The result of all the cross-section measurements performed so far are in agreement with the SM predictions.

The measurement by ATLAS at  $\sqrt{s} = 8 \text{ TeV}$  is presented in this thesis in Chapter 7, and the ATLAS measurement at  $\sqrt{s} = 13 \text{ TeV}$  in the single-lepton channel can be found in Chapter 8.

# CHAPTER 3

---

## Experimental Setup

---

The analyses presented in this thesis are based on the data recorded by the ATLAS detector placed at one of the collision points on the LHC ring. A description of the LHC and the ATLAS detector are presented in Sections 3.1 and 3.2, respectively.

### 3.1 The Large Hadron Collider

The LHC [47] is a circular particle collider at CERN (The European Organisation for Nuclear Research<sup>1</sup>). It is designed to collide protons or heavy ions; namely, proton-proton ( $pp$ ) collisions, lead-ion pair collisions, or collisions between lead-ions and protons<sup>2</sup>. As this thesis focuses on the  $pp$  collision data, the heavy-ion beams will not be discussed.

The LHC is installed in the underground tunnel that previously hosted the LEP collider (Large Electron Positron collider). The tunnel is approximately 27 kilometre in circumference and lied at about 100 meters in average under the ground, beneath the France-Switzerland border, near Geneva (see Figure 3.1).

The LHC provides  $pp$  collisions at the highest centre-of-mass energy and rate ever achieved. It is designed to accelerate two proton beams in opposite directions to reach a beam energy of 7 TeV, leading to a centre-of-mass energy ( $\sqrt{s}$ ) of 14 TeV for the collisions. The designed peak instant luminosity is  $10^{34} \text{ cm}^{-2} \text{ s}^{-1}$ . The protons are bunched together in the beam, with the number of protons in each bunch being at order of  $10^{11}$ . At the peak luminosity, there are 2808 bunches per beam, with a nominal bunch spacing of 25 ns, equivalent to a bunch crossing rate of 40 MHz.

The first  $pp$  collisions at the LHC were recorded in November 2009 at a centre-of-mass energy of 900 GeV. In April 2010 the run-1 of high-energy data taking started, and lasted until 2012. The LHC operated at a centre-of-mass energy of 7 TeV in 2010 and 2011, increased to 8 TeV in 2012. The bunch spacing in run-1 was set to 50 ns. At the end of run-1, the LHC and its detectors underwent a long technical shutdown to make them ready for higher energy and luminosity. The run-2 of data taking started in mid 2015 and ended in 2018, with the LHC operating with a centre-of-mass energy of 13 TeV and bunch spacing of 25 ns. Currently the LHC is in the second long shutdown phase. It is scheduled to restart in the spring of 2021, with its full designed energy.

---

<sup>1</sup> The name CERN is derived from the acronym for the French Conseil Européen pour la Recherche Nucléaire which translates to European Council for Nuclear Research [48].

<sup>2</sup> In 2017, for one day only, xenon nuclei were collide.

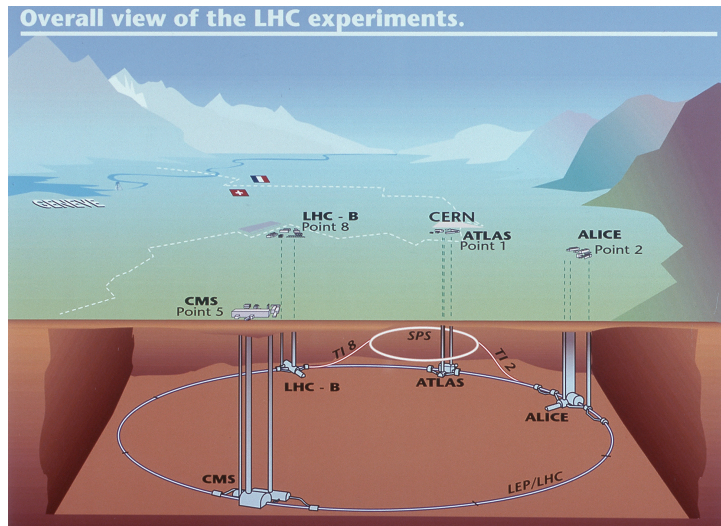


Figure 3.1: Location of the Large Hadron Collider (LHC) and its four main experiments: ALICE, ATLAS, CMS and LHCb. (©1999-2019 CERN)

### 3.1.1 The Collider Setup

Protons are accelerated in several steps to reach the final beam energy and the LHC is the final element of the accelerating chain. They are obtained from ionised Hydrogen atoms, and accelerated up to 450 GeV in the already existing accelerator facilities in CERN, before entering the LHC main ring. These facilities together with the LHC form the accelerator complex shown in Figure 3.2.

The LHC ring is divided in eight straight sections and eight arcs. A total of 9593 superconducting magnets together with radio-frequency cavities form the LHC. The magnets are cooled by super-fluid helium to the operating temperature of 1.9 K. The path of particles are bent in the arcs by 1232 dipole magnets, with a maximum field of 8.33 T. Due to the size restrictions imposed by the already-existing LEP tunnel, a *twin-bore* design for the dipole magnets was realised, where the two counter-rotating beams run in two adjacent beam pipes that share the same mechanical structure. There are 392 quadrupole magnets that focus the beams, specially close to the interaction points where the proton bunches are brought to collide. This increases the chance of head-on collisions between protons. The quadrupole magnets are installed in pairs, where one magnet controls the width of the beam and the other one its height. There are also sextupole, octupole and decapole magnets that are used to correct for imperfections at the extremities of the magnetic field. The acceleration of the particles is provided by the electric field generated by the radio-frequency cavities operating at 400 MHz in the straight sections. The cavities also compensate for energy losses due to synchrotron radiation and keep the beam energy constant. To avoid collisions with gas molecules, the beam pipes are kept in an ultrahigh vacuum.

### 3.1.2 The Experiments

The beams are brought to collide in four points along the LHC ring, in four of the eight straight sections. Along these interaction points, the two beams share an approximately 130 m long common beam pipe. The detectors of the four main experiments at the LHC, ATLAS, CMS, ALICE and LHC-b, are positioned at these interaction points (see Figure 3.2). ATLAS and CMS are the general-purpose detectors, designed to cover the largest range of physics analyses possible and exploit the full potential of the collision data. Having two independent detectors with the same application can provide a confirma-

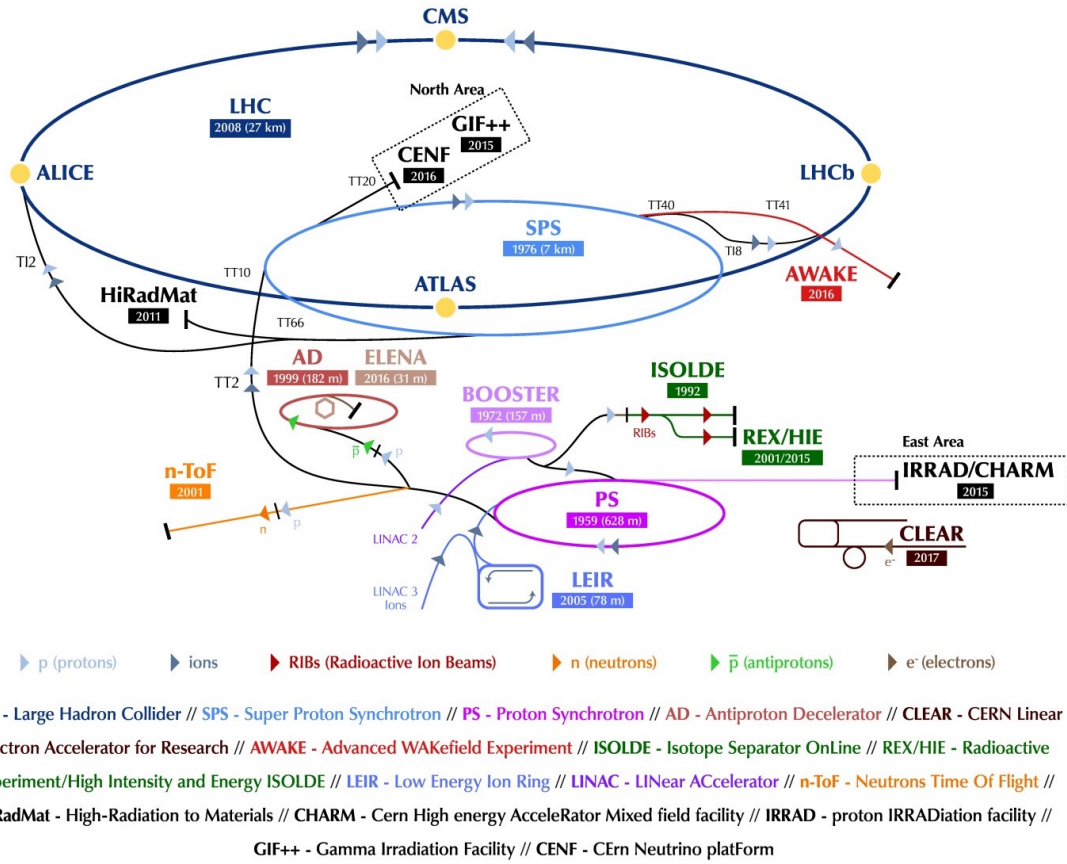


Figure 3.2: The accelerator complex at CERN. The LHC is the last ring (dark blue line) in a chain of particle accelerators. (©1999-2019 CERN)

tion of any new discoveries made, and the datasets can be combined to enhance precision. ALICE and LHC-b are the two specialised detectors, dedicated to studies of heavy ion physics and  $b$ -quarks physics, respectively.

### 3.1.3 Luminosity

The performance of particle colliders can be quantified by the beam energy and the luminosity. While the former quantifies the phase space available for the interactions, the latter quantifies the ability of the collider to produce the required number of interactions. *Instantaneous luminosity*,  $L_{\text{inst}}$ , is the proportionality factor between the number of scattering events of a particular process produced per unit of time and its cross section:

$$\frac{dN_{\text{events}}}{dt} = L_{\text{inst}} \cdot \sigma_{\text{events}}. \quad (3.1)$$

Typically we are not interested in the instantaneous number of events, but rather the total number of events produced during a certain time period. Therefore, the *integrated luminosity*,  $L$ , is a more useful quantity:

$$L = \int L_{\text{inst}} dt, \quad (3.2)$$

which is directly related to the number of observed events of interest:

$$N_{\text{events}} = L \cdot \sigma_{\text{events}}. \quad (3.3)$$

The luminosity for two colliding beams of proton in the LHC is given by:

$$L = \frac{f_{\text{rev}} n_b N_p}{4\pi \sigma_x \sigma_y}, \quad (3.4)$$

where  $f_{\text{rev}}$  is the revolution frequency,  $n_b$  the number of bunches in beam,  $N_p$  the number of protons per bunch, and  $\sigma_x$  and  $\sigma_y$  are the horizontal and vertical beam widths respectively, under the assumption of a Gaussian distribution of particle density around the beam axis.

A precise measurement of the luminosity is crucial for measuring cross sections. The derivation of the luminosity used in the analyses presented in this thesis follows the methodology described in Re. [49].

## 3.2 The ATLAS Detector

The ATLAS<sup>3</sup> detector [50], drawn to scale in Figure 3.3, is a general-purpose particle detector constructed around one of the four interaction points of the LHC. With 25 m in diameter and 44 m in length, it is the largest detector of the LHC. It has a *barrel* part which surrounds the beam pipe cylindrically, and two *endcaps* which are circular structures perpendicular to the beam direction, allowing it to cover almost the full solid angle. It is nominally forward-backward symmetric with respect to the interaction point, and weighs about 7000 tonnes.

The ATLAS detector comprises several sub-detectors, each of them targeting specific measurements. The sub-detectors are ordered in consecutive layers in such a way that when the particles created in the interaction point traverse through the detector, finer details can be resolved at the beginning and in the outer layers their energies can be measured by complete absorption. The sub-detectors are grouped into three main systems:

- The *Inner Detector*, described in Section 3.2.3, is the innermost part as the name suggests. It is surrounded by a solenoidal magnetic field and determines the path of the charged particles and measures their momentum.
- The *Calorimeters*, described in Section 3.2.4, are placed outside the solenoid magnet. The electromagnetic and hadronic calorimeters are designed to stop electrons, photons and hadrons, and measure their energies.
- The *Muon Spectrometer*, described in Section 3.2.5, is the outermost part. It is embedded in a toroid magnet and used to measure the properties of the muons that escape the inner parts of the detector.

Before describing these three sub-detector systems in their corresponding Sections, Section 3.2.1 introduces the ATLAS coordinate system and some important kinematic variables, and Section 3.2.2 gives a description to the magnet system of the ATLAS detector. To reduce the flow of data to manageable levels, ATLAS uses a trigger system which is described in Section 3.2.6.

---

<sup>3</sup> A Toroidal LHC ApparatuS

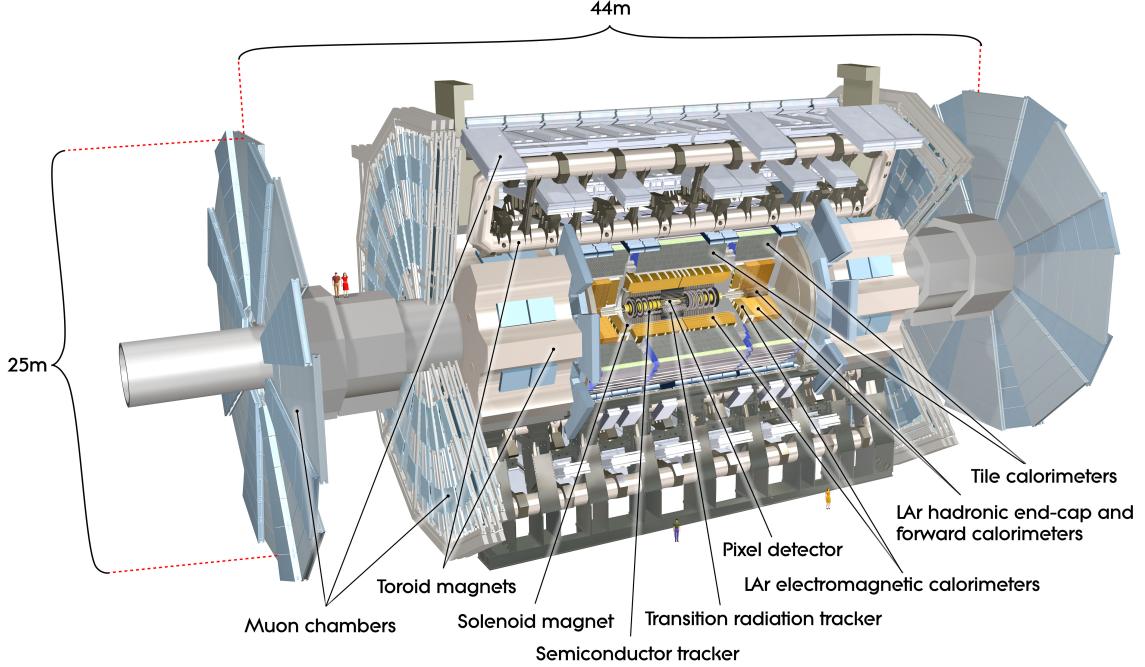


Figure 3.3: Cut-away view of the ATLAS detector [50].

### 3.2.1 Coordinate System and Useful Kinematic Variables

ATLAS uses a right-handed coordinate system with its origin at the nominal interaction point in the centre of the detector. The beam direction defines the  $z$ -axis, with the A-side (C-side) of the detector defining the positive (negative)  $z$ . The positive  $x$ -axis points to the centre of the LHC ring and the positive  $y$ -axis points upward. The  $x$ - $y$  plane is orthogonal to the beam direction, referred to as the transverse plane. The cylindrical coordinates  $(r, \phi)$  are used in the transverse plane, with  $\phi$  being the azimuthal angle around the  $z$ -axis. The polar angle  $\theta$  is measured with respect to the  $z$ -axis. Figure 3.4(a) visualises the ATLAS coordinate system.

As discussed in Section 2.2, in a  $p p$  collision each of the interacting partons carry an unknown fraction of proton momentum. Since they may carry different fractions of proton momentum, their centre-of-mass frame and the laboratory frame may differ. This means that the interaction system might be boosted by an unknown size in the beam direction, i.e.  $z$ -axis. Thus, it is useful to define the transverse component of the kinematic variables of interest, like energy and momentum, which are boost-invariant. The transverse momentum ( $p_T$ ) and transverse energy ( $E_T$ ) are defined in  $x$ - $y$  plane as:

$$\vec{p}_T = (p_x, p_y) \quad (3.5)$$

$$p_T \equiv |\vec{p}_T| = p \sin \theta,$$

and

$$E_T \equiv \sqrt{m^2 + p_T^2} = E \sin \theta. \quad (3.6)$$

Since the partons inside protons have relatively small intrinsic transverse motion, the transverse mo-

momentum of the initial state of the interaction is zero. The momentum conservation implies that the vector sum of the transverse momentum of all final state particles must be zero as well. Any deviation from zero could indicate the presence of particles which are produced in the interaction but not detected. This can be used to recover information about the invisible particles to the ATLAS detector, such as neutrinos (in the context of the SM) or other weakly interacting stable particles that are predicted by theories beyond the SM. This is done through measuring the *missing transverse momentum*. The term *missing transverse energy* is also used interchangeably, since the definition assumes negligible mass of the undetected particles. This is why this quantity is denoted by  $E_T^{\text{miss}}$ .

The *pseudorapidity* ( $\eta$ ) is defined in terms of polar angle  $\theta$  as:

$$\eta \equiv -\ln \tan \frac{\theta}{2}. \quad (3.7)$$

A graphical representation of the pseudorapidity values is shown in Figure 3.4(b). Pseudorapidity is in fact the zero-mass limit of the *rapidity* ( $y$ ) of a relativistic particle ( $\lim_{m \rightarrow 0} y = \eta$ ):

$$y \equiv \frac{1}{2} \ln \frac{E + p_z}{E - p_z}. \quad (3.8)$$

Since the pseudorapidity differences are Lorentz invariant under boosts along the  $z$ -axis, it is conveniently preferred over  $\theta$ . Furthermore, the distance between particles is usually measured in  $\eta$ - $\phi$  space in terms of  $\Delta R$ , defined as:

$$\Delta R \equiv \sqrt{\Delta\phi^2 + \Delta\eta^2}. \quad (3.9)$$

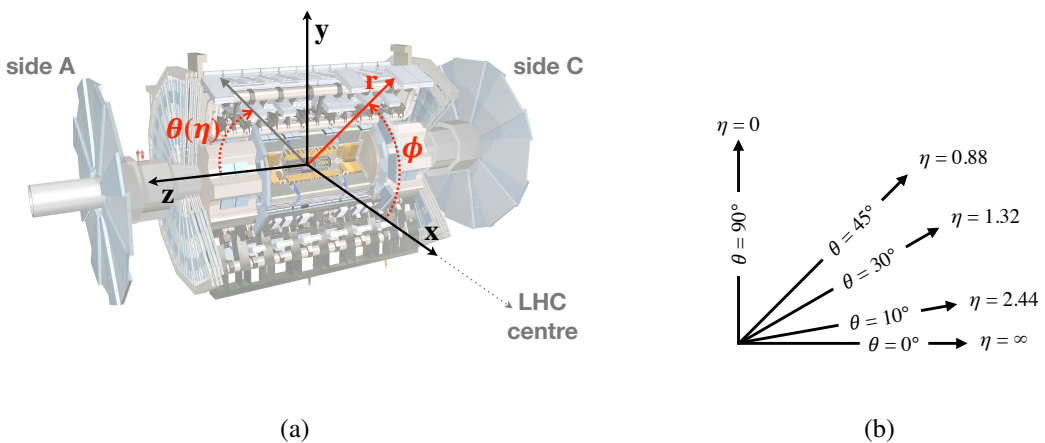


Figure 3.4: (a) A visualisation of the ATLAS coordinate system. (b) Pseudorapidity ( $\eta$ ) values corresponding to polar angle ( $\theta$ ) values.

### 3.2.2 Magnets

The ATLAS magnet system is designed to bend the trajectory of charged particles. The curvature radius of the trajectory is proportional to the particle momentum perpendicular to the magnetic field direction. Also, the curvature direction reveals the particle charge sign.

The ATLAS magnet system is composed of four superconducting magnets:

- One solenoid magnet - The solenoid is aligned to the beam axis and surrounds the Inner Detector. It provides a 2 T axial magnetic field, bending the charged particles in  $r - \phi$  plane . It has a diameter of 2.4 m and a length of 5.3 m.
- One barrel and two endcap open-air toroids magnets - The toroid magnets produce a 4 T field needed by the Muon Spectrometer to deflect particles path in  $r - z$  plane . Each toroid is composed of eight independent coils, with equal azimuthal distance from each other. The barrel toroid is located centrally around the calorimeters, with an outer diameter of 20.1 m and a length of 25.3 m. The endcap toroids are at the two extremes of the detector and have an outer diameter of 10.3 m and a length of 5 m.

A sketch of the ATLAS magnet configuration is shown in Figure 3.5.

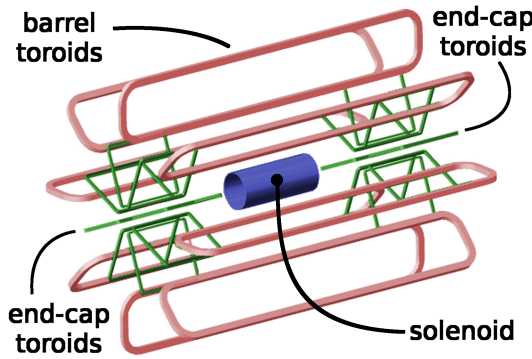


Figure 3.5: Layout of the ATLAS magnet system. Taken from Ref. [51].

### 3.2.3 Inner Detector

The Inner Detector (ID) is devoted to the reconstruction of the path of the charged particles (*tracks*), determination of their momentum, and reconstruction of the interaction vertices. It covers a pseudorapidity range of  $|\eta| < 2.5$  and has a full  $\phi$  coverage. In addition, it provides electron identification over  $|\eta| < 2$  and an energy range of 0.5 GeV to 150 GeV. The ID requires to have high granularity to face the high track density close to the interaction point, high precision to maximise measurement resolution, and fast response to sustain the high bunch crossing rate.

The layout of the ID is shown in Figure 3.6. It consists of three independent but complementary sub-detectors: the *pixel detector*, the *Semi-Conductor Tracker (SCT)* and the *Transition Radiation Tracker (TRT)*. They are arranged in a central barrel part and two endcap regions, immersed in a 2 T solenoid magnetic field (see Section 3.2.2). The ID configuration allows a pseudorapidity coverage of  $|\eta| < 2.5$  in the pixel detector and the SCT and  $|\eta| < 2.0$  in the TRT, and a full azimuthal coverage.

#### 3.2.3.1 Pixel Detector

The closest ID sub-system to the interaction point is the pixel detector. Given its position, the pixel detector has the finest granularity of all the ATLAS sub-detectors, providing the highest spatial resolution along a particle path through the detector. The pixel detector uses the silicon semiconductor technology,

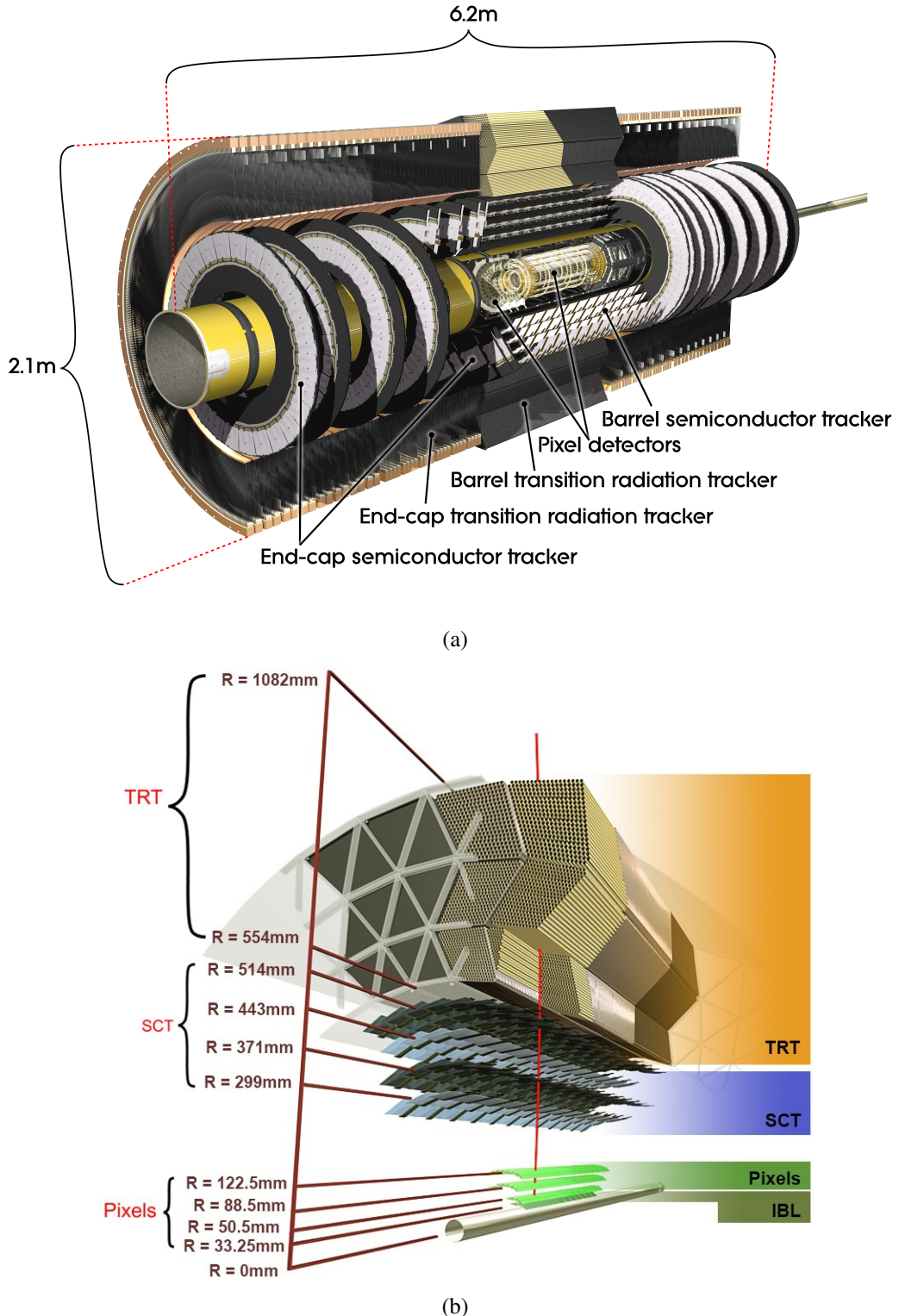


Figure 3.6: (a) Cut-away view of the ATLAS Inner Detector [50]. (b) Cross section of the barrel region of Inner Detector in run-2 of data taking. Taken from Ref. [52].

where the charged particles crossing a p-n junction create electron-hole deposits which are collected by the pixels.

During the run-1 of data taking, the pixel detector consisted of three concentric layers in the barrel region around the beam axis at average radii of 5.05, 8.85 and 12.25 cm, covering a  $z$  range of  $|z| < 40.05$  cm, and three disks in each of the two end-caps at  $z$  distances of 49.5, 58.0 and 65.0 cm from the interaction point, covering a radius range of  $8.88 < r < 14.96$  cm. The innermost barrel layer in this layout was called the *B-Layer* because of its importance for reconstruction of the secondary vertices in decay of the hadrons containing  $b$ -quarks.

In the long shutdown between the run-1 and the run-2, a new innermost barrel layer for the pixel detector was added. This layer which is called *Insertable B-Layer (IBL)* [53] is inserted at a radius of 3.3 cm between the run-1 B-Layer and a new narrower beam pipe. This upgrade was designed as an alternative to the initially planned replacement of the run-1 B-Layer. The IBL compensates for the eventual radiation damages and failures in the B-Layer<sup>4</sup>.

The original 3-layered pixel detector contains 1744 identical pixel modules. Each pixel module contain a planar silicon sensor with 47232 pixels, with the nominal pixel size of  $50 \times 400 \mu\text{m}^2$ <sup>5</sup>. This results to a total of  $\sim 80.4$  million pixels and the intrinsic resolution of  $10 \mu\text{m}$  in  $r - \phi$  and  $115 \mu\text{m}$  in the  $z$  ( $r$ ) direction in the barrel (end-cap) region. The IBL takes advantage of the 3D silicon sensor technology, as well as planar silicon sensors. It has a total of  $\sim 12$  million pixels, with the nominal size of  $50 \times 250 \mu\text{m}^2$ . Its intrinsic resolution is  $8 \mu\text{m}$  in  $r - \phi$  and  $40 \mu\text{m}$  in  $z$  direction.

### 3.2.3.2 Semi-Conductor Tracker

The SCT is another silicon-based detector, located around the pixel detector with four barrel layers and nine disks in each of the end-caps. The barrel layers have a radial extension of  $29.9 < r < 51.4$  cm and cover a  $z$  range of  $|z| < 74.9$  cm. The end-cap layers are located at a range of  $83.9 < |z| < 273.5$  cm from the interaction point and cover a radius range of  $27.5 < r < 56.0$  cm. The functionality of SCT are similar to the pixel detector, but its larger surfaces allows to measure tracks in a longer distance. Since the track density is lower in this part, using silicon micro-strips instead of pixels is good enough to have the required accuracy of measurements.

The SCT consist of 4088 modules, each containing a pair of back-to-back silicon micro-strip sensors. The micro-strips are aligned parallel to the beam direction in the barrel layers and arranged radially in the end-cap discs. The two back-to-back strip sensors of one layer are mounted with a small rotation of 40 mrad with respect to each other around their geometric centre. This tilt allows for a measurement of  $z$ -coordinate in the barrel layers and  $r$ -coordinate in the end-cap disc, hence a 3D particle hit measurement. The total number of readout channels in the SCT is  $\sim 6.3$  millions. The intrinsic resolution achieved by the SCT is  $17 \mu\text{m}$  in  $r - \phi$  and  $580 \mu\text{m}$  in  $z$  ( $r$ ) direction in the barrel (end-cap) region.

### 3.2.3.3 Transition Radiation Tracker

The TRT is the outer sub-system of the ID. It is designed for a precise track curvature measurement rather than high position resolution like in the pixel detector or in the SCT, so it uses a different technology than them. It also provides electron identification through the detection of transition radiation

<sup>4</sup> Irreparable failures appear in time in the B-layer as well as in the other layers. But the inefficiencies in the B-layer are more serious, since the loss of data in the B-layer greatly degrades the impact parameter resolution which directly affects the identification of  $b$ -hadrons.

<sup>5</sup> Some of the pixels (long pixels) have a size of  $50 \times 600 \mu\text{m}^2$ .

photons<sup>6</sup> which are predominantly in the X-ray energy regime. The characteristics of the transition radiations are used to separate electrons from hadrons like pions.

The TRT is a gaseous ionisation detector that operates as a drift chamber. Its drift chambers are made from thin tubes of 4 mm diameter, commonly known as *straws*. The surface of the straws is made out of Kapton and acts as the cathode, while the anode is a 31  $\mu\text{m}$  diameter gold-plated tungsten wire at the centre. The straws are filled with a xenon-based active gas mixture (70% Xe, 27%  $\text{CO}_2$  and 3%  $\text{O}_2$ ). However, during run-1 of data taking large gas leakage appeared in some of the tubes due to mechanical stress of the material and corrosion caused mainly by ozone. Since xenon is an expensive gas, some TRT layers were filled with argon instead of xenon in part of the run-2 data-taking period (see Figure 3.7).

When a charged particle traverses the straw, it ionises the gas. The resulting electrons drift towards the wire and cascade in the strong electric field very close to the wire, thus producing a detectable signal. The signal on each wire is amplified, shaped and discriminated against two adjustable thresholds: a low threshold (LT) and a high threshold (HT). The LT is used to measure an electron drift time which is used for tracking, and the HT is used to identify a large energy deposit due to the absorption of a transition radiations photon.

The TRT consists of  $\sim 300,000$  straws. The straws are aligned parallel to the beam axis in the barrel region which covers from 56.0 to 108.0 cm in radius and  $|z| < 72.0$  cm. They are arranged radially in the end-caps, in a region of  $82.7 < |z| < 277.4$  cm and  $61.7 < r < 110.6$  cm. The TRT does not provide measurement of  $z$ -coordinate, but it records a large number of hits, typically 36 (22) in the barrel (end-cap) for each charge particle within  $|\eta| < 2.0$ . It has an intrinsic resolution of  $\sim 130 \mu\text{m}$  in  $r - \phi$ .

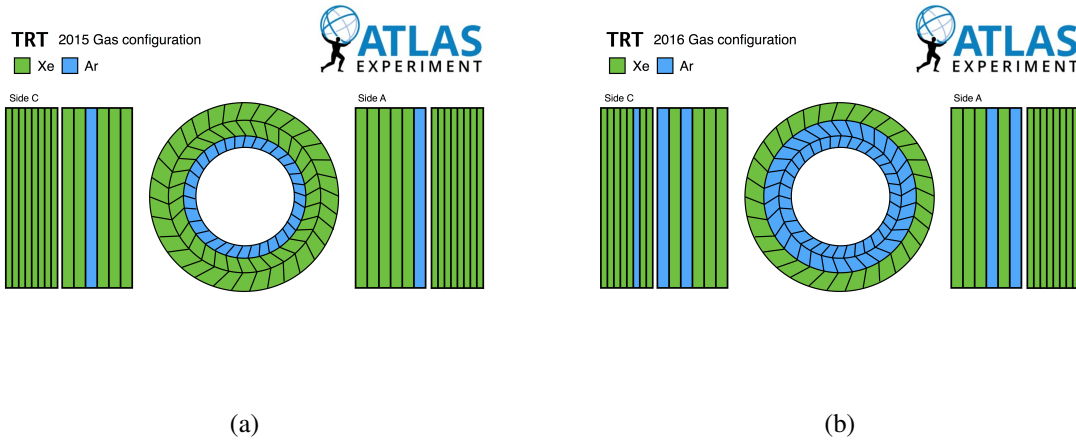


Figure 3.7: ATLAS TRT gas configuration used during run-2 of data taking in (a) 2015 and (b) 2016 [54].

### 3.2.4 Calorimeters

The calorimeter measures the energy of both charged and neutral particles. The incident particles, other than muons and neutrinos, deposit their entire energy to the bulk of matter in the calorimeter and stop. The calorimeter covers a range of  $|\eta| < 4.9$ , which is critical for a precise measurement of the missing transverse momentum. It has a full symmetry and coverage in  $\phi$ .

<sup>6</sup> Transition radiation is an electromagnetic radiation that arises when relativistic charged particles cross a boundary between media with different dielectric constants.

The ATLAS calorimeter system consist of a number of sampling detectors with interchanging layers of absorber and active materials. The incident particles entering the absorber material develop into particle showers, and the active material measure the energy of these showers. The measured energy is proportional to the real energy of the particle, so it needs to be calibrated. Muons leave a measurable trace in the calorimeter but they are not stoped there; they continue their path toward the outermost part of the ATLAS detector, the Muon Spectrometer. The weakly interacting neutrinos do not leave any trace in the calorimeter, and their energy is inferred from momentum conservation, as explained in Section 3.2.1.

The ATLAS calorimeter has three sub-systems, the *Electromagnetic Calorimeter (EMCal)*, the *Hadron Calorimeter (HCal)* and the *Forward Calorimeter (FCal)*. The EMCal, explained in Section 3.2.4.1, is designed to absorb the electrons and photons, whereas the HCal, explained in Section 3.2.4.2, stops the hadrons. The FCal, explained in Section 3.2.4.3, is a combined electromagnetic and hadron calorimeter. The layout of ATLAS calorimeter system can be seen in Figure 3.9.

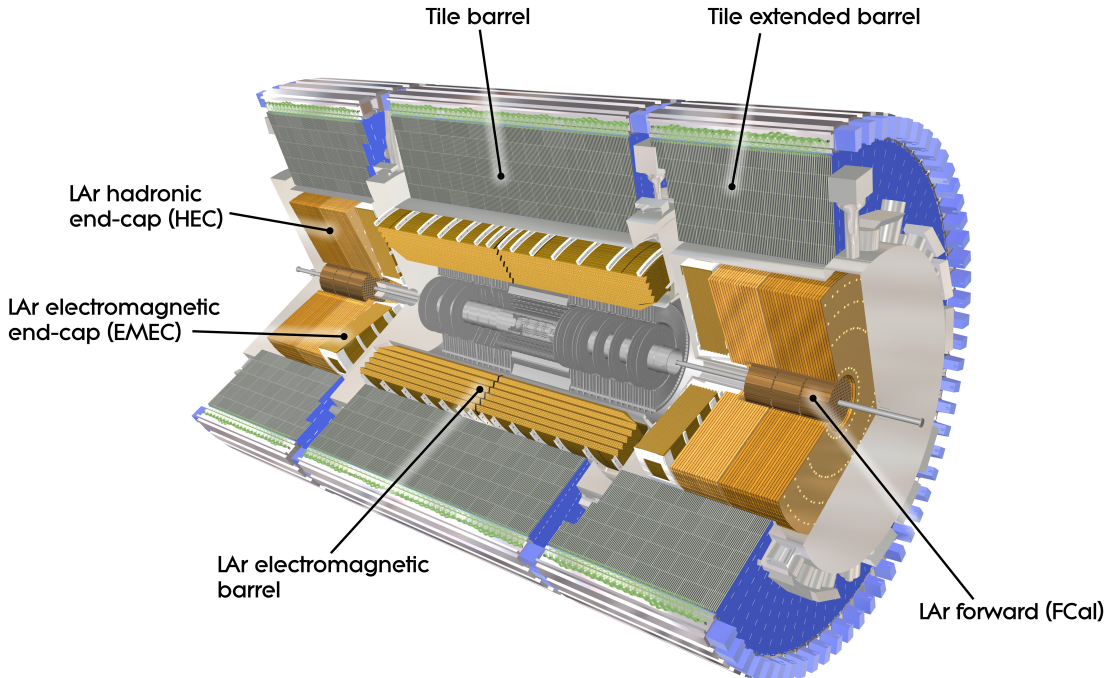


Figure 3.8: Cut-away views of the ATLAS calorimeters system [50].

### 3.2.4.1 Electromagnetic Calorimeter

The EMCal is located right behind the solenoid magnet that surrounds the ID. It is composed of a barrel part and two identical end-caps. The barrel covers a pseudorapidity range of  $|\eta| < 1.475$  and consist of two halves that are separated at  $z = 0$  by a small gap of 4 mm. Each of the endcaps are composed of two coaxial wheels, where the outer wheels covers a range of  $1.375 < |\eta| < 2.5$  and the inner one covers  $2.5 < |\eta| < 3.2$ . In addition, a thin *presampler layer* consists only of active material is placed in front of the EMCal, covering the pseudorapidity range of  $|\eta| < 1.8$ . The presampler provides a measurement of

the energy loss of particles in material upstream of the EMCAL, to allow for a correction of the energy measured by EMCAL.

The EMCAL is a lead-liquid argon detector, with liquid argon (LAr) being the active material while absorber material is made of lead plates of a few mm thickness covered by stainless steel. It has an accordion-shaped geometry which allows a full  $\phi$  coverage with a uniform efficiency in  $\phi$ . The total thickness of the EMCAL is more than 22 times of radiation lengths ( $X_0$ ) in the barrel region and more than  $24X_0$  in the endcaps. When electrons and photons reach the EMCAL, they lose their energy by undergoing bremsstrahlung and pair production triggered by absorber material, leading to formation of electromagnetic showers. The shower particles ionise LAr then drifted charged particles are collected by high-voltage electrodes made of kapton.

The pseudorapidity range of  $|\eta| < 2.5$  covered by the barrel and the outer wheel, which also coincides with the ID coverage range, is referred to as the precision measurement range. There are three longitudinal sampling layers in this range, with different granularity. The first layer (*stripe layer*) has the finest granularity in  $\eta$ , with  $\Delta\eta \times \Delta\phi = 0.0031 \times 0.1$ . The high  $\eta$  resolution of this layer is essential to improve distinguishing signal and background objects, based on their electromagnetic shower profile. The second layer (*middle layer*), has a coarser granularity in  $\eta$  but finer granularity in  $\phi$ , with  $\Delta\eta \times \Delta\phi = 0.025 \times 0.025$ . While the stripe layer has only a  $4.3X_0$  depth, the middle layer with a depth of  $16X_0$  receives most of the electromagnetic shower energy. The third layer (*back layer*) is the shortest layer with a depth of  $2X_0$ , and has a granularity of  $\Delta\eta \times \Delta\phi = 0.05 \times 0.025$ . It measures the tail of the high-energy electromagnetic showers.

The transition region between the barrel and the endcaps of the EMCAL,  $1.37 < |\eta| < 1.52$ , has a rather poor performance due to the higher amount of passive material in front. Therefore, in most of the ATLAS analyses the electrons and photons that are detected in this region, are not considered. This  $\eta$  region is often referred to as the *crack region*.

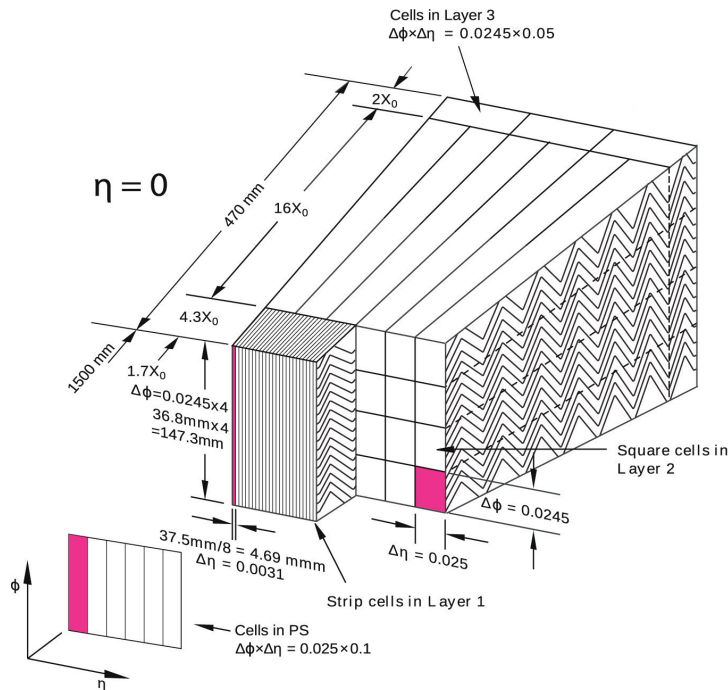


Figure 3.9: Sketch of a EMCAL barrel module (located at  $\eta = 0$ ), showing the granularity in  $\eta$  and  $\phi$  of the cells of its three layers and the presampler layer (PS). Taken and modified from Ref. [55].

### 3.2.4.2 Hadron Calorimeter

The HCal is placed directly behind the EMCal and composed of a *central tile barrel*, two *extended tile barrels*, and two endcaps. The thickness of HCal is  $\sim 11$  times of nuclear interaction lengths ( $\lambda$ ). The HCal occupies a larger volume than the EMCal since the average nuclear interaction length is larger than the average radiation length.

The tile components together cover a pseudorapidity range of  $|\eta| < 1.7$ . They are made of successive scintillating tiles as the active medium and steel plates as the absorber material. The central barrel has a length of 5.8 m and a coverage range of  $|\eta| < 1.0$ , and the two extended barrels are each 2.6 m long and cover  $0.8 < |\eta| < 1.7$ . The tile calorimeters have three layers, with a granularity of  $\Delta\eta \times \Delta\phi = 0.01 \times 0.01$  in the first two layers and  $\Delta\eta \times \Delta\phi = 0.02 \times 0.01$  in the last layer.

The endcaps cover the  $1.5 < |\eta| < 3.2$  range and have the same LAr technology as the EMCal (see Section 3.2.4.1), with copper being the absorber material. The granularity of the HCal endcaps in region  $1.5 < |\eta| < 2.5$  is  $\Delta\eta \times \Delta\phi = 0.01 \times 0.01$ , and for the rest of the pseudorapidity range is  $\Delta\eta \times \Delta\phi = 0.02 \times 0.02$ .

### 3.2.4.3 Forward Calorimeter

The FCal extends the coverage of the ATLAS calorimeter system to the forward pseudorapidity region, to achieve an almost hermetically closed calorimetry. It covers the pseudorapidity range of  $3.1 < |\eta| < 4.9$  and is the closest component of the calorimeter to the beam. The FCal serves as both electromagnetic and hadron calorimeter with a LAr technology same as described in Section 3.2.4.1. It is located in two endcaps of opposite side at about 4.7 m from interaction point and composed of three modules. The first module is dedicated to electromagnetic calorimetry and uses copper plates as absorber medium. The second and last modules provide hadronic calorimetry with tungsten plates as absorber.

### 3.2.5 Muon Spectrometer

The Muon Spectrometer (MS) is the largest and outermost part of the ATLAS detector. It is designed to spot the crossing path of the muons exiting the barrel and endcap calorimeters and measure their momentum in the pseudorapidity  $|\eta| < 2.7$ . It consists of one barrel ( $|\eta| < 1.05$ ) and two endcap sections ( $1.05 < |\eta| < 2.7$ ). The momentum and charge of muons are measured through bending their paths in the magnetic field generated by the toroid magnets introduced in Section 3.2.2. It also serve the purpose of triggering on events when a muon is detected within the ranges  $|\eta| < 2.4$ . It consists of a central barrel part and two endcaps. The layout of the MS together with the toroid magnet system are shown in Figure 3.10.

Over the pseudorapidity range of  $|\eta| < 1.4$  muon trajectories are bent by the barrel toroid, in region  $1.6 < |\eta| < 2.7$  magnetic bending is provided by the endcap fields, and in the transition region  $1.4 < |\eta| < 1.6$  magnetic deflection is done by the combination of barrel and endcap fields. The toroid magnets provide bending in the  $r$ - $z$  plane, therefore the MS can perform precise  $\eta$  measurement.

The MS is composed out of two main sub-systems: the *precision tracking chambers* that are the main tracking instruments and measure the track positions, and the *trigger chambers* that provide fast track information within the time before the next bunch crossing (i.e. a few tens of nanoseconds after the passage of the muon).

The precision chambers are arranged in three layers in the barrel part, at the radii of 5, 7.5 and 10 m, and in three layers in the endcaps, at  $|z| = 7.4, 10.8$  and  $21.5$  m. They consist of *Monitored Drift Tubes* (MDTs) that cover the range  $|\eta| < 2.7$ , assisted by *Cathode-Strip Chambers* (CSCs) for covering the region  $2 < |\eta| < 2.7$ . The MDTs have three to eight layers of drift tubes of 30 mm diameter. The surface

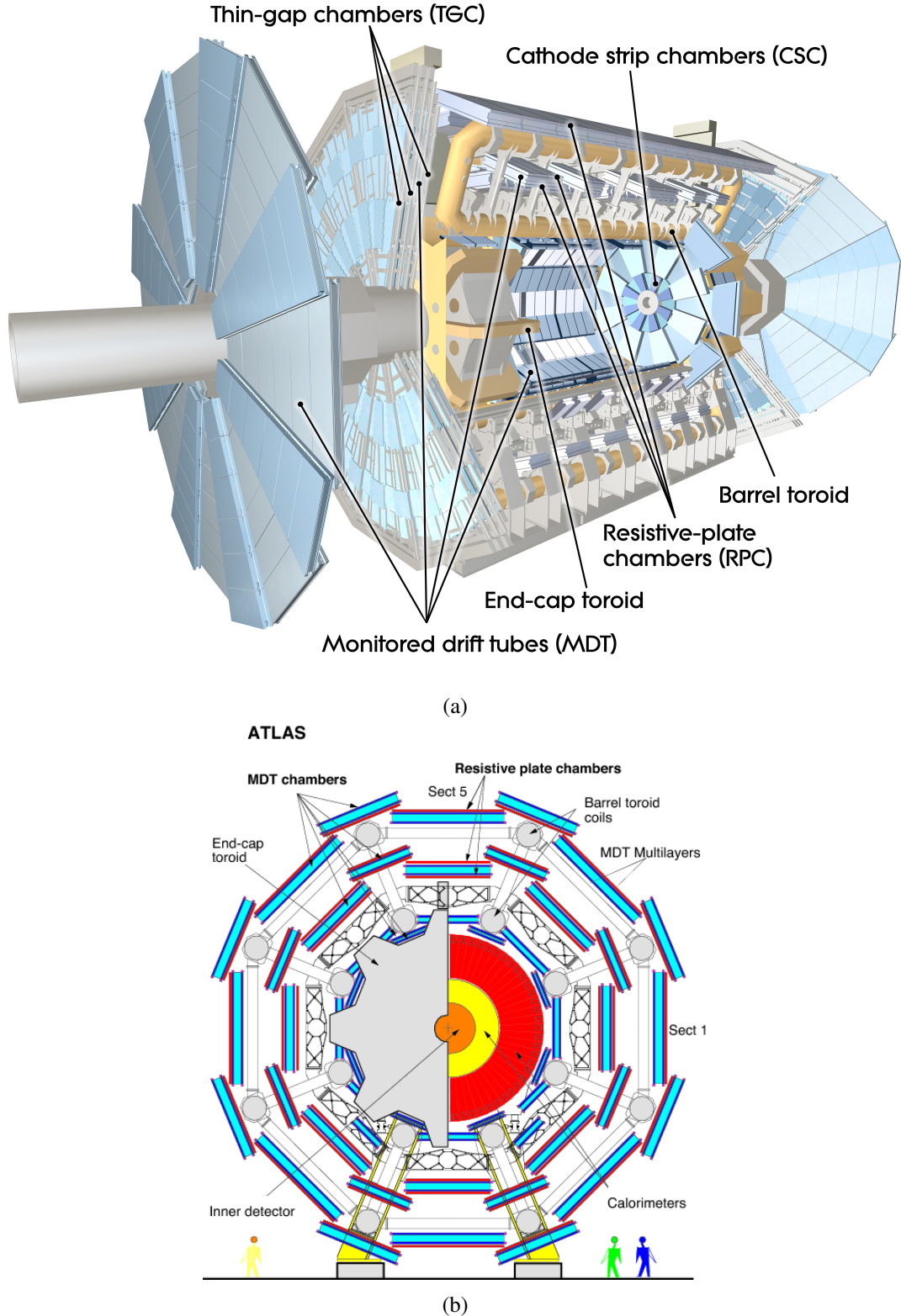


Figure 3.10: (a) Cut-away views of the ATLAS Muon Spectrometer system [50]. (b) Muon Spectrometer system in  $x$ - $y$  projection [56].

of the tubes are made of aluminium and acts as the cathode, a central  $50\ \mu\text{m}$  diameter tungsten-rhenium wire acts as the anode, and the tubes are filled with argon-based gas mixture (93% Ar and 7%  $\text{CO}_2$ ). In the forward region ( $|\eta| > 2$ ) where the counting rate limit of MDTs might get exceeded, the CSCs are used. They are located in the most inner wheel of the endcaps. The CSCs are multi-wire proportional chambers filled with argon mixture gas, consist of arrays of anode wires and cathode planes that are segmented into stripes. The

The trigger chambers consist of *Resistive Plate Chambers (RPCs)* and *Thin Gap Chambers (TGCs)*. The trigger system covers the range of  $|\eta| < 2.4$  by using RPCs in the barrel region and TGCs in the endcap region. The trigger chambers of the MS provide the ATLAS trigger system (explained later in Section 3.2.6) with information about the multiplicity and transverse momentum of the muons. Also, since they can measure the coordinate in the direction orthogonal to that determined by the precision chambers, they provide complementary tracking information by  $(\eta, \phi)$  position measurements.

### 3.2.6 Trigger System

The collisions at the LHC happen in such a high rate that it is not possible to record all the corresponding data, as it exceeds the technical limits of data writing rate to mass storage and the budget of the ATLAS experiment. On the other hand, not all of the scattering events are of interest for later study. Only a small fraction of these events is expected to contain interesting physics with respect to the goals of the experiment. Therefore, an online trigger system is used to filter the events from a given bunch-crossing interaction and reduce the data storing rate.

The ATLAS trigger system is fully described in Refs. [57] and [58]. During run-1 of data taking, the trigger system reduced the event rate from the design bunch-crossing rate of 40 MHz to an average output rate of 200 Hz [57] to 700 Hz [59], depending on the year (increasing toward the end of data-taking period). The average output rate during run-2 of data taking in 2015 and 2016 was 1000 Hz [58, 60].

The trigger system in run-1 selected the events in three levels. The first level (L1) is a hardware-based trigger. Based on the information from calorimeter systems with reduced granularity and from trigger chambers of the MS, the L1 trigger selects events containing high- $p_{\text{T}}$  objects, or high  $E_{\text{T}}^{\text{miss}}$ , or high total  $E_{\text{T}}$ . The coordinate of the detector regions where the events have been triggered by L1 (Regions-of-Interest, RoI) are propagated to a processing farm where they are further analysed, using software-based algorithms. The second (L2) and third (Event Filter, EF) levels are software-based systems, together called the High Level Trigger (HLT). They use information from all sub-detectors at their full granularity. The L2 trigger selection is based on dedicated fast algorithms processing partial event data within the RoI. The EF trigger uses the offline reconstruction algorithms adapted for the trigger and the full event data to further filter the events.

The trigger system was revisited for run-2 of data taking to cope with the greater rates due to the higher energy and collision frequency. For run-2, the L2 and EF farms were merged into a single homogeneous farm of HLT.



# CHAPTER 4

---

## From Detector to Physics: Event Reconstruction

---

The final state particles produced in the  $pp$  collisions traverse through the ATLAS detector and leave behind signals in different components of the detector described in Section 3.2. The collected signals are then processed and translated into physically meaningful objects. This is referred to as *reconstruction*. The reconstruction of particles are based on higher-level detector information, meaning that in first steps tracks and vertices are reconstructed from single hits in the tracking detectors and clustered calorimeter deposits from single calorimeter cell signals, then in next steps these information are combined to reconstruct objects like electrons, muons, jets and photons. The events accepted by the ATLAS online trigger system, as well as the simulated events, go through a chain of dedicated algorithms to reconstruct the physics objects and determine their four momentum and other detector-level properties which can be used in the physics analyses.

Not all the reconstructed objects are considered as the signal objects for a given analysis. To determine whether a reconstructed object is signal-like or background-like, the *identification* algorithms are used. These algorithms use the discriminating properties of signal and background objects to reject the backgrounds as much as possible while keeping high enough efficiency for signals. Since different physics analyses have different needs, typically several menus of selections with various background rejection powers are provided for one object type. In order to further reject the background objects, many analyses require some objects (more specifically, electrons, muons, and/or photons) to pass a set of isolation requirements as well.

The real data and simulated events go through the same algorithms, but imperfections in the detector simulation might lead to discrepancies in the reconstruction, identification, and isolation performances between the simulation and data. Therefore, reference processes are used to obtain correction factors to calibrate the objects in the simulated events accordingly.

The analysis of  $t\bar{t}y$  makes use of reconstructed electrons, muons, jets, photons and missing transverse momentum. This chapter describes their reconstruction and identification, as well as isolation and calibration where it is relevant.

### 4.1 Tracks and Vertices

Track reconstruction determines the trajectories of charged particles in the detector. Reconstructing the common intersection points between sets of reconstructed tracks reveals the primary interaction vertices or secondary decay vertices. The general structure of the ATLAS track and vertex reconstruction are

described in detail in Refs. [52, 61] and Ref. [62], respectively, and a brief overview is given in this Section.

The responses to the crossing charged particles recorded by different layers of the ID (i.e. *hits*) are used to reconstruct the tracks and determine the tracking parameters. The track reconstruction consist of a sequence of algorithms. An *inside-out* algorithm is designed for reconstructing the tracks of primary charged particles, defined as particles with a mean lifetime greater than  $3 \times 10^{-11}$  s. The primary particles are either produced directly in a  $pp$  interaction or from the subsequent decays or interactions of particles with a lifetime shorter than  $3 \times 10^{-11}$  s. A *back-tracking* (also known as *outside-in*) algorithm is aimed to reconstruct the tracks of secondary charged particles, which are the particles produced in the interactions of primary particles. A third algorithm is employed for TRT segments that have no associated hits in the silicon detectors (i.e. pixel and SCT detectors), referred to as the *TRT-standalone tracks*.

The track reconstruction begins by assembling clusters of raw measurements in the silicon detectors and creating three-dimensional measurements referred to as *space-points* from them. A space-point represent the point where a charged particle has traversed the active material of detector. Each cluster in the pixel detector translates to one space-point, while in the SCT the clusters from both sides of a strip layer must be combined in order to get a three-dimensional measurement. Position coordinates of hits in the TRT are measured using drift-time information. Once the drift time is known, it can be translated into the radius of a *drift-circle* around the wires, making use of the relation between drift time and drift distance which is obtained from data [63].

The inside-out algorithm starts from three-point seeds in silicon detectors. The seeds are formed from three space-points in either the pixel or the SCT detector, or two space-points in the pixel detector and one in the SCT. Then moving away from the interaction point, hits are added to the track segment, using a recursive combinatorial Kalman filter [64]. After that, an ambiguity solving procedure is applied to the collection of track candidates found in the silicon detectors, in order to remove the tracks with incorrectly assigned hits. The ambiguity-solver compares and rates the individual tracks by assigning a relative score to each track. The surviving tracks are then extrapolated into the TRT volume and combined with measurements there. The tracks reconstructed by the inside-out algorithm are required to have  $p_T > 400\text{MeV}$ .

The back-tracking algorithm starts from segments reconstructed in the TRT and extrapolates them toward the interaction point by adding silicon hits. The track segments are built by using a Hough transform mechanism [65], while a dedicated tool prevents hits that have already been assigned to tracks in the inside-out approach to be used again.

Once the vertices are reconstructed, tracks of primary particles are re-fitted under the constraint that they originate from a reconstructed primary vertex. A reconstructed track is fully described by the following parameters:

- Transverse impact parameters  $d_0$ : The distance of closest approach of the track to the primary vertex in the transverse plane (i.e.  $x - y$  plane).
- Longitudinal impact parameters  $z_0$ : The  $z$  coordinate of the track at the point of closest approach of the track to the primary vertex.
- Polar angle  $\theta$ : The polar angle of track's momentum vector at the point of closest approach of the track to the primary vertex.
- Azimuthal angle  $\phi$ : The azimuthal angle of track's momentum vector at the point of closest approach of the track to the primary vertex.

- $Q/p_T$ : The electric charge ( $Q$ ) over the transverse momentum, calculated from the curvature radius by knowing the magnetic field. The electric charge sign is determined from the curvature direction.

Primary vertices are reconstructed using two iterative steps: vertex finding and vertex fitting. First, a set of tracks satisfying some quality criteria is selected. Then, a vertex candidate is found by taking the maximum of the distribution of  $z$  coordinates of the selected tracks at the beam-line. Tracks are re-fitted under the assumption of stemming from the vertex candidate. They are weighted according to their compatibility with the vertex candidate and the tracks that are incompatible with the vertex by  $7\sigma$  or more are removed and used for reconstruction of another vertex in the event. The two steps are iteratively repeated, until all the tracks are associated to a vertex. Vertices with less than two associated tracks are discarded. From the vertices found in one event, the one with the largest sum of the squared transverse momentum of associated tracks ( $\sum p_T^2$ ) is identified as the hard-scattering primary vertex and the rest are considered as the vertices of in-time pile-up.

## 4.2 Electron

**Reconstruction** Electrons [66, 67] in the central region of the ATLAS detector ( $|\eta| < 2.47$ )<sup>1</sup> are reconstructed from the energy deposits in the EMCal matched to the reconstructed tracks in the ID.

It starts from reconstructing the electromagnetic clusters in the EMCal. The  $\eta - \phi$  space of the EMCal is divided into a grid of  $N_\eta \times N_\phi = 200 \times 256$  units of the size  $\Delta\eta \times \Delta\phi = 0.025 \times 0.025$ , which corresponds to the granularity of the middle layer of the EMCal (see Section 3.2.4.1). These units are referred to as *towers*. The tower energy is the sum of the energy cells from all the longitudinal layers (strip, middle and back layers, and for  $|\eta| < 1.80$ , also the presampler layer). A sliding-window-algorithm, with the window size of  $3 \times 5$  towers in  $\eta - \phi$ , searches for the towers with  $p_T > 2.5$  GeV. The electromagnetic clusters are then formed around these seed towers.

In the next step, the tracks reconstructed in the ID (see Section 4.1) are matched to the electromagnetic cluster. Tracks are extrapolated to the middle layer of the EMCal and loosely matched to electromagnetic cluster seed, based on their distance in  $\eta$  and  $\phi$ . If the matched tracks have hits in the silicon detector and pass certain precision hit conditions, they are refitted using an optimised Gaussian Sum Filter (GSF) [68]. Then, the refitted tracks are used for the final track-cluster matching which has tighter matching requirements. If more than one track fulfil the matching conditions, the best-matched track is chosen as the primary track<sup>2</sup>.

All seed clusters together with their matching tracks (if there is at least one) are treated as electron candidates at this point. Finally, the cluster of electrons are rebuilt by using a larger window size:  $3 \times 7$  towers in the barrel and  $5 \times 5$  towers in the endcaps of the EMCal. The energy of the clusters is calibrated to the original electron energy based on the Monte Carlo (MC) simulated samples, using Multivariate Analysis (MVA) techniques [69]. The four-momentum of the electron is computed using information from both the calibrated energy cluster and the primary track. The  $\eta$  and  $\phi$  coordinates of the electron are taken from the corresponding track parameters, except for the tracks reconstructed from only TRT hits, in which case the  $\eta$  and  $\phi$  coordinates of the cluster are used.

<sup>1</sup> In this work only electrons within the tracker acceptance region are used, therefore the reconstruction of electrons in the forward detectors are not discussed.

<sup>2</sup> All the tracks assigned to a cluster are kept for the purpose of further analysis, but only the primary track is used to determine the kinematics and charge of the electron and in the electron identification.

**Identification** The reconstructed electron candidates contain not only the prompt electrons, which are considered the signal objects in this thesis, but also the backgrounds-like electrons, including jets that are mis-reconstructed as electrons as well as non-prompt electrons from converted photons, Dalitz decays and semi-leptonic decays of heavy-flavour hadrons. Electron identification algorithms make use of various discriminating variables to reject the background objects. This includes properties of the track in the ID, specific information from the TRT, track-cluster matching quantities, and a set of variables that characterise the lateral and longitudinal shower development in the electromagnetic calorimeter and the shower leakage fraction in the hadronic calorimeter, the so-called *shower-shape variables*. The list of used discriminating variables can be found in Refs [66, 67].

In the 8 TeV analysis, a *cut-based* identification is used, which identifies the objects based on sequential requirements on the discriminating variables. The cut-based selection is optimised in bins of  $E_T$  and  $\eta$ , allowing to take into account the variation of the characteristics of an electron due to the dependence of shower shapes on the amount of passive material traversed before entering the EMCal and the dependences of shower shapes and track properties on the energy [66]. Three sets of identification criteria, corresponding to different background rejection rate to signal efficiency, are available: **Loose**, **Medium**, and **Tight**. By increasing the tightness, more discriminating variables are added and the requirements on the already-used variables in the looser selections are tightened.

The electron identification used in the 13 TeV analysis is based on the *likelihood-based* approach. This approach is a MVA technique, allowing to simultaneously evaluate the properties of an electron candidate when making a selection decision. The likelihood-based identification makes use of signal and background probability density functions of the discriminating variables and calculates an overall probability for the electron to be signal or background. The likelihood-based identification operating points are denoted by **LooseLH**, **MediumLH**, and **TightLH**. They all use the same input variables to define the likelihood discriminant, but the requirement on the discriminant is tightened going from the looser to the tighter identifications. These working points are also optimised in bins of  $E_T$  and  $\eta$ .

The analyses presented in this thesis make use of the **Tight** and **TightLH** electrons. The **Tight** identification used in the 8 TeV analysis equates to signal (background) efficiencies for the electron candidates with  $20 < E_T < 50$  GeV of around 78% (0.5%) which increase (decrease) with  $E_T$ . The **TightLH** identification used in the 13 TeV analysis results in the signal (background) efficiencies of 78% (0.3%) for the electron candidates with  $E_T = 25$  GeV, increasing (decreasing) with  $E_T$ .

**Isolation** In addition to the identification criteria described above, reconstructed electrons can be required to fulfil isolation requirements in order to further suppress the background objects, since prompt electrons are more isolated than electrons originating from hadron decays in jets.

In the 8 TeV analysis, electrons are required to satisfy requirements on both calorimeter- and tracking-based isolation variables. The calorimeter-based isolation variable is  $E_T^{\text{cone}20}$ , which is the sum of transverse energies of topological clusters within a cone of size  $\Delta R = 0.2$  around the direction of the electron candidate, excluding cells associated with the electron energy cluster, and after being calibrated and corrected for energy deposits from pile-up events the underlying activity. For tracking-based isolation the variable  $p_T^{\text{cone}30}$  is used, defined as the sum of  $p_T$  of all tracks within a cone of size  $\Delta R = 0.3$  around the electron candidate, excluding the electron track itself. The cuts on both variables are applied in  $\eta_{\text{cl}}\text{-}p_T$  bins and tuned to achieve uniform efficiency across the  $\eta_{\text{cl}}$  and  $p_T$  spectra. For both isolation variables, requirements are chosen to separately give a 90% electron selection efficiency for electrons from simulated  $Z \rightarrow ee$  events in each  $p_T$  bin.

In the 13 TeV analysis, for the calorimeter-based isolation requirement the same variable  $E_T^{\text{cone}20}$  is used, while for the tracking-based isolation the variable  $p_T^{\text{varcone}20}$  is used. It is defined as the sum

of  $p_T$  of all tracks within a cone of  $\Delta R = \min(0.2, \frac{10 \text{ GeV}}{E_T})$  around the electron candidate, excluding the tracks associated to the electron. The requirements on the quantities  $E_T^{\text{cone}20}/E_T$  and  $p_T^{\text{varcone}20}/E_T$  are optimised to obtain a given electron isolation efficiency as a function of  $E_T$ . This is referred to as a Gradient isolation working point. The default Gradient working point is 90 (99)% for  $E_T = 25$  (60) GeV, estimated for electrons in MC simulated  $Z \rightarrow ee$  process.

**Efficiencies and Scale Factors** The efficiency to detect an electron is divided into different components of the reconstruction, identification, isolation and trigger efficiencies:

$$\epsilon_{\text{total}} = \epsilon_{\text{reconstruction}} \times \epsilon_{\text{identification}} \times \epsilon_{\text{isolation}} \times \epsilon_{\text{trigger}}. \quad (4.1)$$

The efficiencies are measured for data and MC simulated events, using the so-called *tag-and-probe* method. In a sample of selected  $Z \rightarrow ee$  and  $J/\Psi \rightarrow ee$  events, strict selection requirements are applied for one of the electrons in the event (tag), while the second electron candidate (probe) provides an unbiased sample for study. The data-to-MC efficiency ratios as a function of  $E_T$  and  $\eta$  of the electrons are used as scale factors to correct the mismodelings in the MC samples.

## 4.3 Muon

**Reconstruction** The reconstruction of muons [70, 71] is first performed independently in the ID and the MS, then the information from these two sub-systems, and to a lesser extent, from the calorimeter, are combined.

The reconstruction of the muon track in the ID is the same as for any other charged particle, explained in Section 4.1. The track reconstruction in the MS starts with using a Hough transform [65] to search for hits in each MDT chamber and nearby trigger chambers that align on a trajectory in the bending plane of the detector. Then a straight-line fit is performed to the hits found in each layer to reconstruct local MDT segments. The RPC or TGC hits measure the coordinate orthogonal to the bending plane. A separate combinatorial search in the  $\eta$ - $\phi$  plane is used to build segments in the CSC. The muon track candidates are then built by fitting the hits from the segments in different layers. The segments are selected based on hit multiplicity and fit quality and are matched using their relative positions and angles. At least two matching segments are required to build a track, except in the barrel-endcap transition region where one high quality segment with  $\eta$  and  $\phi$  information can be used. Since one segment might have been used for several track candidates, an overlap removal algorithm is applied which decides for best assignment of a segment to a single track, or to allow two tracks to share a segment under the conditions that ensure high reconstruction efficiency for close-by muons. Finally, all the hits associated to a track candidate are fitted by a global  $\chi^2$  fit, and the track is accepted if passes certain selection criteria.

Depending on which sub-detector informations are used, four type of reconstructed muons are defined:

- *Extrapolated or standalone muons*: The muon track is only reconstructed from the hits in the MS, then the MS track is extrapolated to the interaction point. The track parameters (see Section 4.1) are determined at the interaction point taking into account the estimated energy loss of the muon in the calorimeters. This algorithm is mainly used to extend the acceptance for muon reconstruction into the region  $2.5 < |\eta| < 2.7$  which is not covered by the ID.
- *Segment-tagged muons*: A reconstructed ID track is extrapolated toward MS and if it could be associated with at least one local segment in MS chambers, it is classified as a muon. This

algorithm recovers the muons that pass only one layer of MS chambers, either because of their low- $p_T$  or because they passing through the low acceptance regions of the MS.

- *Calorimeter-tagged muons*: A reconstructed ID track is classified as a muon if it can be matched to an energy deposit in the calorimeter consistent with a minimum-ionising particle. This type has the lowest purity among all the muon types, but it is used to recover acceptance in the regions where the MS is only partially instrumented ( $|\eta| < 0.1$ ) in order to allow for cabling and services to the calorimeters and the ID.
- *Combined muons*: First, tracks are reconstructed independently in the ID and the MS, then after an ID and a MS track are found to be matched, a combined track is formed by a global refit to the associated ID and MS hits, while taking into account the energy loss in the calorimeters. Most of the combined muons are reconstructed following an outside-in pattern recognition, meaning that the MS track is extrapolated inward to find its matched ID track. However the complementary inside-out approach is also used to recover the low- $p_T$  muons, where the ID track is extrapolated outward to match a MS track. The combined muon candidates have the highest purity.

The possible overlaps between the different muon types are resolved before producing the collection of muons used in physics analyses [70, 71].

**Identification** Muon identification is performed to discriminate prompt muons (signal) against muons originating from hadron decays (background), mainly coming from pion and kaon decays. Different muon identification selections are provided by ATLAS to address the specific needs of different physics analyses. The defined identification working points have different levels of tightness on muon quality cuts, including requirements on the number of ID and/or MS hits, compatibility of the charge and momentum measurements in the ID and in the MS, and the fit quality of the combined track.

The muons used in the 8 and 13 TeV analyses are respectively identified by the **Tight** [72] and **Medium** [71] criteria. Both criteria include only combined muons within the ID acceptance, i.e.  $|\eta| < 2.5$ , and extrapolated muons in the range of  $2.5 < |\eta| < 2.7$ . Since the event selection in both analyses require the muons to be in the pseudorapidity region of  $|\eta| < 2.5$ , as outlined later in Sections 7.1 and 8.1, in practice only combined muons are used.

**Isolation** To further reduce the background muons originating from heavy-flavour decays, muons are required to be isolated.

In the 8 TeV analysis, only a tracking-based isolation is performed. The ratio of the sum of  $p_T$  of all tracks, excluding the muon track itself, in a cone of the variable size of  $\Delta R = \frac{10 \text{ GeV}}{p_T(\mu)}$  around the muon candidate to the  $p_T$  of muon is required to be less than 0.05. This isolation requirement results to 97% muon selection efficiency for muons from  $Z \rightarrow \mu\mu$  decays.

For the 13 TeV analysis a similar **Gradient** isolation as for the electrons (see Section 4.2) is used, by placing requirements on  $E_T^{\text{cone}20}/p_T(\mu)$  and  $p_T^{\text{varcone}30}/p_T(\mu)$ . The corresponding efficiency is 90 (99)% for muons with  $p_T = 25$  (60) GeV in  $Z \rightarrow \mu\mu$  events.

**Efficiencies, Momentum Calibration, and Scale Factors** The reconstruction and isolation efficiencies of muons, as well as their momentum scale and resolution, are studied in data and MC simulation using  $J/\Psi \rightarrow \mu\mu$  and  $Z \rightarrow \mu\mu$  events. The extracted scale factors are used to bring the simulation in agreement with the data.

## 4.4 Jet

**Reconstruction** Jets are reconstructed from energy deposits forming topological clusters of calorimeter cells (*topo-clusters*), using the anti- $k_t$  algorithm [73] with a radius parameter of  $R = 0.4$ .

A topo-cluster [74] is a three-dimensional cluster of individual calorimeter cells which are topologically connected and have a signal significance above certain thresholds. The signal significance is defined as the ratio of the cell signal to the average expected noise in the cell, estimated from measured calorimeter electronic noise and simulated pile-up effects. The topo-clusters are used as the input to the anti- $k_t$  jet clustering algorithm.

The anti- $k_t$  algorithms uses two distance parameters, the distance  $d_{ij}$  between two entities (particles, pseudo jets)  $i$  and  $j$ , and the distance  $d_{iB}$  between the entity  $i$  and the beam ( $B$ ), defined as:

$$d_{ij} = \min(k_{ti}^{2p}, k_{tj}^{2p}) \frac{\Delta_{ij}^2}{R^2}, \quad (4.2)$$

$$d_{iB} = k_{ti}^{2p}, \quad (4.3)$$

where  $\Delta_{ij}^2 = (y_i - y_j)^2 + (\phi_i - \phi_j)^2$ ,  $k_{ti}$ ,  $y_i$  and  $\phi_i$  are the transverse momentum, rapidity, and azimuthal angle of the entity  $i$ , respectively, and  $R$  is the radius parameter, defining a cut-off for the approximate cone size of the jet. The parameter  $p$  govern the relative power of the energy versus geometrical ( $\Delta_{ij}$ ) scales. In the anti- $k_t$  clustering algorithms,  $p$  is set to  $-1$  (hence the name "anti- $k_t$ "), while  $p = 0$  corresponds to the Cambridge/Aachen algorithm [75] and  $p = 1$  gives the inclusive  $k_t$  algorithm [76].

The clustering proceeds by iteratively identifying the smallest of the two distances: if the minimum is  $d_{ij}$ , then  $i$  and  $j$  are combined into a single object, i.e. a pseudo jet; if the minimum is  $d_{iB}$  then object  $i$  is considered to be a jet and is removed from the list of entities. The process repeats until no entities are left.

With the choice of  $p = -1$ , the soft particles tend to cluster around the hard ones long before they cluster among themselves. If a hard particle has no hard neighbours in a  $2R$  distance, it accumulate all the soft particles within the radius  $R$  which results in a perfectly conical jet. If another hard particle is present within a distance  $2R$  but outside  $R$ , two jets are formed but it is not possible for both of them to be perfectly conical. In the case of presence of another hard particle within  $R$  distance, both hard particles participate in a single jet where the centre of the jet cone depends on their momentum distribution.

**Calibration** The ATLAS hadronic calorimeters are non-compensating, meaning that the response to the electromagnetic and hadronic energy deposition is different. In other words, the measured energy deposits of an electron-initiated shower and that of a hadron-initiated shower for an electron and a hadron carrying the same initial energy is not the same, with the energy of the hadrons being underestimated. The jet energy scale,  $\eta$ , and energy resolution are calibrated in several steps as briefly explained below. The complete calibration procedure can be found in Refs. [77, 78].

Before reconstructing the jets, the individual topo-clusters are calibrated to the electromagnetic energy scale. There are two cluster calibration schemes used in the ATLAS, the electromagnetic (EM)-scale method and the Local Cluster Weighting (LCW) method [77]. In this thesis, the 13 TeV analysis uses the EM scheme and the 8 TeV analysis the LCW.

The reconstructed jets are first corrected to point back to the identified hard-scattering vertex (see Section 4.1). During the jet reconstruction the jets are initially pointed toward the nominal centre of the ATLAS detector. This jet origin correction does not affect the energy but improves the  $\eta$ -resolution.

In the next step, the effect of pile-up is removed. The in-time and the out-of-time pile-up events both affect the jet calibration. The contamination from pile-up is proportional to the area of the jet. An area-based subtraction method [79, 80] is used in order to reduce the effect of the pile-up. The residual pile-up effect is removed by applying additional corrections derived from MC simulation as a function of the number of reconstructed primary vertices ( $N_{\text{PV}}$ , measuring the actual number of collisions in a given event) and the expected average number of interactions per bunch crossing ( $\langle \mu \rangle$ , sensitive to out-of-time pile-up).

After applying the origin and pile-up corrections, the jet energy scale (JES) calibration is performed which is a series of corrections to restore the reconstructed jet energy to the truth jet energy. First, using inclusive jet simulation samples, MC-based corrections are used to bring the absolute reconstructed jet energy to the truth scale and also to remove biases in jet  $\eta$  reconstruction, caused by technology transitions and sudden granularity changes between different parts of the calorimeter. The  $\eta$  calibration alters both the jet  $\eta$  and  $p_T$ . Then, a global sequential calibration is performed to reduce the jet energy dependence on the type of the particle that initiates the jet. Several observables that are sensitive to the dependence of the jet response to the jet flavour are chosen. For each observable, an independent MC-based correction is derived as a function of jet truth  $p_T$  and  $\eta$ . The effect of each correction is to remove the dependence of the jet response on each observable while conserving the overall jet energy scale. Corrections for each observable are applied independently and sequentially to the jet four-momentum. Finally, the *in situ* calibrations are applied to account for differences in the jet response between data and MC simulations. This is done by balancing the  $p_T$  of a jet against other well-measured reference objects. The average response of forward jets are calibrated to that of well-measured central jets using di-jet events, and the average response of central jets are corrected using Z boson, photon, and multijet systems as references. For each in situ calibration, the response  $\mathcal{R}_{\text{in situ}}$  is defined in data and MC as the average ratio of the jet  $p_T$  to the reference object  $p_T$ , then the correction is defined as the ratio of  $\mathcal{R}_{\text{in situ}}$  in data to MC.

***b*-tagging** Identifying the jets that are initiated by *b*-quarks (*b*-jets) plays an important role in top-quark analyses due to the  $t \rightarrow Wb$  branching fraction being close to 100%. Identification of the jets originating from hadronisation of heavy flavour quarks exploits the distinctive properties of such hadrons, such as their long lifetime and heavy mass. Their long life time allows them to travel a measurable distance in the detector before they decay, resulting into displaced tracks that form secondary vertices. Their heavy mass leads to more energetic decay products with respect to the light-flavour jets (i.e. *u*-, *d*-, *s*-, or gluon jets). Also, their sizeable branching ratio for semileptonic decays makes the multiplicity of soft leptons in the jet another handle for heavy-flavour jet identification.

There are several algorithms used in ATLAS to identify *b*-jets [81, 82], commonly referred to as *b*-tagging algorithms. Using MVA techniques, the information from different *b*-tagging algorithms that exploit a particular property of *b*-jets are combined to build the final tagging algorithm. The output of the MVA algorithms is a discriminant value for each jet, meaning that for each jet in an event a *b*-tagging score is assigned. The operating points are defined by a single cut on the discriminant value, corresponding to determined efficiencies for identifying *b*-jets.

To tag the *b*-jets in the 8 and 13 TeV analyses, respectively the MV1 [81] and MV2c10 [82] algorithms are used. They utilise the MVA approach Boosted Decision Trees (BDT) to combine the output of three different algorithms. The jet  $p_T$  and jet  $\eta$  are the additional BDT training variables. The algorithms which provide the input for MV1 and MV2c10, listed below, all exploit the relatively long *b*-hadron lifetime:

- Impact parameter based algorithm IP3D: This algorithm relies on the transverse and longitudinal

track impact parameters (see Section 4.1), taking into account their correlations. Using a log-likelihood ratio method, for each track the measurement  $S \equiv (d_0/\sigma_{d_0}, z_0/\sigma_{z_0})$ <sup>3</sup> is compared to pre-determined two-dimensional probability density functions that are obtained from simulation for both the  $b$ -jet and the light-flavour jet hypotheses.

- Secondary vertex finding algorithm SV1: This is an inclusive secondary vertex reconstruction algorithm for inside the jets. The algorithm aims at finding the vertices formed by the decay products of the  $b$ -hadron, including the products of the possible subsequent  $c$ -hadron decay, since the  $b$ -quark predominantly decays into a  $c$ -quark. The lifetime of charm hadrons are smaller than of bottom hadrons, but are large enough for them to travel measurable distances at high energies. Tracks that are distant enough from the primary vertex but are associated with the jet are used. A likelihood ratio exploit different vertex properties in order to reject the vertices from long-lived particles like  $K_s$  and  $\Lambda$ , or from photon conversions.
- JetFitter: This algorithm exploits the topological structure of weak  $b$ - and  $c$ -hadron decays inside the jet and aims to reconstruct the complete decay chain. It uses a Kalman filter to find a common line on which the primary vertex and the  $b$  and  $c$  vertices lie, approximating the  $b$ -hadron flight path.

The MV1 operating point that is used in the 8 TeV analysis yields a  $b$ -jet tagging efficiency of 70% in simulated  $t\bar{t}$  events for jets with  $p_T > 20$  GeV and  $|\eta| < 2.5$ , which corresponds to a light-favour jet rejection factor of 140<sup>4</sup>. In the 13 TeV analysis, the MV2c10 operating point corresponds to an efficiency of 77% is used, corresponding to a rejection factors for light-favour jet and  $c$ -jet of 134 and 6 respectively.

## 4.5 Photon

**Reconstruction** Photons [55, 83] and electrons have very similar signatures in the EMCal, therefore their reconstruction proceeds in parallel. Before entering the EMCal, electrons leave a track behind in the ID. Photons on the other hand do not interact with the tracker as they are electrically neutral, but there is a certain probability for them to convert into an electron-positron pair when they traverse the ID material.

The electromagnetic clusters in the EMCal are first reconstructed as described in Section 4.2. Then the tracks reconstructed in the ID are matched to the electromagnetic cluster, as also described in Section 4.2. The electromagnetic clusters to which no tracks are matched are classified as unconverted photon candidates. If the tracks matched to an electromagnetic cluster are compatible with a photon conversion vertex, it is considered as a converted photon, otherwise it is set as an electron candidate. Therefore, a crucial step in reconstruction of electrons and photons is the reconstruction of photon conversion secondary vertex.

The two-track conversion vertices are reconstructed from pairs of oppositely charged tracks that are likely to be electrons, as determined from TRT information. Since the tracks of a photon conversion are parallel at the point of conversion, geometric requirements are used to select the track pairs. The track pairs are categorised as Si-Si, TRT-TRT, and Si-TRT, depending on whether both tracks, none, or only

<sup>3</sup>  $d_0/\sigma_{d_0}$  ( $z_0/\sigma_{z_0}$ ) is the transverse (longitudinal) track impact parameter significance, where  $\sigma_{d_0}$  ( $\sigma_{z_0}$ ) is the uncertainty on the reconstructed  $d_0$  ( $z_0$ ).

<sup>4</sup> The rejection factor for light-favour and  $c$ -jets are defined as the inverse of the efficiency for tagging a light-favour jet or a  $c$ -jet as a  $b$ -jet, respectively.

one of them have hits in the silicon detectors, respectively. The applied geometric requirements for each of the three categories are different. Then a vertex fit is performed, using all the five track parameters (see Section 4.1) of each of the two participating tracks, with the constraint that the tracks are parallel at the vertex.

It is not always possible to reconstruct converted photons with two associated tracks. There are cases that one of the two tracks is not reconstructed, either because it is very soft, or because the two tracks are very close to each other and cannot be adequately separated. These effects are specially more significant for conversions taking place in the outermost layers of the ID. Therefore, the single-track conversion vertices are built from tracks without hits in the innermost sensitive layers. These tracks must either have a very high likelihood to be an electrons based on TRT information, or have no hits in the TRT. Since it is not possible to perform a vertex fit with a single track, the location of the first measurement of the track defines the conversion vertex.

Similar to the track-cluster matching (see Section 4.2), a vertex-cluster matching is performed by extrapolating the vertex to the middle layer of the EMCal and matching it to electromagnetic cluster centre based on their distance in  $\eta$  and  $\phi$ . In case of multiple matched conversion vertices to a cluster, the two-track conversions are preferred over single-track conversion, and when the number of tracks are the same the preference is given to the candidates with more tracks with hits in the silicon detectors, and finally if the number of tracks with hits in the silicon detectors are the same, the vertex with the smallest conversion radius<sup>5</sup> is preferred.

The photon energy measurement is performed using information from the calorimeter. Same as for the electrons, first the cluster of reconstructed photon candidates are rebuilt, using a larger window size than the initial ones:  $3 \times 7$  ( $3 \times 5$ ) towers in the barrel region of the EMCal for the converted (unconverted) photons, and  $5 \times 5$  towers in the endcaps. Then the energy of the clusters are determined after performing the calibration procedure described in Ref. [69]. The photon  $E_T$  is computed from the calibrated cluster energy and the pseudorapidity of the centre of the cluster in the second layer of the EMCal ( $\eta_2$ ):  $E_T = E / \cosh \eta_2$ .

**The author's contribution in photon reconstruction for run-2:** The reconstruction efficiency of converted photons are studied under the different scenarios for the TRT gas configuration before starting the run-2. Furthermore, the changes that are made in the photon reconstruction with respect to run-1, in order to improve both reconstruction efficiency and rejection of fake converted photons (i.e. unconverted photons that are wrongly reconstructed as converted photons), are validated. These changes are listed in [83].

**Identification** Photon identification distinguishes between prompt photons and background photons that originate from the decay of hadrons in jets or jets depositing a large energy fraction in the EMCal. Prompt photons typically have narrower energy deposits in the EMCal and smaller leakage to the HCal, compared to the photons originated from jets. In addition, the background photons coming from neutral hadron decays to two photons (dominantly  $\pi^0 \rightarrow \gamma\gamma$ ) are characterised by two separate local energy maxima in the finely segmented first layer of the EMCal (strip layer). Therefore, photon identification is based on a set of cuts on shower-shape variables (see Section 4.2), listed in Table 4.1.

Two sets of photon identification criteria - Loose and Tight- are defined. The Loose selection is based on shower shapes in the second layer of the EMCal and the energy leakage in the HCal. The Tight selection adds information from the strip layer of the EMCal, and is separately optimised for unconverted and converted photons, to account for the generally broader shower profile of the latter.

---

<sup>5</sup> The conversion radius is defined as the distance from the conversion vertex to the beam line in the transverse plane.

Both selection criteria are optimised in bins of photon  $\eta$ , in order to account for the calorimeter geometry and for the effects on the shower shapes from the material upstream of the calorimeter, which is non-uniform as a function of  $\eta$ . While the same set of discriminating variables and the same  $\eta$ -binning are used for the photon identification in run-1 and run-2, the selection cuts are tuned prior to the 2012 data taking in run-1 (when centre-of-mass energy increased from 7 to 8 TeV) and then again prior to run-2, to cope with the higher pileup expected and reduce the dependency of the identification efficiency on pile-up. The presence of pile-up tends to broaden the distributions of the shower-shape variables, thus reduces the separation between prompt and background photon candidates.

Both of the 8 and 13 TeV analyses presented in this thesis use the **Tight** identification criteria. The **Tight** identification used in the 8 TeV analysis provides an efficiency that increases from 50-65% (45-55%) for unconverted (converted) photon candidates at  $E_T \approx 10$  GeV to 94-100% at  $E_T = 100$  GeV, and is greater than 90% for  $E_T > 40$  GeV [55], while for the 13 TeV it increases from 45-60% at  $E_T = 10$  GeV to 95-98% for  $E_T > 100$  GeV [83].

Name	Description	Loose	Tight
Leakage in the HCal			
$R_{\text{had}1}$	Normalised hadronic leakage: Ratio of the transverse energy deposited in the cells of the first layer of the HCal which centre in a window of $\Delta\eta \times \Delta\phi = 0.24 \times 0.24$ behind the photon cluster, to the transverse energy of the photon. This is used over the range of $ \eta  < 0.8$ and $ \eta  > 1.37$ .	✓	✓
$R_{\text{had}}$	Ratio of the transverse energy in HCal to the transverse energy of the electromagnetic cluster. This is used over the range of $0.8 \leq  \eta  \leq 1.37$ .	✓	✓
Variables using the second (middle) layer of the EMCal			
$R_\eta$	Ratio of energy of $3 \times 7$ to $7 \times 7$ cells in $\eta - \phi$	✓	✓
$R_\phi$	Ratio of energy of $3 \times 3$ to $3 \times 7$ cells in $\eta - \phi$	–	✓
$w_{\eta 2}$	Lateral width of the shower	✓	✓
Variables using the first (strip) layer of the EMCal			
$w_{s3}(w_{\eta 1})$	Shower width using three strips around the maximum	–	✓
$w_{s,\text{tot}}$	Total lateral width of the shower	–	✓
$f_{\text{side}}$	Energy within 7 strips without 3 central strips normalised to energy in 3 central strips.	–	✓
$E_{\text{ratio}}$	Ratio between difference of first 2 energy maxima divided by their sum ( $E_{\text{ratio}} = 1$ if there is no second maximum).	–	✓
$\Delta E$	Difference between the second energy maximum and the minimum between first and second maximum ( $\Delta E = 1$ if there is no second maximum).	–	✓

Table 4.1: Discriminating variables used for the photon identification.

**Corrections to Simulated Shower-shapes** The distribution of photon shower-shape variables in MC simulation shows some discrepancy with respect the distributions in data. While the shape of the

distributions in data and MC are rather similar, the observed differences are in the average values of the distributions. This points to a mismodelling of the lateral profile development of the electromagnetic showers in MC simulation, while the longitudinal electromagnetic shower profiles are in general well described. These data-MC differences are measured from  $Z \rightarrow ll\gamma$  ( $l = e, \mu$ ) and single-photon ( $\gamma + \text{jets}$ ) events and parametrised as simple shifts to be applied to the MC simulations to align them with data. Figure 4.1 shows as an example the  $w_{s3}$  distributions in  $Z \rightarrow ll\gamma$  events in 13 TeV, separately for converted and unconverted photons, in data and MC before and after implementing the corrections.

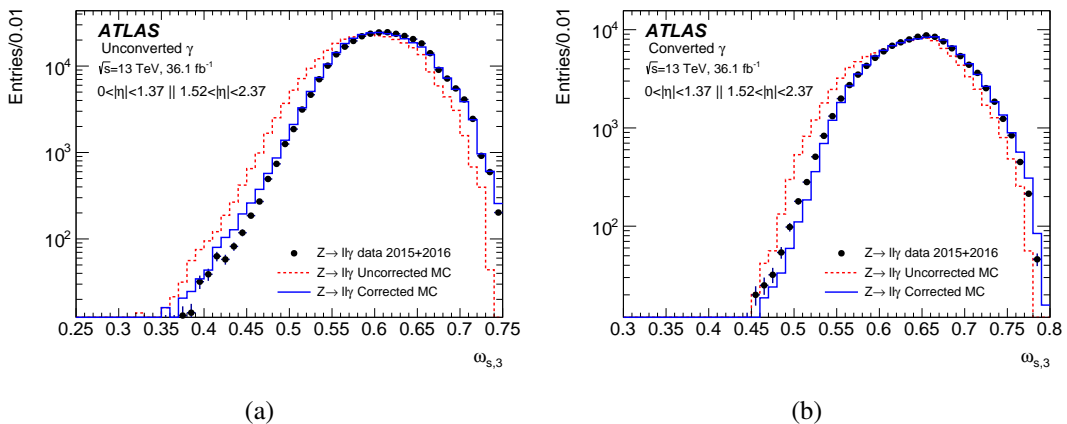


Figure 4.1: Distributions of the photon shower-shape variable  $w_{s3}$  in  $Z \rightarrow ll\gamma$  events in data and MC (before and after correction) for (a) unconverted and (b) converted photons [83].

**Isolation** In the 8 TeV analysis presented in this thesis no photon isolation is required. Instead, the photon isolation is used to built templates for signal and background photons, as explained later in Section 7.2.1.

Photons used in the 13 TeV analysis are isolated. Three different isolation working points are provided by ATLAS, as shown in Table 4.2, from which this analysis has used the `FixedCutTight` working point.

Name	Description
<code>FixedCutLoose</code>	$E_T^{\text{cone}20} < 0.065 p_T(\gamma)$ and $p_T^{\text{cone}20} < 0.05 p_T(\gamma)$
<code>FixedCutTight</code>	$E_T^{\text{cone}40} < 0.022 p_T(\gamma) + 2.45 \text{ GeV}$ and $p_T^{\text{cone}20} < 0.05 p_T(\gamma)$
<code>FixedCutTightCaloOnly</code>	$E_T^{\text{cone}40} < 0.022 p_T(\gamma) + 2.45 \text{ GeV}$

Table 4.2: Photon isolation working points.

**Efficiencies and Scale Factors** The photon identification efficiencies are measured separately for converted and unconverted photon candidates in different  $\eta$  regions, by combination of three complementary data-driven methods as outlined in Refs. [55, 83]. The identification efficiencies are measured in data and MC, after corrections to the simulated shower-shapes are applied, and the Data-to-MC efficiency ratios used as scale factors to correct for the small residual efficiency differences.

## 4.6 Missing Transverse Momentum

As explained in Section 3.2.1, the missing transverse momentum [84, 85] can be associated with neutrinos. The measurement of  $E_T^{\text{miss}}$  strongly depends on the energy scale and resolution of the reconstructed physics objects. The reconstructed  $E_T^{\text{miss}}$  has two types of contributions. The first one, the *hard term*, is computed from all the high- $p_T$  physics objects in the event. This includes the reconstructed and fully calibrated electrons, photons, muons, hadronically decaying  $\tau$ -leptons, and jets. The second one, the *soft term*, consist of the calorimeter energy deposits or tracks (depending on the soft-term definition) that are not associated to the physics objects included in the hard terms, i.e. soft signals.

The missing transverse momentum components,  $E_x^{\text{miss}}$  and  $E_y^{\text{miss}}$ , are given by:

$$E_{x(y)}^{\text{miss}} = - \sum_{i \in \{\text{hard objects}\}} p_{x(y),i} - \sum_{j \in \{\text{soft signals}\}} p_{x(y),j}, \quad (4.4)$$

and the  $E_T^{\text{miss}}$  is calculated from the components as:

$$E_T^{\text{miss}} = |\vec{E}_T^{\text{miss}}| = \sqrt{(E_x^{\text{miss}})^2 + (E_y^{\text{miss}})^2}. \quad (4.5)$$

In the calculation of  $E_{x(y)}^{\text{miss}}$ , the contributing objects need to be reconstructed from mutually exclusive signals in order to avoid possible double counting of contribution. Therefore, the energy deposits in the calorimeters and the tracks are matched to reconstructed physics objects in the following order: electrons, photons, hadronically decaying  $\tau$ -leptons, jets, and finally muons. Generally, if two objects share a signal, the object with lower priority is rejected.

The soft term is a necessary but challenging component of the  $E_T^{\text{miss}}$ . It accounts for the typically low- $p_T$  contributions from hard scattering which are not included in the hard term. While the hard term is characterised by little dependence on pile-up because it includes only fully calibrated objects, where the calibration includes a pile-up correction, the soft term is susceptible to contributions from pile-up and underlying events. Several algorithms for reconstructing and calibrating the soft term, as well as methods to suppress the pileup contributions, are developed in ATLAS. The analyses presented in this thesis make use of the Track Soft Term (TST) algorithm. The TST is reconstructed from ID tracks that match to a hard-scattering vertex (see Section 4.1) and are not associated with any of the objects used in the hard term. Although this approach misses the contribution from soft neutral particles and is limited to the ID coverage region ( $|\eta| < 2.5$ ), its excellent vertex matching strongly suppresses the pile-up contributions to the point that it is preferred to the calorimeter-based approaches.

The performance of  $E_T^{\text{miss}}$  reconstruction is studied by comparing the simulation and data using the  $W \rightarrow l\nu$  and  $Z \rightarrow ll$  processes. The  $W \rightarrow l\nu$  process feature a relatively high expected  $E_T^{\text{miss}}$  and provides a well-defined topology to study the  $E_T^{\text{miss}}$  distributions. The  $Z \rightarrow ll$  process is expected to have an intrinsic  $E_T^{\text{miss}}$  close to zero, therefore it is used to evaluate the modelling of the effects that give rise to fake  $E_T^{\text{miss}}$ . More details can be found in Refs [84, 85].



# CHAPTER 5

---

## Data and Simulated Samples

---

The data and simulated samples used in the analyses presented in this thesis are introduced in this chapter.

### 5.1 Collision Data

The  $t\bar{t}\gamma$  cross-section measurements presented in this thesis are performed in two different energy regimes, using the data collected by the ATLAS detector from proton-proton ( $pp$ ) collisions in the LHC,

- at a centre-of-mass energy of  $\sqrt{s} = 8$  TeV, collected in 2012 from run-1 of data taking, with a corresponding integrated luminosity of  $20.2 \text{ fb}^{-1}$ ,
- at a centre-of-mass energy of  $\sqrt{s} = 13$  TeV, collected in 2015 and 2016 from run-2 of data taking, corresponding to an integrated luminosity of  $36.1 \text{ fb}^{-1}$ .

Throughout this thesis the two analyses are referred to by their centre-of-mass energy.

The configuration of the LHC proton beams and the conditions of the ATLAS detector sub-systems and readout can change during the data taking. Only the data collected in stable beam conditions and satisfying restricted detector and data quality requirements is considered. This includes the full operation of all the sub-systems of ATLAS. Candidate events in data are collected using the trigger menus explained in Section 7.1 and 8.1. Distributions of mean number of interactions per bunch crossing,  $\mu$ , in 8 and 13 TeV data are shown in Figure 5.1. The number of interactions per crossing for each bunch follows a Poisson distribution and  $\mu$  is the mean value of the Poisson distribution. The value of  $\langle \mu \rangle$  is a quantification of the amount of pileup in data.

### 5.2 Monte Carlo Simulated Samples

In order to compare the observed data with theoretical models, MC techniques are used to model the signal and background processes resulted from  $pp$  collisions described in Section 2.2. The first main step in production of the MC simulated samples is the *event generation*. In this step, the scattering process of interest is simulated from the incoming protons up to the stable particles that fly into the detector. The event generation follows with the second step, the *detector simulation*, where the detector response to the stable particles from the event generation is simulated. The MC simulated events then passed to the same reconstruction algorithms that are used for data, outlined in Chapter 4.

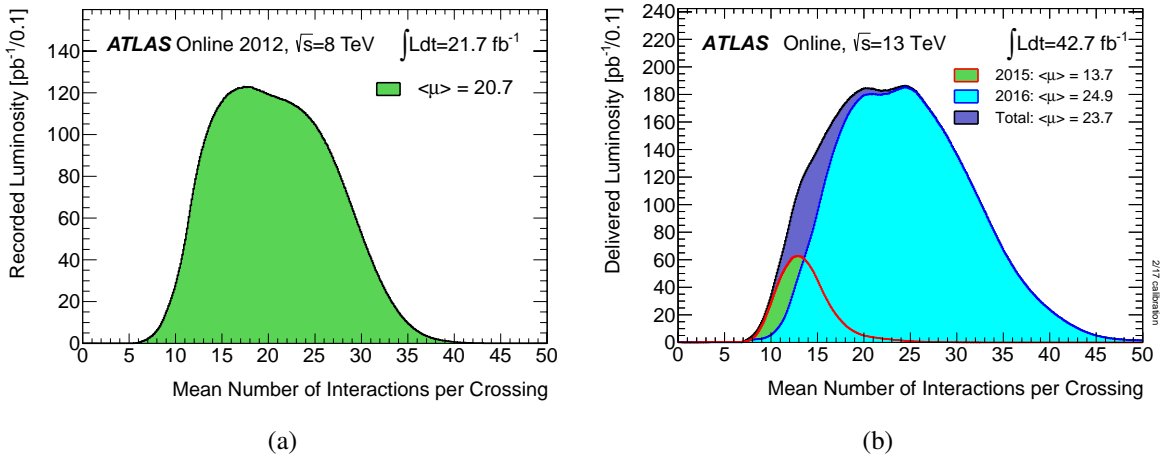


Figure 5.1: The average number of interactions per bunch crossing in  $pp$  collisions (a) at  $\sqrt{s} = 8$  TeV during 2012 [86] (b) at  $\sqrt{s} = 13$  TeV during 2015 and 2016 [87]. All data delivered to ATLAS during stable beams are shown.

The event generation itself is performed in different steps. First the  $2 \rightarrow n$  hard scattering process is simulated, where the MC generators convoluted with the PDFs are used to calculate the ME in a fix order of perturbative QCD calculations, usually LO or NLO. For the case of short lived particles, the decay to stable particles are also performed. In the next step, the hard process events are interfaced with a second MC generator that simulates the non-perturbative evolution of the final state. This includes the extra radiations in the initial and final state (ISR and FSR) and the parton showering, followed by hadronisation. The decay of the long-lived particles are included as well. The simulation of pile-up and underlying events (together referred to as *minimum bias events*) is provided by overlaying extra  $2 \rightarrow 2$  scatterings at low scales. The processes that are non-perturbative could only be approximated from phenomenological methods and their simulations are not as precise as the ME generation. Therefore, their implementations in MC programs rely heavily on tuning to data. Various tune parameters are optimised in order to reasonably well describe certain observable distributions in data. Furthermore, the simulated pile-up distribution is re-weighted to match data.

The MC generators used to perform the ME generation are **MADGRAPH5\_aMC@NLO** [88, 89], **POWHEG-Box** [90–92], **SHERPA** [36] and **ALPGEN** [93]. For the parton showering, hadronisation and underlying event modelling they are interfaced to **PYTHIA** [94, 95] or **HERWIG** [35, 96], except for **SHERPA** that provides its own parton showering and hadronisation modelling. The Lund (String) Model is the model implemented in **PYTHIA** for the hadronisation, while **HERWIG** uses the Cluster Model (see Section 2.2.2). Often **HERWIG** is linked with **JIMMY** [97] in order to simulate the underlying events. The dedicated generator **Photos** [98, 99] is used to improve the simulation of extra QED radiations. The decay of tau-leptons is handled with **TAUOLA** [100, 101], and **EvtGen** [102] is used to simulate the decay of bottom and charm hadrons. The overlaid pile-up are generated by **PYTHIA**.

Finally, the generated events go through the detector simulation, using GEANT4 [103]. The latest and detailed description of the ATLAS detector (material, geometry, magnetic fields, and sub-systems, including trigger) is the input for the GEANT4 simulation toolkit. First the interactions of all traversing particles with the detector are simulated. Then, in the step known as *digitization*, the detector responses are converted to digital signals simulating the readout system of the ATLAS detector. The simulated events at this point are ready to go through the reconstruction algorithms. A description of ATLAS simulation infrastructure is available in Ref. [104].

In the following the detail of MC simulated samples used for the signal and background processes in the 8 and 13 TeV analyses are given. The summary lists of the samples are available in Appendix C.

### 5.2.1 Simulation of Signal Events

The  $t\bar{t}\gamma$  signal sample is simulated as a  $2 \rightarrow 7$  process with **MADGRAPH5\_aMC@NLO** (denoted as **MADGRAPH** hereafter). The ME is generated at the LO accuracy in QCD, including the decays of top quarks, for the single-lepton and dilepton decay channels of  $t\bar{t}\gamma$ . The photon can be radiated from the incoming charged partons, the top quarks, or any of the charged particles in the decay chain (i.e.  $W$  boson,  $b$ -quark, charged leptons).

For the 8 TeV analysis, version 2.1.0 of **MADGRAPH** generator is used. The generated events are interfaced with **PYTHIA** v6.427 for parton showering, hadronisation, and underlying event modelling, using the Perugia2011C tuning [105]. The PDF set CTEQ6L1 (LO) [32] used for both the ME generation and **PYTHIA**.

In the 13 TeV analysis, ME generation is done by version 2.33 of the **MADGRAPH** generator, and interfaced with **PYTHIA** v8.212 using the A14 set of tuned parameters [106]. The PDF set NNPDF2.3LO set [33] is used with both **MADGRAPH** and **PYTHIA**.

The particle masses, the decay widths of the top quark and the  $W$  boson, the fine structure constant ( $\alpha$ ), and the QCD renormalisation ( $\mu_R$ ) and factorisation ( $\mu_F$ ) scales are set to the values listed in Table 5.1. The masses of  $u$ -,  $d$ -,  $s$ -, and  $c$ -quark are set to zero since they are considered as initial state quarks and their masses are much smaller than the typical scale of the hard  $t\bar{t}\gamma$  process. This approximation simplifies the ME calculation. For the signal sample used in the 13 TeV analysis, the  $b$ -quark is also considered as one of the initial state quarks<sup>1</sup>, therefore its mass is approximated to zero, while in the 8 TeV analysis it is considered to be massive because it is not included in the initial state quarks<sup>2</sup>. The mass of electron is also approximated to zero as it is much smaller than the typical scale in the evolution of the final state. While for the 8 TeV sample  $\mu_R$  and  $\mu_F$  are set to two times of the top-quark mass, for the 13 TeV sample they are set dynamically, corresponding to half of the sum of transverse energies of all the particles generated from the ME, where the transverse energy of a particle with rest mass  $m$  and transverse momentum  $p_T$  is defined as  $E_T = \sqrt{m^2 + p_T^2}$ .

Signal sample inputs	$u/d/s/c$ -quark mass [GeV]	$b$ -quark mass [GeV]	top quark mass [GeV]	top quark decay width [GeV]	$W$ boson decay width [GeV]	electron mass [GeV]	muon mass [GeV]	tau mass [GeV]	$\alpha$	$\mu_R / \mu_F$
8 TeV	0	4.7	172.5	1.320	2.085	0	0.105	1.777	$\frac{1}{137}$	$2m_{\text{top}}$
13 TeV		0								dynamic

Table 5.1: Input parameters set for the  $t\bar{t}\gamma$  signal sample simulation in 8 and 13 TeV analyses.

Since real photons are massless, their emission in the infrared limit (emissions of photons with negligible momentum) and the collinear limit (emissions of photons under a very small opening angle with respect to the emitting particle) exhibit divergencies in finite order calculations. To avoid the infrared and collinear singularities, and to increase the production efficiency, the following set of requirements are applied for the generated events:

- At least one photon is required.

<sup>1</sup> This is the so-called *five-flavour scheme*, in which  $u$ -,  $d$ -,  $s$ -,  $c$ -and  $b$ -quarks are treated as active flavours inside the proton.

<sup>2</sup> This corresponds to the so-called *four-flavour scheme*, as opposed to the five-flavour scheme explained above, where  $b$ -quarks are only considered as final state particles.

- Photons are required to have  $p_T > 10$  (15) GeV and  $|\eta| < 5.0$  in the signal sample produced for the 8 (13) TeV analysis.
- At least one lepton is required.
- Leptons must have  $p_T > 15$  GeV and  $|\eta| < 5.0$ .
- The  $\Delta R$  distance (defined as Equation 3.9) between the photon and all the charged particles in the final state must be larger than 0.2.

Additional photon radiation is generated with PHOTOS 2.15.4 and TAUOLA 2.7 is used for the decay of tau-leptons.

The resulting total cross section is calculated to be 1.19 pb and 4.62 pb for the 8 TeV and the 13 TeV signal  $t\bar{t}\gamma$  samples, respectively.

Several alternative signal samples are produced in order to evaluate the signal modelling uncertainties.

For the 8 TeV analysis, the effect of the scale choices are studied by comparing the nominal sample with two alternative samples that are produced with varied  $\mu_R$  and  $\mu_F$  values, by spontaneously changing them by a factor of 1/2 and two. To study the effect of initial- and final-state radiations (ISR and FSR) modelling, alternative samples are produced with the relevant PYTHIA Perugia2011C tunes varied up and down. The uncertainty due to the parton showering, hadronisation and underlying event modelling is obtained by comparing the nominal sample with an alternative sample generated by using HERWIG v6.520/JIMMY v4.31 instead of PYTHIA.

For the 13 TeV analysis, the effect of ISR and FSR modelling is studied through the alternative samples produced with the relevant PYTHIA A14 Var3c tune parameters varied. Also, an alternative sample is generated by using HERWIG v7.0.1 instead of PYTHIA in order to account for the uncertainty due to the parton showering, hadronisation and underlying event modelling. In the 13 TeV analysis, for varied  $\mu_R$  and  $\mu_F$  values no new samples are produced, as they are available as weights in the nominal sample.

### **Next-to-Leading Order $k$ -factor for the Signal Sample**

The theoretical calculations of  $t\bar{t}\gamma$  production in NLO accuracy in QCD are available [107]. Taking advantage of these theory calculations, the  $t\bar{t}\gamma$  signal MC samples in both 8 and 13 TeV analyses are normalised to the NLO predictions. This is done by using  $k$ -factors, defined as the ratio between NLO and LO cross sections.

Although the results presented in Ref. [107] are calculated for  $\sqrt{s} = 14$  TeV, dedicated calculations are performed by the authors of Ref. [107] for  $\sqrt{s} = 8$  and 13 TeV, using the same techniques. The calculation of the  $k$ -factor for the 8 TeV signal sample is presented in Section 7.2.4 and for the 13 TeV sample in Section 8.2.5.

## **5.2.2 Simulation of Background Events**

### **Background Samples for the 8 TeV Analysis**

The  $t\bar{t}$  production is simulated at NLO accuracy in QCD with PowHEG-Box v1.0 using the CT10 (NLO) [108] PDF set, interfaced with PYTHIA v6.427 using the same tune parameters as the signal  $t\bar{t}\gamma$  sample. The  $h_{damp}$  parameter, which controls the  $p_T$  of the first additional parton emission beyond the Born configuration in PowHEG, is set to  $m_{top}$ <sup>3</sup>. In the 8 TeV analysis the  $t\bar{t}$  sample is only used for validation studies,

---

<sup>3</sup> The main effect of this parameter is to regulate the high- $p_T$  emissions against which the  $t\bar{t}$  system recoils [109]

no background is estimation from this sample.

The productions of the  $W$  and  $Z$  bosons in association with a photon ( $W\gamma$  and  $Z\gamma$ ) are simulated with **SHERPA** 1.4.0 at LO (with up to three partons in the final state), using the **CT10** (NLO) PDF set. An alternative  $W\gamma$  sample is used to evaluate the modelling uncertainty of the  $W\gamma$  background. It is generated by **ALPGEN** 2.14 and interfaced to **PYTHIA** 6.426., using **CTEQ6L1** PDF set for both ME calculation and parton showering. Since the contribution from  $Z\gamma$  background is very small, no dedicated sample for evaluating  $Z\gamma$  modelling uncertainties are used.

The single-top production in the  $t$ -  $s$ - and  $Wt$ -channels are generated at NLO with **POWHEG-Box** v1.0 [110, 111], using the **CT10** (NLO) PDF set for ME calculation in the  $s$ - and  $Wt$ -channels and **CT104fs** PDF set for the  $t$ -channel. The generated events are interfaced to **PYTHIA** 6.426 in the  $Wt$  channel and to **PYTHIA** 6.427 in the  $s$ - and  $t$ -channels. The single-top production in  $Wt$ -channel and  $t\bar{t}$  production interfere beyond LO. To remove the overlaps, the  $Wt$ -channel sample is produced using the diagram removal generation scheme [112]. The samples in the  $t$ - and  $Wt$ -channels are normalised to the NNLO calculations by  $k$ -factors.

The diboson production of  $WW$ ,  $WZ$  and  $ZZ$  are generated by **ALPGEN** 2.14 at LO, interfaced to **HERWIG** v6.520/**JIMMY** 4.31, using the **CTEQ6L1** PDF set and the **AUET2** tune [113]. The diboson samples are normalised to the NLO calculations, using  $k$ -factors.

In all above samples, for the QED radiative corrections **Photos** is used. Hence, in the samples that a photon is absent in the ME generation level (i.e.  $t\bar{t}$ , single-top and diboson productions), the photon radiation is simulated in the fragmentation process with **Photos**.

## Background Samples for the 13 TeV Analysis

The nominal MC simulated  $t\bar{t}$  sample is generated with **POWHEG-Box** v2, using the **NNPDF3.0NLO** PDF set [114]. It is interfaced with **PYTHIA** v8.210 using the **A14** tune set and the **NNPDF2.3LO** PDF set [33]. The  $h_{damp}$  parameter is set to  $1.5m_{top}$ .

Two alternative  $t\bar{t}$  samples are used to evaluated the uncertainties due to QCD scale choices and the modelling of the ISR and FSR. One of the samples is generated using the  $\mu_R$  and  $\mu_F$  scales varied down by a factor of two, the  $h_{damp}$  parameter value increased by a factor of two, and varying the **A14 Var3c** tune parameter to the values corresponding to higher radiation activity. The other sample is generated with the  $\mu_R$  and  $\mu_F$  scales varied up by a factor of two, keeping the  $h_{damp}$  parameter at its nominal value, and varying the **A14 Var3c** tune parameter to low radiation. A third alternative  $t\bar{t}$  samples is generated by **SHERPA** v2.2 to evaluate the uncertainty of the choice of the ME generator and the parton showering and hadronisation program.

The  $W\gamma$  and  $Z\gamma$  productions are generated with **SHERPA** v2.2.2, while the inclusive production of  $W$ +jets and  $Z$ +jets are simulated with **SHERPA** v2.2.1. All four samples use the **NNPDF3.0NLO** PDF set.

The production of single top quark in  $t$ -,  $s$ - and  $Wt$ -channels are simulated with **POWHEG-Box** v1. The PDF set used for  $s$ - and  $Wt$ -channels is the **CT10** (NLO) set, while for  $t$ -channel the **CT104fs** PDF set is used. All channels are interfaced with **PYTHIA** v6.428, using the **Perugia2012** tunes [105] and the **CTEQ6L1** PDF set.

The  $WW$ ,  $WZ$  and  $ZZ$  diboson samples are generated by **SHERPA** v2.1, using the **CT10** (NLO) PDF set.

All above samples are generated at NLO precision in QCD, and those for which the NNLO calculations are available are normalised to the NNLO using  $k$ -factors. Same as for the 8 TeV background samples, in the samples that the ME does not include photon radiations (i.e.  $t\bar{t}$ , single-top, diboson,  $W$ +jets and  $Z$ +jets productions), the photon radiation is present through QED radiative corrections by **Photos** in the fragmentation process.

### 5.2.3 Removal of the Event Double Counting between Samples

Because the showering procedure adds photon radiations to the simulated events in inclusive  $t\bar{t}$  and  $V+jets$  samples ( $V = W, Z$ ), they can contain events that are already accounted for by the  $t\bar{t}\gamma$  and  $V\gamma$  samples ( $V = W, Z$ ). Using truth information, this overlap is removed by vetoing the events in the  $t\bar{t}\gamma$  and  $V\gamma$  samples where the selected photon is not originated from the hard interaction before hadronisation (prompt photon), and vetoing the events in the  $t\bar{t}$  and  $V+jets$  samples where the selected photon is a background photon coming from hadron decays within a jet, a jet that is mis-reconstructed as a photon, or an electron mis-reconstructed as a photon. These different categorisations of photons are explained thoroughly in Chapters 7 and 8. After this overlap removal the  $t\bar{t}$  and  $V+jets$  samples only contribute to the backgrounds with non-prompt and fake photons, the  $V\gamma$  sample only contribute to the backgrounds where the photon is prompt, and the  $t\bar{t}\gamma$  sample only contains the signal.

The reconstructed photons are matched to a truth object at the particle level, i.e. after simulation of hadronisation and showering processes and before the detector simulation<sup>4</sup>. If the reconstructed photon is associated to a true electron, or if a true electron (with  $p_T > 10$  GeV and  $|\eta| < 3$ ) in a cone size of 0.05 around the reconstructed photon is found, it is considered as the case of an electron faking a photon. If the reconstructed photon is associated to a true hadron, or a true photon which is not originating from ISR, FSR, a boson, or a prompt lepton, and is originating from a hadron, it is considered as a fake or non-prompt photon from a jet. Any other cases are considered as prompt photons.

---

<sup>4</sup> The truth type and truth origin of the particles are extracted from the algorithms provided by ATLAS in a tool called `MCTruthClassifier` [115].

# CHAPTER 6

---

## Cross-Section Definitions and Likelihood Description

---

Before describing the  $pp \rightarrow t\bar{t}\gamma$  cross-section measurements at  $\sqrt{s} = 8$  and 13 TeV in chapters 7 and 8, respectively, the definitions of total, fiducial and differential cross sections, alongside the description of the likelihood functions used to extract the cross sections are outlined in this chapter. The definitions and descriptions presented here are the common ingredients of both analyses. Any further analysis-specific descriptions will follow in the relevant analysis chapters.

### 6.1 Total Cross Section

The total  $pp \rightarrow t\bar{t}\gamma$  cross section,  $\sigma_{t\bar{t}\gamma}^{\text{tot}}$ , could have been simply calculated from Equation 3.3 by counting the number of  $t\bar{t}\gamma$  signal events in the data-set and knowing the total integrated luminosity of the collected data-set,  $L$ . However, the measured number of  $t\bar{t}\gamma$  signal events from the data-set is not really equal to the *total* number of  $t\bar{t}\gamma$  events that are produced. It is subject to the efficiency of reconstructing the events and selection the signal. Also, it does not correspond to the total phase space, since the measurement is performed in a phase space limited to the geometrical (and kinematical) acceptance of the detector. Therefore, the proper correction and extrapolation factors are needed to be added in Equation 3.3:

$$\sigma_{t\bar{t}\gamma}^{\text{tot}} = \frac{N_{t\bar{t}\gamma}}{L \cdot A \cdot C}. \quad (6.1)$$

Factor  $A$  is called the *acceptance factor*, which extrapolates the measurement from the phase space in which the measurement is performed, to the total phase space. Factor  $C$  is called the *correction factor*, which accounts for the  $t\bar{t}\gamma$  signal events that are produced inside the measurement phase space to be reconstructed and selected. It also corrects for the events that are produced outside of this phase space but are wrongly reconstructed as an event belonging to this volume. More explanation on this will follow later in this Chapter.

Both  $A$  and  $C$  can be derived from the MC simulated  $t\bar{t}\gamma$  sample, as shown later in Section 6.2. As explained in Section 5.2.1, in the production of  $t\bar{t}\gamma$  signal sample some minimum kinematic requirements are applied at the ME generation level, in order to remove divergencies (and also to increase the generation efficiency). Therefore, the acceptance factor  $A$  which is derived from this MC sample can never extrapolate the measurement to a *total* phase space as a conventional meaning of the word "total" may suggest. Rather, it extrapolates the measurement to the phase space defined by the imposed

requirements at generation level, which is still a larger phase space than the one of the measurement. In principle, an acceptance factor could also be derived from theory calculations. In other top-quark related analyses often the total cross section is calculated from theory. However, due to the presence of a photon in the final state this is not possible in the case of  $t\bar{t}\gamma$ , since again in the theory calculations kinematic requirements to avoid divergencies are needed. So wherever in this text the terms total cross section and total phase space are used, one should note that it means the total available phase space of the generated events.

In case of measuring the cross section in a specific decay channel of  $t\bar{t}\gamma$ , Equation 6.1 changes to:

$$\sigma_{t\bar{t}\gamma,l}^{\text{tot}} = \frac{N_{t\bar{t}\gamma,l}}{L \cdot A_l \cdot C_l} = \sigma_{t\bar{t}\gamma}^{\text{tot}} \times \text{BR}_l, \quad (6.2)$$

where index  $l$  indicates the decay channel and  $\text{BR}_l$  is the branching ratio of channel  $l$ .

## 6.2 Fiducial Cross Section

Since the acceptance factor  $A$  extrapolates the measurement into a theoretical phase space where no measurement is performed, it depends on the simulation modelling. Hence, it is subject to theoretical uncertainties. Therefore, it is more convenient to skip such extrapolation and report the cross section in the fiducial phase space of the detector, where the measurement is actually performed. This way, the reported cross section is (ideally) model-independent and depends only on detector related effects, through the correction factor  $C$ . But this is only useful if the theory predictions for the specific fiducial phase space are also available. Therefore, the fiducial region needs to be defined in advance and be agreed upon by experimentalist and theorists. In addition, a direct comparison between the result of different experiments (for example ATLAS and CMS) could be possible if they use a common fiducial region definition.

The fiducial cross section for channel  $l$  is expressed as:

$$\sigma_{t\bar{t}\gamma,l}^{\text{fid}} = \frac{N_{\text{obs},l} - N_{\text{bkg},l}}{L \cdot C_l} = A_l \times (\sigma_{t\bar{t}\gamma}^{\text{tot}} \times \text{BR}_l), \quad (6.3)$$

where  $N_{\text{obs},l}$  is the observed number of events in data and  $N_{\text{bkg},l}$  the estimated number of background events in the observed data, both in decay channel  $l$ . By subtracting the number of background events from the number of observed events in data, and applying the correction factor  $C_l$ , the expected true number of signal events in the fiducial region in channel  $l$  is derived.

Since the definition of the fiducial region is different in the 8 and 13 TeV analyses, they are described later in their relevant chapters, in Sections 7.2.2 and 8.2.2. In the following, the definition of various factors needed to extract the fiducial and total cross sections are given, as they are common between the two analyses. For simplicity, the channel index  $l$  is omitted.

To evaluate  $C$ , the criteria defining the fiducial phase space are applied to the MC simulated signal events at particle level (i.e. before the detector simulation), which mimic the signal selection requirements at reconstruction level (i.e. after the detector simulation)<sup>1</sup>. The reconstruction level corresponds to what is expected to be observed in data, while the particle level is free of detector effects, so their

<sup>1</sup> To summarise, the MC simulated events before adding the simulation of hadronisation and showering processes are referred to be at *generation level* or *parton level*, as opposed to the *particle level* where the simulation of hadronisation and showering is added but the detector simulation is not, and the *reconstruction level* that refers to after adding the detector simulation.

comparison reveals the detection inefficiencies<sup>2</sup>. The ratio of the number of signal events selected at reconstruction level ( $N_{\text{reco}}$ ) to the number of signal events generated in the fiducial region ( $N_{\text{gen}}^{\text{fid}}$ ), defines the correction factor:

$$C = \frac{N_{\text{reco}}}{N_{\text{gen}}^{\text{fid}}} . \quad (6.4)$$

That is to say,  $C$  *unfolds* the number of signal events selected at reconstruction level to the number of signal events generated in the fiducial region. To demonstrate the physical meaning of it,  $C$  can be re-written as:

$$C = \frac{\epsilon}{1 - f_{\text{out}}} , \quad (6.5)$$

where  $\epsilon$  is the *signal efficiency*, i.e. the efficiency of the signal events generated in the fiducial region to be selected at reconstruction level:

$$\epsilon = \frac{N_{\text{reco}}^{\text{fid}}}{N_{\text{gen}}} , \quad (6.6)$$

and  $f_{\text{out}}$  is the *outside migration fraction*, defined as the fraction of signal events selected at reconstruction level that are not generated within the fiducial region:

$$f_{\text{out}} = \frac{N_{\text{reco}}^{\text{non-fid}}}{N_{\text{reco}}} . \quad (6.7)$$

Using Equations 6.5, 6.6 and 6.7, one can write:

$$\frac{N_{\text{reco}}}{C} = \frac{N_{\text{reco}} \times (1 - f_{\text{out}})}{\epsilon} = \frac{N_{\text{reco}}^{\text{fid}}}{\epsilon} = N_{\text{gen}}^{\text{fid}} , \quad (6.8)$$

which is equivalent to Equation 6.4.

Finally, the acceptance factor,  $A$ , is defined as the ratio of the number of signal events generated in the fiducial region ( $N_{\text{gen}}^{\text{fid}}$ ) to the total number of generated signal events ( $N_{\text{gen}}^{\text{all}}$ ):

$$A = \frac{N_{\text{gen}}^{\text{fid}}}{N_{\text{gen}}^{\text{all}}} . \quad (6.9)$$

The analyses presented in this thesis perform the fiducial cross-section measurement of  $pp \rightarrow t\bar{t}\gamma$ . As can be seen from Equation 6.3, by applying  $A$  to the total cross section obtained from the signal MC sample, one can calculate the theoretical prediction of the fiducial cross section, in order to compare it with the experimental result.

A simplified illustration of the different phase spaces and various factors used in the definition of total and fiducial cross sections is shown in Figure 6.1.

---

<sup>2</sup> As long as the selection requirements used to define the fiducial region at particle level are close to, if not identical with, the event selection at the reconstruction level. Otherwise, it will be still subject to some model-dependency which we tried to avoid in the first place.

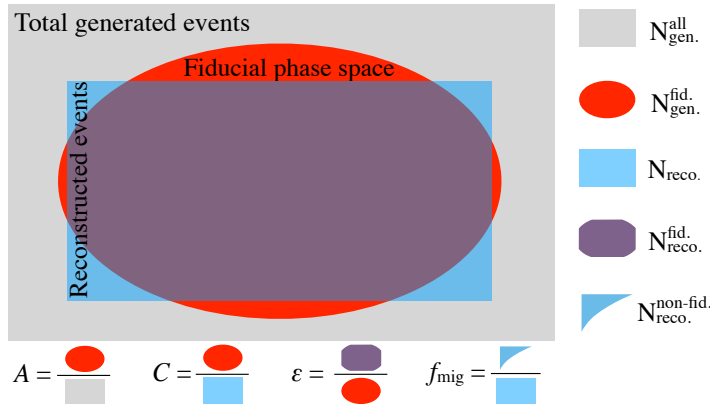


Figure 6.1: An illustration of the different phase spaces and various factors used in the definition of total and fiducial cross sections

### 6.3 Differential Cross Section

Furthermore, the  $t\bar{t}\gamma$  cross section can be measured as a function of an observable of interest, which is called the differential cross section. In the analyses presented in this thesis, the differential cross sections are also measured in the defined fiducial regions.

In the case of differential measurement, not only a migration of events from outside of the fiducial region can happen (illustrated in Figure 6.1), but also the events that are produced inside the fiducial region and in the bin  $k$  of the observable  $x$  might be reconstructed in the bin  $j$  of  $x$ . So one needs to take care of the migrations between the bins as well.

If the migrations between bins of a given observable  $x$  are small ( $\lesssim 10\%$ ), the differential cross-section measurement as a function of  $x$  can be simplified by dividing the fiducial region into  $j$  sub-regions, corresponding to  $j$  bins of  $x$ , and measuring the cross section of each bin independently, with the expression below:

$$\sigma_{t\bar{t}\gamma,j}^{\text{fid}} = \frac{N_{\text{obs},j} - N_{\text{bkg},j}}{L \cdot C_j} = A_j \times (\sigma_{t\bar{t}\gamma}^{\text{tot},j} \times \text{BR}), \quad (6.10)$$

where

$$A_j = \frac{N_{\text{gen}}^{\text{fid},j}}{N_{\text{gen}}^{\text{all}}} \quad (6.11)$$

and

$$C_j = \frac{N_{\text{reco},j}}{N_{\text{gen}}^{\text{fid},j}} \quad (6.12)$$

are the acceptance and correction factors, respectively, in bin  $j$  of  $x$ . In this case, the correction factors  $C_j$  of Equation 6.12 not only correct for the migration of events from outside of the total fiducial region into bin  $j$ , but also for the migrations from other bins which are still inside the total fiducial region but are outside of the bin  $j$ . In this approach, which is called the *bin-by-bin unfolding*, the correlation of the measured cross-sections in the observable bins are ignored. That is why this approach is only applicable if the migration between the bins is small.

In the cases that the migration between the bins of observable  $x$  is large, the unfolding of  $N_{\text{reco},j}$  is more complicated and takes into account:

$$N_{\text{reco},j} = N_{\text{obs},j} - N_{\text{bkg},j} = \frac{1}{1 - f_{\text{out},j}} \times \sum_k (L \times \sigma_{t\bar{t}\gamma,k}^{\text{fid}} \times \epsilon_k \times M_{kj}), \quad (6.13)$$

where:

- $k$  is the binning index of  $x$  at particle level, while  $j$  is its bin index at reconstruction level,
- $f_{\text{out},j}$  is the fraction of signal events selected at reconstruction level in bin  $j$  that are not generated within the fiducial region (i.e. migration to bin  $j$  from outside of fiducial region),
- $\epsilon_k$  is the differential form of the signal efficiency defined in Equation 6.6, i.e. the fraction of signal events generated at particle level in bin  $k$  of the fiducial region that are reconstructed and selected at detector level ( $\epsilon_k = N_{\text{reco}}^{\text{fid},k} / N_{\text{gen}}^{\text{fid},k}$ ),
- and  $M_{kj}$  is the *bin-to-bin migration matrix*, or *migration matrix* for short, representing the probability of the signal events generated at particle level in fiducial region in bin  $k$  to be observed at detector level in bin  $j$ .

Equation 6.13 can be then solved to obtain the differential cross section:

$$\sigma_{t\bar{t}\gamma,k}^{\text{fid}} = \frac{1}{L} \times \frac{1}{\epsilon_k} \times \sum_j (M_{jk}^{-1} \times (N_{\text{obs},j} - N_{\text{bkg},j}) \times (1 - f_{\text{out},j})), \quad (6.14)$$

where  $M_{jk}^{-1}$  is the inverse of the migration matrix. Thus, in order to measure the differential cross sections when the bin-by-bin unfolding approximation is not possible, the challenge is to perform the inversion of the migration matrix  $M_{jk}$ .

In the 8 TeV analysis, the bin-by-bin unfolding approach is used, as the binning of the observables are optimised to keep the migration between the bins at a low level. In the 13 TeV analysis, however, the binning of observables are optimised not only in terms of migration, but also the statistical uncertainties of the expected signal, and the bin-by-bin approximation is not applicable. A techniques called the iterative Bayesian method [116], implemented in the RooUnfold package [117], is used for inversion of the migration matrix. Details of these will follow later in the relevant analysis chapters.

## 6.4 Likelihood Function

### 6.4.1 General Description

Considering a set of  $N$  independent observations of a variable  $\mathbf{x} = \{x_1, \dots, x_N\}$ , if one can make the assumption that they each follow the probability density function  $f$ , which is parametrised by a set of parameters  $\mathbf{a} = \{a_1, \dots, a_m\}$ , then the probability to observe  $\mathbf{x}$  given  $\mathbf{a}$  is the product of the individual probability functions:

$$\mathcal{L}(\mathbf{x} | \mathbf{a}) = \prod_{i=1}^N f(x_i | \mathbf{a}). \quad (6.15)$$

This joint probability density function is called the *likelihood* function.

The maximum-likelihood estimator of the parameters  $\mathbf{a}$  is defined as the values of  $\hat{\mathbf{a}}(x_1, \dots, x_N)$  for which the likelihood function above has its maximum. In other words, solving the  $m$  spontaneous equations

$$\frac{\partial \mathcal{L}(\mathbf{x} | \hat{\mathbf{a}})}{\partial a_j} = 0 \quad \text{for } j = 1, \dots, m \quad (6.16)$$

determines the values of parameters  $\mathbf{a}$  for which the probability of the measurements  $x_1, \dots, x_N$  is maximum<sup>3</sup>.

When  $N$ , the number of measurements, is large, the measurements  $\mathbf{x}$  are conveniently binned into histograms. The number of events in each bin  $k$  of the histogram, denoted by  $n_k$ , is distributed according to a Poisson distribution function with the expectation value of  $\mu_k$ , where  $\mu_k$  depends on the parameters  $\mathbf{a}$ . The *binned likelihood* function has the form of:

$$\mathcal{L} = \prod_{k=1}^{N_{\text{bins}}} P(n_k | \mu_k(\mathbf{a})), \quad (6.17)$$

where  $N_{\text{bins}}$  is the number of histogram bins. Then, maximising the likelihood function to estimate the value of  $\mathbf{a}$  is done through fitting the probability distribution to the content of each bin.

To estimate the uncertainties of the maximum-likelihood estimates, one can find the parameter values  $\mathbf{a}'$  for which the logarithm of likelihood drops by  $1/2$  from its maximum value:

$$\Delta \ln \mathcal{L} \equiv \ln \mathcal{L}(\mathbf{a}') - \ln \mathcal{L}_{\max} = -1/2, \quad (6.18)$$

which defines a confidence interval of  $1\sigma$ , i.e. 68%, for  $\mathbf{a}$ <sup>4</sup>. This means, finding the two points  $a_j^{\text{down}} \equiv \hat{a}_j - \Delta \hat{a}_{j-}$  and  $a_j^{\text{up}} \equiv \hat{a}_j + \Delta \hat{a}_{j+}$  for which  $\Delta \ln \mathcal{L} = -1/2$ , defines a 68% confidence level  $[a_j^{\text{down}}, a_j^{\text{up}}]$  for  $a_j$  around  $\hat{a}_j$ .

It is practical to use the *likelihood ratio* to evaluate these confidence regions, which is defined as the ratio of the unconditional likelihood for  $\mathbf{a}$  to the conditional likelihood of the estimate  $\hat{\mathbf{a}}$ :

$$\lambda(\mathbf{a}) = \frac{\mathcal{L}(\mathbf{x} | \mathbf{a})}{\mathcal{L}(\mathbf{x} | \hat{\mathbf{a}})}. \quad (6.19)$$

In large sample limit, the  $-2 \ln \lambda(\mathbf{a})$  follows a  $\chi^2$  distribution with  $m$  degrees of freedom, then to evaluate the  $1 - \alpha$  confidence regions (for example  $1 - \alpha = 68\%$ , corresponding to  $1\sigma$  interval) one can use the quantities  $\chi^2_{1-\alpha}$  of the  $\chi^2$  distribution.

Often it is the case that one is interested in only one or a few particular parameters of all the unknown parameters  $\mathbf{a}$  that the likelihood function depends on. Then  $\mathbf{a}$  can be partitioned as  $\mathbf{a} = \{\boldsymbol{\mu}, \boldsymbol{\theta}\}$  where  $\boldsymbol{\mu} = \{\mu_1, \dots, \mu_p\}$  ( $p < m$ ) are the *parameters of interest* (p.o.i.) and  $\boldsymbol{\theta} = \{\theta_1, \dots, \theta_q\}$  ( $q < m$ ,  $p + q = m$ ) are the *nuisance parameters*. Then one can use the *profile likelihood ratio*, defined as:

$$\lambda(\boldsymbol{\mu}) = \frac{\mathcal{L}(\mathbf{x} | \boldsymbol{\mu}, \hat{\boldsymbol{\theta}})}{\mathcal{L}(\mathbf{x} | \hat{\boldsymbol{\mu}}, \hat{\boldsymbol{\theta}})}, \quad (6.20)$$

where the quantities with single hats are their unconditional maximum-likelihood estimate, and the quantities with double hats are their conditional maximum-likelihood estimate when  $\boldsymbol{\mu}$  is fixed to a

<sup>3</sup> In practice, since a sum is easier to work with than a product, often the logarithm of the likelihood is taken, and since minimum finding is easier to perform than maximum finding, the negative log-likelihood function is minimised.

<sup>4</sup> Similarly, the  $s\sigma$  confidence intervals can be defined by the contour  $\Delta \ln \mathcal{L} = -s^2/2$

certain value. In this expression the nuisance parameters are *profiled*, and the ratio above is in terms of parameters of interest. The asymptotic distribution of  $-2 \ln \lambda(\mu)$  is  $\chi^2(p)$  in this case.

### 6.4.2 Likelihood Function for $\sigma_{t\bar{t}\gamma}$ Measurement

The likelihood function used for extracting the  $t\bar{t}\gamma$  cross section,  $\sigma_{t\bar{t}\gamma}$ , has the general form of:

$$\mathcal{L} = \mathcal{L}(\text{discr} | \text{p.o.i.}, \theta), \quad (6.21)$$

where `discr` is the observed distribution of the discriminator variable, a variable that is chosen for its power of distinguishing between the  $t\bar{t}\gamma$  signal process and the background processes, and is the binned measurements to be fitted to; p.o.i. is the parameter (or parameters) of interest being estimated, which could be chosen to be the total, fiducial or differential cross sections, or the signal strength; and  $\theta$  is the collection of all the parameters that model the systematic uncertainties, entering the maximum-likelihood estimator as nuisance parameters.

More specifically, the binned maximum-likelihood fit is performed using the likelihood function below:

$$\mathcal{L} = \prod_i P(N_i^{\text{obs}} | N_i^s(\theta) + \sum_b N_i^b(\theta)) \times \prod_t G(0 | \theta_t, 1), \quad (6.22)$$

where:

- $N_i^{\text{obs}}$ ,  $N_i^s$  and  $N_i^b$  are the observed number of events in data, the expected number of signal events, and the estimated number of background of type  $b$ , in bin  $i$  of the `discr` distribution, which are modelled by a Poisson function  $P$  in that bin. The index  $b$  runs on all the background sources.
- $\theta_t \in \theta$  is the nuisance parameter that parametrises the systematic uncertainty  $t$ . The systematic uncertainties are modelled by the Gaussian function  $G$  which has a unit width and the mean value of 0. Both  $N_i^s$  and  $N_i^b$  are affected by  $\theta$  in each bin  $i$ . The index  $t$  runs on all the systematic uncertainty sources.

Using Equation 6.3, the number of signal events is related to the fiducial cross section as:

$$N_i^s = L \times \sigma_{t\bar{t}\gamma}^{\text{fid}} \times C \times f_i^s, \quad (6.23)$$

where  $f_i^s$  is the fraction of signal events falling into bin  $i$  of the `discr` distribution. Through this relation, the fiducial cross section enters the likelihood function and it is the p.o.i. of choice. The number of background events of type  $b$  is expressed by

$$N_i^b = N^b \times f_i^b, \quad (6.24)$$

where  $f_i^b$  is the fraction of the background type  $b$  falling into bin  $i$  of the `discr` distribution, and  $N^b$  is the total number of that background. To summarise, the `discr` shape information of the signal and background  $b$  are carried by  $f_i^s$  and  $f_i^b$ , respectively, and their respective normalisations are given by  $L \times \sigma_{t\bar{t}\gamma}^{\text{fid}} \times C$  and  $N^b$ .

Alternatively, one can use the signal strength as the p.o.i., which is defined as the ratio of the cross section obtained from the measurement to the expected cross section from the SM theory:

$$\mu = \frac{\sigma_{t\bar{t}\gamma}^{\text{obs}}}{\sigma_{t\bar{t}\gamma}^{\text{SM}}}, \quad (6.25)$$

The uncertainty of the fitted value of p.o.i. is evaluated from the profile likelihood ratio constructed based on the definitions in Equation 6.20:

$$\lambda(\text{p.o.i.}) = \frac{\mathcal{L}(\text{discr} | \text{p.o.i.}, \hat{\theta})}{\mathcal{L}(\text{discr} | \widehat{\text{p.o.i.}}, \hat{\theta})}. \quad (6.26)$$

The profile likelihood ratio is evaluated within the RooFit/RooStats framework [118, 119] and used to determine the upper and lower limits on p.o.i. at a 68% confidence level.

# CHAPTER 7

---

## Cross-Section Measurement of $t\bar{t}\gamma$ at 8 TeV

---

This chapter outlines the  $t\bar{t}\gamma$  cross-section measurement at  $\sqrt{s} = 8$  TeV. The data that is used is recorded by the ATLAS detector in 2012, from  $pp$  collisions at a centre-of-mass energy of  $\sqrt{s} = 8$  TeV, and corresponds to an integrated luminosity of  $20.2 \text{ fb}^{-1}$ . The analysis is performed in the single-lepton decay channel of  $t\bar{t}\gamma$  (see Section 2.3), where the final state includes exactly one electron or muon, including those that are decayed from a  $\tau$ -lepton. In addition to the inclusive fiducial cross section, differential fiducial cross sections are measured as a function of  $p_T$  and  $\eta$  of the photon. The inclusive and differential fiducial cross sections are extracted from maximum-likelihood fits to the binned photon isolation distribution of the observed data, using different templates for the signal and background processes.

In this chapter, the event selection for the signal region is presented in Section 7.1. In Section 7.2 the analysis strategy is described. The extraction of the templates used in the likelihood fit are described in Section 7.3, and the estimation of backgrounds in Section 7.4. The systematic uncertainties of the measurements are discussed in Section 7.5. Finally, the results of this analysis are presented in Section 7.6.

This analysis is documented in Ref. [8]. The main contributions of the author of the thesis in this analysis were investigating the events with more than one photon (described in Section 7.1.3), the extraction of hadronic-fake templates (described in Section 7.3.2 and Appendix A.1), estimation of the fake lepton background (described in Section 7.4.3.1), estimation of the jet flavour composition component of the jet energy scale systematic uncertainty (described in Section 7.5.2.1), and partial contribution in the estimation of  $W\gamma$  background (described in Section 7.4.3.2).

### 7.1 Signal Region Selection

The experimental signature of the  $t\bar{t}\gamma$  events in the single-lepton decay channel is the presence of an isolated high- $p_T$  lepton (electron or muon, including those originated from tau lepton decays) and missing transverse momentum ( $E_T^{\text{miss}}$ ) due to the undetectable neutrino originating from the leptonic decay of one of the  $W$  bosons, two high- $p_T$  light- or  $c$ -quark jets originating from the hadronic decay of the other  $W$  boson, two  $b$ -quark jets, and a high- $p_T$  photon. The presence of additional jets is possible, due to the QCD emissions.

Only electrons and muons are considered for the lepton in the final state, due to the short lifetime and difficult reconstruction of tau leptons. The tau leptons contribute implicitly to the signal when they decays leptonically, or to the background when they decay hadronically.

Several background processes mimic the same signature in the detector. One important background source is the events containing a non-prompt photon that is originated from a hadronic decay, or a jet that is mis-identified as a photon. Another important background is due to the events that contain an

electron which is wrongly identified as a photon. These two categories of backgrounds with non-prompt and fake photons have contributions mostly from  $t\bar{t}$ ,  $W+\text{jets}$  or  $Z+\text{jets}$  processes. Smaller contributions come from background events with a prompt photon in their final state. The latter category contains all the processes that are background to the  $t\bar{t}$  production when they are produced with additional prompt photons. This includes the multi-jet production with a prompt photon, when a jet or a non-prompt lepton from a jet segmentation decay is mis-identified as a lepton. Other background processes with a prompt photon are  $W\gamma$ ,  $Z\gamma$ , single top+ $\gamma$  and diboson+ $\gamma$  productions.

Based on the expected topology and kinematics of the signal process, a set of selection cuts is applied that is optimised to compromise between rejecting aforementioned backgrounds as much as possible while keeping enough signal events. Also, selection cuts aiming to enrich the signal region with the  $t\bar{t}\gamma$  events where the photon is radiated from the top-quark (rather than from top-quark's decay products or incoming quarks) are imposed in order for the cross-section measurement to be more sensitive to the top-photon coupling. The description of the signal region selection in object and event levels follows in this section.

### 7.1.1 Selection at Object-level

- **Electrons:** The electron candidates must pass the **Tight** identification criteria, defined in Section 4.2. They are required to have  $p_T > 25$  GeV, and a calorimeter cluster pseudorapidity<sup>1</sup> of  $|\eta_{\text{cl}}| < 2.47$ , excluding the transition region between the barrel and the endcaps in EMCal ( $1.37 < |\eta_{\text{cl}}| < 1.52$ ). In addition, they are required to originate from the primary vertex by demanding to have a longitudinal impact parameter (see Section 4.1) with respect to the primary vertex of the size  $|z_0| < 2$  mm. To suppress the background due to non-prompt electrons or jets mis-identified as electrons, the isolation requirements defined in Section 4.2 are applied.
- **Muons:** The muon candidates are required to be **Tight** combined muons, defined in Section 4.3, and have  $p_T > 25$  GeV and  $|\eta| < 2.5$ . Same as electrons, muons are required to have  $|z_0| < 2$  mm. In addition, a transverse impact parameter (see Section 4.1) significance of  $|d_0/\sigma_{d_0}| < 3$  is required, where  $\sigma_{d_0}$  is the uncertainty on  $d_0$ . In order to reduce the background muons originating from heavy-flavour decays inside jets, muons are required to be isolated, as described in Section 4.3.
- **Jets:** Jets are required to have  $p_T > 25$  GeV and  $|\eta| < 2.5$ . In order to suppress the jets from pile-up and enhance jets from hard scattering, a requirement on Jet Vertex Fraction (JVF) is applied. The JVF is defined as the ratio of the sum of  $p_T$  of the tracks associated to the jet that are coming from the primary vertex, to the sum of  $p_T$  of all tracks associated to the jet. The jets with  $p_T < 50$  GeV and  $|\eta| < 2.4$  must have  $|\text{JVF}| > 0.5$ .
- **Photons:** The photon candidates have to satisfy the **Tight** identification criteria, defined in Section 4.5. They are required to have  $p_T > 15$  GeV and  $|\eta_{\text{cl}}| < 2.37$ , excluding the transition region ( $1.37 < |\eta_{\text{cl}}| < 1.52$ ). No isolation requirement is imposed on photons.
- **Overlap removal:** If the same energy deposit in the EMCal or the same track in the ID is used to reconstruct two different objects, a duplicated object reconstruction occurs. To avoid this, and also to reject non-prompt leptons decaying from jets, an object overlap removal is applied. First, the closest jet in a cone of  $\Delta R = 0.2$  around any electron is removed. Then the electrons that have a distance of  $\Delta R < 0.4$  from remaining jets are removed. After that, the closest jet in a cone of

---

<sup>1</sup> The pseudorapidity of the electromagnetic energy cluster with respect to the geometric centre of the detector

size  $\Delta R = 0.1$  around any photon is removed. Finally, muons within a distance of  $\Delta R < 0.4$  from remaining jets are removed.

### 7.1.2 Selection at Event-level

Based on the object definitions in Section 7.1.1, events are selected as following:

- The selected events are required to have fired one of the single-lepton triggers listed in Table 7.1. Depending on whether the electron or the muon trigger is fired, the event is categorised into  $e+jets$  or  $\mu+jets$  channel.

Channel	Trigger name	Trigger description
$e+jets$	<code>EF_e24vhi_medium1</code> or <code>EF_e60_medium1</code>	At least one isolated <sup>2</sup> electron with $p_T > 24$ GeV or At least one electron with $p_T > 60$ GeV independent of isolation
	<code>EF_mu24i_tight</code> or <code>EF_mu36_tight</code>	At least one isolated <sup>2</sup> muon with $p_T > 24$ GeV or At least one muon with $p_T > 36$ GeV independent of isolation

Table 7.1: The single-lepton triggers used in the event selections for the 8 TeV analysis.

- In order to reject the non-collision background, events must have a primary vertex with at least four associated tracks with  $p_T > 400$  MeV. If more than one vertex in the event fulfil the conditions, the vertex with the largest sum of track  $p_T^2$  is selected.
- Events in  $e+jets$  ( $\mu+jets$ ) channel are required to have exactly one electron (muon), and no muon (electron). The electron (muon) must geometrically match the lepton that has triggered the event.
- The selected event must contain at least four jets.
- Different requirements on  $E_T^{\text{miss}}$  and the reconstructed transverse mass of the leptonically decaying  $W$  boson ( $m_T^W$ )<sup>3</sup> for the  $e+jets$  and  $\mu+jets$  channels are imposed. In the  $e+jets$  channel, events are required to fulfil  $E_T^{\text{miss}} > 30$  GeV and  $m_T^W > 30$  GeV, and in the  $\mu+jets$  channel  $E_T^{\text{miss}} > 20$  GeV and  $E_T^{\text{miss}} + m_T^W > 60$  GeV. The imposed cut on  $E_T^{\text{miss}}$  discriminates the events with presence of neutrinos against the multi-jet background events, which are expected to be balanced in the transverse plane. The requirement on  $m_T^W$  aims for selecting events with a true  $W$  boson, therefore it suppresses some of the multi-jet processes, the  $Z\gamma$  and the  $Z+jets$  backgrounds. The requirements for the  $e+jets$  channel are tighter because the contribution of multi-jet background is expected to be higher in this channel.
- At least one of the jets in the event must be tagged as a  $b$ -jet. This requirement suppresses various backgrounds, but is specially important for reducing the  $W\gamma$  and the  $W+jets$  backgrounds. The  $b$ -tagging working point used in this selection corresponds to 70% efficiency for jets with  $p_T > 20$  GeV and  $|\eta| < 2.5$  in the MC simulated  $t\bar{t}$  events.
- Events are required to have exactly one photon. In Section 7.1.3, a study on events with more than one photon is presented.

<sup>2</sup> The isolation requirement at the trigger level is looser than at the offline level.

<sup>3</sup> It is calculated as  $m_T^W = \sqrt{2 p_T^{\text{lepton}} E_T^{\text{miss}} (1 - \cos(\Delta\phi))}$ , where  $\Delta\phi$  is the azimuthal angle between the lepton and the missing transverse momentum.

- To reduce the background contribution from  $Z+jets$  process when an electron is misidentified as a photon, the invariant mass of the photon and the electron ( $m_{e\gamma}$ ) in the  $e+jets$  channel have to be outside of a 5 GeV window around the  $Z$  boson mass ( $m_Z$ ).
- Finally, in order to suppress the photons radiated from the incoming partons or the top quark decay products (quarks and leptons), the event is discarded if the angular distance between the photon and any of the jets  $\Delta R(\gamma, \text{jet})$  is less than 0.5, or the angular distance between the photon and the lepton  $\Delta R(\gamma, \text{lepton})$  is less than 0.7.

The number of events in data passing the signal selection is found to be 1256 in  $e+jets$  channel and 1816 in  $\mu+jets$  channel. Table 7.2 shows the data event yields after each selection cut.

Requirement	Number of events	
	$e+jets$ channel	$\mu+jets$ channel
Initial number of events in the data stream	712787500	705961299
Trigger	299226148	218113950
Primary vertex with $N_{tracks} \geq 4$	296035461	214490599
Exactly one lepton	85735086	103494734
Lepton trigger matching	85618904	103246883
At least four jets	467423	510571
$E_T^{\text{miss}}$	321982	446636
$m_T^W$	263659	—
$m_T^W + E_T^{\text{miss}}$	—	409136
At least one $b$ -tagged jet	135133	211073
At least one photon ( $p_T(\gamma) > 10$ GeV)	2128	2664
Exactly one photon ( $p_T(\gamma) > 15$ GeV)	2101	2591
$ m_{e\gamma} - m_Z  > 5$ GeV	1894	—
$\Delta R(\gamma, \text{jet}) > 0.5$	1546	2023
$\Delta R(\gamma, \text{lepton}) > 0.7$	1256	1816

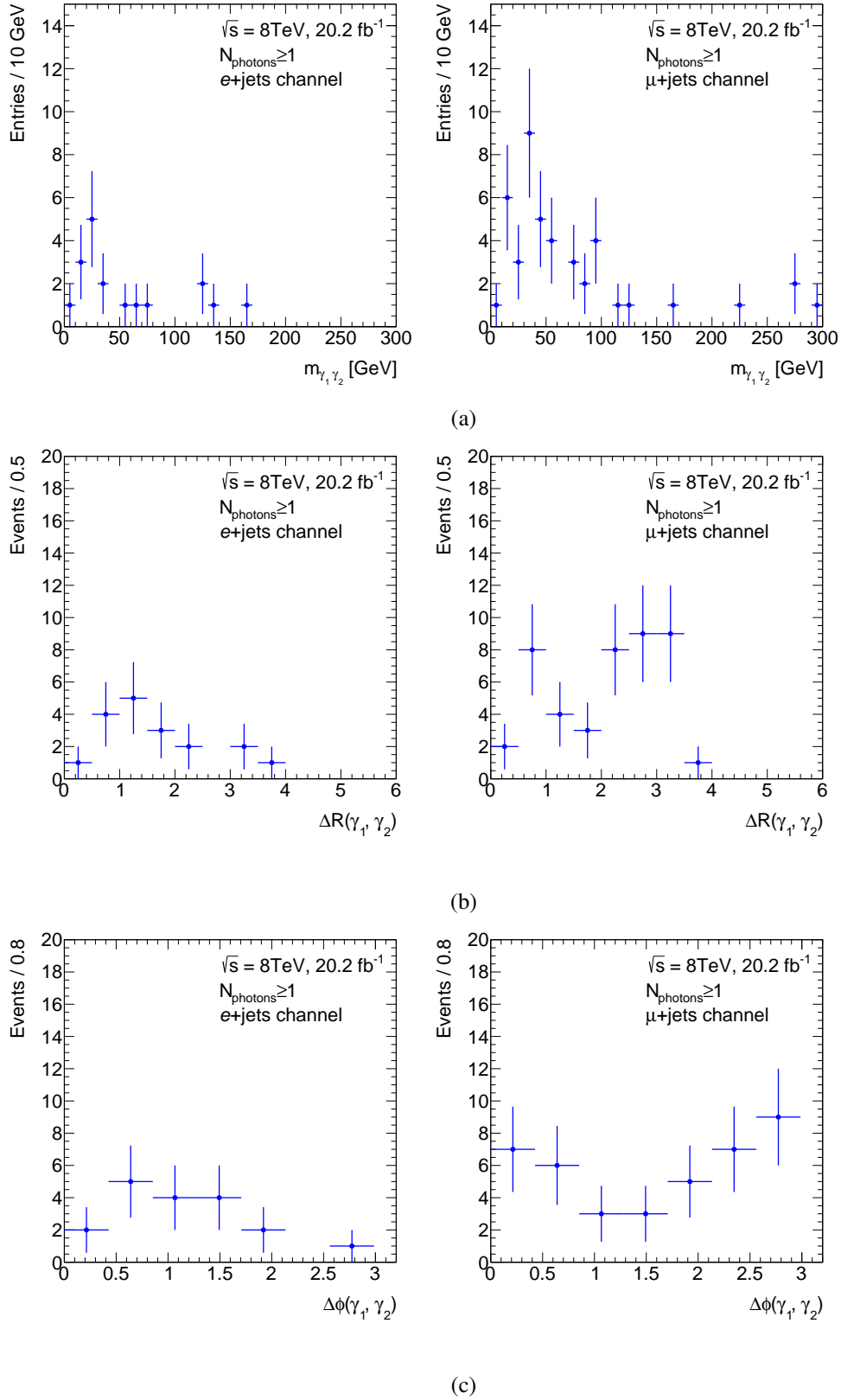
Table 7.2: Data event yields after each selection cut for the signal selection in the 8 TeV analysis.

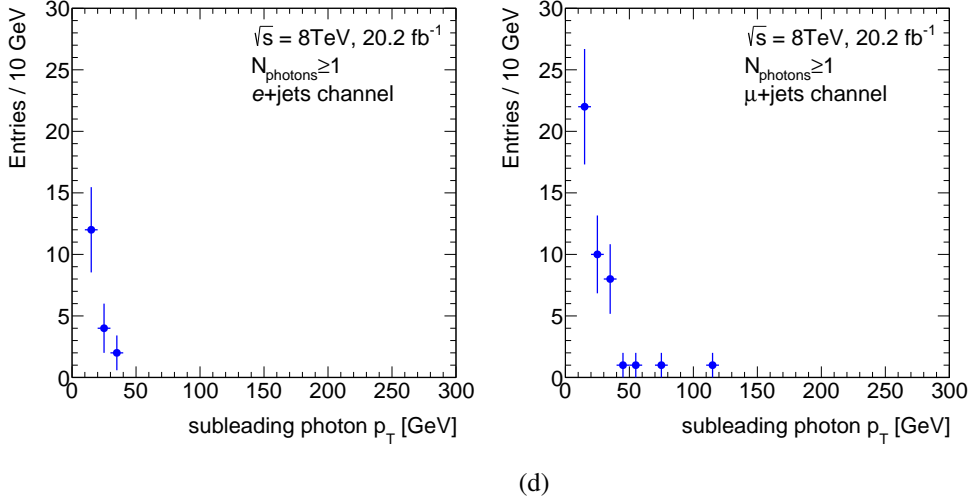
### 7.1.3 Events with More Than One Photon

To perform a study on  $t\bar{t}$  production with more than one photon, events are selected from data by applying the same object-level selection as in Section 7.1.1, and modifying the event-level selection in Section 7.1.2 to require at least one photon in the event and removing the requirements on  $m_{e\gamma}$ ,  $\Delta R(\gamma, \text{jet})$ , and  $\Delta R(\gamma, \text{lepton})$ . While for the leading photon (ordered in  $p_T$ ) the requirement of  $p_T > 15$  GeV is kept, for the rest of the photons in the event it is lowered to  $p_T > 10$  GeV in order to gain more statistics.

Figure 7.1 shows some kinematic distributions of the data events after the aforementioned selection. The distributions of the invariant mass of the leading and sub-leading photons are shown in Figure 7.1(a), their  $\Delta R$  distance in Figure 7.1(b), their  $\Delta\phi$  distance in Figure 7.1(c), and the  $p_T$  spectrum of the sub-leading photons in Figure 7.1(d), separately for  $e+jets$  and  $\mu+jets$  channels.

Figure 7.2 shows how photon multiplicity in the events changes, after adding the photon related selection cuts one by one, in the order of first applying the  $|m_{e\gamma} - m_Z| > 5$  GeV requirement (only for  $e+jets$  channel), then  $\Delta R(\gamma, \text{jet}) > 0.5$ , and then  $\Delta R(\gamma, \text{lepton}) > 0.7$ , while Table 7.3 summarises the number





(d)

Figure 7.1: Data events with at least one photon, where the leading photon (ordered in  $p_T$ ) is required to have  $p_T > 15$  GeV and the rest  $p_T > 10$  GeV. The plots in row (a) show the invariant mass of the leading and sub-leading photons, rows (b) and (c) show the  $\Delta R$  and  $\Delta\phi$  distance between the leading and sub-leading photons respectively, and row (d) shows the  $p_T$  spectrum of the sub-leading photons. The left plot in each row is for the  $e+jets$  channel and the right one corresponds to the  $\mu+jets$  channel.

of events with more than one photon after applying each of these selection cuts. The requirements are applied to all the photons in the event.

A clear conclusion about the source of the extra photons can not be made, considering the high statistical fluctuations, as well as whether any extra selection requirement or tightening the current requirements can help with removing the non-signal-type extra photons. As a result of this study, and considering the very low number of multi-photon events, the selection cut requiring exactly one photon with  $p_T > 15$  GeV is decided for the signal region of this analysis.

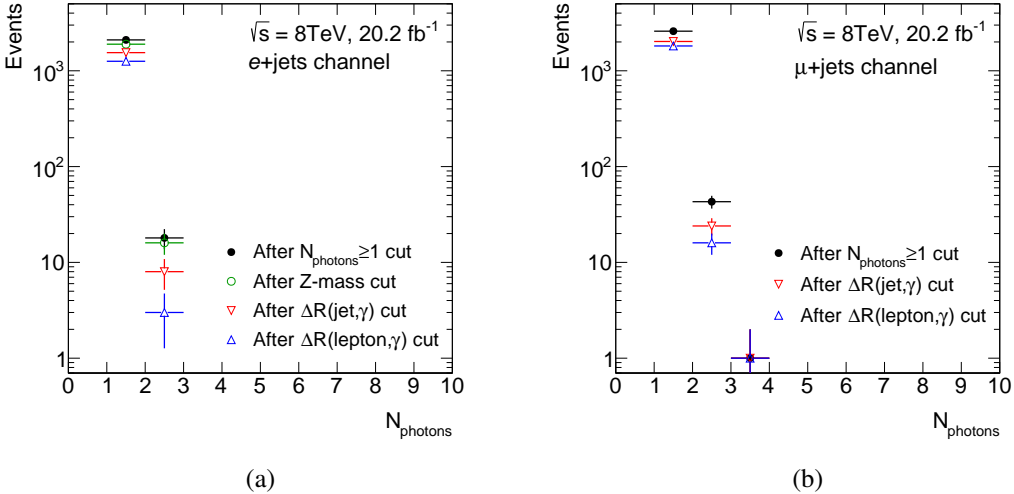


Figure 7.2: Evolution of photon multiplicity in selected multi-photon data events, in (a)  $e+jets$  channel and (b)  $\mu+jets$  channel.

Requirement	Number of events	
	$e + \text{jets}$ channel	$\mu + \text{jets}$ channel
More than one photon	18	44
$ m_{e\gamma} - m_Z  > 5 \text{ GeV}$	16	—
$\Delta R(\gamma, \text{jet}) > 0.5$	8	25
$\Delta R(\gamma, \text{lepton}) > 0.7$	3	17

Table 7.3: Multi-photon data yields after adding photon-related cuts.

## 7.2 Analysis Strategy

The inclusive and differential fiducial cross sections of  $t\bar{t}\gamma$  production at  $\sqrt{s} = 8 \text{ TeV}$  are extracted from a maximum-likelihood fit to the photon isolation distribution of the observed data. This is done by using different templates for the signal and background processes. The template fit method is explained in Section 7.2.1, including the description of the chosen discriminator variable. The cross section measurement is performed in a fiducial volume which is described in Section 7.2.2. The likelihood function used to perform the fit and the fit strategy are described in Section 7.2.3. Finally, the theoretical predictions which the result of this analysis are being compared to are given in Section 7.2.4.

### 7.2.1 Utilisation of Template Fit Method

After applying the event selection of Section 7.1, three category of events based on the type of the selected photon in the event enter the signal region:

- **Events with a prompt photon:** A prompt photon is a photon radiated from any of the charged particles within the hard scattering process, before the hadronisation of the particles in the final state. This class of events includes the  $t\bar{t}\gamma$  signal process, as well as the background processes that are produced with an additional prompt photon.
- **Events with a hadronic-fake photon:** A so-called *hadronic-fake* photon is either a non-prompt photon originating from a hadronic decay or a hadron that is mis-identified as a photon<sup>4</sup>. Such misidentification can happen when a hadron inside a jet carries most of the energy of the jet and decays into two or three collimated photons. This results in an energy deposit in the EMCAL that has characteristics similar to those of a real prompt photon and can fulfil the Tight photon identification criteria (see Section 4.5). Also, the energy deposit of a hadron itself could be mis-reconstructed as a photon. The hadronic-fake photons stem mostly from  $\pi^0$  decays, while they can also be produced from other neutral mesons like  $\eta$  or in baryons decay chains. This category of the events form the largest background of this analysis, which will be referred to as *hadronic-fake background*.
- **Events with an electron-fake photon:** The *electron-fake* photon (sometimes denoted as  $e \rightarrow \gamma$  fake) is the name given to the electrons mis-identified as photons. Electrons and photons have very similar signatures in the calorimeter. If the track of an electron is poorly reconstructed and does not pass the track quality criteria, the energy deposit of the electron in the EMCAL can wrongly be reconstructed as an unconverted photon. Also, close-by jet activities can cause a second track or

<sup>4</sup> It should be mentioned that a non-prompt photon from a hadronic decay is a *real* photon, while a hadron that is wrongly identified as a photon is a *fake* one. However, for simplicity both cases will be called hadronic-fake.

a conversion vertex to get wrongly associated to the energy deposit of the electron in the EMCal and be reconstructed as a converted photon. Events containing an electron-fake photon will be referred to as *electron-fake background* and are the second largest background in this analysis.

More than two third of the events in the signal region do not come from  $t\bar{t}\gamma$  production. The core of the analysis strategy lies on using a specific feature of the signal events that could distinct them from background processes. In particular, the analysis strategy is designed to tackle the sizeable hadronic-fake background.

The photon isolation provides a good discrimination power for this purpose. The prompt photons are well isolated, while hadronic-fake photons are not, since they are surrounded by jet activities. The electron-fake photons are expected to also be fairly well isolated, but their isolation distribution is observed to be different from that of the prompt photons, as will be shown later. Therefore, the photon isolation distribution shape of prompt photons, hadronic-fake photons and electron-fake photons are exploited and used as templates.

The inclusive and differential fiducial cross sections are extracted from a maximum-likelihood fit to the photon isolation distribution of the observed data, using these three templates. The *prompt-photon template* is used for the signal events as well as for the background events with a prompt photon, the *hadronic-fake template* is used for the hadronic-fake background events, and the *electron-fake template* is used for the electron-fake background events. The photon isolation variable that is used as the discriminator variable for building the templates is the tracking-based isolation,  $p_T^{\text{cone}20}$ , introduced in Section 7.2.1.1. The extraction of the templates is described in Sections 7.3.

The templates used for the inclusive cross-section measurement in the fiducial volume are shown in Figure 7.3. The prompt photons are peaking at low isolation values, while the hadronic-fake photons have a broad distribution. The isolation distribution of electron-fake photons (denoted by  $e \rightarrow \gamma$  fake) also peaks at lower isolation values, but with a slight shift toward higher values with respect to the prompt photons.

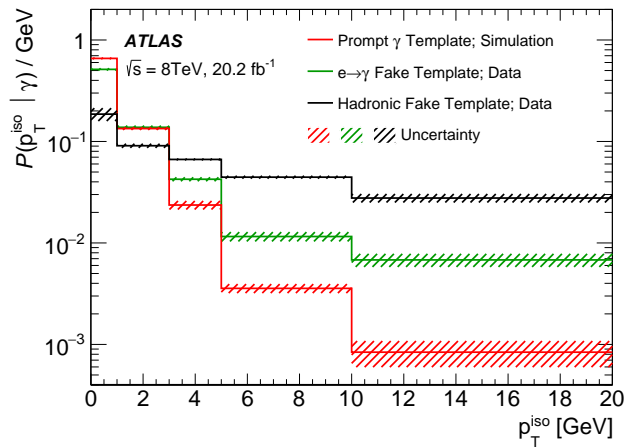


Figure 7.3: The templates for the inclusive fiducial cross-section measurement at 8 TeV for the prompt photons, the hadronic-fake photons and the electron-fake photons (denoted by  $e \rightarrow \gamma$  fake) [8]. Here,  $p_T^{\text{iso}}$  is another notation for the isolation variable  $p_T^{\text{cone}20}$ . The last bin contains the overflow. The dashed bands show the total uncertainty for each template.

### 7.2.1.1 Photon Isolation as Discriminator Variable

There are several photon isolation variables that are constructed from either the energy in the calorimeter surrounding the photon candidate or the tracks close to the photon candidate direction. The calorimeter-based variables are defined as the sum of all energy deposits within a cone of radius  $R_0$  around the photon, after removing the photon energy itself and correcting for the noise from pile-up. These variables are denoted by  $E_T^{\text{cone}20}$ ,  $E_T^{\text{cone}30}$  and  $E_T^{\text{cone}40}$  for the cases of  $R_0 = 0.2$ ,  $R_0 = 0.3$  and  $R_0 = 0.4$  respectively. The tracking-based variables are defined as the scalar sum of  $p_T$  of the tracks in a cone of radius  $R_0$  around the photon direction. Only tracks that have a  $p_T$  larger than 1 GeV and a longitudinal impact parameter less than 1 mm are considered, in order to reduce the contribution from pile-up tracks. These variables are denoted by  $p_T^{\text{cone}20}$ ,  $p_T^{\text{cone}30}$  and  $p_T^{\text{cone}40}$  for the radius of  $R_0 = 0.2$ ,  $R_0 = 0.3$  and  $R_0 = 0.4$  respectively.

The calorimeter-based isolation variables show a dependency on  $\eta$ , since the photon traverses through different amount of material in different  $\eta$  regions until it reaches the calorimeter. The tracking-based variables are preferred for this reason, and also because of being very pile-up robust. The variable  $p_T^{\text{cone}20}$  provided the highest discriminating power, therefore was chosen as the discriminator variable<sup>5</sup>.

### 7.2.2 Definition of the Fiducial Region

The fiducial region is defined for the MC simulated events at particle level (i.e. before detector simulation), using particle definitions and selection requirements on phase space that mimic the selections at reconstruction level (i.e. after detector simulation) described in Section 7.1.

The objects used in the fiducial region definition are constructed from the stable particles in the event record of the generator, with lifetime greater than  $3 \times 10^{-11}$  s.

- **Leptons:** First, electrons and muons with  $p_T > 10$  GeV and  $|\eta| < 2.7$  are selected. Then, the four-momenta of the photons that do not originate from hadron decays and are within a cone of  $\Delta R = 0.1$  around the lepton are added to the four-momentum of the lepton. It is said that the lepton is *dressed* with such photons. The modified leptons are then required to have  $p_T > 25$  GeV,  $|\eta| < 2.5$ , and do not originate from hadron decays.
- **Jets:** Jets are clustered with the anti- $k_t$  algorithm with a radius parameter of  $R = 0.4$ . Muons and neutrinos are not considered in the clustering. Jets are required to have  $p_T > 25$  GeV and  $|\eta| < 2.5$ .
- ***b*-jets:** If a jet contains a *b*-hadron with  $p_T > 5$  GeV within  $\Delta R = 0.3$  from the jet axis, it is considered as a *b*-jet.
- **Photons:** Photons are required to have  $p_T > 15$  GeV and  $|\eta| < 2.37$ , must not originate from hadron decays, and have not been used in the lepton dressing.
- **Overlap removal:** The same overlap removal procedure as for the reconstructed objects, described in Section 7.1.1, is applied.

Events are selected based on the above object definitions. Events are required to have exactly one electron or muon from a  $W$  boson decay, at least four jets among which at least one is a *b*-jet, and

<sup>5</sup> Note that in some plots in this Chapter (namely in Figure 7.3, Figure 7.20 and Figure 7.21) the variable  $p_T^{\text{cone}20}$  is noted as  $p_T^{\text{iso}}$ .

exactly one photon. Events are discarded if the  $\Delta R$  distance between the photon and any of the jets is less than 0.5, or the  $\Delta R$  distance between the photon and the lepton is less than 0.7.

Motivated by using a common fiducial region for  $e$ -jets and  $\mu$ -jets channels, the requirements on  $E_T^{\text{miss}}$ ,  $m_T^W$  and  $m_{e\gamma}$  in the reconstruction level (which are channel dependent) are not included in the fiducial region definition.

### 7.2.3 Fit Strategy

Based on descriptions given in Chapter 6, and using Equations 6.21 and 6.22, the likelihood function for the inclusive and differential fiducial cross-section measurements in the 8 TeV analysis can be summarised in the following form:

$$\mathcal{L}(p_T^{\text{cone}20} | \sigma_{t\bar{t}\gamma, \text{sl}, j}^{fid}, \boldsymbol{\theta}) = \prod_i \prod_j P(N_{i,j}^{\text{obs}} | N_{i,j}^s(\boldsymbol{\theta}) + \sum_b N_{i,j}^b(\boldsymbol{\theta})) \times \prod_t G(0 | \theta_t, 1), \quad (7.1)$$

where sl stands for the single-lepton channel,  $i$  denotes the bins of the  $p_T^{\text{cone}20}$  distribution, and  $j$  indicates the bins of photon  $p_T$  or photon  $\eta$ ; the observables as a function of which the differential cross sections are measured. These observables are chosen because the kinematic properties of the photon are sensitive to the  $t$ - $\gamma$  coupling. All other parameters and terms in the above function are introduced before in Chapter 6.

In the inclusive fiducial measurement there is only one  $j$  bin, while for the differential measurement there are either five  $j$  bins of photon  $p_T$ :

$$15 \leq p_T < 25, 25 \leq p_T < 40, 40 \leq p_T < 60, 60 \leq p_T < 100, 100 \leq p_T < 300 \text{ [GeV]},$$

or five  $j$  bins for photon  $\eta$ :

$$|\eta| < 0.25, 0.25 \leq |\eta| < 0.55, 0.55 \leq |\eta| < 0.90, 0.90 \leq |\eta| < 1.37, 1.37 \leq |\eta| < 2.37.$$

As mentioned in Section 6.3, in this analysis the binning of photon  $p_T$  or photon  $\eta$  for the differential measurements are optimised to keep the migration between the bins at a low level, so that the bin-by-bin unfolding approach can be used. The migrations between the bins are smaller than 7%.

The events in the  $e$ -jets and  $\mu$ -jets channels are merged into one channel, the single-lepton channel, before performing the fit. The parameter of interest,  $\sigma_{t\bar{t}\gamma, \text{sl}, j}^{fid}$ , is either the inclusive or the differential cross section of the  $j^{\text{th}}$  bin of photon  $p_T$  or photon  $\eta$  for the single-lepton channel in the fiducial volume defined in Section 7.2.2. It enters the likelihood function through  $N_{i,j}^s$  using Equation 6.23.

There are two free parameters in the maximum-likelihood fit: the number of signal events and the number of hadronic-fake background events. The normalisation of the rest of the backgrounds are fixed to their estimated values, being varied within their uncertainties. The shape of the signal as well as all the backgrounds with prompt photons are described by the prompt-photon template, while the electron-fake and hadronic-fake templates are used respectively for the shape of the electron-fake and hadronic-fake backgrounds.

To obtain the confidence interval for the cross sections which result from the fit, a profile likelihood ratio as described in Section 6.4.2 is evaluated.

### 7.2.4 Theoretical Prediction

The measured cross sections in this analysis are compared with the theoretical cross section predictions by the SM for the fiducial region, at NLO accuracy in QCD.

The  $t\bar{t}\gamma$  signal MC sample that is used in this analysis is generated at LO by **MADGRAPH** (see Section 5.2.1). Since the theoretical calculation of  $t\bar{t}\gamma$  production in NLO is available [107], the predictions from the signal sample are normalised to NLO, using  $k$ -factors.

Although the results presented in Ref. [107] are calculated for  $\sqrt{s} = 14$  TeV, a dedicated calculation at  $\sqrt{s} = 8$  TeV is performed by the theory team at LO and at NLO in the single-lepton channel, using the same techniques of Ref. [107]. For the LO (NLO) calculation, the CTEQ6L1 (CT10) PDF set is used. A fine-structure constant of  $\alpha = 1/137$  and renormalisation and factorisation scales of  $\mu_R = \mu_F = m_{top}$  are used in both LO and NLO calculations. The computation is repeated after varying the scales to  $\mu_R = \mu_F = 2m_{top}$  and  $\mu_R = \mu_F = 1/2 m_{top}$ , and also after varying the PDF sets, in order to evaluate the modelling uncertainties.

The theory calculation at LO agrees with the cross section predicted by **MADGRAPH** within 2% for both scale choices of  $m_{top}$  and  $2m_{top}$ . The  $k$ -factor is then obtained from the ratio of the NLO theory calculation with the scales at  $m_{top}$  to the LO **MADGRAPH** sample, which has a setting for the scales to be at  $2m_{top}$ . Before comparing the LO theory calculation with the cross section from **MADGRAPH** sample, and also before obtaining the  $k$ -factor as mentioned, the same phase space requirements that are used in the LO and NLO theory calculations are applied to the **MADGRAPH** sample at parton level.

The overall  $k$ -factor results  $1.90 \pm 0.25 \pm 0.12$  [8], with the first error accounting for the uncertainty due to the scale choices and the second error coming from the variation of PDF sets. The  $k$ -factor is also calculated differentially, in bins of photon  $p_T$  and  $\eta$ , to be used for normalising the **MADGRAPH** sample predictions for the differential cross sections.

The obtained  $k$ -factors are then used to calculate the predicted SM  $t\bar{t}\gamma$  cross section at the NLO accuracy from the  $t\bar{t}\gamma$  **MADGRAPH** sample in the fiducial region defined in Section 7.2.2. The predicted inclusive cross section for this fiducial volume calculated to be  $151 \pm 24$  fb [8]. The predicted cross sections in each of the photon  $p_T$  and  $\eta$  bins of the differential measurement are calculated in a similar way.

## 7.3 Extraction of Templates

As explained in Section 7.2, the inclusive and differential fiducial cross sections are extracted from a maximum-likelihood fit using three different templates, one for each category of the events that enter the signal region: 1) *prompt-photon template* is used for the signal events as well as for the background events with a prompt photon, 2) *hadronic-fake template* describes the background events with a hadronic-fake photon in the fit, and 3) *electron-fake template* is used for the background events with an electron-fake photon. The discriminator variable used for building the templates is the photon tracking-based isolation,  $p_T^{\text{cone}20}$ . In this Section the extraction of the three templates is discussed.

### 7.3.1 Prompt-Photon Template

The prompt-photon template is extracted from the  $t\bar{t}\gamma$  MC sample. This is due to the difficulty of finding a region in data which is purely populated by prompt photons, is statistically sufficient, and has a topology similar enough to that of the  $t\bar{t}\gamma$  signal region that does not bias the photon isolation distribution shape.

After applying the nominal  $t\bar{t}\gamma$  event selection (see Section 7.1), the reconstructed photons that are geometrically matched to a true prompt photon are used for the template. This *truth matching* process is done by requiring the  $\Delta R$  distance between the reconstructed photon and the true photon according to the particle level information (i.e. before detector simulation) to be less than 0.1. This condition is fulfilled by 95% of all the reconstructed photons in the selected events.

The extracted prompt-photon from the  $t\bar{t}\gamma$  MC sample is compared to templates that are similarly extracted from the  $W\gamma$  and  $Z\gamma$  MC samples. They are found to be consistent within the statistical uncertainties. This comparison ensures that the background events with a prompt photon can be represented in the final fit also by the prompt-photon template extracted from the  $t\bar{t}\gamma$  MC sample.

For the differential cross-section measurement, the prompt-photon template is extracted for each bin of the observables.

### 7.3.2 Hadronic-fake Template

The hadronic-fake template is extracted from data, because the hadronic-fake photons are not expected to be well modelled in simulation. The modelling of the hadronisation process is only approximate (see Section 2.2.2) and the description of jet fragmentations is difficult to model. This leads to inaccuracy in the modelling of hadronic-fake photons that rise from jet fragmentations. Also, the exact simulation of the geometric shapes of the electromagnetic clusters is not possible, as it requires very detailed understanding of the detector material. Data-driven corrections are applied to the photon shower-shape variables in the MC samples (see Section 4.5), but these corrections are only calculated for prompt photons. Since photon identification relies on shower-shape variables, misidentification rates are not expected to be accurately modelled in simulation.

A control region in data enriched with the hadronic-fake photon candidates is used to extract the hadronic-fake template. The differences of the  $p_T$  and  $\eta$  distributions of the hadronic-fake photons in this control region and in the signal region are taken into account by re-weighting the template accordingly. The weights are calculated from another control region in data, where hadronic-fake photon candidates replace the nominal photons in the signal selection. The contamination from prompt photons is taken into account as a systematic uncertainty. The detailed descriptions follow.

#### 7.3.2.1 Hadronic-fake Enriched Control Region

This control region is selected from data by applying the following set of selection cuts:

- Events are required to have a primary vertex same as in the signal region, described in Section 7.1.2.
- Events must have at least one hadronic-fake photon candidate. The hadronic-fake photon candidates are required to satisfy all criteria of a nominal photon described in Section 7.1.1, but not the **Tight** identification. They are required to fail at least one of the **Tight** identification requirements on the shower-shape variables  $f_{side}$ ,  $w_{s3}$ ,  $\Delta E$  and  $E_{ratio}$  (see Table 4.1 for variable definitions), while satisfying the rest of the **Tight** identification requirements.

These four shower-shape variables are constructed from the energy deposited in the first layer of the EMCal, the strip layer. The strip layer is finely segmented in  $\eta$ , with the purpose of suppressing the background photons which typically have a broader shower profile and often two separate local energy maxima in the EMCal<sup>6</sup>. These variables are chosen because their correlations with

---

<sup>6</sup> A typical source of hadronic-fake photons are neutral mesons like  $\pi^0$  and  $\eta$  decaying into two collimated photons. This results into two (often very close) maxima in the energy cluster.

the photon isolation variables, such as  $p_T^{\text{cone}20}$ , are at a negligible level [55], while they have strong discriminating power between prompt and hadronic-fake photons.

- Events are required to have at least four jets. This is because a large variation of the template shape is observed with the jet multiplicity variation, as can be seen in Figure 7.4. Therefore, the control region is defined with the same jet multiplicity requirement as the signal region. A complementary study on this subject is available in Appendix A.1.1.
- To prevent the electrons that are misidentified as photons (electron-fake photons) contaminating the control sample, events are rejected if they contain an electron with a  $\Delta R$  distance less than 0.1 from the hadronic-fake photon candidate.

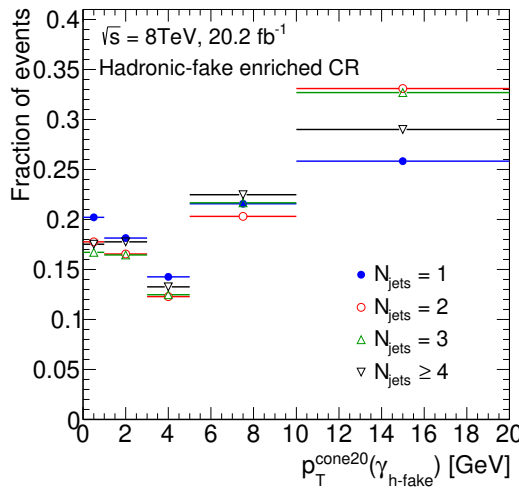


Figure 7.4: The  $p_T^{\text{cone}20}$  distribution of hadronic-fake photons in the hadronic-fake enriched control region in data, for different jet multiplicities in the event. The distributions are normalised to unity and the last bin contains the overflow. The statistical uncertainties are too small to be visible in the plot.

### 7.3.2.2 Hadronic-fake Template for Inclusive Measurement

The  $p_T^{\text{cone}20}$  distributions of hadronic-fake photon candidates in the hadronic-fake enriched control region in data are shown in Figure 7.5 for different  $p_T$  and  $\eta$  regions. The  $\eta$  intervals are chosen according to the detector geometry while the choice of  $p_T$  intervals is motivated by statistics. A clear dependency on both  $p_T$  and  $\eta$  can be seen.

From Figure 7.5(a), it can be seen that the hadronic-fake photon candidates are less isolated at higher  $p_T$  values. This is expected for two reasons; high- $p_T$  hadronic-fake photons are more likely to arise from more energetic jets, and they are radiated more collinear to the jet direction. In both of the cases the hadronic-fake photon is surrounded by more tracks, or more high- $p_T$  tracks, hence has a higher  $p_T^{\text{cone}20}$  value.

The template shape dependency on  $\eta$  is smaller than on  $p_T$ , and it is detector related. From Figure 7.5(b) only two distinct  $\eta$  regions can be recognised:  $|\eta| < 1.81$  and  $1.81 < |\eta| < 2.37$ . One possible explanation could be the  $\eta$  dependency of the efficiency of track reconstruction. In higher  $\eta$  regions the track reconstruction efficiency drops, which could lead to the observed shift of the  $p_T^{\text{cone}20}$  distribution

toward lower values for the high  $\eta$  region. Investigating the exact reasons of  $\eta$ -dependency is out of the scope of this thesis.

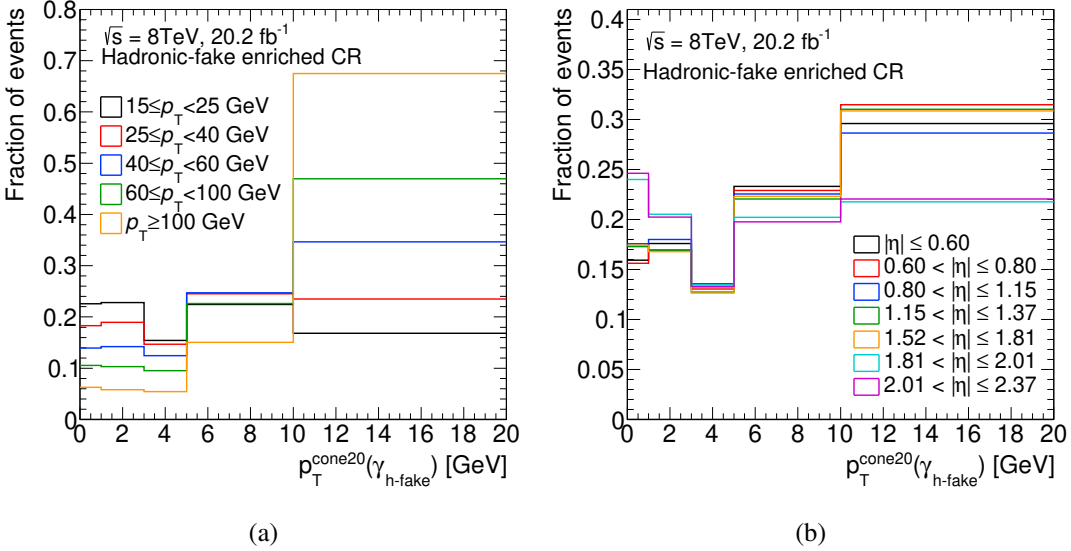


Figure 7.5: The  $p_T^{\text{cone}20}$  distribution of the hadronic-fake photons in the hadronic-fake enriched control region in data, for different (a)  $p_T$  and (b)  $\eta$  regions. The distributions are normalised to unity and the last bin contains the overflow. The statistical uncertainties are too small to be visible in the plot.

Because of the observed dependencies, and in order to account for any differences between the  $p_T$  and  $\eta$  spectra of the hadronic-fake photons in the control region and in the signal region, the hadronic-fake template used for the inclusive fiducial measurement is extracted from the weighted sum of the hadronic-fake templates derived in  $p_T$  and  $\eta$  bins. This is referred to as template re-weighting in this text.

In order to obtain the weights, an estimation of the  $p_T$  and  $\eta$  spectra of hadronic-fake photons in the signal region is needed. This is done by using another control region in data, which will be referred to as  $t\bar{t}\gamma_{\text{h-fake}}$  control region in the following. The  $t\bar{t}\gamma_{\text{h-fake}}$  control region is selected by modifying the signal selection (see Section 7.1) by replacing the nominal photon with a hadronic-fake candidate. The hadronic-fake candidate is selected by inverting requirements on the electromagnetic shower shapes, as described before in Section 7.3.2.1. A total of 497 events are selected in the  $e+\text{jets}$  channel and 896 events in the  $\mu+\text{jets}$  channel of the  $t\bar{t}\gamma_{\text{h-fake}}$  control region in data.

The  $p_T$  and  $\eta$  spectra can be seen in Figure 7.6 for the combined  $e+\text{jets}$  and  $\mu+\text{jets}$  channels. To validate the control region, the hadronic-fake candidates in the  $t\bar{t}\gamma_{\text{h-fake}}$  control region in data (in black) are compared with the photon candidates in signal region that are truth matched to be a hadron or originated from a hadron, using the  $t\bar{t}$  MC sample (in red). The comparison shows a good agreement within the statistical uncertainties.

The  $p_T$  distribution of the hadronic-fake photon candidates in the  $t\bar{t}\gamma_{\text{h-fake}}$  control region is plotted for different  $\eta$  regions in Figure 7.7. The two  $\eta$  regions are chosen according to what is observed in Figure 7.5(b). The  $p_T$  distribution shapes are consistent in different  $\eta$  regions within the statistical uncertainty. Thus, the expected  $p_T$  and  $\eta$  of the hadronic-fake photons in the signal region are not correlated, and the template dependencies on  $p_T$  and on  $\eta$  can be treated separately.

The hadronic-fake template for the inclusive fiducial measurement is derived by:

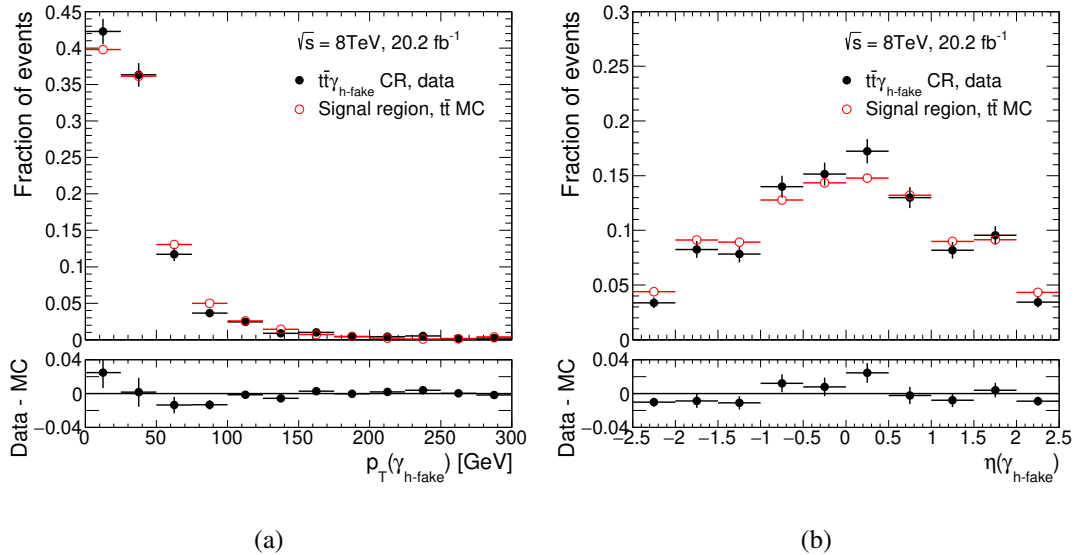


Figure 7.6: The distributions of (a)  $p_T$  and (b)  $\eta$  of hadronic-fake candidates in the  $t\bar{t}\gamma_{\text{h-fake}}$  control region in data and true hadronic-fake photons in signal region from  $t\bar{t}$  MC sample. The distributions are normalised to unity. The last bin in Figure (a) contains the overflow.

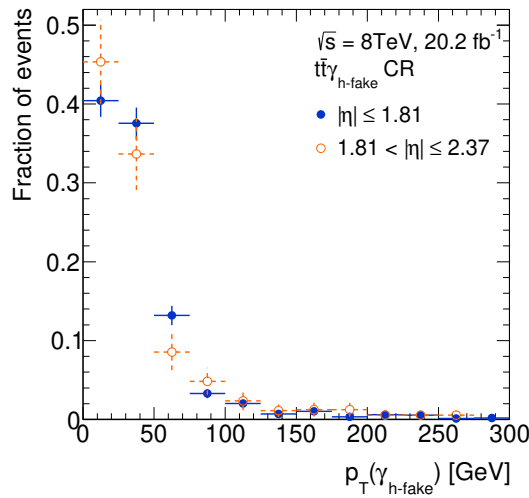


Figure 7.7: The  $p_T$  distributions of hadronic-fake candidates in different  $\eta$  regions in the  $t\bar{t}\gamma_{\text{h-fake}}$  control region in data. The distributions are normalised to unity and the last bin contains the overflow. The error bars show the statistical uncertainties.

$$T^{\text{h-fake}} = \frac{1}{2} \left( \sum_i w_{p_T,i} T_i^{\text{h-fake}}(p_T) \oplus \sum_j w_{\eta,j} T_j^{\text{h-fake}}(\eta) \right), \quad (7.2)$$

where  $T_i^{\text{h-fake}}(p_T)$  is the hadronic-fake template determined for the bin  $i$  of  $p_T$  and  $w_{p_T,i}$  is its corresponding weight, while  $T_j^{\text{h-fake}}(\eta)$  is the hadronic-fake template determined for the bin  $j$  of  $\eta$ , with  $w_{\eta,j}$  being its associated weight. The index  $i$  runs over five  $p_T$  bins:  $15 \leq p_T < 25$  GeV,  $25 \leq p_T < 40$  GeV,  $40 \leq p_T < 60$  GeV,  $60 \leq p_T < 100$  GeV and  $p_T \geq 100$  GeV, and index  $j$  over two  $\eta$  bins:  $|\eta| \leq 1.81$  and  $1.81 < |\eta| < 2.37$ .

The weights are obtained from the fraction of data events in the  $t\bar{t}\gamma_{\text{h-fake}}$  control region in each bin:

$$w_{p_T,i} = \frac{N_i}{\sum_i N_i}, \quad (7.3)$$

$$w_{\eta,j} = \frac{N_j}{\sum_j N_j}. \quad (7.4)$$

The  $p_T$  and  $\eta$  weights ( $w_{p_T,i}$  and  $w_{\eta,j}$ ) are summarised in Table 7.4 and Table 7.5, respectively, with their uncertainties. The weight uncertainties are of statistical nature only.

$i$	$15 \leq p_T < 25$ GeV	$25 \leq p_T < 40$ GeV	$40 \leq p_T < 60$ GeV	$60 \leq p_T < 100$ GeV	$p_T \geq 100$ GeV
$w_{p_T,i}$	$0.42 \pm 0.01$	$0.28 \pm 0.01$	$0.136 \pm 0.009$	$0.098 \pm 0.008$	$0.060 \pm 0.006$

Table 7.4: The  $p_T$  weights ( $w_{p_T,i}$ ) used for weighting the hadronic-fake template for the inclusive fiducial measurement. The uncertainties are statistical.

$j$	$ \eta  \leq 1.80$	$1.80 <  \eta  \leq 2.37$
$w_{\eta,j}$	$0.877 \pm 0.009$	$0.123 \pm 0.009$

Table 7.5: The  $\eta$  weights used for weighting the hadronic-fake template for the inclusive fiducial measurement. The uncertainties are statistical.

The derived weighted hadronic-fake template for the inclusive fiducial measurement is shown in Figure 7.8, where its uncertainty band comes from the weight uncertainties. It is also compared with the template without any  $p_T$ - $\eta$  weighting. The difference is more noticeable in the last  $p_T^{\text{cone}20}$  bin. The weighted template is the final template that is used in the fit for the cross-section measurement.

As a cross check, the re-weighting process is repeated by using finer  $\eta$  bins (i.e. all seven  $\eta$  bins seen in Figure 7.5(b) instead of the two  $\eta$  bins  $|\eta| \leq 1.81$  and  $1.81 < |\eta| < 2.37$ ). The resulting weighted template shows no significant difference with the nominal weighted template. This study can be found in Appendix A.1.2.

### 7.3.2.3 Hadronic-fake Template for Differential Measurement

For the differential fiducial cross-section measurement, the hadronic-fake template is extracted for each bin of the two observables: five templates for the five bins of photon  $p_T$  and five templates for the five bins of photon  $\eta$ .

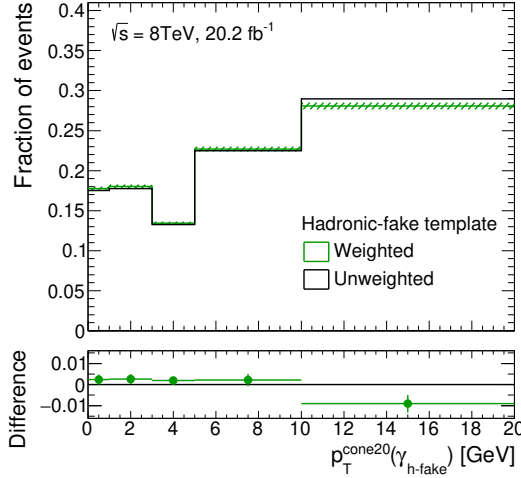


Figure 7.8: Hadronic-fake templates for the inclusive fiducial measurement, before (black) and after (green) re-weighting, with their difference shown in the lower panel. Distributions are normalised to unity and the last bin contains the overflow. The statistical uncertainties are too small to be visible, while the green error band shows the weighting uncertainties. The weighted template is the nominal template used in the cross-section measurement.

Similar as for the inclusive template, each of the five hadronic-fake templates for the  $\eta$  differential measurement are weighted according to the expected  $p_T$  spectrum of the hadronic-fake in the signal region in that  $\eta$  bin:

$$T_k^{\text{h-fake}}(\eta) = \sum_i w_{p_T,k,i} T_{k,i}^{\text{h-fake}}(\eta, p_T), \quad (7.5)$$

and each of the five hadronic-fake templates for the  $p_T$  differential measurement are weighted according to the expected  $\eta$  spectrum of the hadron-fakes in the signal region in that  $p_T$  bin:

$$T_t^{\text{h-fake}}(p_T) = \sum_j w_{\eta,t,j} T_{t,j}^{\text{h-fake}}(p_T, \eta). \quad (7.6)$$

The index  $k$  ( $t$ ) indicates the five  $\eta$  ( $p_T$ ) bins for the differential measurement (see Section 7.2.3), while index  $i$  ( $j$ ) runs over the five  $p_T$  (two  $\eta$ ) bins used for the re-weighting, which were introduced in the previous part.

The weights are obtained from the  $t\bar{t}\gamma_{\text{h-fake}}$  control region in a similar way as for the inclusive template, and are summarised in Tables 7.6 and 7.7. Their uncertainties are of statistical nature only.

The hadronic-fake templates derived for the differential fiducial measurement as a function of photon  $\eta$  and as a function of photon  $p_T$  are shown in Figures 7.9 and 7.10 respectively. The uncertainty bands come from the weight uncertainties. The derived templates are compared with the templates without  $p_T/\eta$  re-weighting. Even though the weighted templates for some of the differential bins are not different from the unweighted ones within the uncertainties, the final templates used in the fit are the weighted templates. This is to account for the uncertainty of the weighted templates, as it is showing the uncertainty of mapping the  $p_T$  and  $\eta$  of hadronic-fake photons from the hadronic-fake enriched control region to the signal region.

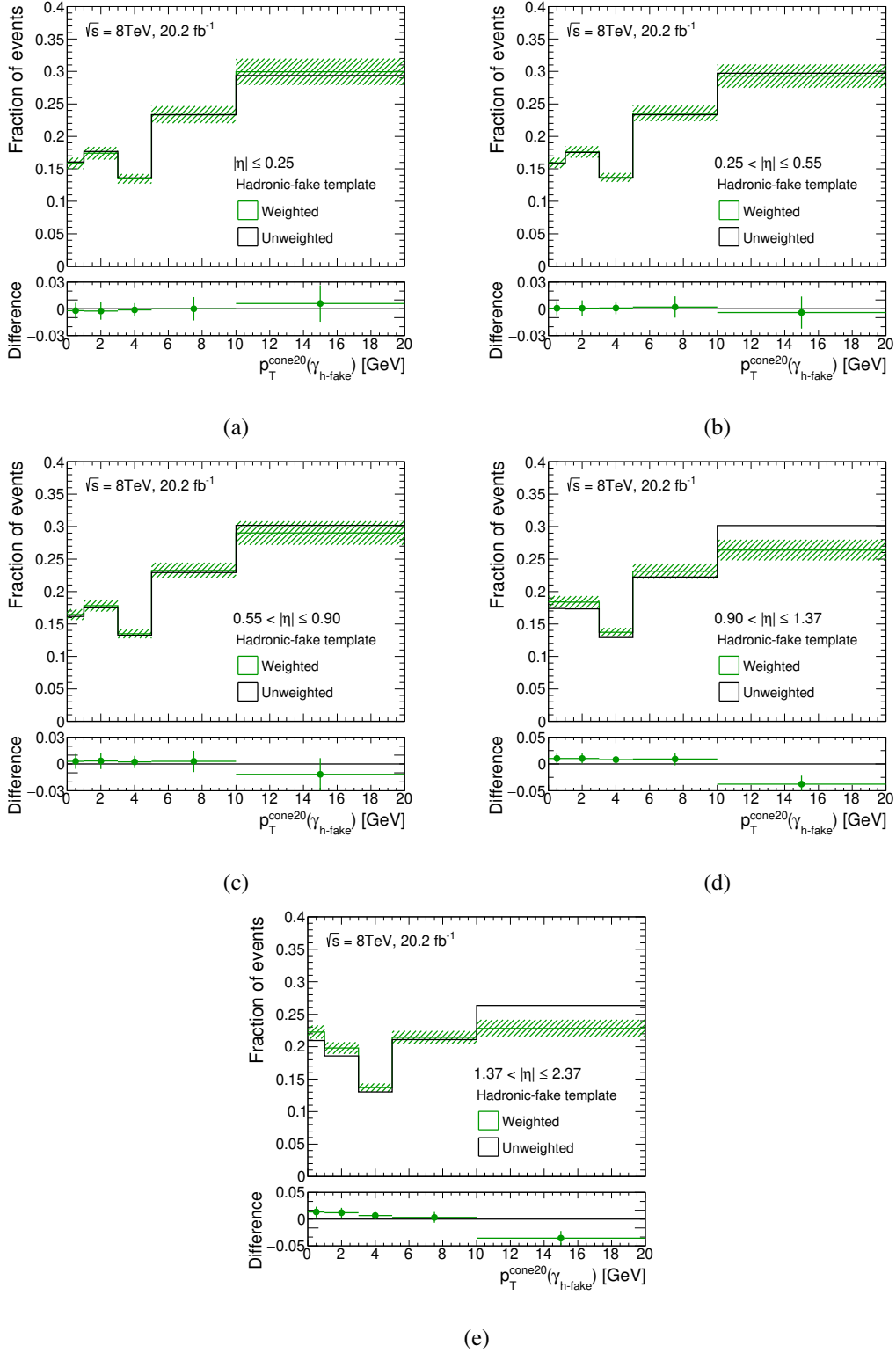


Figure 7.9: Hadronic-fake templates for differential fiducial measurements in photon  $\eta$  bins of (a)  $|\eta| \leq 0.25$ , (b)  $0.25 < |\eta| \leq 0.55$ , (c)  $0.55 < |\eta| \leq 0.90$ , (d)  $0.90 < |\eta| \leq 1.37$  and (e)  $1.37 < |\eta| \leq 2.37$ , before (black) and after (green) re-weighting, with their difference shown in the lower panels. Distributions are normalised to unity and the last bin contains the overflow. The statistical uncertainties are too small to be visible, while the green bands show the weighting uncertainties. The weighted templates are the nominal templates used in the cross-section measurements.

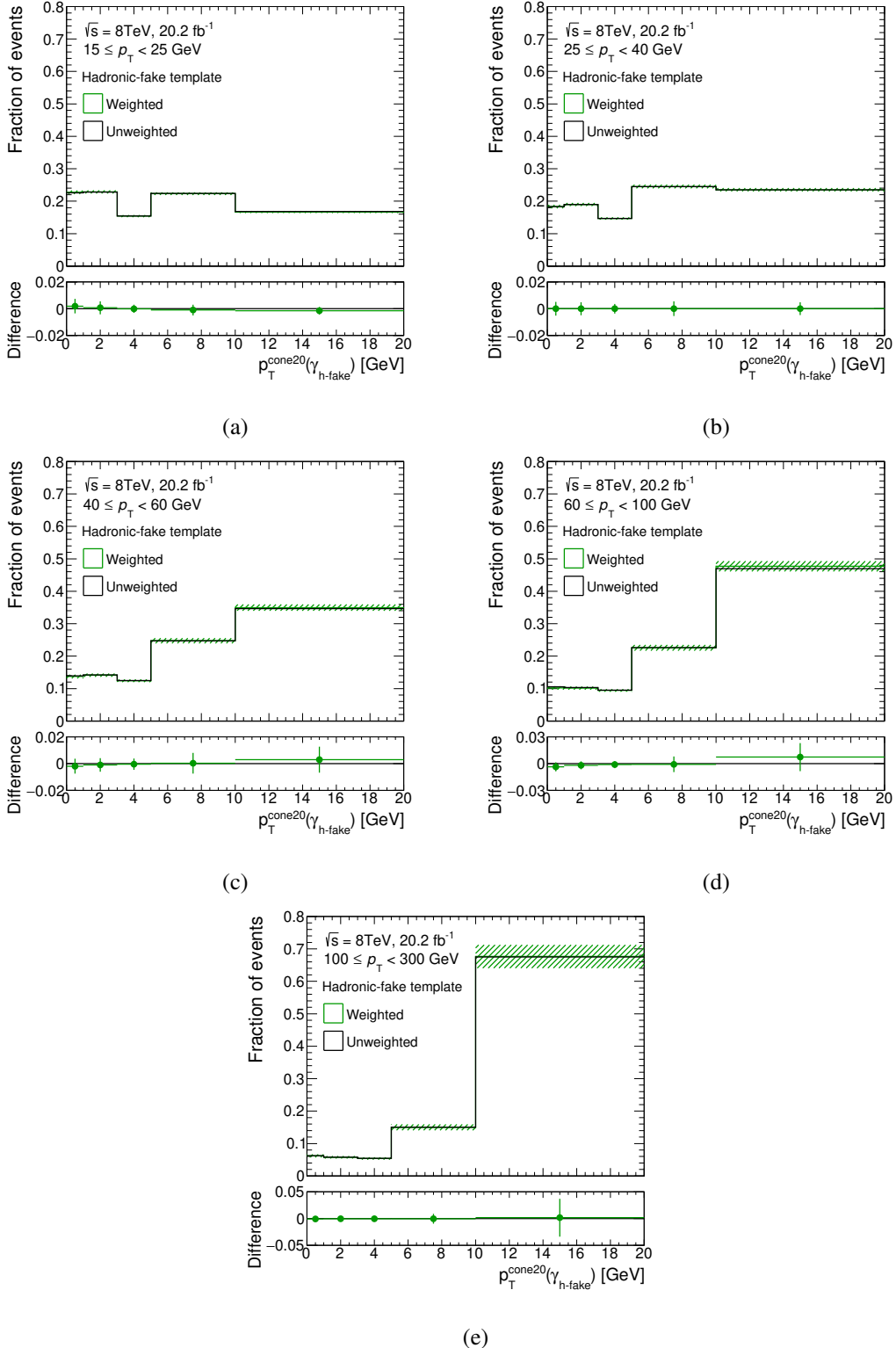


Figure 7.10: Hadronic-fake templates for differential measurements in photon  $p_T$  bins of (a)  $15 \leq p_T < 25$  GeV, (b)  $25 \leq p_T < 40$  GeV, (c)  $40 \leq p_T < 60$  GeV, (d)  $60 \leq p_T < 100$  GeV and (e)  $100 \leq p_T < 300$  GeV, before (black) and after (green) re-weighting, with their difference shown in the lower panels. Distributions are normalised to unity and the last bin contains the overflow. The statistical uncertainties are too small to be visible, while the green bands show the weighting uncertainties. The weighted templates are the nominal templates used in the cross-section measurements.

$w_{p_T,k,i}$	$i : 15 \leq p_T < 25$ GeV	$i : 25 \leq p_T < 40$ GeV	$i : 40 \leq p_T < 60$ GeV	$i : 60 \leq p_T < 100$ GeV	$i : p_T \geq 100$ GeV
$k :  \eta  \leq 0.25$	$0.45 \pm 0.03$	$0.26 \pm 0.03$	$0.11 \pm 0.02$	$0.12 \pm 0.02$	$0.07 \pm 0.02$
$k : 0.25 <  \eta  \leq 0.55$	$0.44 \pm 0.03$	$0.27 \pm 0.03$	$0.12 \pm 0.02$	$0.09 \pm 0.02$	$0.06 \pm 0.01$
$k : 0.55 <  \eta  \leq 0.90$	$0.45 \pm 0.03$	$0.24 \pm 0.03$	$0.14 \pm 0.02$	$0.10 \pm 0.02$	$0.07 \pm 0.01$
$k : 0.90 <  \eta  \leq 1.37$	$0.38 \pm 0.04$	$0.33 \pm 0.03$	$0.16 \pm 0.02$	$0.09 \pm 0.02$	$0.04 \pm 0.01$
$k : 1.37 <  \eta  \leq 2.37$	$0.40 \pm 0.03$	$0.29 \pm 0.02$	$0.14 \pm 0.02$	$0.09 \pm 0.02$	$0.07 \pm 0.01$

Table 7.6: The  $p_T$  weights ( $w_{p_T,k,i}$ ) for weighting the hadronic-fake templates used in the differential measurement as a function of  $\eta$  ( $T_k^{\text{h-fake}}(\eta)$ ). The uncertainties are statistical.

$w_{\eta,t,j}$	$j :  \eta  \leq 1.81$	$j : 1.81 <  \eta  \leq 2.37$
$t : 15 \leq p_T < 25$ GeV	$0.87 \pm 0.01$	$0.13 \pm 0.01$
$t : 25 \leq p_T < 40$ GeV	$0.89 \pm 0.02$	$0.12 \pm 0.02$
$t : 40 \leq p_T < 60$ GeV	$0.89 \pm 0.02$	$0.10 \pm 0.02$
$t : 60 \leq p_T < 100$ GeV	$0.90 \pm 0.03$	$0.10 \pm 0.03$
$t : 100 \leq p_T < 300$ GeV	$0.84 \pm 0.04$	$0.15 \pm 0.04$

Table 7.7: The  $\eta$  weights ( $w_{\eta,t,j}$ ) for weighting the hadronic-fake templates used in the differential measurement as a function of  $p_T$  ( $T_t^{\text{h-fake}}(p_T)$ ). The uncertainties are statistical.

### 7.3.2.4 Prompt Photon Contamination in Hadronic-fake Templates

If a prompt photon passes the identification requirement of the hadronic-fake photon candidates (Section 7.3.2.1), it enters the hadronic-fake enriched control region and eventually affects the hadronic-fake template shape. The amount of this contamination is studied, in order to either correct the hadronic-fake template shape or assign proper systematics uncertainties for it.

Using MC for correcting the hadronic-fake template for prompt photon contamination is not a reliable option, since it is observed that the MC samples do not model the hadronic-fake enriched control region well. More specifically, they do not describe well the jet multiplicity and the jet  $p_T$  spectrum in data, as can be seen from Figure 7.11. This is checked by using the di-jet MC sample, generated with PYTHIA. The sample description is in Table C.9.

As a better alternative, a data-driven systematic uncertainty is assigned to the hadronic-fake template shape to take into account the prompt-photon contamination. This is done by extracting a modified data-driven hadronic-fake template that contains less prompt-photon contamination, and taking the shape difference between the modified and the nominal templates as the systematic uncertainty.

The nominal hadronic-fake template is built out of hadronic-fake candidates which are selected by requiring at least one of the Tight identification requirements on the four stripe shower-shape variables  $f_{\text{side}}$ ,  $w_{s3}$ ,  $\Delta E$ , and  $E_{\text{ratio}}$  to fail, as outlined in Section 7.3.2.1. From Figure 7.12, it can be seen that by requiring more of these four cuts to fail, the  $p_T^{\text{cone}20}$  distribution is shifting more to the higher values. This indicates the reduction of prompt-photon contamination, as prompt photons are isolated objects and are expected to show up specifically in the first  $p_T^{\text{cone}20}$  bin. This hypothesis is also validated by using the di-jet MC sample, as shown in Figure 7.13. The MC-based hadronic-fake templates which are built from hadronic-fake photon candidates that fail one cut (Figure 7.13(a)), two cuts (Figure 7.13(b)), three cuts (Figure 7.13(c)) and four cuts (Figure 7.13(d)) are compared before and after the reconstructed hadronic-fake photon candidates get matched to a true hadronic-fake photon. It can be seen that by requiring more cuts to fail, the probability of the reconstructed hadronic-fake photon being a true hadronic-fake photon

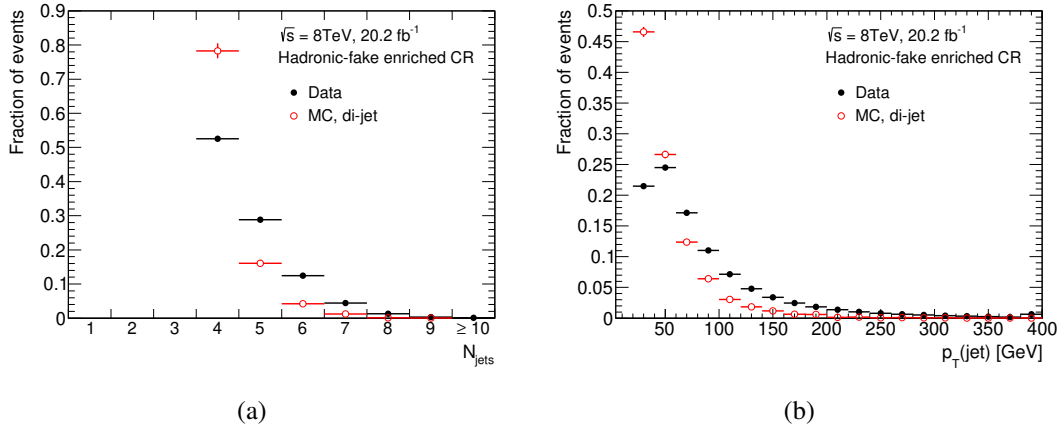


Figure 7.11: Comparison of the shape of (a) jet multiplicity and (b) jet  $p_{\text{T}}$  distributions between data and MC in the hadronic-fake enriched control region. Distributions are normalised to unity and the last bin contains the overflow.

increases. Therefore, the modified template corresponding to less prompt-photon contamination is built out of the hadronic-fake candidates that are selected by requiring *all* of these four cuts to fail.

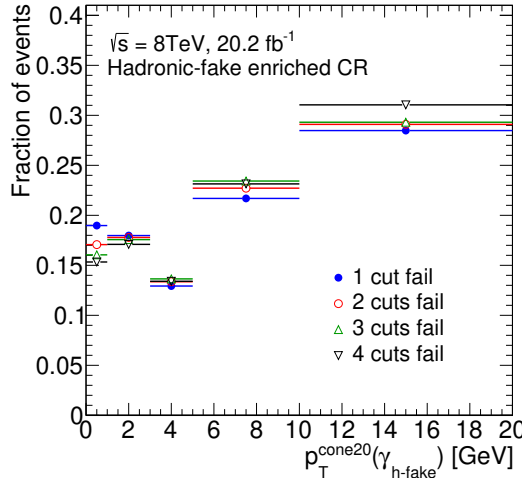


Figure 7.12: The  $p_{\text{T}}^{\text{cone20}}$  distribution of the hadronic-fake photon candidates in the hadronic-fake enriched control region in data selected by requiring exactly one to four specific Tight identification cuts to fail. The distributions are normalised to unity and the last bin contains the overflow. The statistical uncertainties are too small to be visible.

The shape differences between the modified template corresponding to less prompt-photon contamination and the nominal templates can be seen in Figure 7.14 for the inclusive fiducial measurement, and in Figure 7.15 and Figure 7.16 for the differential measurements. These shape differences are extracted from the templates before the re-weighting, since the  $t\bar{t}\gamma_{\text{h-fake}}$  control region from which the weights should be extracted has a very low statistic when hadronic-fake candidates fail all the four cuts, especially in the case of differential templates<sup>7</sup>.

<sup>7</sup> The data event yield in the  $t\bar{t}\gamma_{\text{h-fake}}$  control region for the combined  $e+\text{jets}$  and  $\mu+\text{jets}$  channels is 1393 with the nominal

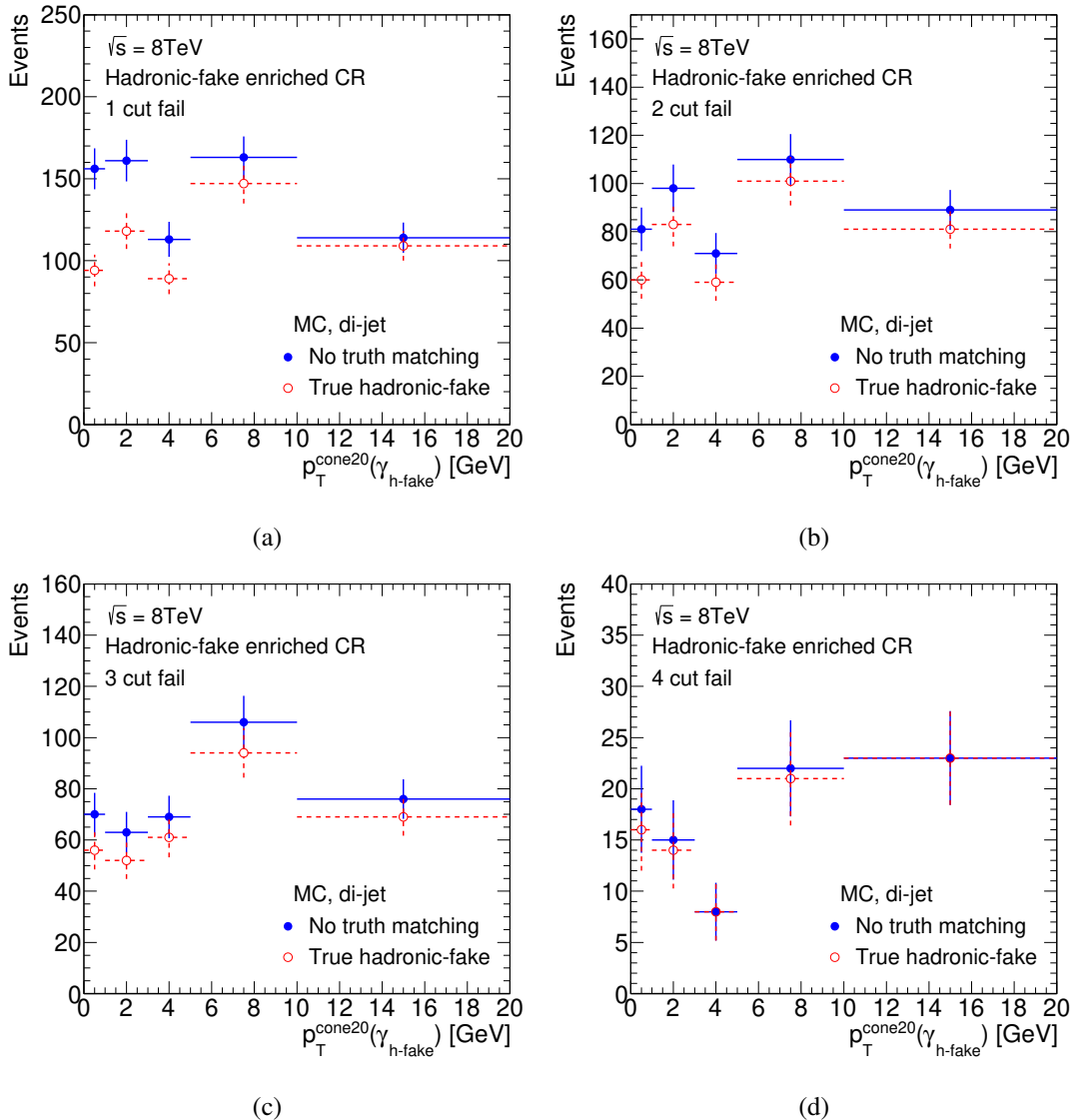


Figure 7.13: The  $p_T^{\text{cone}20}$  distribution of the hadronic-fake photon candidates in the hadronic-fake enriched control region using the di-jet MC sample, selected by requiring exactly (a) one, (b) two, (c) three, or (d) all four specific **Tight** identification cuts to fail, before (in blue) and after (in red) the reconstructed hadronic-fake photons being matched to a true hadronic-fake photon. The error bars show the statistical uncertainties and the last bin contains the overflow.

hadronic-fake photon selection, and it reduces to only 83 events for the modified hadronic-fake photon selection (i.e. when all four shower-shape cuts fail).

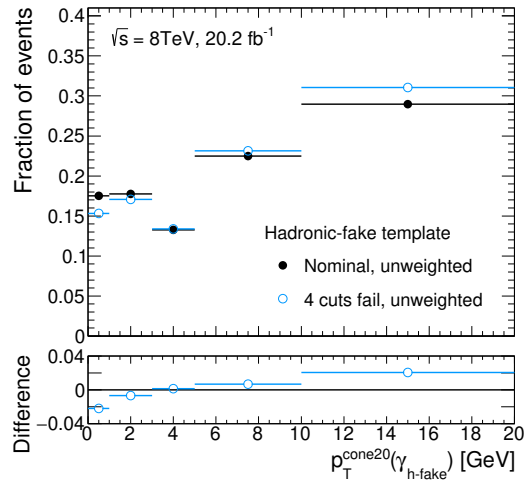


Figure 7.14: The  $p_T^{\text{cone}20}$  distribution of nominal hadronic-fake candidates (black) and hadronic-fake candidates from a tighter selection corresponding to less prompt-photon contamination (blue), for the inclusive measurement. Distributions are normalised to unity and the last bin contains the overflow. The statistical uncertainties are too small to be visible. The difference between distributions shown in the lower panel is assigned as a systematics uncertainty to the hadronic-fake template.

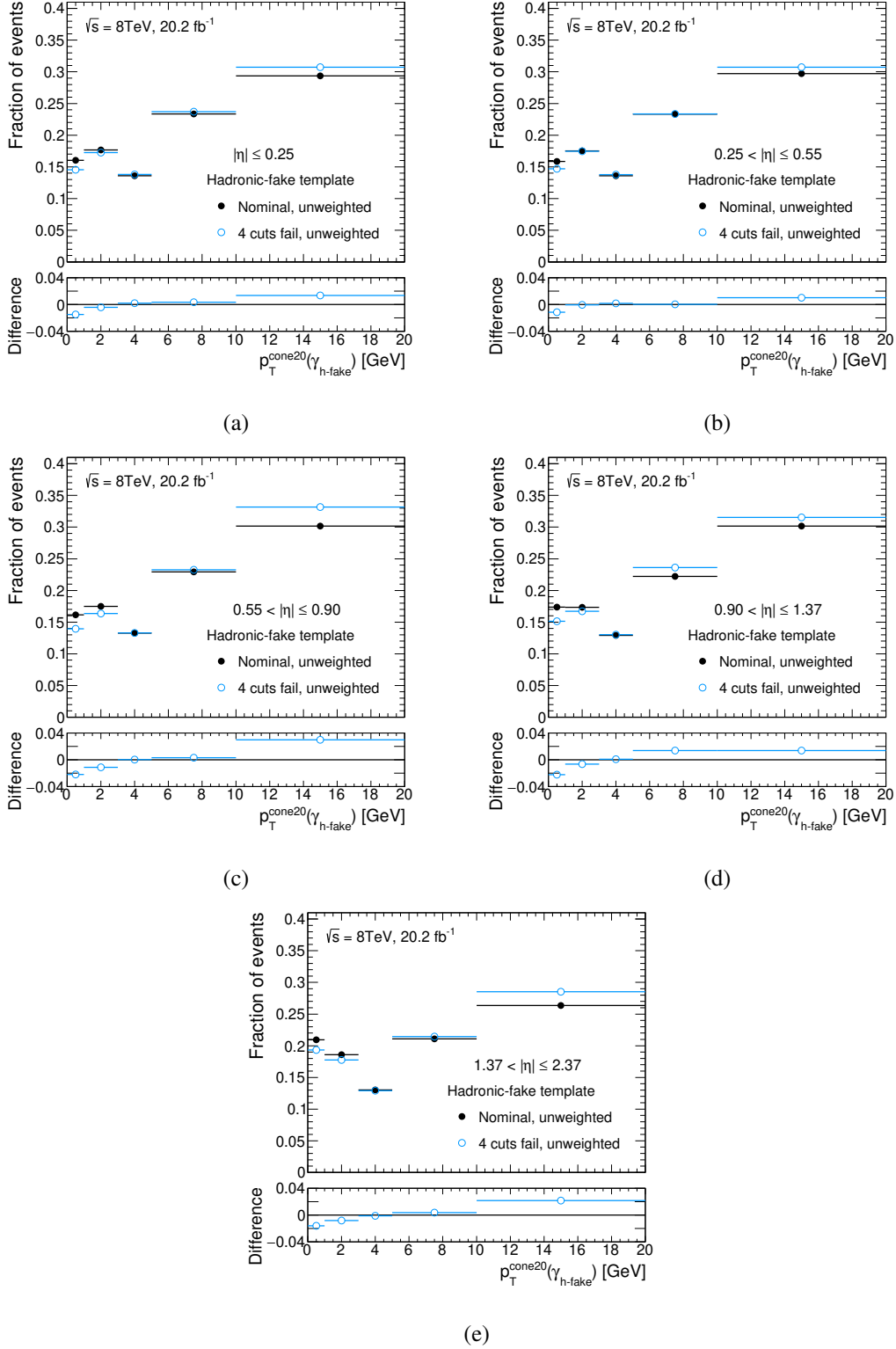


Figure 7.15: The  $p_T^{\text{cone}20}$  distribution of nominal hadronic-fake candidates (black) and hadronic-fake candidates from a tighter selection corresponding to less prompt-photon contamination (blue), for five  $\eta$  bins of the differential measurement: (a)  $|\eta| \leq 0.25$ , (b)  $0.25 < |\eta| \leq 0.55$ , (c)  $0.55 < |\eta| \leq 0.90$ , (d)  $0.90 < |\eta| \leq 1.37$  and (e)  $1.37 < |\eta| \leq 2.37$ . Distributions are normalised to unity and the last bin contains the overflow. The statistical uncertainties are too small to be visible. The differences between the distributions shown in the lower panels are assigned as a systematics uncertainty to the hadronic-fake template of each  $\eta$  bin.

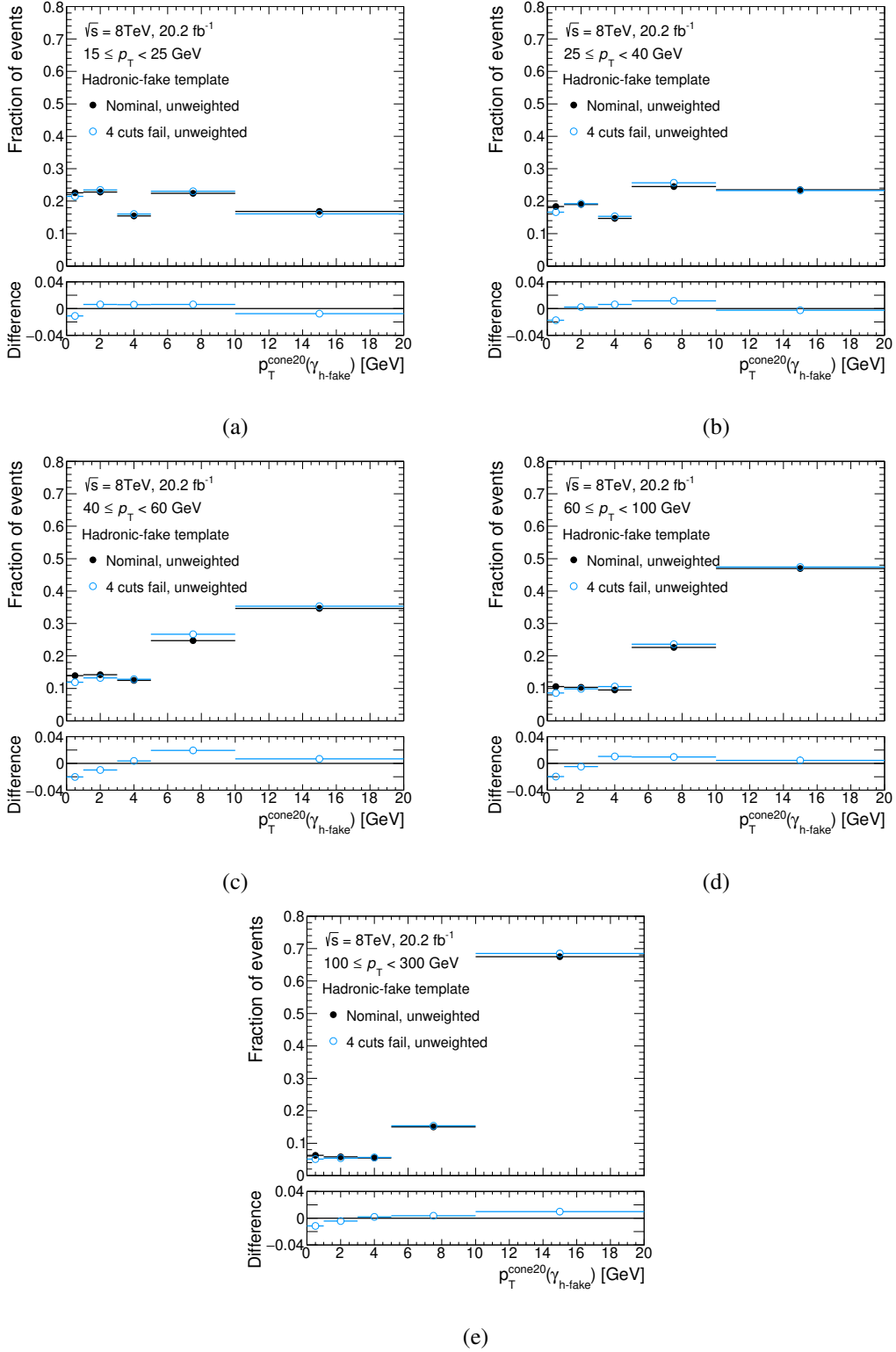


Figure 7.16: The  $p_T^{\text{cone}20}$  distribution of nominal hadronic-fake candidates (black) and hadronic-fake candidates from a tighter selection corresponding to less prompt-photon contamination (blue), for five  $p_T$  bins of the differential measurement: (a)  $15 \leq p_T < 25$  GeV, (b)  $25 \leq p_T < 40$  GeV, (c)  $40 \leq p_T < 60$  GeV, (d)  $60 \leq p_T < 100$  GeV and (e)  $100 \leq p_T < 300$  GeV. Distributions are normalised to unity and the last bin contains the overflow. The statistical uncertainties are too small to be visible. The differences between distributions shown in the lower panels are assigned as a systematics uncertainty to the hadronic-fake template of each  $p_T$  bin.

### 7.3.2.5 The Effect of Applying $\Delta R(\gamma, \text{jet})$ Requirement

In the signal selection, a requirement of  $\Delta R(\gamma, \text{jet}) > 0.5$  is applied to reduce the photons radiated from the incoming partons or the quarks in the final state (see Section 7.1.2). This requirement could potentially reduce the hadronic-fake photons radiated from jets. This requirement is not originally included in the selection of hadronic-fake enriched control region (Section 7.3.2.1), from which the hadronic-fake templates are extracted. A study is done to check the effect of this difference between the topology of the events used for the hadronic-fake template construction and events in the signal region.

The  $\Delta R(\gamma, \text{jet}) > 0.5$  requirement is added to the control region selection of Section 7.1.2, and a new template is extracted with the same re-weighted process as for the nominal template (Section 7.3.2.2). The template systematic uncertainty due to prompt-photon contamination is estimated with the same method as for the nominal template (Section 7.3.2.4).

The resulting template for the inclusive fiducial measurement is shown in Figure 7.17, in dashed red line, and is compared to the nominal template, in solid black line. The shapes are well consistent within the uncertainties. The same result is obtained for the templates for the differential measurements. Thus, the  $\Delta R(\gamma, \text{jet}) > 0.5$  requirement is not needed to be added to the control region selection.

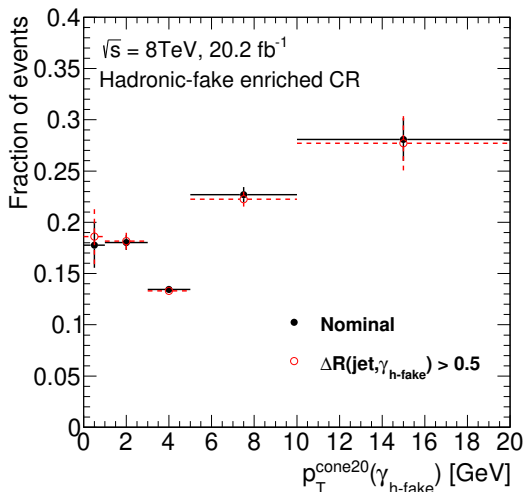


Figure 7.17: Comparison between nominal hadronic-fake template and the template after adding the  $\Delta R(\gamma, \text{jet}) > 0.5$  requirement. Distributions are normalised to unity and the last bin contains the overflow. Error bars show the total template uncertainty, including the uncertainty due to the prompt-photon contamination and the re-weighting uncertainty.

### 7.3.3 Electron-fake Template

The template for electron-fake photons is extracted from a control region in data that is enriched by events that will be denoted as  $Z \rightarrow e + \text{fake-}\gamma$  events hereafter. They are the  $Z \rightarrow ee$  events where one of the electrons has radiated a high- $p_T$  photon which is collinear to the direction of the mother electron. In this case, only the high- $p_T$  photon might get reconstructed, and wrongly be identified as a prompt photon. Hence, the  $Z \rightarrow e + \text{fake-}\gamma$  events contain an electron-photon pair with an invariant mass compatible with the  $Z$  boson mass, and the photon has the characteristic of an electron-fake photon.

The control region is selected by requiring a back-to-back  $e\gamma$  pair ( $\Delta\phi(e, \gamma) > 150^\circ$ ) with an invariant mass of  $70 < m_{e\gamma} < 110$  GeV. The  $p_T$  of the electron must be larger than the  $p_T$  of the photon. In order

to be closer to the topology of the signal events, events are required to fulfil  $E_T^{\text{miss}} > 30 \text{ GeV}$ .

After the event selection, the backgrounds are subtracted using a sideband fit to the  $m_{e\gamma}$  distribution. The  $p_T^{\text{cone}20}$  distribution of the photons in the background-subtracted  $Z \rightarrow e + \text{fake-}\gamma$  sample is used as the electron-fake template. The data-driven template is validated by MC, using  $Z \rightarrow ee$  MC sample and applying the  $Z \rightarrow e + \text{fake-}\gamma$  selection.

For the differential cross-section measurement, the electron-fake template is extracted for each bin of the observables. However, for the last two bins of  $p_T$  ( $60 \leq p_T < 100 \text{ GeV}$  and  $100 \leq p_T < 300 \text{ GeV}$ ) there is not enough statistics in the  $Z \rightarrow e + \text{fake-}\gamma$  control region to extract a template. Therefore, the template of the bin  $40 \leq p_T < 60 \text{ GeV}$  is also used for these two bins, but with additional extrapolation uncertainty. The extrapolation uncertainty is defined by the difference between the average of all available templates for  $p_T$  bins and the last available template, i.e. the template of bin  $40 \leq p_T < 60 \text{ GeV}$ .

To estimate the systematic uncertainties of the template, the requirement of  $E_T^{\text{miss}} > 30 \text{ GeV}$  is varied to  $E_T^{\text{miss}} > 35 \text{ GeV}$  and the difference between the template derived from the modified condition with the nominal template is taken as the uncertainty. The same procedure is also done by removing the requirement of  $p_T(e) > p_T(\gamma)$ , and by varying the mass range that is used when performing the sideband fit to the  $m_{e\gamma}$  distribution.

## 7.4 Background Estimation

The background processes that enter the signal region are sorted in three categories based on their photon: 1) background events with hadronic-fake photons, 2) background events with electron-fake photons, 3) Background events with prompt photons. Definition of prompt, hadronic-fake and electron-fake photons are given in Section 7.2.1. While the shapes of these backgrounds are described by their corresponding templates in the likelihood function, their normalisation (i.e. total number of corresponding background events) are estimated from different methods as outlined in this section.

### 7.4.1 Hadronic-fake Background

The largest background contribution in this analysis is due to hadronic-fake photons. The dominant contribution to this background is from  $t\bar{t}$  events with a hadronic-fake photon. Other processes like  $W+\text{jets}$  and single-top production have a small contribution in this background. This background is estimated from data, using the template fit. As mentioned before, the number of hadronic-fake background events is treated as a free parameter in the maximum-likelihood fit. The extraction of data-driven templates for hadronic-fake photon is described in Section 7.3.2.

### 7.4.2 Electron-fake Background

The second largest background contribution comes from events containing an electron-fake photon (also denoted as  $e \rightarrow \gamma$  fake). The main source of this background are the  $t\bar{t}$  events in their dilepton decay channel when at least one of the leptons is an electron ( $e\mu$  and  $ee$  channels). There is also smaller contribution from  $Z+\text{jets}$  events when the  $Z$  boson decays into electrons.

The contribution from electron-fake background is estimated from data. The  $e \rightarrow \gamma$  fake rate, the probability of a an electron to be mis-identified as a photon, is calculate using two control regions: the  $Z \rightarrow e + \text{fake-}\gamma$  control region, introduced before in Section 7.3.3, and  $Z \rightarrow ee$  control region.

The  $Z \rightarrow ee$  ( $Z \rightarrow e + \text{fake-}\gamma$ ) control region is selected by requiring a back-to-back  $e^+e^- (e-\gamma)$  pair, where the  $\Delta\phi$  distance between the two objects is greater than  $150^\circ$ , and their invariant mass is

required to be in a  $\pm 50$  GeV window around the  $Z$  boson mass. The object definitions are the same as in Section 7.1.1, except that in the  $Z \rightarrow ee$  control region the  $p_T$  threshold for the second electron is lowered from 25 GeV to 15 GeV. In the  $Z \rightarrow e+\text{fake-}\gamma$  control region, the electron must have a larger  $p_T$  than the photon. In both regions the object with largest  $p_T$  is called the *tag* and the other one the *probe* object. Therefore, the tag object is always an electron, while the probe object is either the photon in  $Z \rightarrow e+\text{fake-}\gamma$  events which has the properties of an electron-fake photon (as explained in Section 7.1.1), or the second electron in the  $Z \rightarrow ee$  region which has the same  $p_T$  requirement as for the photons in the signal region ( $p_T > 15$  GeV). To avoid a trigger bias, the tag electron in both control regions must match the trigger.

The  $e \rightarrow \gamma$  fake rate is calculated as a function of  $p_T$  and  $\eta$  of photons, from the ratio of number of  $Z \rightarrow e+\text{fake-}\gamma$  events to number of  $Z \rightarrow ee$  events. The number of events is derived from a fit to the invariant mass distribution of either  $e\gamma$  or  $e^+e^-$  pair, using the sum of a Crystal-Ball (for signal) and a Gaussian function (for background), performed in a range of [70, 110] GeV.

The  $p_T - \eta$  binned fake rates are then applied to a modified signal region, where the photon in  $t\bar{t}\gamma$  event selection (Section 7.1) is replaced by an electron which fulfils the same kinematic requirements as for the photon. This results to a total of  $317 \pm 7(\text{stat.}) \pm 41(\text{syst.})$  for estimate number of electron-fake background in the  $e+\text{jets}$  channel and  $385 \pm 6(\text{stat.}) \pm 42(\text{syst.})$  in the  $\mu+\text{jets}$  channel [8]. The first error for each channel shows the statistical uncertainty while the second one is the systematic uncertainty. The systematic uncertainty is due to the uncertainty of the fake rates, estimated by varying the choice of the range and the functions that are used when performing the fit to the  $e^+e^-$  and  $e\gamma$  invariant mass distributions.

### 7.4.3 Backgrounds with Prompt Photons

Background events with a prompt photon have a smaller contribution in the signal region.

Smaller contributions come from background events with a prompt photon in their final state. The latter category contains all the processes that are background to the  $t\bar{t}$  production when they are produced with additional prompt photons. This includes the multi-jet production with a prompt photon, when a jet or a non-prompt lepton from a jet segmentation decay is mis-identified as a lepton. Other background processes with a prompt photon are  $W\gamma$ ,  $Z\gamma$ , single top+ $\gamma$  and diboson+ $\gamma$  productions.

#### 7.4.3.1 Multi-jet Production with a Prompt Photon

Multi-jet processes can mimic the signature of  $t\bar{t}$  single-lepton channel when either a jets or a non-prompt lepton originating from a jet is misidentified as a prompt lepton. Jets can be misidentified as electrons when they have a high electromagnetic fraction. This could be due to early showering in the calorimeter, or from the hadronisation to  $\pi^0$  mesons. The non-prompt muon and electrons originate from semi-leptonic decays of the heavy flavour hadrons in jets. Additionally, non-prompt electrons can arise from photon conversions inside the jets. For simplicity, all these background-type reconstructed leptons will be called *fake leptons* in this text<sup>8</sup>, in contrast to the signal leptons that are from the prompt decays of  $W$  bosons and will be referred to as *real leptons*.

The multi-jet processes are dominated by the QCD multi-jet production. They also include the  $t\bar{t}$  all-hadronic decay channel and the  $t\bar{t}$  decay into  $\tau$ -leptons where then they decay hadronically. The multi-jet processes can be produced with an additional prompt photon and enter the  $t\bar{t}\gamma$  signal region when they contain a fake lepton. A multi-jet event that is not produced with an additional prompt photon can still enter the  $t\bar{t}\gamma$  signal region when it contains not only a fake lepton but also a hadronic-fake photon. Since

---

<sup>8</sup> Even though the non-prompt leptons that are misidentified as a prompt lepton are indeed real.

in this analysis all the possible background events with a hadronic-fake photon, regardless of the process and regardless of their leptons being fake or real, are treated as outlined in Section 7.4.1, the contribution of the multi-jet background is specifically estimated for the case of multi-jet production with a prompt photon.

This background is estimated in two steps:

- (i) First, the background events with a fake lepton are estimated, where the photons in the event could be either prompt or fake. In this step, a control sample of  $t\bar{t}\gamma$  events in data where the lepton in the event is fake is extracted by using a data-driven technique called the *matrix method*.
- (ii) Then, the background events with a fake lepton where the photon in the event is prompt are distinguished. The prompt photon template (see Section 7.3.1) and the hadronic-fake template (see Section 7.3.2) are fitted to the photon  $p_T^{\text{cone}20}$  distribution of the control sample from step (i), in order to extract the  $t\bar{t}\gamma$  events with a fake lepton and a prompt photon. This is to avoid double counting of the hadronic-fake background events, because of the way that the hadronic-fake background is estimated in this analysis (see Section 7.4.1).

**Step (i): Using Matrix method to extract  $t\bar{t}\gamma$  events with fake leptons** The Matrix method is based on classifying two categories of reconstructed leptons, by defining a *tight* and a *loose* set of lepton selection requirements.

The tight electron and muon selection criteria are identical to the nominal selections for the signal region, described in Section 7.1.1. The loose muons are selected by removing the isolation requirements. To select the loose electrons, in addition to removing the isolation requirements, some electron identification requirements are also relaxed: the TRT-based identification requirements and the track-cluster matching requirement based on the ratio of the cluster energy to the track momentum ( $E/p$ ).

Based on these two lepton categories, two samples of  $t\bar{t}\gamma$  events in data are selected: the *tight sample* contains  $t\bar{t}\gamma$  event candidates with tight leptons, and the *loose sample* is made of  $t\bar{t}\gamma$  event candidates with loose leptons. The two samples only differ in their lepton selection criteria, while the rest of their object- and event-level selections are the same as for the  $t\bar{t}\gamma$  signal selection described in Section 7.1. Therefore, the tight sample is identical to the signal region. Also, since the loose leptons are selected by relaxing some of the tight lepton requirements, the tight sample is a subset of the loose sample. Because the relaxed requirements are specifically designed to reject the fake leptons, the loose sample is enriched with fake leptons.

The core of the matrix method is the assumption that the number of events in loose and tight samples,  $N^{\text{loose}}$  and  $N^{\text{tight}}$  respectively, can be expressed as a linear sum of number of events with real leptons ( $N_{\text{real}}$ ) and number of events with fake leptons ( $N_{\text{fake}}$ ):

$$\begin{aligned} N^{\text{loose}} &= N_{\text{real}}^{\text{loose}} + N_{\text{fake}}^{\text{loose}} \\ N^{\text{tight}} &= N_{\text{real}}^{\text{tight}} + N_{\text{fake}}^{\text{tight}}. \end{aligned} \quad (7.7)$$

By defining  $\epsilon_{\text{real}}$  ( $\epsilon_{\text{fake}}$ ) as the fraction of real (fake) leptons in the loose sample that also pass the tight selection, one can write:

$$N^{\text{tight}} = \epsilon_{\text{real}} N_{\text{real}}^{\text{loose}} + \epsilon_{\text{fake}} N_{\text{fake}}^{\text{loose}}. \quad (7.8)$$

The  $\epsilon_{\text{real}}$  and  $\epsilon_{\text{fake}}$  are called *real efficiency* and *fake efficiency*, respectively. If the values of efficiencies are known, then by counting  $N^{\text{loose}}$  and  $N^{\text{tight}}$  one can calculate the number of  $t\bar{t}\gamma$  events with a fake lepton ( $N_{\text{fake}}^{\text{tight}}$ ) from Equations 7.7 and 7.8:

$$N_{\text{fake}}^{\text{tight}} = \frac{\epsilon_{\text{fake}}}{\epsilon_{\text{real}} - \epsilon_{\text{fake}}} (\epsilon_{\text{real}} N^{\text{loose}} - N^{\text{tight}}). \quad (7.9)$$

Both real and fake efficiencies depend on lepton kinematics, such as lepton  $p_{\text{T}}$  and  $\eta$ , as well as event properties, including number of jets, number of  $b$ -tagged jets,  $\Delta R$  between the objects, and jet  $p_{\text{T}}$ . Also, Equation 7.9 can only be used to get the total estimated number of  $t\bar{t}\gamma$  events with a fake lepton (i.e.  $N_{\text{fake}}^{\text{tight}}$ ), while in order to perform step (ii) the photon  $p_{\text{T}}^{\text{cone}20}$  distribution of these events is also needed. For these two reasons, it is more convenient to introduce an event weight,  $w_i$ , by generalising Equation 7.9 and using  $\epsilon_{\text{real}}$  and  $\epsilon_{\text{fake}}$  that are parametrised as a function of various lepton kinematics and event properties:

$$w_i = \frac{\epsilon_{\text{fake}}}{\epsilon_{\text{real}} - \epsilon_{\text{fake}}} (\epsilon_{\text{real}} - \delta_i). \quad (7.10)$$

The index  $i$  runs over the data events in the loose sample, and  $\delta_i$  is equal to 1 if the loose lepton in the event also passes the tight selection, and it is equal to 0 otherwise.

The real and fake efficiencies are measured separately for electrons and muons, from control regions in data that are enriched in real and fake leptons. The detail of the extraction of the efficiencies and their parametrisation can be found in Ref. [120].

By applying the  $w_i$  weights to the loose sample, a control sample of  $t\bar{t}\gamma$  events with fake leptons is obtained, which yields  $12.5 \pm 3.8$  events in the  $e+\text{jets}$  channel,  $24.4 \pm 5.3$  in the  $\mu+\text{jets}$  channel, and  $37.9 \pm 6.6$  in the combined single-lepton channel<sup>9</sup>, where the errors are statistical uncertainties. The photons in these events could be either prompt or fake. This will cause a double counting of background events in the case of events containing a hadronic-fake photon. Therefore, step (ii) is performed to extract the  $t\bar{t}\gamma$  events with fake leptons and prompt photons.

**Step (ii): Extracting  $t\bar{t}\gamma$  events with fake leptons and prompt photons** A template fit is performed on photon  $p_{\text{T}}^{\text{cone}20}$  distribution of the control sample of  $t\bar{t}\gamma$  events with fake leptons that is extracted in step (i) and shown in Figure 7.18, marked as data. The template fit is using the prompt photon template described in Section 7.3.1 and the hadronic-fake template described in Section 7.3.2. The fit result gives the estimated background contribution from multi-jet production with a prompt photon, which is  $7.5 \pm 3.6$  events in the  $e+\text{jets}$  channel,  $8.3 \pm 5.2$  events in the  $\mu+\text{jets}$  channel (also summarised in Table 7.10), and  $15.8 \pm 6.3$  events in the combined single-lepton channel. The errors are coming from the statistical uncertainties. The post-fit photon isolation distributions are also shown in Figure 7.18.

For the differential measurements, step (i) and (ii) are repeated for each bin of the observables. When performing step (ii), the prompt-photon and hadronic-fake templates of each bin is used. The resulting estimated backgrounds are summarised in Tables 7.8 and 7.9.

$p_{\text{T}}$ bin [GeV]	$15 \leq p_{\text{T}} < 25$	$25 \leq p_{\text{T}} < 40$	$40 \leq p_{\text{T}} < 60$	$60 \leq p_{\text{T}} < 100$	$p_{\text{T}} \geq 100$
$e+\text{jets}$	$2.2 \pm 1.7$	$1.9 \pm 1.7$	$0.8 \pm 1.4$	$1.7 \pm 1.5$	$0.4 \pm 0.7$
$\mu+\text{jets}$	$5.2 \pm 3.6$	$0.0 \pm 2.1$	$3.0 \pm 2.0$	$0.0 \pm 1.1$	$0.0 \pm 0.1$
single-lepton	$7.4 \pm 4.0$	$1.9 \pm 2.7$	$3.7 \pm 2.4$	$1.7 \pm 1.8$	$0.4 \pm 0.7$

Table 7.8: The estimated background contribution from multi-jet production with a prompt photon in each photon  $p_{\text{T}}$  bin for the differential measurement. The uncertainties are statistical only.

<sup>9</sup> Note that since the events are weighted and the matrix-method event weight in Equation 7.10 can also be negative, the number of events in combined single-lepton channel is not expected to be the sum of number of events in the two  $e+\text{jets}$  and  $\mu+\text{jets}$  channels.

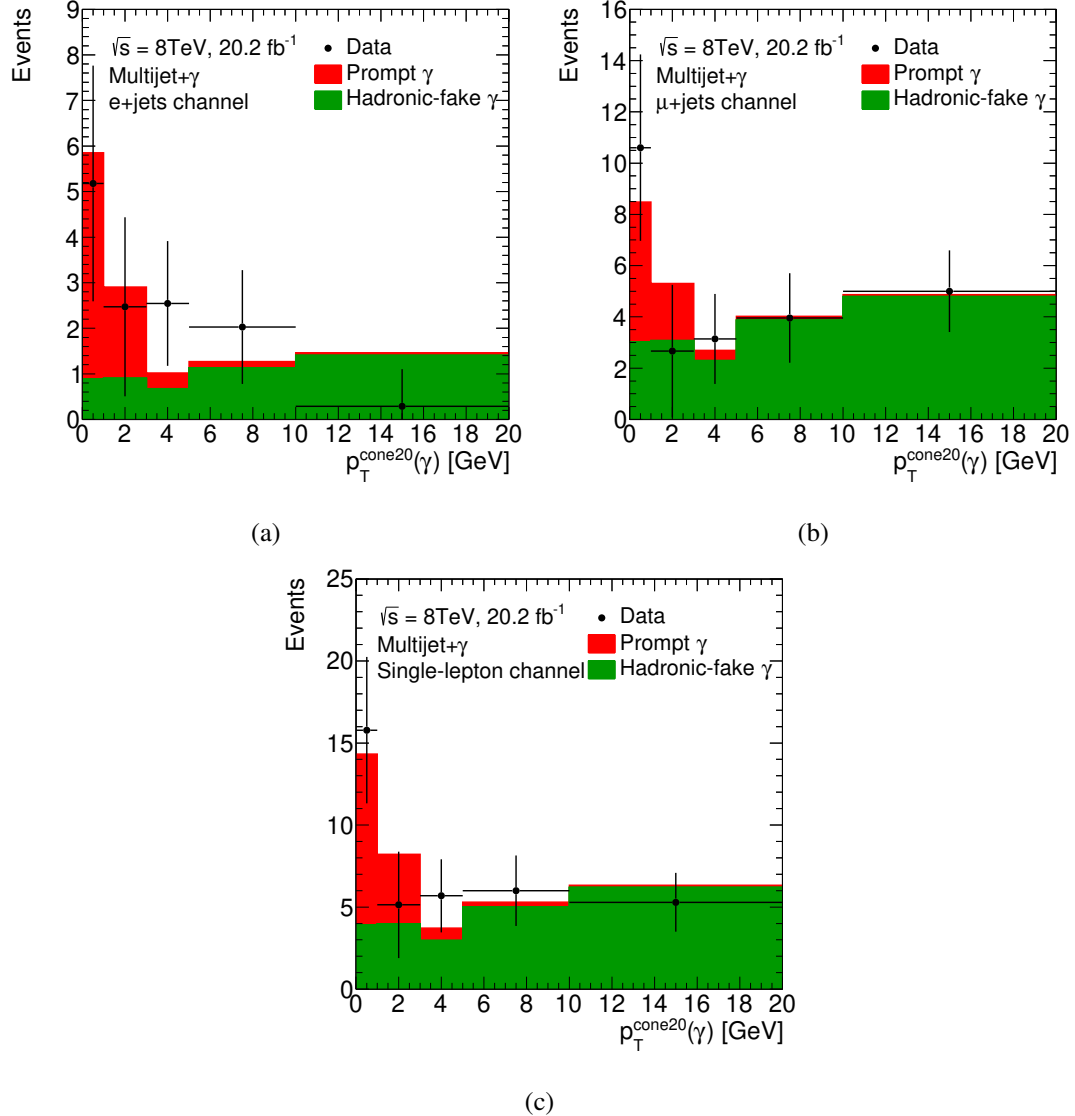


Figure 7.18: The  $p_T^{\text{cone}20}$  distribution of photons in the control sample of  $t\bar{t}\gamma$  events in data where the lepton in the event is a fake lepton, fitted by the prompt-photon and hadronic-fake templates, in (a) the  $e+\text{jets}$  channel, (b) the  $\mu+\text{jets}$  channel, and (c) the combined single-lepton channel. The filled areas show the results of the fit. The last bin contains the overflow.

$\eta$ bin	$ \eta  \leq 0.25$	$0.25 <  \eta  \leq 0.55$	$0.55 <  \eta  \leq 0.90$	$0.90 <  \eta  \leq 1.37$	$1.37 <  \eta  \leq 2.37$
$e+\text{jets}$	$2.6 \pm 1.3$	$0.0 \pm 0.3$	$2.0 \pm 1.3$	$2.9 \pm 1.5$	$2.7 \pm 1.8$
$\mu+\text{jets}$	$1.6 \pm 1.8$	$2.1 \pm 2.5$	$0.0 \pm 0.8$	$0.5 \pm 3.2$	$1.4 \pm 2.5$
single-lepton	$4.2 \pm 2.2$	$2.1 \pm 2.6$	$2.0 \pm 1.5$	$3.3 \pm 3.5$	$4.0 \pm 3.0$

Table 7.9: The estimated background contribution from multi-jet production with a prompt photon in each photon  $\eta$  bin for the differential measurement. The uncertainties are statistical only.

### 7.4.3.2 $W\gamma$ Production with Additional Jets

The background contribution from  $W\gamma$  production is estimated from MC simulation and then is scaled by a data-driven scale factor. The MC simulated  $W\gamma$  events do not agree well with data, as the fraction of heavy-flavour jets observed in data is smaller than what is obtained from simulation. Therefore, a scale factor is derived from a control region in data and applied to the prediction of the simulation.

The  $W\gamma$  control region is selected by applying the same selection cuts as for the signal region (see Section 7.1), except for the requirement on jet multiplicity which is changed to  $1 \leq N_{\text{jets}} \leq 3$ , the number of  $b$ -tagged jets which is changed to exactly one, and adding a requirement on the invariant mass of the lepton and photon ( $m_{l\gamma}$ ) which has to be less than 40 GeV. The requirements on number of jets and number of  $b$ -jets suppress the  $t\bar{t}\gamma$  contribution<sup>10</sup> and the requirement on  $m_{l\gamma}$  suppresses mainly the contamination from electron-fake photons, as well as other backgrounds.

Although the control region is dominated by  $W\gamma$  events, the hadronic-fake background, electron-fake background and other backgrounds with prompt photons also contribute. The contribution of non- $W\gamma$  processes must be subtracted from data before being able to calculate the  $W\gamma$  scale factor. Therefore, the same procedure of maximum-likelihood fit as for the signal region is performed in this control region, to estimate the number of  $W\gamma$  events, along side the hadronic-fake background contribution.

The fit is using the same prompt-photon and electron-fake templates that are extracted for the signal region, described in Section 7.3.1 and 7.3.3 respectively. However, the hadronic-fake template derived for the signal region can not be used here, due to the template shape dependency on the jet multiplicity. Thus, the hadronic-fake template for the  $W\gamma$  control region is extracted in the same manner as for the signal region, described in Section 7.3.2, but with changing the jet multiplicity requirement to  $1 \leq N_{\text{jets}} \leq 3$ . Also, the re-weighting process is not performed, since as seen in Sections 7.3.2.2 and 7.3.2.3, the weighted and unweighted templates do not differ significantly in shape. The systematic uncertainty due to prompt-photon contamination in hadronic-fake template is estimated with the same method as in Section 7.3.2.4.

The normalisation of the hadronic-fake background is a free parameter in the fit, while for all the other backgrounds it is fixed to their estimated values. The contribution from electron-fake background and multi-jet production with a prompt photon are estimated with repeating the same data-driven methods described in Section 7.4.2 and 7.4.3.1, respectively, for the  $W\gamma$  control region<sup>11</sup>. The  $t\bar{t}\gamma$  contribution, as well as the minor contributions from  $Z\gamma$ , single top+ $\gamma$  and diboson+ $\gamma$  productions are all estimated from MC simulations.

After subtracting the non- $W\gamma$  contamination from data, the  $W\gamma$  scale factor is derived from the ratio of the number of events in data to the MC predicted number from the  $W\gamma$  sample generated by SHERPA.

<sup>10</sup> By requiring the number of  $b$ -jets to be zero, the  $t\bar{t}\gamma$  contribution is even more suppressed, but then the event topology in the control region gets further away from the signal region and the extrapolation uncertainty increases. Therefore, the requirement of  $N_{b\text{-jets}} = 1$  is applied.

<sup>11</sup> The calculation of  $e \rightarrow \gamma$  fake rates used for electron-fake background estimation is not needed to be repeated, as they are not specified for the signal or any control regions.

The statistical and systematic uncertainties due to the subtraction of non- $W\gamma$  contaminations are considered in the scale factor calculation. The evaluation of systematic uncertainty of each background modelling follows the same way they are done for the signal region. Also, all the experimental and template-shape uncertainties discussed in Section 7.5 are considered. Additionally, the nominal  $W\gamma$  MC samples generated by SHERPA are compared with the samples generated by ALPGEN, which accounts for an additional 20% uncertainty. The resulting scale factors and their uncertainties for the  $e+\text{jets}$  and  $\mu+\text{jets}$  channels are  $0.69 \pm 0.16$  and  $0.76 \pm 0.14$ , respectively [8]. The estimated  $W\gamma$  background yield is shown in Table 7.10.

#### 7.4.3.3 Other Prompt-Photon Backgrounds

Additional backgrounds from  $Z\gamma$  and single top quark and diboson productions with a prompt photon have smaller contributions and are estimated from MC simulations.

The estimated yields of all the background processes with a prompt photon are summarised in Table 7.10.

Process	$e+\text{jets}$	$\mu+\text{jets}$
$W\gamma$	$65 \pm 25$	$97 \pm 25$
$Z\gamma$	$35 \pm 19$	$38 \pm 20$
Single top+ $\gamma$	$13 \pm 7$	$19 \pm 10$
Multijet+ $\gamma$	$7.5 \pm 3.6$	$8.3 \pm 5.2$
Diboson+ $\gamma$	$2.6 \pm 1.5$	$2.5 \pm 1.4$

Table 7.10: Estimated yields of the background processes with a prompt photon and their uncertainties. Except the Multijet+ $\gamma$  background, the other numbers are taken from Ref. [8].

## 7.5 Systematic Uncertainties

Systematic uncertainties affect the result of the  $t\bar{t}\gamma$  cross-section measurement at 8 TeV through their impact on the normalisation of expected signal and estimated backgrounds and/or the shape of their corresponding template. The sources of systematic uncertainties considered in this analysis can be categorised into three groups: modelling uncertainties of signal and background, described in Section 7.5.1, experimental uncertainties, described in Section 7.5.2, and uncertainties related to the template shapes, described in Section 7.5.3.

The effect of the systematic uncertainties on the measured cross sections are summarised in the next Section together with the results of cross section measurements (Section 7.6).

### 7.5.1 Modelling Uncertainties

This category includes the uncertainties that affect the result due to the modelling of the signal process in MC simulations, and modelling of the background processes either in MC simulations or through the methods that are used to estimate their normalisation. The signal modelling uncertainties are discussed below first and are followed by the description of background modelling uncertainties. The *alternative* MC samples described in this section are listed in Appendix C.1.2 as well, and detail of their production is given in Section 5.2.

## Signal Modelling

- The effect of the choices of renormalisation scale ( $\mu_R$ ) and factorisation scale ( $\mu_F$ ) is estimated using the alternative  $t\bar{t}\gamma$  MC samples which are produced similar as the nominal  $t\bar{t}\gamma$ , with `MADGRAPH5_aMC@NLO` interfaced to `PYTHIA`, but with different settings for  $\mu_R$  and  $\mu_F$ . While in the nominal signal sample the scale choices are  $\mu_R = \mu_F = 2m_{top}$ , the two alternative samples are produced with simultaneous variation of the scales by a factor 1/2 and 2;  $\mu_R = \mu_F = m_{top}$  and  $\mu_R = \mu_F = 4m_{top}$ .
- The uncertainty due to the modelling of parton shower and hadronisation is evaluated by the alternative  $t\bar{t}\gamma$  sample which is produced by replacing `PYTHIA` in the nominal sample with `HERWIG` and `JIMMY`.
- The modelling of initial- and final-state radiation is varied by using different tunes of `PYTHIA` 6, corresponding to higher (`Perugia2011C radHi`) and lower (`Perugia2011C radLo`) QCD radiation activity.
- Other signal modelling uncertainties found to be negligible: Uncertainties due to modelling of PDF, colour reconnection, underlying event and QED radiation were studied separately, using  $t\bar{t}$  MC samples, as their effects are expected to be similar in  $t\bar{t}\gamma$  production. Since the effect of their variation on prompt photon  $p_T^{\text{cone}20}$  distribution and event yield found to be negligible, no dedicated alternative  $t\bar{t}\gamma$  samples were produced for them and these sources are not considered. The effect of the choice of matrix-element event generator has been found to be negligible in a previous analysis [45], so it is also not considered.

## Background Modelling

- The uncertainty of the  $e \rightarrow \gamma$  fake rates used to estimate the electron-fake background results in a 6.1% uncertainty in the measured inclusive cross section. The uncertainty of fake rates are estimated as described in Section 7.4.2.
- The uncertainties in the estimation of  $W\gamma$  background that are taken into account are the uncertainty of the scale factor used to normalise the sample, described in Section 7.4.3.2, as well as the difference between the predictions from baseline  $W\gamma$  MC samples produced by `SHERPA`, and the  $W\gamma$  MC samples produced by `ALPGEN`.
- The uncertainties in the estimation of  $Z\gamma+\text{jets}$ , single top+ $\gamma$  and diboson+ $\gamma$  backgrounds, which are purely estimated from MC simulation, are estimated using the 48% uncertainty in the normalisation of the samples in the four-jet bin from the Berends–Giele scaling [121].

### 7.5.2 Experimental Uncertainties

The experimental uncertainties are mainly the uncertainties of event reconstruction where detector simulation is used. These are uncertainties associated to the objects used in the analysis, namely electrons, muons, jets, photons and  $E_T^{\text{miss}}$ , in terms of reconstruction and identification efficiency, momentum and energy scale, momentum and energy resolution, isolation efficiency, trigger efficiency (in case of the objects that fired the trigger), jet flavour tagging and jet vertex fraction. Also, this category includes the uncertainties of integrated luminosity and pile-up simulation. Experimental uncertainty sources are common to signal and background processes. These uncertainties are listed below.

## Leptons

As mentioned in Section 4.2 and 4.3, several corrections are applied to leptons in MC simulated samples to better match the data and correct for detector mis-modelings. This includes scale factors for reconstruction, identification, trigger and isolation efficiencies, correction factors for calibration of lepton energy and momentum, and the smearing to correct the lepton energy and momentum resolution. The scale and correction factors and the smearing parameter are varied separately by  $\pm 1\sigma$  to evaluate the impact of the uncertainties of lepton efficiencies, energy scale and resolution.

## Photons

The scale factors used in MC samples to correct the photon identification efficiency, explained in Section 4.5, are varied by  $\pm 1\sigma$ . The impact of photon energy scale and resolution is estimated similarly as for the electrons.

## Jets

The calibration of jet energy scale and resolution (JES and jet energy resolution (JER)) are introduced in Section 4.4. The assigned systematic uncertainty for both of the JES and the JER has many components which are grouped into independent categories. In each group there could be more than one source for uncertainty. Each source is varied independently and their resulting uncertainties are added quadratically in order to get the uncertainty arising from JES or JER. The JES uncertainty is the dominant experimental systematic uncertainty in this analysis. The systematic uncertainty associated to the JVFC cut is evaluated by varying the cut value up and down.

The JES uncertainties due to flavour composition and flavour response depend on the fraction of the gluon initiated jets,  $f_g$ , and its uncertainty,  $\Delta f_g$ , in a given sample. Since  $f_g$  and  $\Delta f_g$  depend on the event topology, a dedicated study is done to estimate  $f_g$  and  $\Delta f_g$  as functions of jet  $p_T$  and  $\eta$  from the signal sample. This is presented in Section 7.5.2.1.

## *b*-tagging

The uncertainty in *b*-tagging is evaluated by independently varying the calibration scale factors of the *b*-, *c*- and light-flavour jets in their corresponding uncertainty range.

## Missing Transverse Momentum

The uncertainties of the energy scales and resolutions of the leptons, jets and photons are propagated to the  $E_T^{\text{miss}}$ . Additional uncertainties due to the modelling of the soft terms of  $E_T^{\text{miss}}$  (see Section 4.6) are considered.

## Pile-up

To match the pile-up condition in the data, the distribution of mean number of interactions per bunch crossing (see Section 5.1) in simulation is re-weighted to that of the data. The uncertainty associated to the modelling of pile-up events is studied by varying the pile-up re-weighting parameter from its nominal value of 1.09, to 1.05 or 1.13.

## Luminosity

The uncertainty on the integrated luminosity is 1.9%, estimated as described in Ref. [49] and provided centrally by ATLAS.

### 7.5.2.1 Estimating the Fraction of Gluon-initiated Jets in the $t\bar{t}\gamma$ Signal Sample

The calorimeter response to jets in the MC simulation ( $p_T^{\text{jet}}/p_T^{\text{truth}}$ ) shows a dependency on the flavour of the jet. More specifically, jets labelled as originating from gluons have a significant different response from those labelled as originating from quarks, due to differences in their fragmentation and showering properties. A quark-initiated jet often contain hadrons that have a higher fraction of the jet  $p_T$  and could penetrate further into the calorimeter, while a gluon-initiated jet typically include more particles with softer  $p_T$ , leading to a lower calorimeter response and a wider transverse profile [122].

On the other hand, the jet energy scale is not a function of jet flavour, and the jet flavour composition in the MC samples that are used for calibration (see Section 4.4) might be very different from the samples being used in a specific analysis. Therefore, a systematic uncertainty is dedicated to account for this effect. The jet energy scale systematic uncertainty due to flavour composition and flavour response,  $\Delta R_S^{12}$ , is established as [123]:

$$\Delta R_S = \Delta f_g \times |R_g - R_q| \oplus f_g \times \Delta R_g, \quad (7.11)$$

where  $R_g$  and  $R_q$  refer to the response to the jets initiated by gluons and light quarks, respectively,  $f_g$  is the fraction of gluon-initiated jets, and  $\Delta$  denotes the uncertainty on the respective variable. Both  $R_g$  and  $R_q$  are estimated from MC simulated di-jet events and  $\Delta R_g$  is estimated by comparing several generators [77]. But both  $f_g$  and  $\Delta f_g$  depend on the event topology, making  $\Delta R_S$  an analysis-dependent uncertainty. Therefore, they are derived from the  $t\bar{t}\gamma$  signal MC sample as explained in the following.

First, the flavour of jets is determined. For this, the reconstructed jets in the events that pass the full  $t\bar{t}\gamma$  selection (see Section 7.1) are matched to the true jets at particle level within a  $\Delta R < 0.3$  distance. The partonic flavour of the jet is determined based on the highest-energy ghost-associated parton inside the jet<sup>13</sup>. Then,  $f_g$  is calculated in bins of jet true  $p_T$  and jet  $\eta$ . To estimate  $\Delta f_g$ , the calculation of  $f_g$  is repeated by using alternative signal MC samples, introduced in Section 7.5.1, to take into account the uncertainties due to the choice of QCD scales, modelling of initial- and final-state radiation, and modelling of hadronisation and parton showering.

Figure 7.19 shows the resulting  $f_g$  in different jet  $\eta$  regions as a function of jet  $p_T$ . The blue band shows  $\Delta f_g$ , the total uncertainty of  $f_g$ , including systematic uncertainties due to MC modelling.

### 7.5.3 Template Uncertainties

#### Prompt-Photon Template

The prompt-photon template is affected by the signal modelling described in Section 7.5.1 and all the experimental systematic uncertainties described in Section 7.5.2.

<sup>12</sup>  $R_S$  denotes the sample response.

<sup>13</sup> The particle-level jets are re-clustered, using the jets constituents along with all *ghost* partons, meaning that the parton is scaled to an infinitely small momentum and then participates in the clustering. This procedure is called *ghost-association* [124].

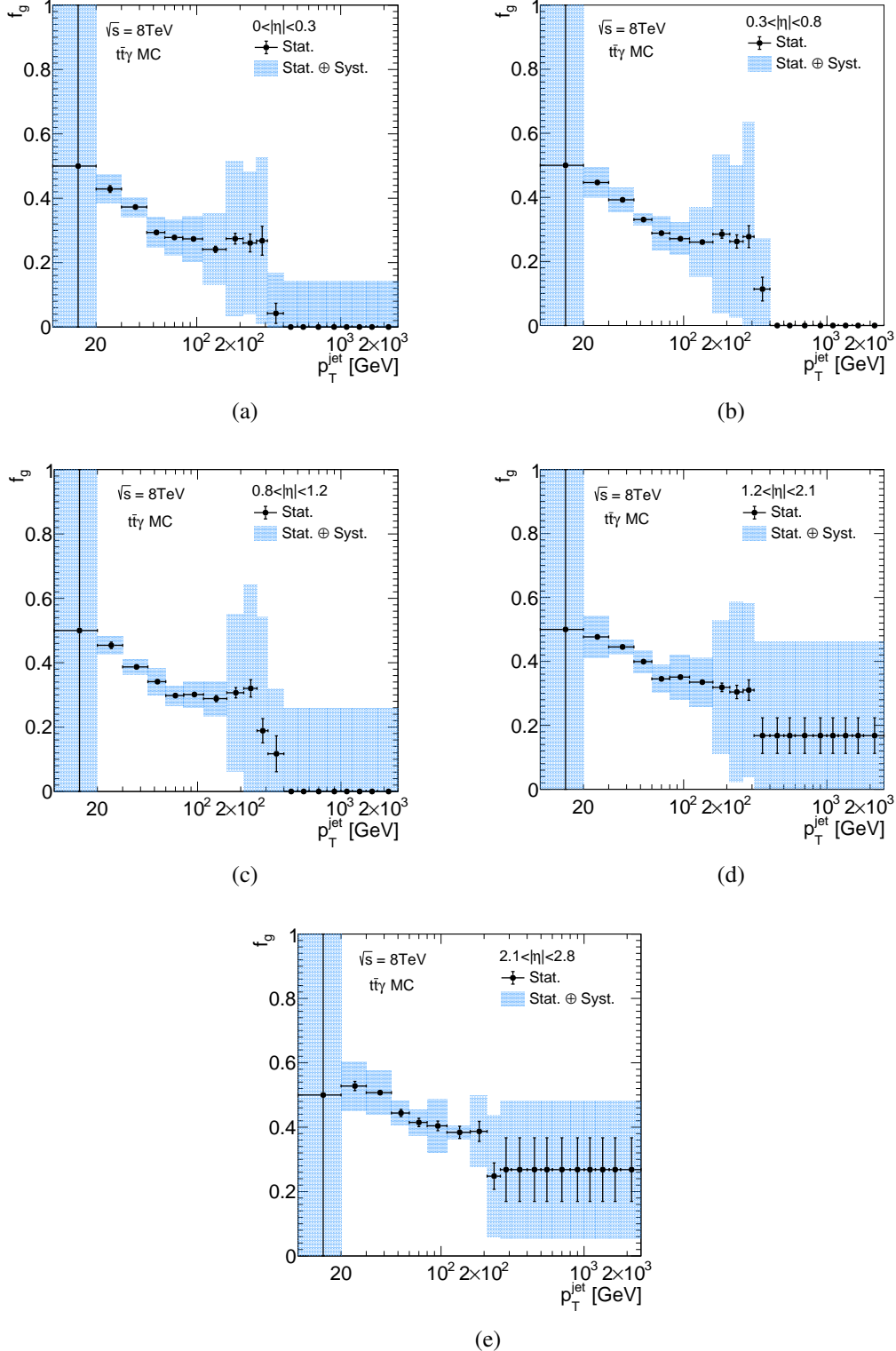


Figure 7.19: Fractions of gluon initiated jets ( $f_g$ ) in  $t\bar{t}\gamma$  MC simulated sample, as a function of jet  $p_T$  in different  $\eta$  region of (a)  $|\eta| < 0.3$ , (b)  $0.3 < |\eta| < 0.8$ , (c)  $0.8 < |\eta| < 1.2$ , (d)  $1.2 < |\eta| < 2.1$  and (e)  $2.1 < |\eta| < 2.8$ . The error bars show the statistical uncertainty while the blue bands correspond to the total uncertainty ( $\Delta f_g$ ). There are no jets with  $p_T < 25$  GeV after the full  $t\bar{t}\gamma$  event selection, therefore the first bin is filled with  $f_g = 0.5 \pm 0.5$ .

### Hadronic-fake Template

The systematic uncertainty for the hadronic-fake template is dominated by the the uncertainty due to prompt-photon contamination, described in Section 7.3.2.4. A much smaller contribution comes from the weight uncertainties described in Sections 7.3.2.2 and 7.3.2.3. The effect of hadronic-fake template uncertainty on the fitted cross section for the inclusive measurement is 6.3%, making it one of the dominant uncertainties in this analysis.

### Electron-fake Template

The systematic uncertainties considered for the electron-fake template are described before in Section 7.3.3. Amongst them, the variation of  $E_T^{\text{miss}}$  requirement has the dominant effect. The combination of the electron-fake template uncertainty and the uncertainties of the  $e \rightarrow \gamma$  fake rates results to a systematic uncertainty of 6.3% for the inclusive cross section. This combined uncertainty and the uncertainty of hadronic-fake template share the first place in the ranking of uncertainties on the measurement of the inclusive cross section.

## 7.6 Results

The inclusive and differential cross sections of  $pp \rightarrow t\bar{t}\gamma$  production at a centre-of-mass-energy of  $\sqrt{s} = 8$  TeV are measured in a fiducial region for the single-lepton decay channel. A total number of 3072 events is observed in data. The cross sections are extracted by performing a maximum-likelihood fit to the binned photon isolation ( $p_T^{\text{cone}20}$ ) distribution in data.

The post-fit event yields for the inclusive measurement are summarised in Table 7.11, and the post-fit  $p_T^{\text{cone}20}$  distribution is shown in Figure 7.20(b).

$t\bar{t}\gamma$	Hadronic-fake	Electron-fake	$W\gamma$	$Z\gamma$	Single top+ $\gamma$	Multijet+ $\gamma$	Diboson+ $\gamma$	Data
$1060 \pm 130$	$1020 \pm 90$	$710 \pm 90$	$160 \pm 40$	$73 \pm 32$	$32 \pm 15$	$16 \pm 6$	$5 \pm 2$	3072

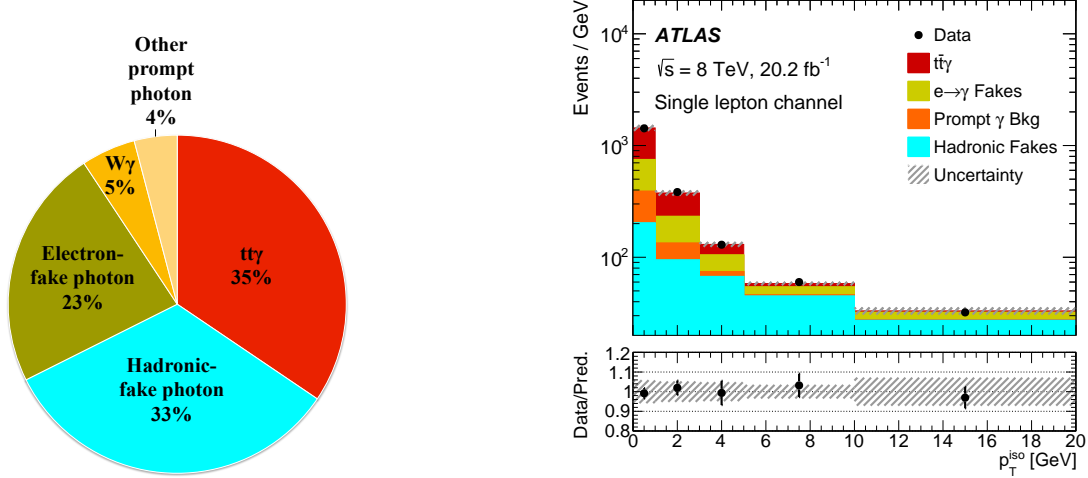
Table 7.11: The post-fit event yields for the signal and backgrounds for the inclusive fiducial  $t\bar{t}\gamma$  cross-section measurement at 8 TeV. The uncertainties include the statistical and systematic uncertainties.

The measured inclusive fiducial cross section in the single-lepton channel is:

$$\sigma_{t\bar{t}\gamma, \text{sl}}^{\text{fid}} = 139 \pm 7 \text{ (stat.)} \pm 17 \text{ (syst.) fb} = 139 \pm 18 \text{ fb},$$

which is in agreement with the SM prediction at the NLO accuracy in QCD that is  $151 \pm 24$  fb (see Section 7.2.4). The total uncertainty of 13%, which is dominated by systematic uncertainties (statistical uncertainty accounts for 5%), is an improvement in accuracy with respect to the previous  $t\bar{t}\gamma$  cross section measurement in ATLAS at  $\sqrt{s} = 7$  TeV [45]. A summary of the effect of the most important systematic uncertainty groups from Section 7.5 on the inclusive fiducial measurement is shown in Table 7.12. It can be seen that the dominating systematic uncertainties come from the fake photon background estimations.

The measured differential cross sections in five bins of photon  $p_T$  and five bins of photon  $\eta$  are shown in Figures 7.21(a) and 7.21(b) respectively. As can be seen, the differential measurements are also in agreement with the SM NLO predictions. These results were the first ever reported differential measurement performed for the  $t\bar{t}\gamma$  production.



(a) A pie chart of the post-fit event yields for the inclusive fiducial  $t\bar{t}\gamma$  cross-section measurement at 8 TeV.

(b) The post-fit  $p_T^{\text{cone}20}$  distribution for the inclusive fiducial  $t\bar{t}\gamma$  cross-section measurement at 8 TeV [8]. The uncertainty band includes the statistical and systematic uncertainties.

Figure 7.20

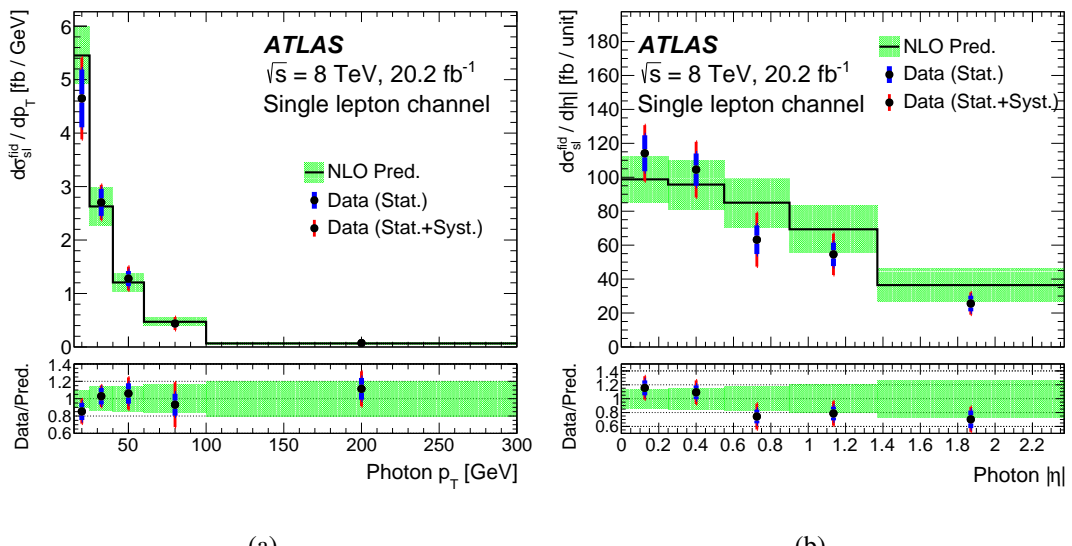


Figure 7.21: Measured differential  $t\bar{t}\gamma$  cross section at 8 TeV as a function of (a)  $p_T$  and (b)  $\eta$  of photons, and their corresponding SM NLO predictions [8].

Source	Relative uncertainty (%)
Hadronic-fake template	$\pm 6.3$
Electron-fake	$\pm 6.3$
Jet energy scale	$\pm 4.9$
$W\gamma$	$\pm 4.0$
$Z\gamma$	$\pm 2.8$
Initial- and final state radiation	$\pm 2.2$
Luminosity	$\pm 2.1$
Photon	$\pm 1.4$
Single top+ $\gamma$	$\pm 1.2$
Muon	$\pm 1.2$
Electron	$\pm 1.0$
QCD scale choices	$\pm 0.6$
Parton shower and hadronisation	$\pm 0.6$
Systematic uncertainty	$\pm 12$
Statistical uncertainty	$\pm 5$
Total uncertainty	$\pm 13$

Table 7.12: Summary of the effects of systematic uncertainties with highest effect on the inclusive fiducial  $t\bar{t}\gamma$  cross-section measurement at 8 TeV [8].

## CHAPTER 8

---

# Cross-Section Measurement of $t\bar{t}\gamma$ at 13 TeV

---

In this chapter, the  $t\bar{t}\gamma$  cross-section measurement at  $\sqrt{s} = 13$  TeV is presented. This measurement uses the data recorded by the ATLAS detector in 2015 and 2016, from  $pp$  collisions at a centre-of-mass energy of  $\sqrt{s} = 13$  TeV, corresponding to an integrated luminosity of  $36.1 \text{ fb}^{-1}$ .

Same as in the 8 TeV analysis, the inclusive and differential cross sections are measured in the single-lepton decay channel, and in a fiducial phase space. However, the strategy of the analysis is quite different from the previous analysis. A brief summary of the notable changes in this analysis is given below, while the detailed explanations are presented in the relevant Sections in this Chapter:

- The inclusive fiducial cross section is extracted from a maximum-likelihood fit to the distribution of the output of a Neural Network (NN) that is trained to discriminate between the signal and total background events.
- The differential fiducial cross sections that are normalised to unity are measured without performing the maximum-likelihood fit. Instead of the bin-by-bin unfolding approach, the iterative Bayesian method is used for unfolding to the particle level. In addition to photon  $p_T$  and photon  $\eta$ , the  $\Delta R$  distance between the photon and the lepton is used as the observable for the differential measurement.
- Signal region selection: Photons are required to be isolated and their  $p_T$  requirement is increased to  $p_T > 20$  GeV. The requirement for object overlap removal between jets and photons is increased to  $\Delta R(\gamma, \text{jet}) > 0.4$ , and subsequently no  $\Delta R(\gamma, \text{jet})$  requirement at the event level is imposed. The cut value of the requirement on  $\Delta R(\gamma, \text{lepton})$  is increased to 1.0. No requirements on  $E_T^{\text{miss}}$  and  $m_T^W$  are applied.
- Theoretical prediction: The  $k$ -factor is calculated in a phase space very close to the fiducial region, rather than being estimated in a more inclusive phase space like in the 8 TeV analysis.
- The estimation of hadronic-fake background is performed by a totally different method. The number of hadronic-fake background is estimated from data using the so-called ABCD method. The data-driven estimate is used to derive a set of scale factors for correcting the shape of this background extracted from MC, to match data.
- For estimation of the electron-fake background, the same method of the 8 TeV analysis is used to derive  $e \rightarrow \gamma$  fake rates. But the application of fake rates is different. The data-driven fake rates are used to derive a set of scale factors for correcting the  $e \rightarrow \gamma$  fake rates in MC simulation to match data.

- The number of  $W\gamma$  background events is treated as a free parameter in the maximum-likelihood fit.
- The background due to fake leptons is estimated from the same matrix method as in the the 8 TeV analysis, but the background events with a prompt or a fake photon are not distinguished.

In this chapter, first the selection of signal events is described in Section 8.1. It is followed by the description of the analysis strategy in Section 8.2. Section 8.3 is dedicated to the hadronic-fake background estimation. The estimations of rest of the backgrounds are outlined in Section 8.4. The systematic uncertainties that affect the measurements are explained in Section 8.5. Finally, Section 8.6 presents the results of this analysis.

This analysis is documented in Ref. [9]<sup>1</sup>. The main contribution of the author of thesis in this analysis was the estimation of the hadronic-fake background, described in Section 8.3 and Appendix B.1. Also, the author has contributed in the reconstruction of photons used in this analysis (see Section 4.5).

## 8.1 Signal Region Selection

The signature of the single-lepton decay channel of the  $t\bar{t}\gamma$ , and also the background processes that mimic this signature, are explained previously in Chapter 7. Similar to the 8 TeV analysis, the selection cuts are optimised to suppress the background contribution and to enrich the  $t\bar{t}\gamma$  events, specially where photons are radiated from the top quark.

With respect to the 8 TeV analysis, the object-level selections are changed to the latest recommendations by the ATLAS Top working group that were available at the time. The photons are required to be isolated, since the analysis strategy is changed and the photon isolation distribution is no longer used for performing the maximum-likelihood fit. The photon isolation requirement has reduced the contribution from fake photon backgrounds significantly, especially the hadronic-fake background. In the object overlap removal, the jets are removed unless they pass  $\Delta R(\gamma, \text{jet}) > 0.4$ , which is a tighter requirement with respect to  $\Delta R(\gamma, \text{jet}) > 0.1$  used in the 8 TeV analysis. Also, the photon  $p_T$  requirement is increased to be greater than 20 GeV. At the event-level, the requirement on  $\Delta R(\gamma, \text{lepton})$  is increased to be greater than 1.0. This requirement is very efficient in rejecting the events where the photon is emitted from the decay products of the top quark, rather than the top quark itself. A requirement on  $\Delta R(\gamma, \text{jet})$  beyond the value imposed in the object overlap removal did not show the same efficiency, therefor no  $\Delta R(\gamma, \text{jet})$  cut at the event level is applied. Also, no requirements on  $E_T^{\text{miss}}$  and  $m_T^W$  are applied. These requirements typically target the background from multi-jet events (i.e. fake lepton background), and the  $Z\gamma$  and  $Z+\text{jets}$  backgrounds. These background were found to be distributed rather flat against  $E_T^{\text{miss}}$  and  $m_T^W$ , and their contributions are very small. Also, since after the event selection a NN algorithm is used to discriminated between the signal and background events, removing these selection cuts is fine.

The full description of the object- and event-level selections of the  $t\bar{t}\gamma$  signal events at 13 TeV are given in the following.

### 8.1.1 Selection at Object-level

- **Electrons:** The electron candidates are required to pass the likelihood-based tight identification, **TightLH**, and the **Gradient** isolation criteria, both defined in Section 4.2. They are required to have  $p_T > 27$  GeV and  $|\eta_{\text{cl}}| < 2.47$ , excluding the EMCAL transition region ( $1.37 < |\eta_{\text{cl}}| < 1.52$ ).

---

<sup>1</sup> Note that in Ref. [9] the cross-section measurement in the single-lepton and dilepton decay channels are presented, while this thesis does not include the measurement in the dilepton channel.

In addition, the electrons are required to have a longitudinal impact parameter with respect to the primary vertex of  $|z_0| < 0.5$  mm and their transverse impact parameter significance must be  $|d_0|/\sigma_{d_0} < 5$ .

- **Muons:** The muon candidates are required to satisfy the `Medium` cut-based identification and the `Gradient` isolation criteria, both defined in Section 4.3. They must have  $p_T > 27.5$  GeV,  $|\eta| < 2.5$ ,  $|z_0| < 0.5$  mm, and  $|d_0|/\sigma_{d_0} < 3$ .
- **Jets:** Jets are required to have  $p_T > 25$  GeV and  $|\eta| < 2.5$ . The jets from pile-up are suppressed by using a multivariate jet-track association algorithm called Jet Vertex Tagger (JVT). The jets with  $p_T < 60$  GeV and  $|\eta| < 2.4$  are required to have  $|\text{JVT}| > 0.59$ .
- **Photons:** The photon candidates must pass the `Tight` identification and the `FixedCutTight` isolation criteria, both defined in Section 4.5. They are required to have  $p_T > 20$  GeV and  $|\eta_{\text{cl}}| < 2.37$ , excluding the transition region.
- **Objects overlap removal:** First, the electrons that share a track with a muon are removed. Then, all jets within a cone of  $\Delta R = 0.2$  around an electron are removed. After that the electrons that have a distance of  $\Delta R < 0.4$  from the remaining jets are removed. The jet-muon overlap removal is performed afterwards, where the jet is removed if it is closer than  $\Delta R = 0.2$  from a muon and has no more than two associated tracks, or the muon is removed if it is closer than  $\Delta R = 0.4$  from a jet that has more than two associated tracks. Next, photons within a cone of  $\Delta R = 0.4$  from remaining electrons or muons are removed. Finally, the jets closer than  $\Delta R = 0.4$  from the remaining photons are removed.

### 8.1.2 Selection at Event-level

Based on the object definitions in Section 8.1.1, events are selected as following:

- The selected events must have fired one of the single-lepton triggers listed in Table 8.1, based on the year in which the data is collected (2015 or 2016). Whether the electron trigger or the muon trigger is fired determines if the event is categorised in  $e+\text{jets}$  channel or in  $\mu+\text{jets}$  channel.
- Events are required to have a primary vertex with at least two associated tracks with  $p_T > 400$  MeV. If more than one such vertex in the event is found, the vertex with the largest sum of track  $p_T^2$  is considered as the primary vertex.
- Events in  $e+\text{jets}$  ( $\mu+\text{jets}$ ) channel must contain exactly one electron (muon), and no muon (electron), where the electron (muon) is required to match the lepton that has triggered the event.
- Events are required to have at least four jets.
- At least one of the jets must be tagged as a  $b$ -jet. The  $b$ -tagging working point that is used corresponds to 77% efficiency for jets with  $p_T > 20$  GeV and  $|\eta| < 2.5$  in MC simulated  $t\bar{t}$  events.
- The selected event is required to have exactly one photon.
- In the  $e+\text{jets}$  channel, events are rejected if the invariant mass of the photon and the electron ( $m_{e\gamma}$ ) is not outside of a 5 GeV window around the  $Z$  boson mass ( $m_Z$ ).

<sup>2</sup> The isolation requirement at the trigger level is looser than at the offline level.

Channel	Year	Trigger name	Trigger description
$e+jets$	2015	HLT_e24_lhmedium_L1EM20VH or HLT_e60_lhmedium or HLT_e120_lhloose	At least one isolated <sup>2</sup> electron with $p_T > 24$ GeV or At least one electron with $p_T > 60$ GeV independent of isolation or At least one electron with $p_T > 120$ GeV independent of isolation
		HLT_e26_lhtight_nod0_ivarloose or HLT_e60_lhmedium_nod0	At least one isolated <sup>2</sup> electron with $p_T > 26$ GeV or At least one electron with $p_T > 60$ GeV independent of isolation or
		HLT_e140_lhloose_nod0	At least one electron with $p_T > 140$ GeV independent of isolation
	2016	HLT_mu20_iloose_L1MU15 or HLT_mu50	At least one isolated <sup>2</sup> muon with $p_T > 20$ GeV or At least one muon with $p_T > 50$ GeV independent of isolation
		HLT_mu26_ivarmedium or HLT_mu50	At least one isolated <sup>2</sup> muon with $p_T > 26$ GeV or At least one muon with $p_T > 50$ GeV independent of isolation

Table 8.1: The single-lepton triggers used in the event selections for the 13 TeV Analysis.

- To suppress photons radiated from leptons, the angular distance between the photon and the lepton  $\Delta R(\gamma, \text{lepton})$  is required to be greater than 1.0.

A total number of 6002 events in data pass the signal selection in  $e+jets$  channel and 5660 in the  $\mu+jets$  channel.

## 8.2 Analysis Strategy

### 8.2.1 Neural Networks

In this analysis the signal is discriminated from backgrounds using a NN algorithm, called the Event-level discriminator (ELD). The ELD is used in the likelihood fit to data to extract the inclusive fiducial cross section. Also, a dedicated object-level NN algorithm called the Prompt-photon tagger (PPT) is trained to discriminate between prompt photons and hadronic-fake photons. The PPT is used as one of the inputs of the ELD. Both NN's are binary classifiers, trained by using Keras [125] and evaluated by using LWTNN [126].

#### 8.2.1.1 Prompt-Photon Tagger

In the 8 TeV analysis, the hadronic-fake background contribution was significant, also its corresponding systematic uncertainty turned out as one of the highest ranked uncertainties of the result (see Section 7.6). This was the motivation to take advantage of multivariate analysis methods, namely a NN, to discriminate between the prompt and hadronic-fake photons.

The PPT is trained using six of the photon discriminating variables, introduced in Section 4.5, as the input variables:  $R_{\text{had}}$ ,  $R_\eta$ ,  $R_\phi$ ,  $w_{\eta 2}$ ,  $w_{s3}$ ,  $f_{\text{side}}$ . The variable definitions can be found in Table 4.1. The input variables are chosen based on their separation power between prompt and hadronic-fake photons in MC simulated events. The separation power is quantified by:

$$\mathcal{S} = \frac{1}{2} \sum_{i \in \text{bins}} \frac{(s_i - b_i)^2}{s_i + b_i}, \quad (8.1)$$

where  $s_i$  and  $b_i$  are the number of signal and background events in bin  $i$  of the input variable distribution, respectively.

Two MC simulated samples, one for the signal and one for the background photons, are used for the training and testing of the PPT. For the prompt photons (signal), the simulated QCD-Compton processes are used, and the hadronic-fake photons (background) are taken from the simulated di-jet events. The photon candidates used for the training are required to pass the Tight identification criteria, have  $p_T > 25$  GeV and  $|\eta_{\text{cl}}| < 2.37$ , excluding the EMCal transition region<sup>3</sup>.

In order to correct the PPT mis-modelling in MC simulation, dedicated PPT scale factors for prompt photons are extracted, by comparing the PPT distribution shape of the prompt photons in data and MC in a  $Z \rightarrow ll\gamma$  ( $l = e, \mu$ ) control region. The control region is defined by requiring one photon and two opposite sign leptons with an invariant mass of  $60 < m_{ll} < 100$  GeV. The scale factors are derived in 2-dimentional bins of photon  $p_T\eta$ , and applied to the PPT shape of the prompt photons in simulation. The PPT uncertainties are discussed in Section 8.5.2.

### 8.2.1.2 Event-Level Discriminator

The training and testing of the ELD is carried out using the simulated  $t\bar{t}\gamma$  signal and background events which pass the signal region selection of Section 8.1. The only exception is for the fake-lepton background, where its data-driven estimation described in Section 8.4.2 is used. The MC simulated samples that are used are described in Sections 5.2.1 and 5.2.2.

Fifteen input variables are used for the ELD training. They are listed in Table 8.2 in the order of their separation power according to Equation 8.1. The input variables are chosen based on their separation power as well as the physics motivation. The  $b$ -tagging related variables are important in the ELD training because of their significant discrimination against the backgrounds without any heavy-flavour jets. Using PPT as an input improves the discrimination power of the ELD against the hadronic-fake background, because this background is dominated by the  $t\bar{t}$  process which has kinematic properties and jet flavour compositions similar to the signal.<sup>4</sup>

---

<sup>3</sup> In the development of PPT, the initial goal was to keep it an analysis-independent tool so that more ATLAS analyses can benefit from it. Therefore, no isolation requirement is applied on the photons, as different analyses use different isolation requirements. Also, the MC samples that are used for signal and background are the samples provide by the ATLAS photon identification group, where a  $p_T > 25$  GeV requirement for the photons is already placed in the n-tuple production level.

<sup>4</sup> Photon  $p_T$  and  $\eta$ , as well as  $\Delta R(\gamma, \text{lepton})$  and  $\Delta R(\gamma, \text{jet})$ , are not used in the ELD training as they were being considered as the observables for the differential cross-section measurement, and the initial plan of using maximum-likelihood fit with ELD as the discriminator variable to extract the differential cross sections would have introduced a bias. Note that the ELD was trained when the differential cross-section measurement strategy was not finalised, the final strategy that is actually followed is explained in Section 8.2.4.

Variable	Description
$b_1(j)$	highest $b$ -tagging score of all jets
$b_2(j)$	second highest $b$ -tagging score of all jets
$b_3(j)$	third highest $b$ -tagging score of all jets
$N_{b\text{-jets}}$	$b$ -jet multiplicity
PPT	Prompt-photon tagger output
$p_T(j_1)$	$p_T$ of the leading jet (ordered in $p_T$ )
$H_T$	Scalar sum of the $p_T$ of the lepton and jets
$p_T(j_2)$	$p_T$ of the sub-leading jet
$p_T(j_3)$	$p_T$ of the third jet
$p_T(j_4)$	$p_T$ of the fourth jet
$p_T(j_5)$	$p_T$ of the fifth jet (For events without the fifth jet, this is set to zero)
$m_T^W$	Reconstructed transverse mass of the leptonically decaying $W$ -boson
$E_T^{\text{miss}}$	Missing transverse energy
$N_{\text{jets}}$	Jet multiplicity
$m_{e\gamma}$	Invariant mass of the photon and the electron

Table 8.2: Input variables of the ELD, in the ranking order of their separation power between signal and sum of all backgrounds, calculated by Equation 8.1.

### 8.2.2 Definition of the Fiducial Region

The fiducial region is defined at particle level in a way that mimics the selections at reconstruction level, given in Section 8.1.

Leptons and jets are defined exactly the same as in the 8 TeV analysis, described in Section 7.2.2. The photon definition is also the same as Section 7.2.2 but the  $p_T$  threshold requirement is increased to 20 GeV. In addition, photons are required to be isolated. This is done by requiring the ratio of the scalar sum of  $p_T$  of all stable charged particles around the photon to the  $p_T$  of photon to be smaller than 0.1. For the  $b$ -jets, a ghost-association method (defined in Section 7.5.2.1) is used to determine the flavour of the jets. The object overlap removal is simplified to only removing the jets within a  $\Delta R < 0.4$  distance from a selected muon, electron or photon.

Based on the above object definitions, events are required to have exactly one electron or muon, at least four jets from which at least one is  $b$ -tagged, and exactly one photon. The  $\Delta R$  distance between the photon and the lepton must be larger than 1.0.

### 8.2.3 Strategy of Inclusive Cross-Section Measurement

The inclusive  $t\bar{t}\gamma$  cross section at 13 TeV is measured in the fiducial volume defined in Section 8.2.2, by performing a maximum-likelihood fit to the ELD distribution, and profiling the nuisance parameters. Using Equations 6.21 and 6.22, the likelihood function is written as:

$$\mathcal{L}(\text{ELD} | \sigma_{t\bar{t}\gamma, \text{sl}}^{fid}, \boldsymbol{\theta}) = \prod_i P(N_i^{\text{obs}} | N_i^s(\boldsymbol{\theta}) + \sum_b N_i^b(\boldsymbol{\theta})) \times \prod_t G(0 | \theta_t, 1), \quad (8.2)$$

where  $i$  is the bin index of ELD distribution. The rest of the parameters and terms in Equation 8.2 are already introduced in Chapter 6.

The free parameters in the fit are the number of  $t\bar{t}\gamma$  signal events and the number of  $W\gamma$  background

events. The normalisation of the rest of the backgrounds are fixed to their estimated values, described in Sections 8.3 and 8.4, being varied within their uncertainties.

To extract the cross section for the combined single-lepton channel, spontaneous fitting to the ELD distributions of the individual  $e+\text{jets}$  and  $\mu+\text{jets}$  channels are performed, where the two channels share the same signal strength (Equation 6.25) that scales the cross section of each of the two channels coherently.

### 8.2.4 Strategy of Differential Cross-Section Measurement

The differential cross sections at 13 TeV is measured as a function of photon  $p_{\text{T}}$ , photon  $\eta$ , and  $\Delta R(\gamma, \text{lepton})$ , in the same fiducial region defined in Section 8.2.2.

First, using Equation 6.13 (with  $l = \text{sl}$ , for the single-lepton channel), the photon  $p_{\text{T}}$ , photon  $\eta$ , and  $\Delta R(\gamma, \text{lepton})$  distributions of the observed signal at reconstruction level are unfolded to the particle level. These reconstruction-level distributions are obtained by subtracting the background distributions from the data distributions, where the normalisation and uncertainties of the  $W\gamma$  background are taken from a maximum-likelihood fit performed by the likelihood function in Equation 8.2 but without systematic uncertainties included.

The signal efficiency ( $\epsilon_k$ ), migration matrix ( $M_{kj}$ ), and outside migration fraction ( $f_{\text{out},j}$ ) are calculated from the signal MC sample. The signal efficiency is calculated as the fraction of events falling into bin  $k$  of the observable in fiducial region that are also selected in reconstruction level and the reconstructed object which defines the observable to be unfolded<sup>5</sup> matches to a true object at particle level within  $\Delta R < 0.1$ . The migration matrix is calculated from events that pass both the fiducial region definition and the reconstruction-level selections and the object matching condition as above. The matrix maps the binned particle-level events to the binned reconstruction-level events. The outside migration fraction is calculated as the fraction of events generated outside of the fiducial region but pass the reconstruction-level selections and fall into bin  $j$  of the observable in reconstruction level, or fail the above object matching condition.

As mentioned in Section 6.3, the iterative Bayesian unfolding method is used. This method proceeds iteratively, computing at each iteration a new estimate of the unfolded distribution of the observable, from the distribution obtained in the previous iteration. The prior information in the first iteration corresponds to the truth distribution (at particle level) from the signal simulation.

The reported results of this analysis are in the form of normalised differential cross section, defined as:

$$\sigma_{t\bar{t}\gamma,k,\text{norm}}^{\text{fid}} = \frac{\sigma_{t\bar{t}\gamma,k}^{\text{fid}}}{\sum_k \sigma_{t\bar{t}\gamma,k}^{\text{fid}}}, \quad (8.3)$$

where  $\sigma_{t\bar{t}\gamma,k}^{\text{fid}}$  is expressed by Equation 6.14 (with  $l = \text{sl}$  for the single-lepton channel), and same as before,  $k$  is the index bin of the observable at particle level. Because of the normalisation, the systematic uncertainties that are correlated across all bins cancel out.

The binning of each observable is optimised based on the detector resolution and the expected statistical uncertainty. More specifically, the bin sizes are chosen to be at least twice of the observable resolution (i.e. more than 68% of the events to be on the diagonal in the migration matrix), and the statistical uncertainty of the observed signal in each bin should not be more than 10%. In cases where after performing the unfolding the statistical uncertainty of a bin got larger, a re-binning has been performed.

---

<sup>5</sup> Photon for the case of unfolding photon  $p_{\text{T}}$  or photon  $\eta$ , photon and electron or muon for unfolding  $\Delta R(\gamma, \text{lepton})$

There are nine bins for photon  $p_T$ :

$$20 \leq p_T < 35, 35 \leq p_T < 50, 50 \leq p_T < 65, 65 \leq p_T < 80, 80 \leq p_T < 95, \\ 95 \leq p_T < 110, 110 \leq p_T < 140, 140 \leq p_T < 180, 180 \leq p_T < 300 \text{ [GeV]},$$

eight bins of photon  $\eta$ :

$$|\eta| < 0.2, 0.2 \leq |\eta| < 0.4, 0.4 \leq |\eta| < 0.6, 0.6 \leq |\eta| < 0.8, \\ 0.8 \leq |\eta| < 1.0, 1.0 \leq |\eta| < 1.2, 1.2 \leq |\eta| < 1.7, 1.7 \leq |\eta| < 2.37,$$

and nine bins for  $\Delta R(\gamma, \text{lepton})$ :

$$1.0 \leq \Delta R < 1.2, 1.2 \leq \Delta R < 1.4, 1.4 \leq \Delta R < 1.6, 1.6 \leq \Delta R < 1.8, \\ 1.8 \leq \Delta R < 2.0, 2.0 \leq \Delta R < 2.2, 2.2 \leq \Delta R < 2.4, 2.4 \leq \Delta R < 2.6, 2.6 \leq \Delta R < 6.0,$$

### 8.2.5 Theoretical Prediction

The measured cross sections at 13 TeV are compared with the theoretical predictions at NLO accuracy in QCD, by normalising the  $t\bar{t}\gamma$  signal MC sample generated by **MADGRAPH** at LO with the NLO  $k$ -factors. The authors of Ref. [107] performed a dedicated theory calculation at 13 TeV, with the same techniques in the referenced document. In the theory calculations, the renormalisation and factorisation scales are chosen to be  $\mu_R = \mu_F = m_{\text{top}}$ , while all the rest of parameters are set to the same values used in the **MADGRAPH**  $t\bar{t}\gamma$  signal sample production, described in Section 5.2.1.

In this analysis the  $k$ -factor is estimated in a phase space that is very close to the fiducial region defined in Section 8.2.3. This is done in order to achieve a better data-MC agreement, since a phase-space dependency in  $k$ -factor has been observed. In comparison, the  $k$ -factor used in the 8 TeV analysis is estimated in a more inclusive phase space.

The theory calculation at NLO is performed at the parton level, while the LO cross-sections are obtained from the LO **MADGRAPH** signal sample at the particle level. The NLO and LO calculations are performed in the same phase space, which as mentioned is very close to the fiducial region. Special attention is given to define the objects at particle level in the **MADGRAPH** sample to mimic the parton level objects used in the NLO calculation, so the objects kinematic properties properly correspond.

The extracted overall  $k$ -factor is 1.30 for the single-lepton channel [9]. While its statistical uncertainties are negligible, the relative systematic uncertainty is 20%. The systematic uncertainty has contributions from the following sources: For the NLO calculation the QCD scale and PDF choices introduce 14% uncertainty (with the effect of scale choices being dominant). For the LO **MADGRAPH** cross section the jet cone size is varied from the nominal size of 0.4 to 0.3 and 0.5, to evaluate the additional QCD radiation impact on the particle-level jets, resulting in 11% uncertainty, also the non-perturbative effects in the parton shower modelling are evaluated by separately turning off the multiple parton interaction and hadronisation of **PYTHIA**, resulting to 8% uncertainty.

Using this  $k$ -factor, the predicted inclusive cross section at NLO in the fiducial region is  $495 \pm 99$  fb [9]. The same overall  $k$ -factor is also used to obtain the differential cross section predictions.

## 8.3 Estimation of Hadronic-fake Background

The background contribution from hadronic-fake photons is largely reduced in the 13 TeV analysis with respect to the 8 TeV analysis, because of applying the photon isolation requirement, but it is still one of the main backgrounds.

The normalisation of this background in the likelihood fit is fixed to its estimated data-driven value (within its uncertainties). Its ELD shape - which is initially taken from MC simulation - is as well corrected by data-driven scale factors. First, the so-called *ABCD method* is used to estimate the hadronic-fake background from data, as a function of photon conversion status<sup>6</sup>,  $p_T$ , and  $\eta$ . Then, the ratio of the data-driven estimate to the MC-predicted background is calculated, in 3-dimensional bins of photon  $p_T$ - $\eta$ -conversion status. These ratios are used as scale factors to correct the MC-simulated hadronic-fake background.

### 8.3.1 The ABCD Method

In the ABCD method, the number of events in the sidebands<sup>7</sup> of a two-dimensional distribution of uncorrelated variables are used to estimate the background yield in the signal region. Here, the two dimensions are defined by the photon identification and photon isolation. Four orthogonal regions, A, B, C and D, are defined in data as explained below:

- Photon candidates in region D satisfy the nominal isolation and identification criteria, i.e. pass the `FixedCutTight` isolation working point and the `Tight` identification menu, both described in Section 4.5.
- In region C, photon candidates are non-isolated but satisfy the `Tight` identification criteria. The non-isolated photons are defined by requiring them to fail the `FixedCutTight` working point and in addition their tracking-based isolation  $p_T^{\text{cone}20}$  must be larger than 3 GeV.
- Photon candidates in region B are required to be non-isolated and also fail the `Tight` identification criteria. Instead, they are required to pass an orthogonal identification criteria which will be called `fail-Tight` hereafter. The `fail-Tight` photons must pass all the `Tight` identification criteria except the ones on the four narrow stripe shower-shape variables  $f_{\text{side}}$ ,  $w_{s3}$ ,  $\Delta E$  and  $E_{\text{ratio}}$  (see Table 4.1): at least two of these four selection requirements must fail.
- Photon candidates in region A are isolated but required to pass the `fail-Tight` identification.

Figure 8.1 summarises the above bullet points. The four regions only differ in photon identification and isolation requirements, the rest of their object- and event-level selections remain the same as for the signal region, described in Sections 8.1. Therefore, region D is identical to the signal region, while regions A, B, and C are enriched by hadronic-fake photons.

The `fail-Tight` identification makes use of the same four shower-shape variables for reversing the `Tight` requirements that were used in a similar way in the 8 TeV analysis in order to select hadronic-fake candidates in data, as described in Section 7.3.2.1. As explained there, these variables have strong discriminating power between hadronic-fake and prompt photons but their correlation with the photon isolation is smaller than any other photon discriminating variables. The more of the four requirements

<sup>6</sup> i.e. whether photon is unconverted or converted.

<sup>7</sup> In high energy physics, sideband refers to a relatively clean background sample which shares most of the properties of the signal events. In one dimension of the phase space, the sideband events lie just next to where the signal events are, for example just outside the expected signal particle mass peak. [127]

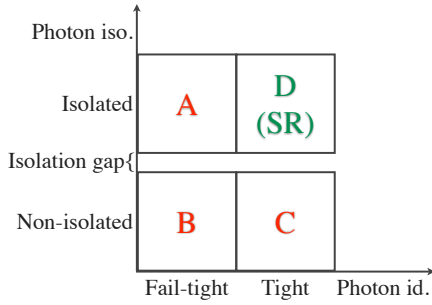


Figure 8.1: An illustration of the ABCD method to estimate the hadronic-fake background, using four categories of photons based on their identification (id.) and isolation (iso.). The *isolation gap* indicates the  $p_T^{\text{cone}20} > 3 \text{ GeV}$  requirement.

that fail, the more purified control regions one can get, as can be seen in Figure 8.2. The choice on the number of requirements to fail (i.e. at least two) is based on a compromise between reducing the prompt photon contamination while keeping large enough number of data events<sup>8</sup> and also avoiding to introduce photon isolation-identification correlation. The extra selection requirement of  $p_T^{\text{cone}20} > 3 \text{ GeV}$  for the non-isolated photons is also applied in order to reduce the contamination from prompt photons. The adequacy of this requirement, which causes a *gap* between isolated and non isolated regions, can be seen from Figure 8.3.

An important consideration in the optimisation of the fail-Tight and non-isolated photon criteria is that tightening them might introduce, or increase, a photon identification-isolation correlation throughout the hadronic-fake backgrounds in the four regions, which eventually prevents one from using the ABCD method. This is due to the small residual correlation of the four narrow stripe shower-shape variables with the photon isolation. During the optimisation procedure, the possible correlation is quantified by MC-based ratios  $N_{D,\text{MC}}^{\text{h-fake}}/N_{C,\text{MC}}^{\text{h-fake}}$  and  $N_{A,\text{MC}}^{\text{h-fake}}/N_{B,\text{MC}}^{\text{h-fake}}$ . The two ratios are checked to be as less deviated from each other as possible, within their statistical uncertainties, while keeping the prompt photon contamination under control.

If one could assume that there is no correlation between photon identification and its isolation, the ratio between the number of hadronic-fake background events with isolated photons to those with non-isolated photons should be the same in the Tight and fail-Tight regions<sup>9</sup>. In other words, under this assumption the following relation holds:

$$\frac{N_A^{\text{h-fake}}}{N_B^{\text{h-fake}}} = \frac{N_D^{\text{h-fake}}}{N_C^{\text{h-fake}}}. \quad (8.4)$$

This can be used to estimate the hadronic-fake background contribution in the signal region (region D) from data:

$$N_{\text{est.}}^{\text{h-fake}} = \frac{N_{A,\text{data}}^{\text{h-fake}} \times N_{C,\text{data}}^{\text{h-fake}}}{N_{B,\text{data}}^{\text{h-fake}}}, \quad (8.5)$$

where  $N_{i,\text{data}}^{\text{h-fake}}$  ( $i \in A, B, C$ ) is the number of hadronic-fake background events in regions A, B and C in

<sup>8</sup> For performing the ABCD method, having large enough statistics in the four regions is essential. Here, another goal was also pursued: with the available statistics it was possible to estimate the background in bins of photon  $p_T$ ,  $\eta$  and conversion-type.

<sup>9</sup> It should also be true if we formulate it the other way around: the ratio between the number of background events with Tight photons to those with fail-Tight photons should be the same in the isolated and non-isolated regions

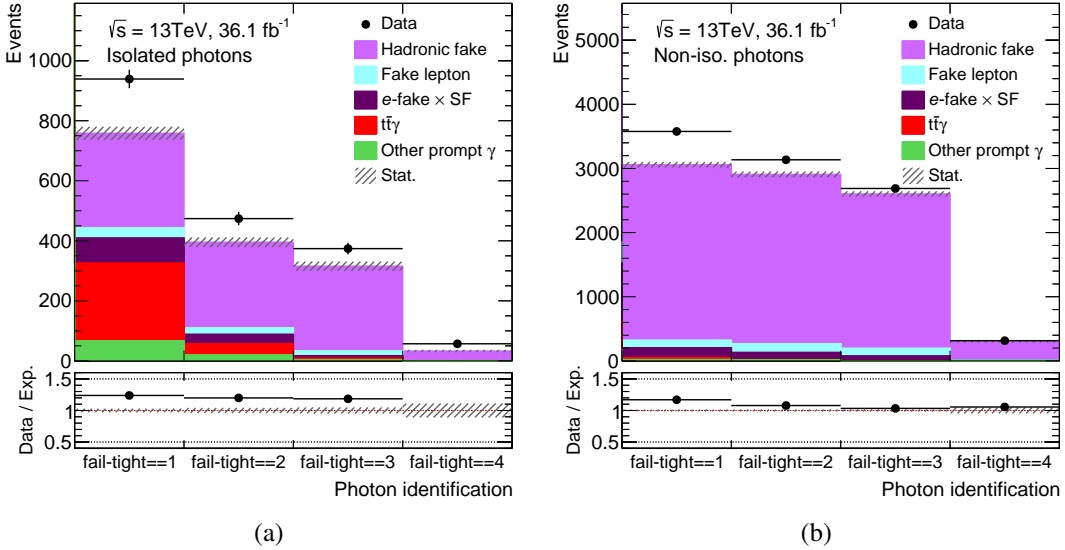


Figure 8.2: (a) Isolated and (b) non-isolated photons passing the fail-Tight identification when exactly one, two, three or all of the four requirements on the narrow stripe shower-shapes are required to fail. The three last bins in (a) form the control region A and the three last bin in (b) form the control region B. Only the statistical uncertainties are shown.

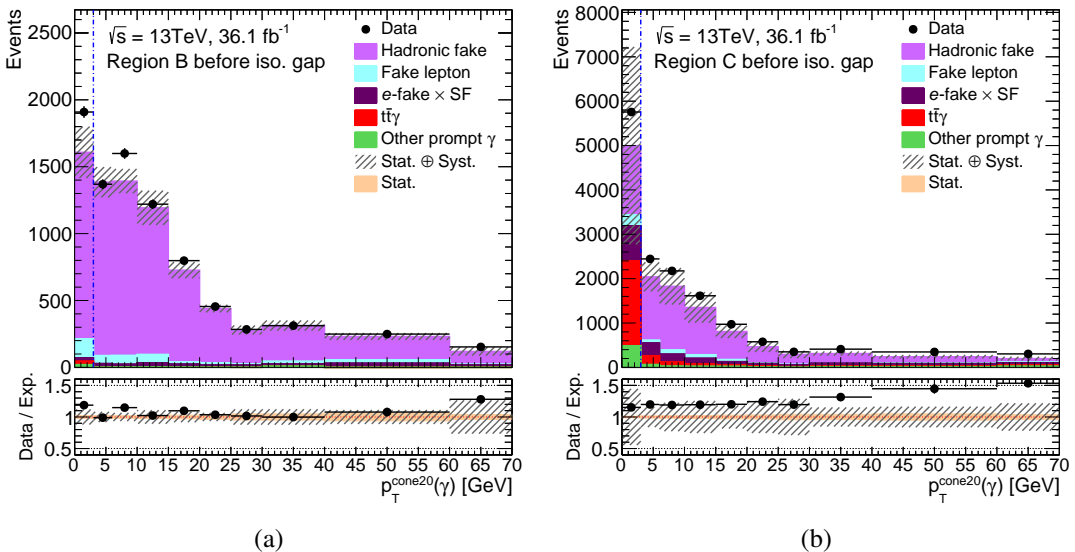


Figure 8.3: Photon  $p_T^{\text{cone}20}$  distributions before adding isolation gap, i.e. the  $p_T^{\text{cone}20} > 3$  GeV requirement, in (a) region B and (b) region C. The right side of the vertical dashed line in figure (a) is the final region B and in figure (b) the final region C.

data. Thus, any contamination from prompt photons or fakes of a different type needs to be subtracted from data, in order to use Equation 8.5. In addition, the contribution from events with fake leptons must be subtracted, because as described later in Section 8.4.2, the fake lepton background is estimated from data without distinguishing between prompt and hadronic-fake photons (unlike in the 8 TeV analysis). This means that  $N_{\text{est}}^{\text{h-fake}}$  in Equation 8.5 has to be the estimated number of hadronic-fake background events with real leptons, otherwise a double counting of backgrounds occurs.

The contamination from events with prompt photons are subtracted using MC. For the  $t\bar{t}\gamma$  contribution, a 100% systematic uncertainty is considered and for the rest (denoted by "other prompt  $\gamma$ ", composed of  $W\gamma$ ,  $Z\gamma$ , single-top+ $\gamma$  and diboson+ $\gamma$ ) 50%. These uncertainties are conservatively chosen because there are no scale factors for correcting the photon identification and isolation efficiencies in MC for the case of fail-Tight photons and photons with reversed isolation criteria.

The contamination from events with electron-fake photons is subtracted using MC that is scaled by the data-driven scale factor  $SF^{e\text{-fake}}$  which is later described in Section 8.4.1. The considered uncertainty for this is a conservative 50%, due to the fact that the fake rates that are used in the electron-fake background estimation are derived from Tight and isolated photons.

The fake lepton contribution is subtracted using the data-driven background estimation explained later in Section 8.4.2. Its assigned uncertainty is estimated the same way as described in the same Section.

Therefore:

$$N_{i,\text{data}}^{\text{h-fake}} = N_{i,\text{data}} - N_{i,\text{MC}}^{t\bar{t}\gamma} - N_{i,\text{MC}}^{\text{other prompt } \gamma} - SF^{e\text{-fake}} \times N_{i,\text{MC}}^{e\text{-fake}} - N_{i,\text{d.d.}}^{\text{fake-lepton}}, \quad (8.6)$$

where  $i \in A, B, C$ .

Before performing the background estimation using the ABCD method, first several distributions in the control regions are checked to gain confidence on the well description of the non-hadronic-fake events in these regions, in order to use Equation 8.6. This is presented in Section 8.3.1.1 and Appendix B.1.2. Also, any possible photon isolation-identification correlation must be taken into account, as discussed in Section 8.3.2. Furthermore, the origin of the hadronic-fake photons in the regions A, B, C and D are studied and presented in Appendix B.1.1.

### 8.3.1.1 Control Plots and Event Yields

A selection of distributions comparing data to predictions for regions A, B and C for the combined single-lepton channel are shown in Figures 8.4, 8.5 and 8.6, respectively. More plots can be found in Appendix B.1.2.

In all these plots, as well as in Figures 8.2 and 8.3, the MC samples used for the hadronic-fake and electron-fake contributions are  $t\bar{t}$ ,  $W$ +jets,  $Z$ +jets, single top, and diboson samples, while the "other prompt  $\gamma$ " is composed of  $W\gamma$ ,  $Z\gamma$ , single top, and diboson samples. The event overlap removal between the samples, as explained in Section 5.2.3, is applied. The electron-fake contribution is scaled by the data-driven electron-fake scale factor ( $SF^{e\text{-fake}}$ ) described in Section 8.4.1. The fake lepton contribution is estimated from data as described in Section 8.4.2. The dominating systematic uncertainties are included in the plots, which are the  $t\bar{t}$  MC modelling uncertainties (more description in Section 8.3.2.1) and the systematic uncertainties assigned for the non-hadronic-fake contributions as described in Section 8.3.1.

A data-MC agreement is not specifically expected in the plots. The assumption is that the modelling of hadronic-fake photons in MC samples is not accurate (this was discussed before in Section 7.3.2), hence the hadronic-fake background is estimated from data, and the data-driven estimation is used to correct the MC predictions via 3D-binned scale factors.

The event yields in regions A, B and C are summarised in Table 8.3. It can be seen that the contaminations from prompt photons are under 7%, and from electron-fake photons under 10%. The contribution of events with fake leptons is under 5%.

Number of events	Region A	Region B	Region C
Data	934	6439	9196
Hadronic-fake	622.61	5582.10	5592.24
$t\bar{t}\gamma$	44.29	8.82	486.41
Other prompt $\gamma$	25.26	15.56	199.53
Electron-fake $\times$ SF <sup>e-fake</sup>	40.82	192.54	919.53
Fake lepton	43.05	279.82	344.50

Table 8.3: Event yields in regions A, B and C.

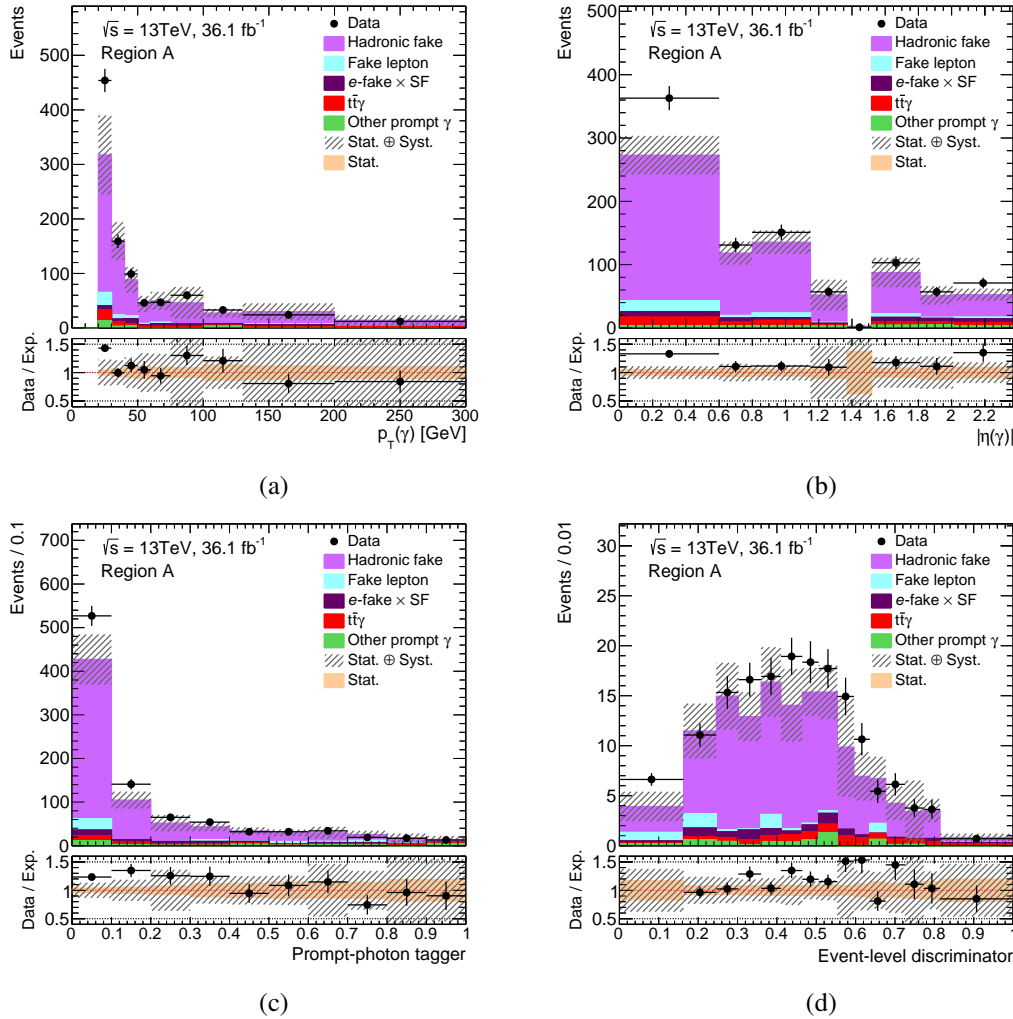


Figure 8.4: Plots of region A in single-lepton channel, where photons are isolated and identified as fail-Tight. In each plot, the dashed area shows the total uncertainty of the total expectation while the solid band in the ratio panel shows the statistical uncertainty of the total expectation.

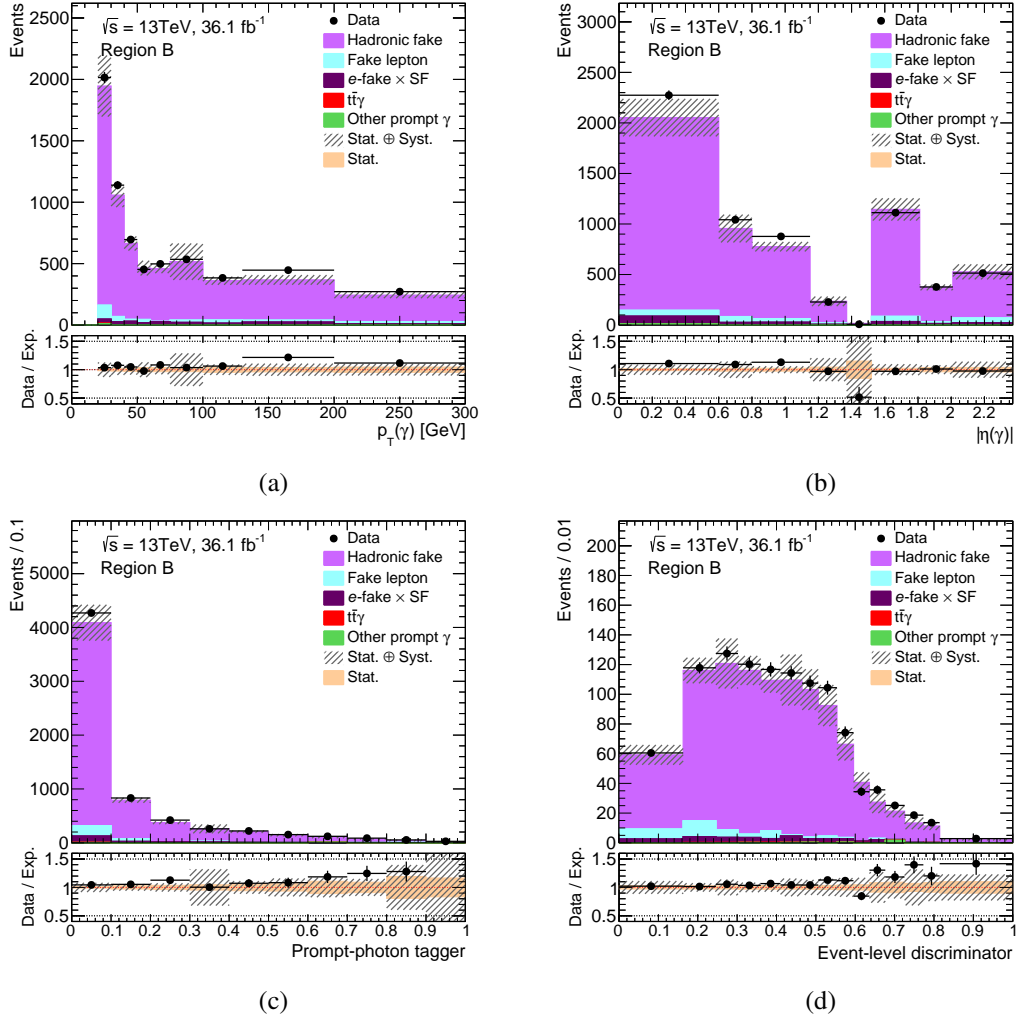


Figure 8.5: Plots of region B in single-lepton channel, where photons are identified as fail-Tight as well being non-isolated. In each plot, the dashed area shows the total uncertainty of the total expectation while the solid band in the ratio panel shows the statistical uncertainty of the total expectation.

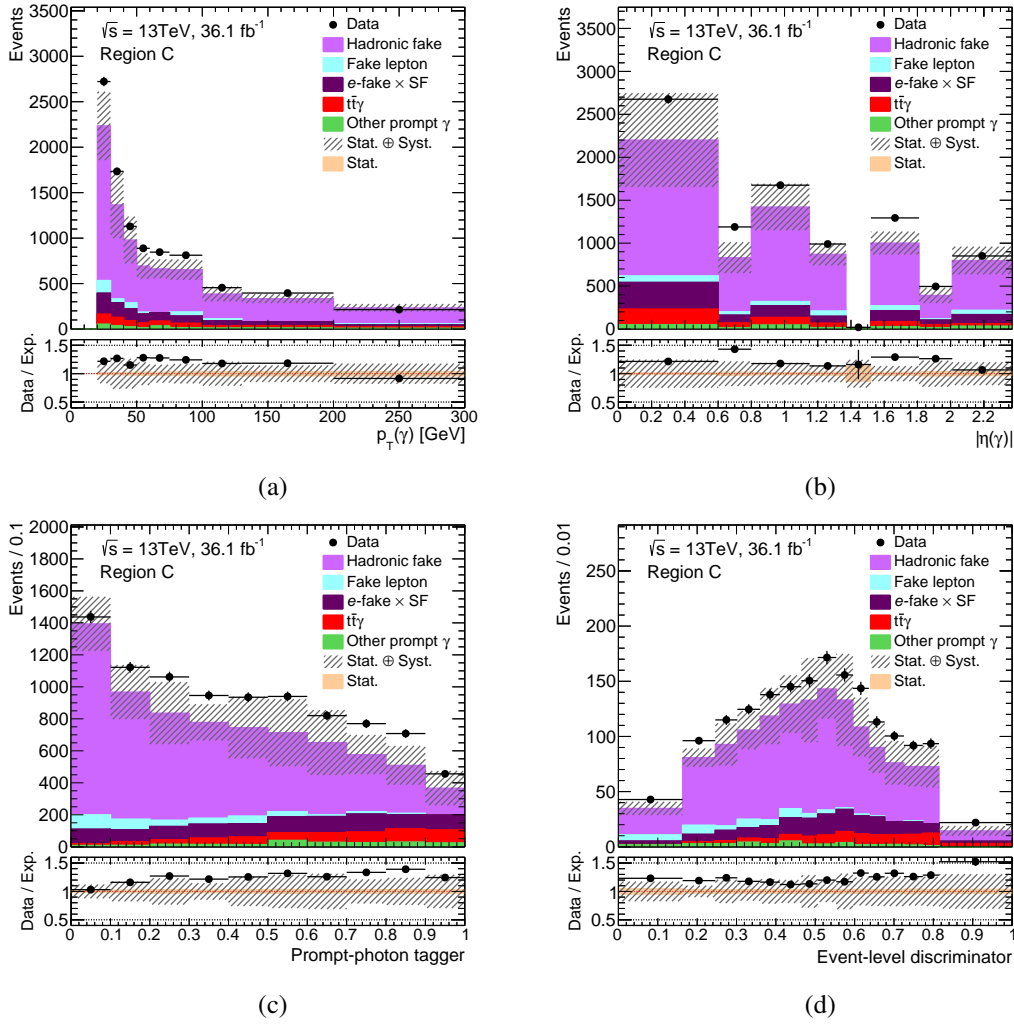


Figure 8.6: Plots of region C in single-lepton channel, where photons are non-isolated and identified as Tight. In each plot, the dashed area shows the total uncertainty of the total expectation while the solid band in the ratio panel shows the statistical uncertainty of the total expectation.

### 8.3.2 Treatment of the Photon Isolation–Identification Correlation

The ABCD method is based on the assumption of no correlation between the two variables which define the two dimensional sidebands, in the background events that are being measured. As a result of a deviation from this assumption, a relation as the one in Equation 8.4 does not hold and Equation 8.5 can not be used as it is.

Although the photon isolation and identification criteria used here are chosen to minimise such correlation, any possible residual correlation between them in the hadronic-fake background events must be measured and taken into account. In order to quantify this correlation, a MC-based method described in Sections 8.3.2.1 is used to add a correction factor to Equation 8.5 in order to take into account the photon isolation and identification correlation.

In addition, a data-driven method is performed in an attempt to avoid the MC modelling uncertainties. This study can be found in Appendix B.1.4. However, at the end the data-driven method is only used as a cross check for the benchmark MC-based method. The argument behind this choice is discussed in the same Appendix.

#### 8.3.2.1 MC-based Double Ratio

The correlation between photon identification and isolation in the hadronic-fake background can be quantified by the following double ratio derived from MC simulation:

$$\theta_{MC} = \frac{N_{D,MC}^{h\text{-fake}} / N_{C,MC}^{h\text{-fake}}}{N_{A,MC}^{h\text{-fake}} / N_{B,MC}^{h\text{-fake}}} . \quad (8.7)$$

Any deviation of  $\theta_{MC}$  from unity indicates such correlation.

The systematic uncertainties on  $\theta_{MC}$  due to the MC modelling uncertainties are evaluated. Because the simulated hadronic-fake backgrounds in all three control regions are largely dominated by the  $t\bar{t}$  process (see Appendix B.1.1), only the  $t\bar{t}$  MC modelling is taken into account:

- The uncertainty on modelling of the hard scattering, parton shower and hadronisation is estimated by replacing the nominal  $t\bar{t}$  sample produced by PowHEG and interfaced by PYTHIA, with the  $t\bar{t}$  sample produced by SHERPA.
- The uncertainty due to the QCD scale choices and the modelling of ISR and FSR is estimated by replacing the nominal  $t\bar{t}$  sample with two alternative  $t\bar{t}$  samples that are produced with different PYTHIA tunes, modified factorisation and renormalisation scales and a modified NLO radiation controlled by the  $h_{damp}$  parameter.

All the used alternative and nominal samples are fully described in Section 5.2.2. The detector related systematic uncertainties are not taken into account as they are much smaller with respect to the  $t\bar{t}$  modelling uncertainties.

Since the goal is to estimate the hadronic-fake background in bins of photon  $p_T$ - $\eta$ -conversion status, the  $\theta_{MC}$  is also measured in those same 3-dimensional bins. The results can be seen in Figures B.9 and B.8, and also summarised in Table 8.4. In most of the bins the measured  $\theta_{MC}$  is consistent with unity within the total uncertainties. But as they are subjected to large MC modelling uncertainties, a photon isolation-identification correlation can not be ignored. Therefore, the  $\theta_{MC}$  is used as a correction factor to Equation 8.5 for the estimation of hadronic-fake background:

$$N_{\text{est.}}^{\text{h-fake}} = \frac{N_{A, \text{data}}^{\text{h-fake}} \times N_{C, \text{data}}^{\text{h-fake}}}{N_{B, \text{data}}^{\text{h-fake}}} \times \theta_{\text{MC}}, \quad (8.8)$$

where  $N_{i, \text{data}}^{\text{h-fake}}$  ( $i \in A, B, C$ ) are derived from Equation 8.6.

For a comparison, the  $\theta_{\text{MC}}$  measured inclusively, as well as only as a function of photon  $p_{\text{T}}$  or photon  $\eta$  for all, converted, or unconverted photons can be seen in Appendix B.1.3.

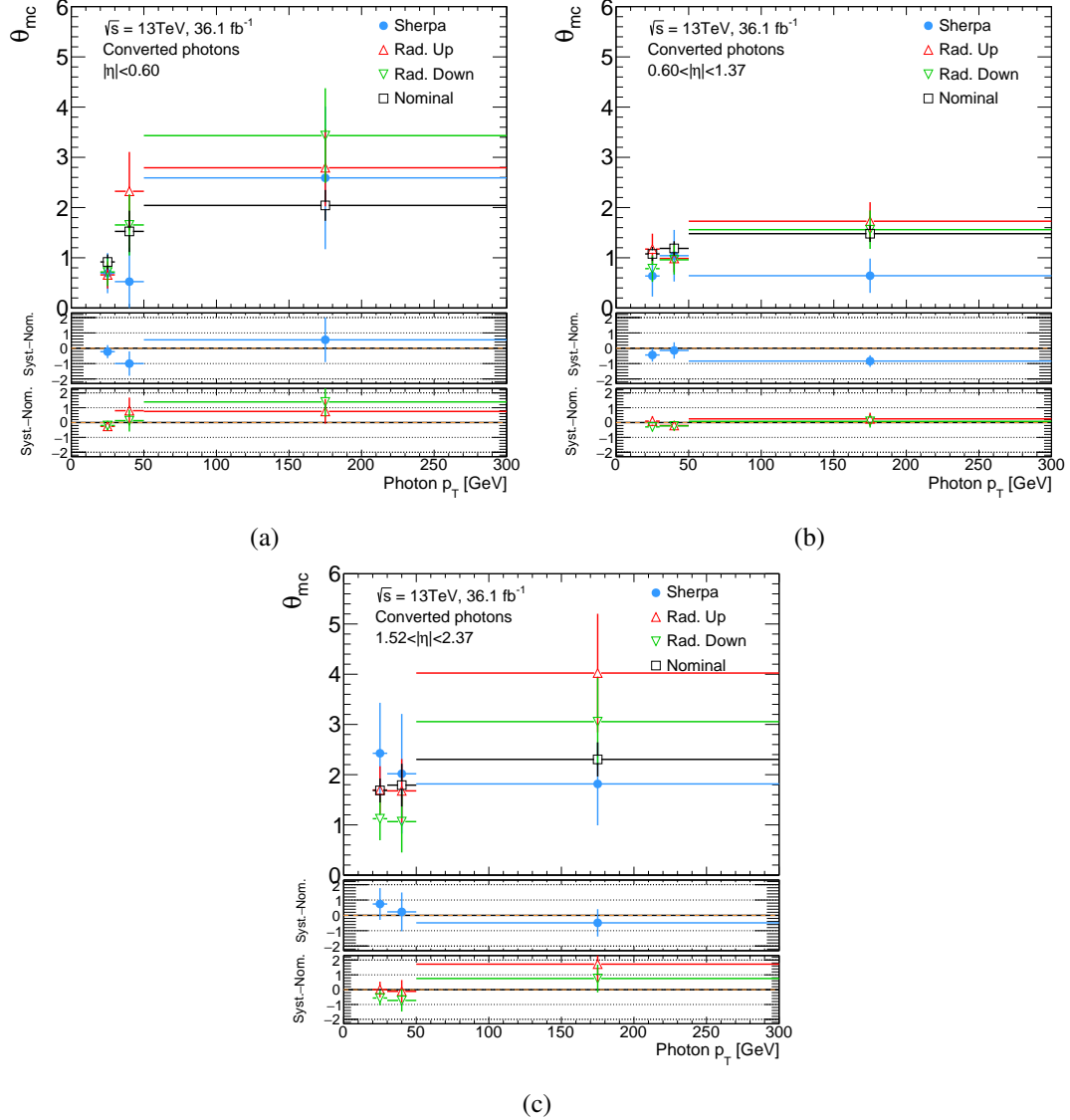


Figure 8.7: The MC-based double ratio  $\theta_{\text{MC}}$  measured in three different photon  $\eta$  slices as function of photon  $p_{\text{T}}$  for converted photons, from nominal MC and alternative MC samples that are used for systematic uncertainty evaluation. The error bars show the statistical uncertainties.

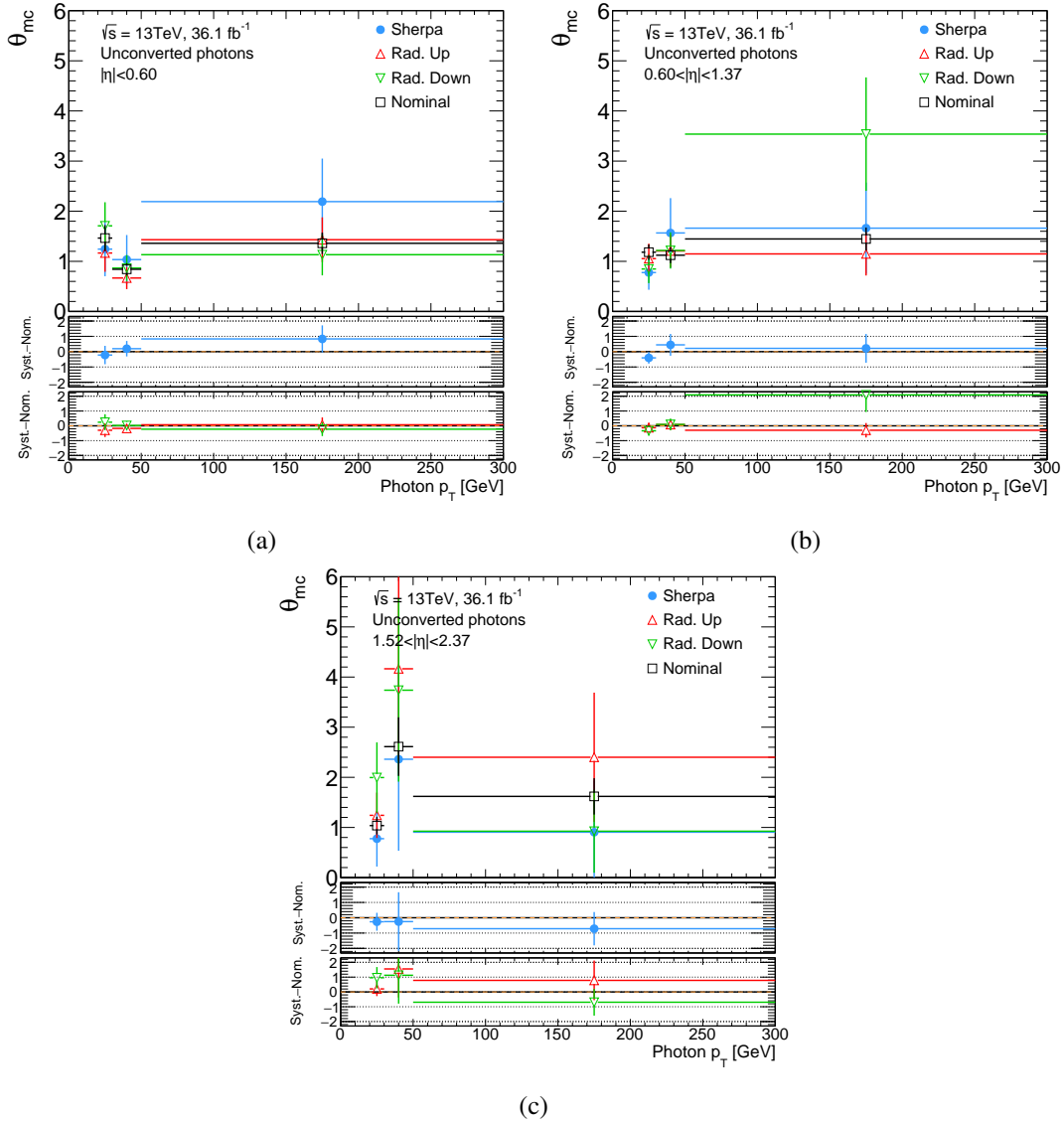


Figure 8.8: The MC-based double ratio  $\theta_{MC}$  measured in three different photon  $\eta$  slices as function of photon  $p_T$  for unconverted photons, from nominal MC and alternative MC samples that are used for systematic uncertainty evaluation. The error bars show the statistical uncertainties.

Photon conversion status	Photon $\eta - p_T$ [GeV]	$\theta_{MC} \pm$ Total uncertainty	Stat. uncertainty	Syst. uncertainty		
				rad.-up	rad.-down	Gen. & PS
Converted	$ \eta  < 0.60, p_T > 20$	$1.45 \pm 0.47$	$\pm 0.17$	$+0.25$	$-0.17$	$\pm 0.36$
	$0.60 <  \eta  < 1.37, 20 < p_T < 30$	$1.08 \pm 0.55$	$\pm 0.14$	$+0.10$	$-0.29$	$\pm 0.44$
	$0.60 <  \eta  < 1.37, p_T > 30$	$1.34 \pm 0.64$	$\pm 0.11$	$+0.00$	$-0.12$	$\pm 0.62$
	$1.52 <  \eta  < 2.37, 20 < p_T < 50$	$1.73 \pm 0.89$	$\pm 0.23$	$+0.05$	$-0.60$	$\pm 0.61$
	$1.52 <  \eta  < 2.37, p_T > 50$	$2.30 \pm 1.82$	$\pm 0.34$	$+1.72$	$-0.75$	$\pm 0.49$
Unconverted	$ \eta  < 0.60, 20 < p_T < 30$	$1.46 \pm 0.45$	$\pm 0.26$	$-0.30$	$-0.24$	$\pm 0.22$
	$ \eta  < 0.60, p_T > 30$	$1.03 \pm 0.46$	$\pm 0.11$	$-0.10$	$-0.06$	$\pm 0.44$
	$0.60 <  \eta  < 1.37, 20 < p_T < 30$	$1.18 \pm 0.55$	$\pm 0.15$	$-0.13$	$-0.33$	$\pm 0.41$
	$0.60 <  \eta  < 1.37, p_T > 30$	$1.23 \pm 0.74$	$\pm 0.13$	$-0.07$	$-0.67$	$\pm 0.29$
	$1.52 <  \eta  < 2.37, p_T > 20$	$1.45 \pm 0.55$	$\pm 0.17$	$+0.44$	$-0.45$	$\pm 0.28$

Table 8.4: The MC-based double ratio  $\theta_{MC}$ , in 3-dimensional bins of photon  $p_T$ - $\eta$ -conversion status, together with a break down of the uncertainties. The  $t\bar{t}$  modelling uncertainty on hard scattering and parton shower and hadronisation denoted by Gen. & PS. The uncertainty on  $t\bar{t}$  modelling due to scale choices and the modelling of ISR and FSR are denoted by rad.-up/-down.

### 8.3.3 Extraction of Hadronic-fake Scale Factor

The hadronic-fake scale factor is calculated as:

$$SF^{h\text{-fake}} = \frac{N_{\text{est.}}^{\text{h-fake}}}{N_{\text{MC}}^{\text{h-fake}}}, \quad (8.9)$$

where the data-driven hadronic-fake background ( $N_{\text{est.}}^{\text{h-fake}}$ ) is estimated from Equation 8.8.

The  $SF^{h\text{-fake}}$  is calculated separately for converted and unconverted photons in bins of photon  $p_T$ - $\eta$  (hence, 3-dimensional scale factors). This is done by using the  $\theta_{MC}$  that is measured for the same  $p_T$ - $\eta$  bin and conversion status. The choice of binning for  $p_T$  is based on the statistics and the  $|\eta|$  bins are chosen according to the detector geometry. Then the  $p_T$ - $\eta$  bins are re-optimised again to reduce the statistical uncertainties. The neighbouring kinematic bins that resulted to consistent hadronic-fake scale factors within the statistical uncertainties are merged together. This leads to five bins for each of the converted and unconverted photon category. The resulting scale factors are shown in Figure 8.9 and summarised in Table 8.5.

The systematics uncertainty of  $SF^{h\text{-fake}}$  includes the uncertainties of  $\theta_{MC}$  as explained in Section 8.3.2.1, the uncertainties of the subtraction of non-hadronic-fake and fake lepton backgrounds in control regions A, B and C (see Equation 8.6) as explained in Section 8.3.1, and the statistical uncertainties of the three control regions.

In the final fit, the systematics uncertainties of  $SF^{h\text{-fake}}$  due to the  $t\bar{t}$  modelling (coming from  $\theta_{MC}$  factor) are correlated to the other relevant same systematics sources. The systematic uncertainties due to the statistical uncertainty of  $SF^{h\text{-fake}}$  (i.e. statistical uncertainty of data-driven factor of  $SF^{h\text{-fake}}$  and statistical uncertainty of  $\theta_{MC}$  factor) are uncorrelated bin-by-bin, by considering one Nuisance parameter for statistical uncertainty in each bin of  $SF^{h\text{-fake}}$ . Also, the anti-correlation of  $SF^{h\text{-fake}}$  with the signal strength  $\mu$  (defined in Equation 6.25) due to  $t\bar{t}\gamma$  subtraction, is considered. This is done by using the expression:

$$SF^{h\text{-fake}}(\mu) = SF^{h\text{-fake}}(\mu = 1) \times (1 - 0.12(\mu - 1)), \quad (8.10)$$

where the factor -0.12 is the relative change in hadronic-fake background normalisation if the  $t\bar{t}\gamma$  normalisation goes up by 100% (i.e. if  $\mu = 2$ ). Although  $SF^{h\text{-fake}}$  is binned, since the  $t\bar{t}\gamma$  subtraction

systematics effect on the ELD distribution is more or less flat, and for simplicity, the overall change (i.e. -0.12) is used.

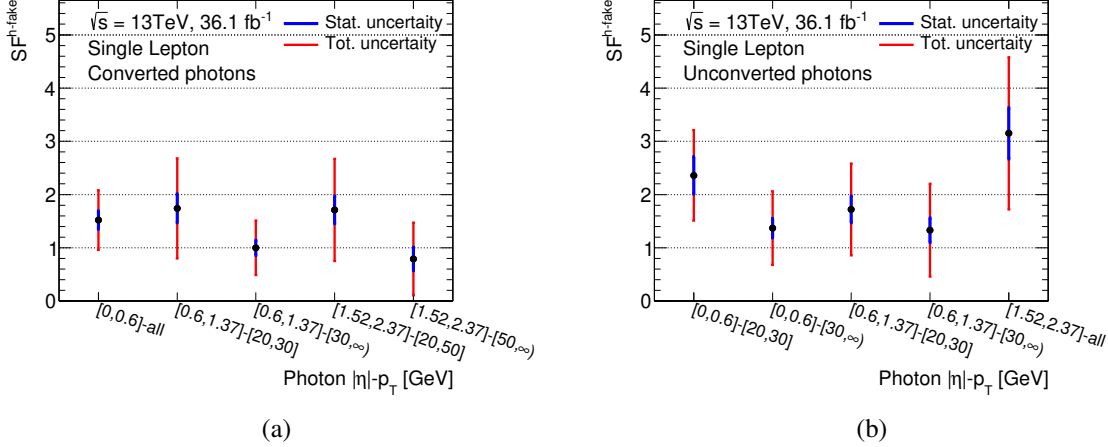


Figure 8.9: Final  $SF^{h\text{-fake}}$ , derived for  $p_T$ - $\eta$  bins separately for (a) converted and (b) unconverted photons.

Photon conversion status	Photon $\eta - p_T$ [GeV]	$SF^{h\text{-fake}}$	stat.	syst.				
				$t\bar{t}\gamma$ subtract.	rest subtract.	$\theta_{MC}$ stat.	$\theta_{MC}$ rad.-up/-down	$\theta_{MC}$ Gen. & PS
All	Inclusive	1.60	$\pm 0.07$	$\pm 0.19$	$\pm 0.12$	$\pm 0.07$	$+0.09/-0.03$	$\pm 0.24$
Conv.	$ \eta  < 0.60, p_T > 20$	1.52	$\pm 0.17$	$\pm 0.13$	$\pm 0.15$	$\pm 0.18$	$+0.26/-0.18$	$\pm 0.38$
	$0.60 <  \eta  < 1.37, 20 < p_T < 30$	1.74	$\pm 0.27$	$\pm 0.14$	$\pm 0.09$	$\pm 0.23$	$+0.16/-0.47$	$\pm 0.71$
	$0.60 <  \eta  < 1.37, p_T > 30$	1.00	$\pm 0.14$	$\pm 0.07$	$\pm 0.09$	$\pm 0.08$	$+0.00/-0.09$	$\pm 0.46$
	$1.52 <  \eta  < 2.37, 20 < p_T < 50$	1.71	$\pm 0.26$	$\pm 0.15$	$\pm 0.23$	$\pm 0.23$	$+0.05/-0.59$	$\pm 0.60$
	$1.52 <  \eta  < 2.37, p_T > 50$	0.79	$\pm 0.22$	$\pm 0.06$	$\pm 0.12$	$\pm 0.12$	$+0.59/-0.26$	$\pm 0.17$
Unconv.	$ \eta  < 0.60, 20 < p_T < 30$	2.36	$\pm 0.35$	$\pm 0.25$	$\pm 0.13$	$\pm 0.42$	$-0.49/-0.39$	$\pm 0.36$
	$ \eta  < 0.60, p_T > 30$	1.37	$\pm 0.18$	$\pm 0.24$	$\pm 0.12$	$\pm 0.15$	$-0.13/-0.08$	$\pm 0.58$
	$0.60 <  \eta  < 1.37, 20 < p_T < 30$	1.72	$\pm 0.25$	$\pm 0.18$	$\pm 0.05$	$\pm 0.22$	$-0.19/-0.48$	$\pm 0.60$
	$0.60 <  \eta  < 1.37, p_T > 30$	1.33	$\pm 0.23$	$\pm 0.23$	$\pm 0.14$	$\pm 0.14$	$-0.08/-0.72$	$\pm 0.31$
	$1.52 <  \eta  < 2.37, p_T > 20$	3.15	$\pm 0.48$	$\pm 0.57$	$\pm 0.27$	$\pm 0.37$	$+0.95/-0.98$	$\pm 0.61$

Table 8.5: The hadronic-fake scale factor ( $SF^{h\text{-fake}}$ ) derived for inclusive and 3-dimensional bins of photon  $p_T$ - $\eta$ -conversion status. The binned scale factors are used in the analysis and the inclusive scale factor is just shown for comparison. All the individual uncertainty components considered for the  $SF^{h\text{-fake}}$  are shown: the uncertainty due to the statistics of  $N_{i,\text{data}}^{\text{h-fake}}$  with  $i \in A, B, C$  (stat.), the uncertainty due to the subtraction of  $t\bar{t}\gamma$  ( $t\bar{t}\gamma$  subtract.), the uncertainty due to the subtraction of other events with prompt and electron-fake photons and the fake-lepton background (rest subtract.), the uncertainty due to the statistical uncertainty of the  $\theta_{MC}$  factor ( $\theta_{MC}$  stat.), the uncertainty due to modelling of additional QCD radiation in  $t\bar{t}\text{MC}$  ( $\theta_{MC}$  rad.-up/-down), and finally the uncertainty due to the hard scattering and parton shower and hadronisation modelling of  $t\bar{t}\text{MC}$  ( $\theta_{MC}$  Gen. & PS).

## 8.4 Estimation of other Backgrounds

In this analysis, the backgrounds are categorised into four groups: The hadronic-fake background, the electron-fake background, the fake-lepton background, and the backgrounds with a prompt photon. This is different from the categorisation of backgrounds in the 8 TeV analysis which was based on the type of

their photon (hadronic-fake, electron-fake, or prompt). This was needed in the 8 TeV analysis because each of the backgrounds must be described by one of the hadronic-fake, electron-fake, or prompt-photon templates in the fit, depending on their photon type. Essentially, the difference is that in this analysis in the fake-lepton background the events with prompt or fake photons are not distinguished.

The estimation of hadronic-fake background was explained in the previous Section, and the estimation of the rest of background are outlined in this Section.

### 8.4.1 Electron-fake Background

To estimation the electron-fake background, the same method explained in Section 7.4.2 is used to extract the  $e \rightarrow \gamma$  fake rates. But the difference is that the fake rates are derived from both data and MC simulation, and their ratio is taken as the fake-rate scale factor,  $SF^{e\text{-fake}}$ . Then, a set of  $SF^{e\text{-fake}}$  is used to correct the MC-derived ELD distribution of the electron-fake background entering the maximum-likelihood fit, to match data.

The  $Z \rightarrow e + \text{fake-}\gamma$  and  $Z \rightarrow ee$  control regions introduced in Section 7.4.2 are used for extracting the  $e \rightarrow \gamma$  fake rates in data and in MC, by taking the ratio of the number of  $Z \rightarrow e + \text{fake-}\gamma$  events to the number of  $Z \rightarrow ee$  events in photon  $p_{\text{T}}\text{-}\eta$  bins. To calculate the fake rates in MC, the  $Z + \text{jets}$  sample in  $ee$  channel is used, where in the  $Z \rightarrow e + \text{fake-}\gamma$  control region the probe photon is matched to a true electron before detector simulation. To calculate the data-driven fake rates, a fit to the invariant mass distribution of either the  $ey$  or the  $e^+e^-$  pair is performed in order to subtract the non- $Z$  background. A double-sided Crystal-Ball function is used to model the signal and the background is modelled by a Bernstein forth order polynomial function. The fitted signal in the  $Z \rightarrow e + \text{fake-}\gamma$  control region is contaminated by  $Z \rightarrow eey$  events, where the photon is a prompt photon and not an electron-fake. This contamination is subtracted using the  $Z\gamma$  sample in  $ee$  channel.

Several variations to the procedure of  $SF^{e\text{-fake}}$  derivation are applied in order to account for the systematics uncertainties. This includes changing the signal model in the invariant mass fit from Crystal-Ball function to MC-predicted template, changing the non- $Z$  background model from Bernstein function to Gaussian, varying the fitting mass range, and in the  $Z \rightarrow eey$  subtraction replacing the  $Z\gamma$  MC sample with the  $Z + \text{jets}$  sample, where the photon radiation is described by the parton shower.

The central values of the  $SF^{e\text{-fake}}$  range from 0.8 to 2.1 for different  $p_{\text{T}}\text{-}\eta$  bins, and the uncertainties from 5% to 42% [9]. In most of the bins the scale factor is consistent with one within the uncertainties.

The final step of this background estimation is the validation of the estimate, using a control region enriched by electron-fake photons. The control region is selected by replacing the photon in the  $t\bar{t}\gamma$  signal selection (Section 8.1) with an electron. The ratio of data to the MC prediction in this region is  $0.98 \pm 0.01$  [9], where the uncertainty is statistical. This ratio, although is very close to one, is used as an extra overall scale factor in addition to the binned  $SF^{e\text{-fake}}$  to correct the MC-predicted electron-fake background in the signal region.

### 8.4.2 Fake-Lepton Background

The background due to fake leptons is introduced in Section 7.4.3.1. In the 8 TeV analysis the multi-jet production with an additional prompt photon was categorised under the backgrounds with a prompt photon, while the multi-jet processes containing a fake lepton and also a hadronic-fake photon were absorbed in the hadronic-fake background category. This categorisation of the backgrounds based on their photon type was needed to make use of one of the three prompt, electron-fake or hadronic-fake templates as explained in Section 7.2.1. This categorisation is not needed in the 13 TeV analysis because of using ELD, which discriminates between signal and all backgrounds based on the event-level

information.

The fake-lepton background background is estimated using the same matrix-method explained in Section 7.4.3.1 and the event weights of Equation 7.10.

The tight electron and muon are identical to the nominal objects described in Section 8.1.1, while the loose muons and electrons are selected by removing their isolation requirements and requiring the electrons to pass the electron MediumLH identification criteria instead of the nominal TightLH. In addition, for the data sample with loose muons the low- $p_T$  muon trigger for 2016 is changed from the nominal trigger (see Table 8.1) to the HLT\_mu24 trigger with a pre-scale of 50, in order to avoid possible trigger bias.

Different parametrisation are available for the real and fake efficiencies ( $\epsilon_{\text{real}}$  and  $\epsilon_{\text{fake}}$ ). For the background estimation in  $e+\text{jets}$  ( $\mu+\text{jets}$ ) channel the efficiencies are parametrised as a function of lepton  $\eta$  and  $m_T^W$  (lepton  $p_T$  and  $m_T^W$ ). Alternative parameterisations, resulting to larger and smaller background yields, are used to evaluated the systematic uncertainty. For the background estimation in  $e+\text{jets}$  ( $\mu+\text{jets}$ ) channel the efficiencies are parametrised as a function of lepton  $\eta$ , number of  $b$ -jets and  $m_T^W$  (jet  $p_T$  and number of  $b$ -jets) for the up variation, and as a function of lepton  $\eta$ , jet  $p_T$  and  $\Delta R$  of the lepton and the closest jet (lepton  $p_T$ , lepton  $\eta$  and  $\Delta R$  of the lepton and the closest jet) for the down variation.

### 8.4.3 Backgrounds with Prompt Photons

The dominant background process with a prompt photon is the  $W\gamma$  process. The normalisation of the  $W\gamma$  background is a free parameter in the maximum-likelihood fit, since it is well separated from the  $t\bar{t}\gamma$  signal by ELD. Its ELD shape is taken from MC simulation. The shape is checked in dedicated  $W\gamma$  validation regions to ensure a good modelling.

Two  $W\gamma$  validation regions are used. The heavy-flavour validation region is selected by modifying the signal region selection outlined in Section 8.1.2 to require the number of jets to be exactly two or three, the number of  $b$ -jets to be exactly one, and  $m_{e\gamma} < 80$  GeV. In addition, events are required to have  $E_T^{\text{miss}} > 40$  GeV and  $ELD < 0.04$ . The requirement on  $m_{e\gamma}$  reduces the contamination from electron-fake photons and the ELD requirement suppresses the  $t\bar{t}\gamma$  contamination. The light-flavour validation region is selected the same, except that the number of  $b$ -jets are required to be zero and the requirement on ELD is removed, since this region is less contaminated by  $t\bar{t}\gamma$  due to its zero  $b$ -jet requirement. Both validation regions showes good modelling of  $W\gamma$  process by MC.

The rest of the prompt-photon backgrounds are the  $Z\gamma$  process, and the single top quark and diboson productions with a prompt photon. As they have smaller contribution, they are estimated from MC. They are grouped as "other prompts" in Table 8.6 where the estimation of all backgrounds are summarised.

### 8.4.4 Summary of Background Yields

The estimated backgrounds before performing the likelihood fit are summarised in Table 8.6. The data-driven scale factors for the hadronic-fake and electron-fake backgrounds are applied. The uncertainties include statistic and systematic uncertainties.

Hadronic-fake	$1440 \pm 290$
Electron-fake	$1650 \pm 170$ [9]
Fake lepton	$360 \pm 200$ [9]
$W\gamma$	-
Other prompts	$690 \pm 260$ [9]

Table 8.6: The pre-fit estimated yields of background processes, including all data-driven corrections and systematic uncertainties. The  $W\gamma$  background is a free parameter in the likelihood fit.

## 8.5 Systematic Uncertainties

The result of  $t\bar{t}\gamma$  cross-section measurement at 13 TeV is affected by the systematic uncertainties through their impact on the normalisation of expected signal and estimated backgrounds, and/or the shape of their corresponding ELD distributions and the distributions of the observables that are unfolded.

The signal and background modelling uncertainties are described in Section 8.5.1. Each of the signal and background modelling uncertainties is correlated between the  $e+\text{jets}$  and  $\mu+\text{jets}$  channels for the relevant signal or background process. The experimental systematics are explained in Section 8.5.2. Each experimental uncertainty is correlated between the channels and also between signal and simulated backgrounds.

The effect of systematic uncertainties are summarised in the next Section where the result of the cross section measurements are given (Section 8.6).

### 8.5.1 Modelling Uncertainties

The alternative MC samples used to estimate the signal or background modelling uncertainties which are described in this section are listed in Appendix C.2.2 as well, and their production detail are given in Section 5.2.

#### Signal Modelling

The uncertainties of modelling of the signal process in MC simulations affect both the normalisation and the shape of the ELD distribution. The effect on the normalisation is through the correction factor  $C$  (Equations 6.4 and 6.12).

- The effect of the choices of renormalisation scale ( $\mu_R$ ) and factorisation scale ( $\mu_F$ ) is evaluated by varying the scales up and down by a factor of two with respect to the nominal value. The scales are varied either one by one or spontaneously, resulting in eight variations in total, which are carried on in terms of event weights. The largest variations on  $C$  or ELD shapes with respect to the nominal are taken as the uncertainty.
- The uncertainty due to the modelling of parton shower and hadronisation is evaluated by comparing an alternative signal sample produced with **MADGRAPH** and interfaced with **HERWIG**, with the nominal signal sample which is produced with **MADGRAPH** and interfaced with **PYTHIA**.
- To evaluate the uncertainty due to the modelling of initial- and final-state radiations, the nominal sample is compared with two alternative samples produced by varying the tune parameters of **PYTHIA** (**A14 var3c** eigentune), corresponding to higher and lower QCD radiation activity.

- Evaluation of uncertainties due to the modelling of PDF makes use of the 100 eigenvector set of the NNPDF2.3LO set which are stored in the signal sample in terms of event weights. The standard deviation of the distribution formed by the 100 eigenvectors is considered as the uncertainty.

### Background Modelling

- The normalisation of hadronic-fake background is subject to the systematic uncertainties of  $SF^{h\text{-fake}}$  that are discussed in detail in Section 8.3. The shape uncertainty of the ELD distribution, as well as for the distributions of the observables that are unfolded, are evaluated from  $t\bar{t}$  MC samples, since the hadronic-fake background is dominated by the  $t\bar{t}$  process. This is done by comparing the distributions extracted from the nominal  $t\bar{t}$  sample with those extracted from the alternative  $t\bar{t}$  samples described in Section 8.3.2.1.
- Evaluation of the systematic uncertainties of the normalisation of the electron-fake background are fully explained in Section 8.4.1. Same as for the hadronic-fake background, the shape uncertainties of this background are evaluated from  $t\bar{t}$  alternative MC samples, as this background is also dominated by the  $t\bar{t}$  process.
- The uncertainty of fake-lepton background estimation due to different parametrisation choices for the real and fake efficiencies used in the matrix method are described in Section 8.4.2. This results to an uncertainty of around 50%, and since this background has a small contribution no other systematic uncertainty is considered for it.
- The ELD shape uncertainties for the  $W\gamma$  background is evaluated by varying the  $\mu_R$  and  $\mu_F$  scale choices in the same way that is explained for the signal in Section 8.5.1. No shape uncertainty is considered for the other prompt backgrounds, as their contributions are very small. The normalisation of the  $W\gamma$  background is a free parameter in the fit but for the normalisation of each of the other prompt backgrounds a 50% uncertainty is assigned.

#### 8.5.2 Experimental Uncertainties

The experimental systematic uncertainties affect the normalisation and the shape of the signal and the MC-derived backgrounds. For the backgrounds that are normalised to data by using the data-driven scale factors (i.e. hadronic-fake and electron-fake backgrounds), only the effect on the shape is considered.

The sources of the experimental systematic uncertainties and the methods for their estimation are very similar to what already described in Section 7.5.2 for the 8 TeV analysis. In the case of leptons,  $b$ -tagging, and missing transverse momentum nothing is changed. This is also the case for the jets, except that in the 13 TeV analysis the systematic uncertainty contribution from JVF cut is replaced by the contribution from JVT cut, but the method for its estimation is the same. In the following the systematic uncertainties related to photons, pile-up and luminosity are outlined, as there are differences with respect to Section 7.5.2.

#### Photons

The photon identification and isolation scale factors and the corrections to its momentum scale and resolution are varied up and down and their effects on the final result are studied.

The PPT systematic uncertainty is studied separately for the prompt, electron-fake, and hadronic-fake photons, in photon  $p_T$ - $\eta$  bins.

The dedicated data-driven PPT scale factors for the prompt photons, explained in Section 8.2.1.1, are removed and the resulting shape difference with respect to the nominal case (i.e. when the scale factors are applied) is assigned as the systematic uncertainty for the PPT modelling of prompt photons. The same systematic uncertainty is also assigned for the electron-fake photons, since the studies showed the electron-fake photons have a similar PPT shape as the prompt photons, and a similar shape difference between data and MC.

For the PPT modelling uncertainty of the hadronic-fake photons, the control region C from Section 8.3.1 is used. The  $t\bar{t}\gamma$  contamination in this control region is varied up and down by 50% and the resulting maximum shape difference between data and prediction is used for the systematic uncertainty estimation of the PPT modelling of the hadronic-fake photons. However, since the hadronic-fake photons in region C are non-isolated while those in the signal region are isolated, the shape difference between data and prediction in the control region A from Section 8.3.1 is assigned as an additional systematic for the PPT modelling of hadronic-fake photons.

### Pile-up

The uncertainty due to the pile-up modelling is studied by varying the pile-up re-weighting parameter,  $\mu$ , from its nominal value 1.09 to 1.0 or 1.18.

### Luminosity

The uncertainty of the total integrated luminosity is 2.1%, provided centrally by ATLAS using a methodology similar to what is described in Ref. [49].

## 8.6 Results

The inclusive fiducial cross section of  $pp \rightarrow t\bar{t}\gamma$  production at a centre-of-mass-energy of  $\sqrt{s} = 13$  TeV is measured for the single-lepton decay channel by performing a maximum-likelihood fit to the binned ELD distribution in data. The post-fit event yields are summarised in Table 8.7, and the post-fit ELD distribution can be seen in Figure 8.10(b).

$t\bar{t}\gamma$	Hadronic-fake	Electron-fake	$W\gamma$	Other prompts	Fake lepton	Total expectation	Data
7040 $\pm$ 350	1470 $\pm$ 180	1620 $\pm$ 160	900 $\pm$ 370	570 $\pm$ 180	186 $\pm$ 68	11790 $\pm$ 180	11662

Table 8.7: The post-fit event yields for the signal and backgrounds for the inclusive fiducial  $t\bar{t}\gamma$  cross-section measurement at 13 TeV [9]. The uncertainties include the statistical and systematic uncertainties.

The measured inclusive cross section in the fiducial region in the single-lepton channel is [9]:

$$\sigma_{t\bar{t}\gamma, sl}^{fid} = 521 \pm 9 \text{ (stat.)} \pm 41 \text{ (sys.) fb} = 521 \pm 42 \text{ fb},$$

which is in agreement with the SM prediction at NLO accuracy of  $495 \pm 99$  fb (see Section 8.2.5). The achieved total uncertainty of 8% is an improvement in accuracy with respect to the result of the measurement at 8 TeV (Section 7.6). A summary of the effect of all systematic uncertainties (introduced in Section 8.5) on the inclusive measurement is shown in Table 8.8.

The normalised differential cross sections measured in the fiducial region as a function of photon  $p_T$ , photon  $\eta$  and  $\Delta R(\gamma, \text{lepton})$  are shown in Figure 8.11. They are compared with the nominal  $t\bar{t}\gamma$  signal sample produced with **MADGRAPH +PYTHIA**, as well as with the alternative signal samples produced with

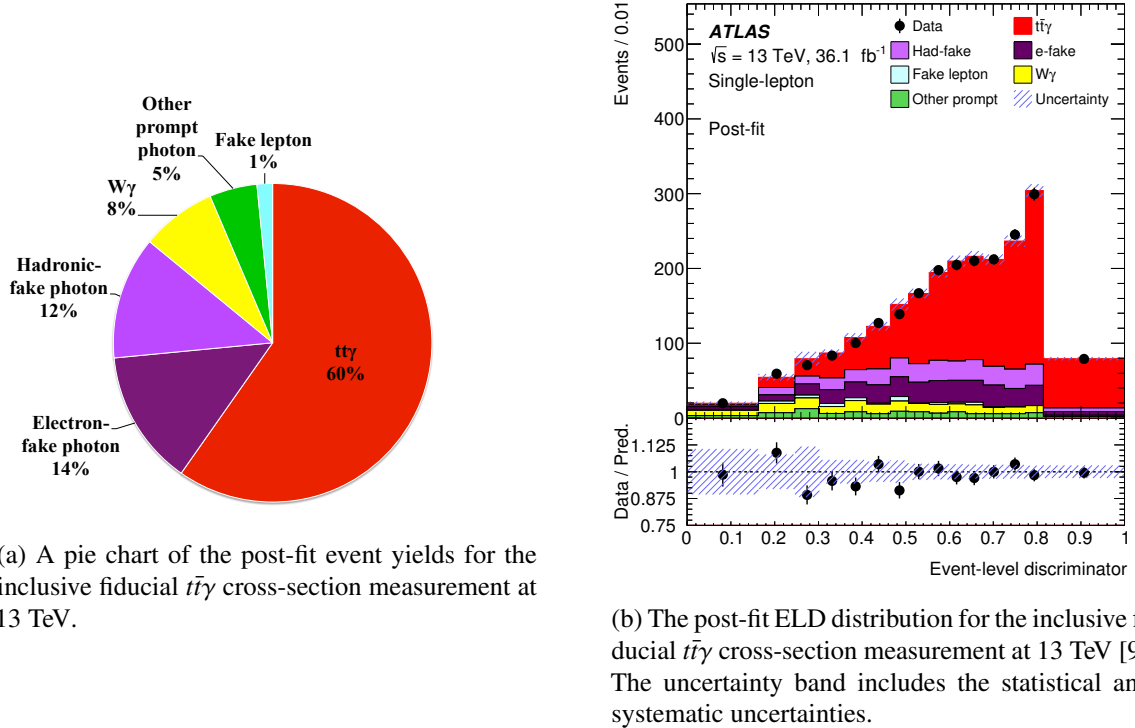


Figure 8.10

PYTHIA A14 tune parameters varied up and down, and with HERWIG replacing PYTHIA. The  $t\bar{t}\gamma$  samples are normalised to the NLO prediction by using the  $k$ -factor. Also, a comparison with the nominal  $t\bar{t}$  sample produced with PowHEG +PYTHIA is included, where the radiation of prompt photons is modelled in the parton shower. The different  $t\bar{t}\gamma$  samples all predict very similar shapes. The unfolded data is in good agreement with the predictions by the  $t\bar{t}\gamma$  samples.

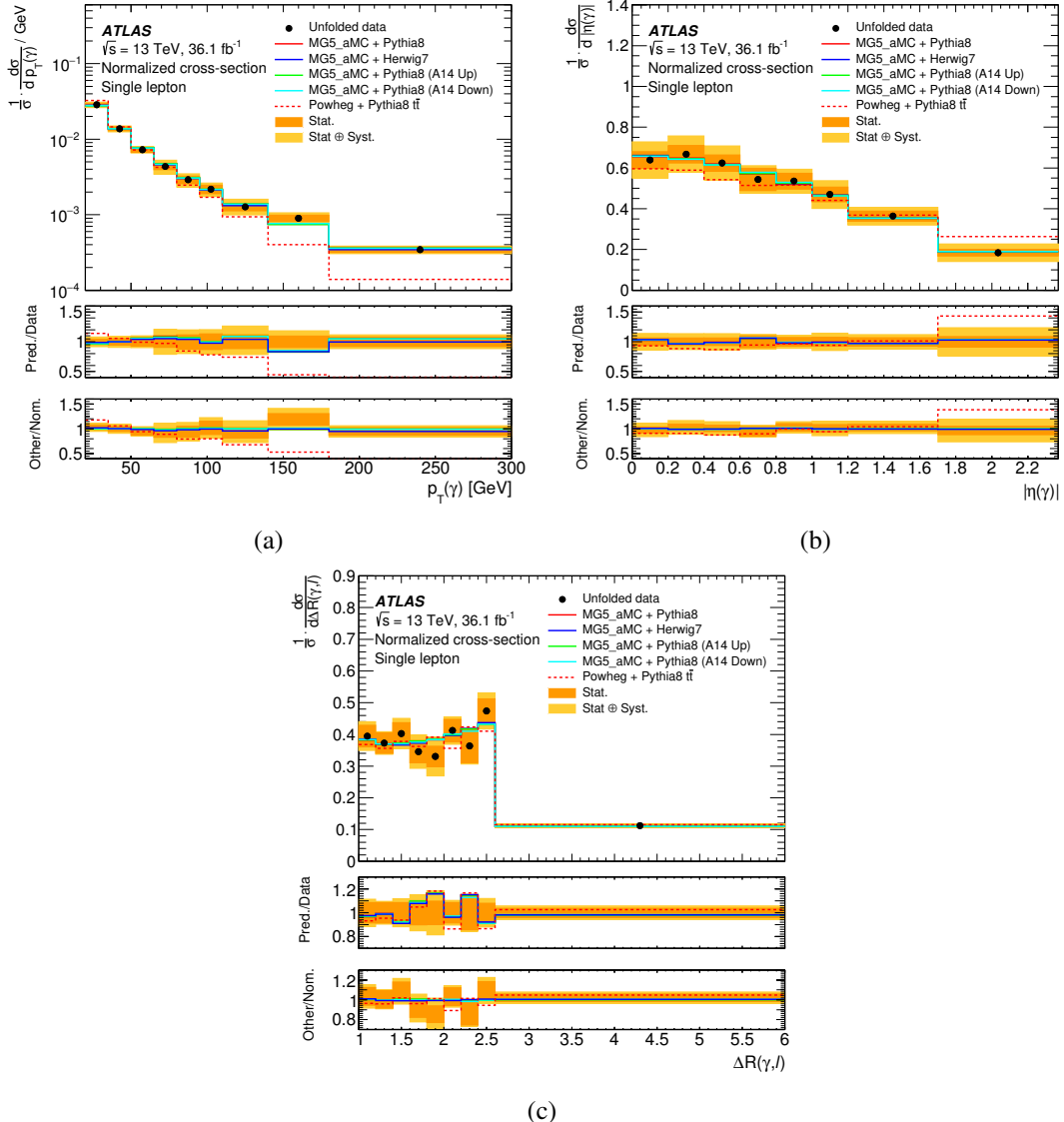


Figure 8.11: Measured normalised  $t\bar{t}\gamma$  differential fiducial cross section at 13 TeV as a function of (a) photon  $p_T$ , (b) photon  $\eta$  and (c)  $\Delta R(\gamma, \text{lepton})$ , compared with their corresponding SM predictions at NLO by using different  $t\bar{t}\gamma$  MC samples, as well as a  $t\bar{t}$  MC sample with prompt-photon radiation modelled in the parton shower. In each plot the top ratio panel shows the ratios of all the samples over data, and the bottom ratio panel shows that ratios of the alternative  $t\bar{t}\gamma$  samples and the  $t\bar{t}$  sample over the nominal  $t\bar{t}\gamma$  sample. [9]

Source	Relative uncertainty (%)
Jets	$\pm 5.4$
Background modelling	$\pm 4.8$
Prompt-photon tagger	$\pm 4.0$
Luminosity	$\pm 2.3$
Pile-up	$\pm 2.0$
MC sample size	$\pm 1.9$
Signal modelling	$\pm 1.6$
Photon	$\pm 1.1$
$b$ -tagging	$\pm 0.9$
Leptons	$\pm 0.3$
Systematic uncertainty	$\pm 7.9$
Statistical uncertainty	$\pm 1.5$
Total uncertainty	$\pm 8.1$

Table 8.8: Summary of the effects of the groups of systematic uncertainties on the inclusive fiducial  $t\bar{t}\gamma$  cross-section measurement at 13 TeV.

# CHAPTER 9

---

## Summary and Conclusion

---

The cross-section measurement of production of a top-quark pair in association with a photon ( $t\bar{t}\gamma$ ) probes the top-photon coupling.

The  $t\bar{t}\gamma$  production cross section is measured using  $20.2 \text{ fb}^{-1}$  of data from proton-proton collisions at  $\sqrt{s} = 8 \text{ TeV}$ , and  $36.1 \text{ fb}^{-1}$  of data from collisions at  $\sqrt{s} = 13 \text{ TeV}$ , collected by the ATLAS detector at the LHC. The measurements are performed inclusively and differentially, in specific fiducial phase spaces. The cross sections are measured for the single-lepton decay channel of  $t\bar{t}\gamma$ , where the final state includes exactly one electron or muon, including those that are decayed from a  $\tau$ -lepton.

In the first measurement (the 8 TeV analysis), the inclusive and differential fiducial cross sections are extracted from maximum-likelihood fits to the photon isolation distribution of the observed data. Exploiting the tracking based isolation of photons  $p_T^{\text{cone}20}$ , three different templates are built: a template for the hadronic-fake photons, which are jets mis-reconstructed as photons of non-prompt photons originated from hadrons within the jets; a template for the electron-fake photons, which are electrons that are misidentified as photons; and a template for prompt photons. The prompt-photon template describes the shape of signal events and the background events with a prompt photon, and the hadronic-fake and electron-fake templates describe the background events containing a hadronic-fake or an electron-fake photon candidate. The normalisations of the backgrounds are estimated from data-driven methods or MC simulations, except for the hadronic-fake background which is treated as a free parameter in the fit. The differential cross sections are measured as a function of photon  $p_T$  and photon  $\eta$ , using the bin-by-bin unfolding approach. All measured cross sections found to be in agreement with their NLO theoretical prediction.

For the second measurement (the 13 TeV analysis), the analysis strategy has significantly changed by taking advantage of MVA techniques. The inclusive fiducial cross section is extracted from a maximum-likelihood fit to the output of a NN that is trained to discriminate between the signal and background events. This NN algorithm, called ELD, has different inputs related to the kinematic and topological properties of the selected events. Also, a dedicated NN called PPT that is trained to discriminate between prompt and hadronic-fake photons serves as an input for ELD. The differential fiducial cross sections that are normalised to unity are measured as a function of photon  $p_T$ , photon  $\eta$ , and  $\Delta R(\gamma, \text{lepton})$ , without performing the maximum-likelihood fit. For the unfolding, the iterative Bayesian method is used. The estimation of hadronic-fake background is carried on by a different and more sophisticated data-driven method. The other backgrounds are estimated from data or MC simulations with more or less same methods as the previous analysis, except for the  $W\gamma$  background which is treated as a free parameter in the fit. All the results agree with the NLO theoretical predictions.

Figure 9.1 summarises the result of these two measurements, as well as a previous measurement

performed by ATLAS at  $\sqrt{s} = 7$  TeV [45]. In this Figure, the measured inclusive fiducial cross sections in the single-lepton channel ( $\sigma_{t\bar{t}\gamma, sl}^{fid}$ ) are compared to the SM predictions at the NLO accuracy. It can be seen that in each analysis, the accuracy of the measurement is increased with respect to the previous one. The total uncertainty of  $\sigma_{t\bar{t}\gamma, sl}^{fid}$  measured at  $\sqrt{s} = 8$  TeV is 13%, where the statistical uncertainty accounts for 5%. The uncertainty of this measurement is dominated by the systematic uncertainties due to the hadronic-fake template and the electron-fake background estimation and template. The total uncertainty of  $\sigma_{t\bar{t}\gamma, sl}^{fid}$  measured at  $\sqrt{s} = 13$  TeV is reduced to 8%, with the statistical uncertainty accounting for only 1.5%. The dominant uncertainty in this measurement is the systematic uncertainties stemming from jets. This is followed by the background modelling systematic uncertainties, and then the PPT systematic uncertainties. The individual systematic uncertainty contributions from the hadronic-fake and electron-fake backgrounds, which are components of the background modelling uncertainty group, are reduced comparing to the previous analysis. The NLO theory predictions in Figure 9.1 are affected by the uncertainties of the  $k$ -factors used to normalised the LO predictions to NLO. In the 13 TeV analysis, the uncertainty of the  $k$ -factor is increased to 20%, comparing to the 15% uncertainty in the 8 TeV analysis. This is due to the extra contributions to the  $k$ -factor uncertainty from the LO calculation at the particle level.

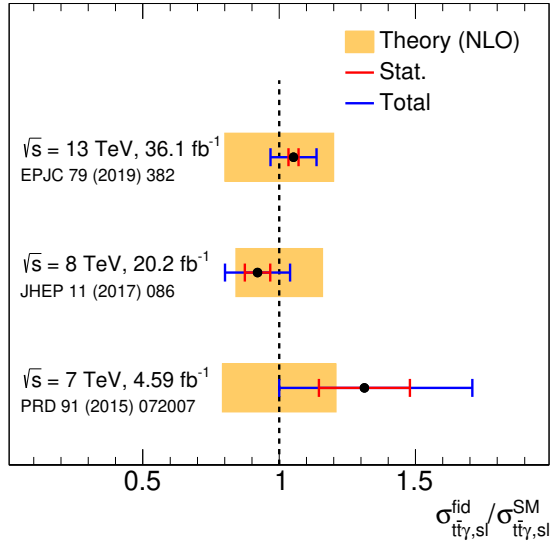


Figure 9.1: Summary of fiducial measurements of the  $t\bar{t}\gamma$  cross sections in the single-lepton channel by ATLAS at  $\sqrt{s} = 7$  TeV [45],  $\sqrt{s} = 8$  TeV [8], and  $\sqrt{s} = 13$  TeV [9], normalised to the SM predictions at the NLO accuracy. The latter two measurements are presented in this thesis.

The accuracy of the results can be improved in the future  $t\bar{t}\gamma$  analyses by performing the analysis in the dilepton channel with one electron and one muon in the final state, the  $e\mu$  channel. This will reduce the background modelling uncertainty, since the  $e\mu$  channel is expected to have very small background contribution. The  $t\bar{t}\gamma$  cross section measurement in the dilepton channel has already been reported in Ref. [9], in all three possible final states of the dilepton channel,  $ee$ ,  $\mu\mu$ , and  $e\mu$ . With more data that has become available from run-2, a measurement only in the  $e\mu$  channel would not suffer from statistical uncertainty. The PPT is very powerful in discriminating the prompt and hadronic-fake photons, however its assigned conservative uncertainties can be revised with more studies. Another possible change could be that the shower-shape variables of the photons in the selected events directly be used as inputs in the ELD. Also, future analyses can focus on developing techniques to more efficiently distinguish the

---

$t\bar{t}\gamma$  events where the photon is radiated from the top quark, rather than the top quark decay products or incoming partons. The future analyses can greatly benefit from more precise theory predictions. In future works, the results of  $t\bar{t}\gamma$  measurements can be interpreted in the framework of effective field theories to constrain the coefficients of the operators that affect the  $t\bar{t}\gamma$  production via electroweak dipole moments and chromomagnetic dipole moments [7]. In addition, the measurement of cross section ratio  $\sigma_{t\bar{t}\gamma}/\sigma_{t\bar{t}}$  can be included in the future analyses.



# Bibliography

---

- [1] CDF Collaboration, *Observation of Top Quark Production in  $\bar{p}p$  Collisions with the Collider Detector at Fermilab*, Phys. Rev. Lett. **74** (14 1995) 2626.
- [2] D0 Collaboration, *Observation of the Top Quark*, Phys. Rev. Lett. **74** (14 1995) 2632.
- [3] U. Baur et al., *Probing electroweak top quark couplings at hadron colliders*, Phys. Rev. **D71** (2005) 054013, arXiv: hep-ph/0412021 [hep-ph].
- [4] A. O. Bouzas and F. Larios, *Electromagnetic dipole moments of the Top quark*, Phys. Rev. **D87** (2013) 074015, arXiv: 1212.6575 [hep-ph].
- [5] M. Schulze and Y. Soreq, *Pinning down electroweak dipole operators of the top quark*, Eur. Phys. J. **C76** (2016) 466, arXiv: 1603.08911 [hep-ph].
- [6] B. Lillie, J. Shu and T. M. P. Tait, *Top Compositeness at the Tevatron and LHC*, JHEP **04** (2008) 087, arXiv: 0712.3057 [hep-ph].
- [7] O. Bessidskaia Bylund et al., *Probing top quark neutral couplings in the Standard Model Effective Field Theory at NLO in QCD*, JHEP **05** (2016) 052, arXiv: 1601.08193 [hep-ph].
- [8] ATLAS Collaboration, *Measurement of the  $t\bar{t}\gamma$  production cross section in proton–proton collisions at  $\sqrt{s} = 8$  TeV with the ATLAS detector*, JHEP **11** (2017) 086, arXiv: 1706.03046 [hep-ex].
- [9] ATLAS Collaboration, *Measurements of inclusive and differential fiducial cross-sections of  $t\bar{t}\gamma$  production in leptonic final states at  $\sqrt{s} = 13$  TeV in ATLAS*, Eur. Phys. J. C **79** (2019) 382, arXiv: 1812.01697 [hep-ex].
- [10] D. H. Perkins, *Introduction to High Energy Physics*, 4th ed., Cambridge University Press, 2000, ISBN: 9780521621960.
- [11] D. Griffiths, *Introduction to Elementary Particles; 2nd rev. version*, Wiley, 2008, ISBN: 9783527406012.
- [12] F. Halzen and A. D. Martin, *Quarks and Lepton: An Introductory Course in Modern Particle Physics*, Wiley, 1984, ISBN: 0471887412.
- [13] A. Pich, “The Standard Model of Electroweak Interactions”, *Proceedings, Based on lectures given at the 6th CERN-Fermilab Hadron Collider Physics Summer School (Geneva, Switzerland, 2011), 18th European School of High-Energy Physics (Raseborg, Finland, 2010), 2010 Int. School on Astroparticle Physics (Zaragoza, Spain), 2010 IDPASC School (Sesimbra, Portugal), and 2009 Int. Summer School and Conference on High-Energy Physics (Mugla, Turkey, 2009)*, 2012, arXiv: 1201.0537 [hep-ph].

- [14] J. Ellis, “Higgs Physics”, *Proceedings, Lectures presented at 2013 European School of High-Energy Physics (ESHEP 2013): Paradfurdo, Hungary, June 5-18, 2013*, 2015 117, arXiv: 1312.5672 [hep-ph].
- [15] Particle Data Group, *Review of Particle Physics*, Phys. Rev. D **98** (3 2018) 030001.
- [16] A. Deur, S. J. Brodsky and G. F. de Teramond, *The QCD Running Coupling*, Prog. Part. Nucl. Phys. **90** (2016) 1, arXiv: 1604.08082 [hep-ph].
- [17] S. L. Glashow, *Partial-symmetries of weak interactions*, Nuclear Physics **22** (1961) 579, URL: <http://www.sciencedirect.com/science/article/pii/0029558261904692>.
- [18] S. Weinberg, *A Model of Leptons*, Phys. Rev. Lett. **19** (21 1967) 1264.
- [19] A. Salam, *Weak and Electromagnetic Interactions*, Conf. Proc. **C680519** (1968) 367.
- [20] P. W. Higgs, *Broken symmetries, massless particles and gauge fields*, Phys. Lett. **12** (1964) 132.
- [21] F. Englert and R. Brout, *Broken Symmetry and the Mass of Gauge Vector Mesons*, Phys. Rev. Lett. **13** (1964) 321.
- [22] DESY, [http://www.desy.de/e409/e116959/e119238/media/2891/Proton\\_Quark-Gluon-Gewimmel\\_blau.jpg](http://www.desy.de/e409/e116959/e119238/media/2891/Proton_Quark-Gluon-Gewimmel_blau.jpg).
- [23] G. P. Salam, “Elements of QCD for hadron colliders”, *High-energy physics. Proceedings, 17th European School of High-Energy Physics (ESHEP 2009): Bautzen, Germany, June 14-27, 2009*, 2010, arXiv: 1011.5131 [hep-ph].
- [24] J. M. Campbell, J. W. Huston and W. J. Stirling, *Hard interactions of quarks and gluons: a primer for LHC physics*, Rep. Prog. Phys. **70** (2006) 89.
- [25] T. Sjostrand, “Monte Carlo Generators”, *High-energy physics. Proceedings, European School of High-Energy Physics (ESHEP 2006): Aronsborg, Sweden, June 18 - July 1, 2006*, 2006 51, arXiv: hep-ph/0611247 [hep-ph].
- [26] M. A. Dobbs et al., “Les Houches guidebook to Monte Carlo generators for hadron collider physics”, *Physics at TeV colliders. Proceedings, Workshop, Les Houches, France, May 26 - June 3, 2003*, 2004 411, arXiv: hep-ph/0403045 [hep-ph].
- [27] V. N. Gribov and L. N. Lipatov, *Deep inelastic ep scattering in perturbation theory*, Sov. J. Nucl. Phys. **15** (1972) 438, [Yad. Fiz. 15, 781(1972)].
- [28] L. N. Lipatov, *The parton model and perturbation theory*, Sov. J. Nucl. Phys. **20** (1975) 94, [Yad. Fiz. 20, 181(1974)].
- [29] G. Altarelli and G. Parisi, *Asymptotic Freedom in Parton Language*, Nucl. Phys. **B126** (1977) 298.
- [30] Y. L. Dokshitzer, *Calculation of the Structure Functions for Deep Inelastic Scattering and  $e^+ e^-$  Annihilation by Perturbation Theory in Quantum Chromodynamics.*, Sov. Phys. JETP **46** (1977) 641, [Zh. Eksp. Teor. Fiz. 73, 1216(1977)].
- [31] A. D. Martin et al., *Parton distributions for the LHC*, Eur. Phys. J. **C63** (2009) 189, arXiv: 0901.0002 [hep-ph].

- 
- [32] J. Pumplin et al.,  
*New generation of parton distributions with uncertainties from global QCD analysis*, JHEP **07** (2002) 012, arXiv: hep-ph/0201195 [hep-ph].
  - [33] R. D. Ball et al., *Parton distributions with LHC data*, Nucl. Phys. B **867** (2013) 244, arXiv: 1207.1303 [hep-ph].
  - [34] B. Andersson et al., *Parton Fragmentation and String Dynamics*, Phys. Rept. **97** (1983) 31.
  - [35] G. Corcella et al., *HERWIG 6: an event generator for hadron emission reactions with interfering gluons (including supersymmetric processes)*, JHEP **01** (2001) 010, arXiv: hep-ph/0011363.
  - [36] T. Gleisberg et al., *Event generation with SHERPA 1.1*, JHEP **02** (2009) 007, arXiv: 0811.4622 [hep-ph].
  - [37] W. J. Stirling, *Parton Luminosity and Cross Section Plots*, tech. rep., Imperial College London, 2012,  
URL: <http://www.hep.ph.ic.ac.uk/~wstirlin/plots/plots.html>.
  - [38] A. Quadt, *Top quark physics at hadron colliders*, Eur. Phys. J. C**48** (2006) 835.
  - [39] U. Husemann, *Top-Quark Physics: Status and Prospects*, Prog. Part. Nucl. Phys. **95** (2017) 48, arXiv: 1704.01356 [hep-ex].
  - [40] M. Kobayashi and T. Maskawa,  
*CP-Violation in the Renormalizable Theory of Weak Interaction*, Prog. Theor. Phys. **49** (1973) 652.
  - [41] S. W. Herb et al.,  
*Observation of a Dimuon Resonance at 9.5 GeV in 400-GeV Proton-Nucleus Collisions*, Phys. Rev. Lett. **39** (5 1977) 252.
  - [42] W. R. Innes et al., *Observation of Structure in the  $\Upsilon$  Region*, Phys. Rev. Lett. **39** (20 1977) 1240.
  - [43] *First combination of Tevatron and LHC measurements of the top-quark mass*, (2014), Work within the Tevatron Electroweak (TEV-EW-WG) and the Top Physics LHC (TOP-LHC-WG) working groups, arXiv: 1403.4427 [hep-ex].
  - [44] CDF Collaboration, *Evidence for  $t\bar{t}\gamma$  production and measurement of  $\sigma_{t\bar{t}\gamma}/\sigma_{t\bar{t}}$* , Phys. Rev. D **84** (2011) 031104(R), arXiv: 1106.3970 [hep-ex].
  - [45] ATLAS Collaboration,  
*Observation of top-quark pair production in association with a photon and measurement of the  $t\bar{t}\gamma$  production cross section in  $pp$  collisions at  $\sqrt{s} = 7$  TeV using the ATLAS detector*, Phys. Rev. D **91** (2015) 072007, arXiv: 1502.00586 [hep-ex].
  - [46] CMS Collaboration,  
*Measurement of the semileptonic  $t\bar{t} + \gamma$  production cross section in  $pp$  collisions at  $\sqrt{s} = 8$  TeV*, JHEP **10** (2017) 006, arXiv: 1706.08128 [hep-ex].
  - [47] L. Evans and P. Bryant, *LHC Machine*, JINST **3** (2008) S08001.
  - [48] *CERN website*, <https://home.cern/about/who-we-are/our-history>.
  - [49] ATLAS Collaboration,  
*Luminosity determination in  $pp$  collisions at  $\sqrt{s} = 8$  TeV using the ATLAS detector at the LHC*, Eur. Phys. J. C **76** (2016) 653, arXiv: 1608.03953 [hep-ex].

- [50] ATLAS Collaboration, *The ATLAS Experiment at the CERN Large Hadron Collider*, JINST **3** (2008) S08003.
- [51] ATLAS Collaboration, *ATLAS magnet system: Technical Design Report, 1*, CERN-LHCC-97-018 ATLAS-TDR-6, CERN, 1997,  
URL: <https://cds.cern.ch/record/338080>.
- [52] ATLAS Collaboration, *Performance of the ATLAS track reconstruction algorithms in dense environments in LHC Run 2*, Eur. Phys. J. C **77** (2017) 673, arXiv: 1704.07983 [hep-ex].
- [53] ATLAS IBL Collaboration, *Production and Integration of the ATLAS Insertable B-Layer*, JINST **13** (2018) T05008, arXiv: 1803.00844 [physics.ins-det].
- [54] ATLAS Collaboration, *TRT performance results from 13 TeV collision data (2015/2016)*, (2016),  
URL: <https://atlas.web.cern.ch/Atlas/GROUPS/PHYSICS/PLOTS/TRT-2016-001/>.
- [55] ATLAS Collaboration, *Measurement of the photon identification efficiencies with the ATLAS detector using LHC Run-1 data*, Eur. Phys. J. C **76** (2016) 666, arXiv: 1407.5063 [hep-ex].
- [56] ATLAS Collaboration, *Commissioning of the ATLAS Muon Spectrometer with Cosmic Rays*, Eur. Phys. J. C**70** (2010) 875, arXiv: 1006.4384 [physics.ins-det].
- [57] ATLAS Collaboration, *Performance of the ATLAS Trigger System in 2010*, Eur. Phys. J. C **72** (2012) 1849.
- [58] ATLAS Collaboration, *Performance of the ATLAS Trigger System in 2015*, Eur. Phys. J. C**77** (2017) 317, arXiv: 1611.09661 [hep-ex].
- [59] ATLAS Collaboration, *Identification and energy calibration of hadronically decaying tau leptons with the ATLAS experiment in pp collisions at  $\sqrt{s}=8$  TeV*, Eur. Phys. J. C**75** (2015) 303, arXiv: 1412.7086 [hep-ex].
- [60] ATLAS Collaboration, *Trigger Menu in 2016*, tech. rep. ATL-DAQ-PUB-2017-001, CERN, 2017, URL: <https://cds.cern.ch/record/2242069>.
- [61] T. Cornelissen et al.,  
*Concepts, Design and Implementation of the ATLAS New Tracking (NEWT)*, tech. rep. ATL-SOFT-PUB-2007-007. ATL-COM-SOFT-2007-002, CERN, 2007,  
URL: <https://cds.cern.ch/record/1020106>.
- [62] ATLAS Collaboration, *Reconstruction of primary vertices at the ATLAS experiment in Run 1 proton–proton collisions at the LHC*, Eur. Phys. J. C **77** (2016) 332. 52 p,  
arXiv: 1611.10235 [physics.ins-det].
- [63] ATLAS Collaboration, *Performance of the ATLAS Transition Radiation Tracker in Run 1 of the LHC: tracker properties*, JINST **12** (2017) P05002, arXiv: 1702.06473 [hep-ex].
- [64] R. Fruhwirth, *Application of Kalman filtering to track and vertex fitting*, Nucl. Instr. Meth. A**262** (1987) 444.
- [65] R. O. Duda and P. E. Hart,  
*Use of the Hough Transformation to Detect Lines and Curves in Pictures*, Commun. ACM **15** (1972) 11.
- [66] ATLAS Collaboration, *Electron efficiency measurements with the ATLAS detector using 2012 LHC proton–proton collision data*, Eur. Phys. J. C **77** (2017) 195,  
arXiv: 1612.01456 [hep-ex].

- 
- [67] ATLAS Collaboration, *Electron efficiency measurements with the ATLAS detector using the 2015 LHC proton–proton collision data*, ATLAS-CONF-2016-024, 2016, URL: <https://cds.cern.ch/record/2157687>.
  - [68] ATLAS Collaboration, *Improved electron reconstruction in ATLAS using the Gaussian Sum Filter-based model for bremsstrahlung*, tech. rep. ATLAS-CONF-2012-047, CERN, 2012, URL: <https://cds.cern.ch/record/1449796>.
  - [69] The ATLAS Collaboration, *Electron and photon energy calibration with the ATLAS detector using LHC Run 1 data*, Eur. Phys. J. C **74** (2014) 3071, arXiv: [1407.5063](https://arxiv.org/abs/1407.5063) [hep-ex].
  - [70] ATLAS Collaboration, *Measurement of the muon reconstruction performance of the ATLAS detector using 2011 and 2012 LHC proton–proton collision data*, Eur. Phys. J. C **74** (2014) 3130, arXiv: [1407.3935](https://arxiv.org/abs/1407.3935) [hep-ex].
  - [71] ATLAS Collaboration, *Muon reconstruction performance of the ATLAS detector in proton–proton collision data at  $\sqrt{s} = 13$  TeV*, Eur. Phys. J. C **76** (2016) 292, arXiv: [1603.05598](https://arxiv.org/abs/1603.05598) [hep-ex].
  - [72] ATLAS Top Working Group, *Object selection and calibration, background estimations and MC samples for top quark analyses using the full 2012 data set*, ATL-COM-PHYS-2013-1016, 2013, URL: <https://cds.cern.ch/record/1563201>.
  - [73] M. Cacciari, G. P. Salam and G. Soyez, *The anti- $k_t$  jet clustering algorithm*, JHEP **2008** (2008) 063, arXiv: [0802.1189](https://arxiv.org/abs/0802.1189) [hep-ph].
  - [74] ATLAS Collaboration, *Topological cell clustering in the ATLAS calorimeters and its performance in LHC Run 1*, Eur. Phys. J. C **77** (2017) 490, arXiv: [1603.02934](https://arxiv.org/abs/1603.02934) [hep-ex].
  - [75] M. Wobisch and T. Wengler, “Hadronization corrections to jet cross-sections in deep inelastic scattering”, *Monte Carlo generators for HERA physics. Proceedings, Workshop, Hamburg, Germany, 1998-1999*, 1998 270, arXiv: [hep-ph/9907280](https://arxiv.org/abs/hep-ph/9907280) [hep-ph].
  - [76] S. D. Ellis and D. E. Soper, *Successive combination jet algorithm for hadron collisions*, Phys. Rev. D **48** (1993) 3160, arXiv: [hep-ph/9305266](https://arxiv.org/abs/hep-ph/9305266) [hep-ph].
  - [77] ATLAS Collaboration, *Jet energy measurement and its systematic uncertainty in proton–proton collisions at  $\sqrt{s} = 7$  TeV with the ATLAS detector*, Eur. Phys. J. C **75** (2015) 17, arXiv: [1406.0076](https://arxiv.org/abs/1406.0076) [hep-ex].
  - [78] ATLAS Collaboration, *Jet energy scale measurements and their systematic uncertainties in proton-proton collisions at  $\sqrt{s} = 13$  TeV with the ATLAS detector*, Phys. Rev. D **96** (2017) 072002, arXiv: [1703.09665](https://arxiv.org/abs/1703.09665) [hep-ex].
  - [79] M. Cacciari and G. P. Salam, *Pileup subtraction using jet areas*, Phys. Lett. B **659** (2008) 119, arXiv: [0707.1378](https://arxiv.org/abs/0707.1378) [hep-ph].
  - [80] *Pile-up subtraction and suppression for jets in ATLAS*, tech. rep. ATLAS-CONF-2013-083, CERN, 2013, URL: <https://cds.cern.ch/record/1570994>.
  - [81] *Performance of b-jet identification in the ATLAS experiment*, JINST **11** (2016) P04008, arXiv: [1512.01094](https://arxiv.org/abs/1512.01094) [hep-ex].

- [82] The ATLAS collaboration, *Measurements of  $b$ -jet tagging efficiency with the ATLAS detector using  $t\bar{t}$  events at  $\sqrt{s} = 13$  TeV*, JHEP **2018** (2018) 89, arXiv: [1805.01845 \[hep-ex\]](#).
- [83] ATLAS Collaboration, *Measurement of the photon identification efficiencies with the ATLAS detector using LHC Run 2 data collected in 2015 and 2016*, Eur. Phys. J. C **79** (2019) 205, arXiv: [1810.05087 \[hep-ex\]](#).
- [84] ATLAS Collaboration, *Performance of algorithms that reconstruct missing transverse momentum in  $\sqrt{s} = 8$  TeV proton–proton collisions in the ATLAS detector*, Eur. Phys. J. C **77** (2017) 241, arXiv: [1609.09324 \[hep-ex\]](#).
- [85] ATLAS Collaboration, *Performance of missing transverse momentum reconstruction with the ATLAS detector using proton–proton collisions at  $\sqrt{s} = 13$  TeV*, Eur. Phys. J. C **78** (2018) 903, arXiv: [1802.08168 \[hep-ex\]](#).
- [86] ATLAS Collaboration, *Luminosity Public Results, 2012 pp Collisions*, URL: <https://twiki.cern.ch/twiki/bin/view/AtlasPublic/LuminosityPublicResults>.
- [87] ATLAS Collaboration, *Luminosity Public Results Run2, 2016 pp Collisions*, URL: <https://twiki.cern.ch/twiki/bin/view/AtlasPublic/LuminosityPublicResultsRun2>.
- [88] J. Alwall et al., *The automated computation of tree-level and next-to-leading order differential cross sections, and their matching to parton shower simulations*, JHEP **07** (2014) 079, arXiv: [1405.0301 \[hep-ph\]](#).
- [89] J. Alwall et al., *MadGraph 5: going beyond*, JHEP **2011** (2011) 128, arXiv: [1106.0522 \[hep-ph\]](#).
- [90] P. Nason, *A new method for combining NLO QCD with shower Monte Carlo algorithms*, JHEP **11** (2004) 040, arXiv: [hep-ph/0409146](#).
- [91] S. Frixione, P. Nason and C. Oleari, *Matching NLO QCD computations with parton shower simulations: the POWHEG method*, JHEP **11** (2007) 070, arXiv: [0709.2092 \[hep-ph\]](#).
- [92] S. Alioli et al., *A general framework for implementing NLO calculations in shower Monte Carlo programs: the POWHEG BOX*, JHEP **06** (2010) 043, arXiv: [1002.2581 \[hep-ph\]](#).
- [93] M. L. Mangano et al., *ALPGEN, a generator for hard multiparton processes in hadronic collisions*, JHEP **07** (2003) 001, arXiv: [hep-ph/0206293](#).
- [94] T. Sjöstrand, S. Mrenna and P. Skands, *PYTHIA 6.4 physics and manual*, JHEP **05** (2006) 026, arXiv: [hep-ph/0603175](#).
- [95] T. Sjöstrand et al., *An Introduction to PYTHIA 8.2*, Comput. Phys. Commun. **191** (2015) 159, arXiv: [1410.3012 \[hep-ph\]](#).
- [96] J. Bellm et al., *Herwig 7.0/Herwig++ 3.0 release note*, Eur. Phys. J. C **76** (2016) 196, arXiv: [hep-ph/1512.01178](#).
- [97] J. M. Butterworth, J. R. Forshaw and M. H. Seymour, *Multiparton interactions in photoproduction at HERA*, Z. Phys. C **72** (1996) 637, arXiv: [hep-ph/9601371](#).
- [98] E. Barberio and Z. Was, *PHOTOS: A universal Monte Carlo for QED radiative corrections: version 2.0*, Comput. Phys. Commun. **79** (1994) 291.

- 
- [99] P. Golonka and Z. Was,  
*PHOTOS Monte Carlo: a precision tool for QED corrections in Z and W decays*,  
Eur. Phys. J. C **45** (2006) 97, arXiv: hep-ph/0506026.
  - [100] S. Jadach, J. H. Kühn and Z. Was,  
*TAUOLA — a library of Monte Carlo programs to simulate decays of polarized  $\tau$  leptons*,  
Comput. Phys. Commun. **64** (1991) 275.
  - [101] P. Golonka et al.,  
*The Tauola photos F environment for the TAUOLA and PHOTOS packages: Release. 2.*,  
Comput. Phys. Commun. **174** (2006) 818, arXiv: hep-ph/0312240 [hep-ph].
  - [102] D. J. Lange, *The EvtGen particle decay simulation package*,  
Nucl. Instr. Meth. A **462** (2001) 152.
  - [103] S. Agostinelli et al., *GEANT4 — a simulation toolkit*, Nucl. Instr. Meth. A **506** (2003) 250.
  - [104] ATLAS Collaboration, *The ATLAS Simulation Infrastructure*, Eur. Phys. J. C **70** (2010) 823,  
arXiv: 1005.4568 [physics.ins-det].
  - [105] P. Z. Skands, *Tuning Monte Carlo generators: The Perugia tunes*,  
Phys. Rev. D **82** (2010) 074018, arXiv: 1005.3457 [hep-ph].
  - [106] ATLAS Collaboration, *ATLAS Run 1 Pythia8 tunes*, tech. rep. ATL-PHYS-PUB-2014-021,  
CERN, 2014, url: <https://cds.cern.ch/record/1966419>.
  - [107] K. Melnikov, M. Schulze and A. Scharf,  
*QCD corrections to top quark pair production in association with a photon at hadron colliders*,  
Phys. Rev. D **83** (2011) 074013, arXiv: 1102.1967 [hep-ph].
  - [108] H.-L. Lai et al., *New parton distributions for collider physics*, Phys. Rev. D **82** (2010) 074024,  
arXiv: 1007.2241 [hep-ph].
  - [109] ATLAS Collaboration, *Top Group MC12 Common Conventions, MC12 Powheg hdamp setting*,  
url: [https://twiki.cern.ch/twiki/bin/view/AtlasProtected/TopCommonParametersMC12#MC12\\_Powheg\\_hdamp\\_setting](https://twiki.cern.ch/twiki/bin/view/AtlasProtected/TopCommonParametersMC12#MC12_Powheg_hdamp_setting).
  - [110] S. Alioli et al.,  
*NLO single-top production matched with shower in POWHEG: s- and t-channel contributions*,  
JHEP **09** (2009) 111, arXiv: 0907.4076 [hep-ph].
  - [111] E. Re,  
*Single-top Wt-channel production matched with parton showers using the POWHEG method*,  
Eur. Phys. J. C **71** (2011) 1547, arXiv: 1009.2450 [hep-ph].
  - [112] S. Frixione et al., *Single-top hadroproduction in association with a W boson*,  
JHEP **07** (2008) 029, arXiv: 0805.3067 [hep-ph].
  - [113] ATLAS Collaboration, *New ATLAS event generator tunes to 2010 data*,  
ATL-PHYS-PUB-2011-008, 2011, url: <https://cds.cern.ch/record/1345343>.
  - [114] R. D. Ball et al., *Parton distributions for the LHC Run II*, JHEP **04** (2015) 040,  
arXiv: 1410.8849 [hep-ph].
  - [115] ATLAS Collaboration, *ATLAS TWiki page: MCTruthClassifier*,  
<https://twiki.cern.ch/twiki/bin/view/AtlasProtected/MCTruthClassifier>.
  - [116] G. D’Agostini, *A multidimensional unfolding method based on Bayes’ theorem*,  
Nucl. Instr. Meth. A **362** (1995) 487.

- [117] T. Adye, “Unfolding algorithms and tests using RooUnfold”, *Proceedings, PHYSTAT 2011 Workshop on Statistical Issues Related to Discovery Claims in Search Experiments and Unfolding: CERN, Geneva, Switzerland, 17-20 January 2011*, 2011 313, arXiv: 1105.1160 [physics.data-an].
- [118] W. Verkerke and D. Kirkby, *The RooFit toolkit for data modeling*, arXiv: physics/0306116.
- [119] L. Moneta et al., *The RooStats Project*, arXiv: 1009.1003 [physics.data-an].
- [120] ATLAS Collaboration, *Estimation of non-prompt and fake lepton backgrounds in final states with top quarks produced in proton–proton collisions at  $\sqrt{s} = 8$  TeV with the ATLAS Detector*, ATLAS-CONF-2014-058, 2014, URL: <https://cds.cern.ch/record/1951336>.
- [121] F. A. Berends et al., *On the production of a  $W$  and jets at hadron colliders*, Nucl. Phys. B **357** (1991) 32.
- [122] ATLAS Collaboration, *Jet Calibration and Systematic Uncertainties for Jets Reconstructed in the ATLAS Detector at  $\sqrt{s} = 13$  TeV*, tech. rep. ATL-PHYS-PUB-2015-015, CERN, 2015, URL: <https://cds.cern.ch/record/2037613>.
- [123] ATLAS Collaboration, *JetUncertainties package, MultijetJESUncertaintyProvider tool*, version 00.08.25, release date 05.10.2014, <https://svnweb.cern.ch/trac/atlasoff/browser/Reconstruction/Jet/JetUncertainties/tags/JetUncertainties-00-08-25/JetUncertainties/MultijetJESUncertaintyProvider.h> and <https://svnweb.cern.ch/trac/atlasoff/browser/Reconstruction/Jet/JetUncertainties/tags/JetUncertainties-00-08-25/Root/MultijetJESUncertaintyProvider.cxx>.
- [124] M. Cacciari, G. P. Salam and G. Soyez, *The catchment area of jets*, JHEP **2008** (2008) 005, arXiv: 0802.1188 [hep-ph].
- [125] F. Chollet et al., *Keras*, 2015, URL: <https://github.com/fchollet/keras>.
- [126] D. H. Guest et al., *lwtnn: Release for Athena v21*, 2017, URL: <https://doi.org/10.5281/zenodo.290682>.
- [127] O. Behnke et al., *Data Analysis in High Energy Physics: A Practical Guide to Statistical Methods*, Wiley, 2013, ISBN: 9783527653430.

# APPENDIX A

---

## Extra Material for the 8 TeV Analysis

---

### A.1 Hadronic-fake Template

#### A.1.1 Hadronic-fake Template and the Jet Multiplicity

As shown in Section 7.3.2.1, the shape of the hadronic-fake template has a dependency on the number of jets in the event. For this reason, events in the hadronic-fake enriched control region are required to have at least four jets, to have the same topology as the signal events. However, the jet multiplicity distributions in the control region and the signal region show some discrepancy, as can be seen from Figure A.1. Therefore, a study is performed to check if it is needed to assign a systematic uncertainty to cover any potential bias due to the extrapolation from a control region with a different topology than the signal region.

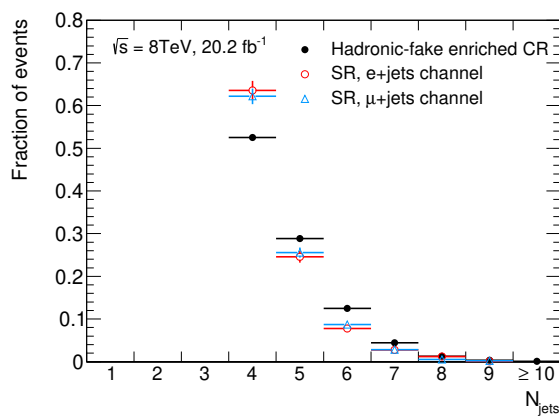


Figure A.1: The jet multiplicity distribution in the hadronic-fake enriched control region and the signal region. The distributions are normalised to unity and the last bin contains the overflows.

The nominal hadronic-fake template, which is extracted requiring  $N_{\text{jets}} \geq 4$ , is compared to templates extracted by varying the required  $N_{\text{jets}}$ , with the aim of taking the shape differences as the systematic uncertainty. This comparison is shown in Figure A.2. The total uncertainty of the nominal template in Figure A.2, which includes the systematic uncertainties due to the prompt-photon contamination and re-weighting, is shown by error bars. The shape difference of the modified and the nominal templates is small and covered by the uncertainty band of the nominal template. Any additional systematic un-

certainty due to the  $N_{\text{jets}}$  is specially much smaller than the prompt-photon contamination systematic uncertainty, so it will not affect the final result. As a result of this study, no additional systematic uncertainty is considered.

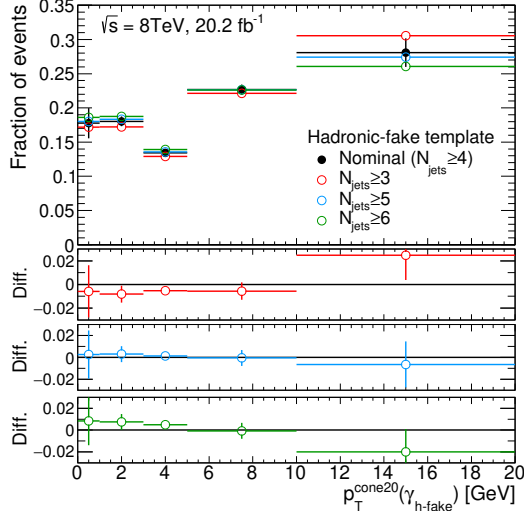


Figure A.2: The nominal hadronic-fake template, extracted by requiring  $N_{\text{jets}} \geq 4$ , and modified templates extracted by varying the required  $N_{\text{jets}}$ . The distributions are normalised to unity and the last bin contains the overflows. The uncertainty of nominal template includes all systematic uncertainties. The shape difference of each modified template with respect to the nominal one are shown in the three lower panels.

### A.1.2 Hadronic-fake Template Re-weighting Using More $\eta$ Bins

As a cross check, the hadronic-fake template re-weighting process is repeated by increasing the number of  $\eta$  bins in Equation 7.2 from two to seven. The seven photon  $\eta$  bins that are used here can be seen in Figure 7.5(b), which are motivated by detector geometry. The resulted weighted template and the nominal weighted template are compared in Figure A.3. No significant difference in the shape of the templates can be seen. The only visible difference is the larger uncertainty for the template weighted by seven bins, which is due to the larger statistical uncertainty when the  $t\bar{t}\gamma_{\text{h-fake}}$  control region is divided into finer bins.

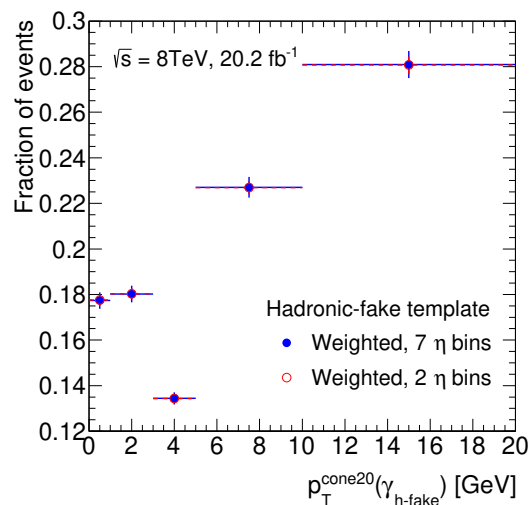


Figure A.3: Hadronic-fake templates for the inclusive measurement, weighted by using seven photon  $\eta$  bins (blue) and two photon  $\eta$  bins (red), with the same number of photon  $p_T$  bins. Distributions are normalised to unity and their last bin contains the overflow.



---

## Extra Material for the 13 TeV Analysis

---

### B.1 Hadronic-fake Background Estimation

#### B.1.1 Origin of Hadronic-fake Photons

In this appendix the studies on the origin of hadronic-fake photons in the four regions of A, B, C and D (i.e. signal region) are presented.

Based on the yields from the MC samples, the dominant process that contribute to the hadronic-fake background in all the four regions and in both  $e$ +jets and  $\mu$ +jets channels is  $t\bar{t}$ . The  $t\bar{t}$  contribution is 91%(87%) in region A, 85%(85%) in region B, 89%(89%) in region C and 91%(90%) in signal region in the  $e$ +jets ( $\mu$ +jets) channel. The second and third ranks switch between  $W$ +jets and single top processes across the regions and channels, but with very small difference, and together their contributions are 7%(12%) in region A, 13%(13%) in region B, 9%(10%) in region C and 7%(9%) in signal region in the  $e$ +jets ( $\mu$ +jets) channel.

In Figures B.1 and B.2 the truth origin of hadronic-fake photons at the particle level (i.e. after simulation of hadronisation and showering processes and before adding the detector simulation) in all the processes that contribute to the hadronic-fake background are shown for  $e$ +jets and  $\mu$ +jets channels, respectively, in the four regions. The truth photon origin information is extracted as explained in Section 5.2.3. From these figures one can see that hadronic-fakes are dominantly originated from  $\pi^0$  decays, with a smaller contribution coming from other light meson decays, and this is consistent across the four regions and the two channels.

Another study is performed by using the truth information at the parton level (i.e. before simulation of hadronisation and showering processes and before the detector simulation). The reconstructed hadronic-fake photons in the four regions are matched to the partons within a  $\Delta R < 0.2$  distance. In this study, only the  $t\bar{t}$  MC sample is used, as it is the dominant process. The results are shown in Figures B.3(a) and B.3(b) for  $e$ +jets and  $\mu$ +jets channels, respectively. The first bin in all plots ("non.") shows the fraction of events where no parton matched to the hadronic-fake photon within  $\Delta R < 0.2$  is found, therefore it contains the events where hadronic-fake photons are originated from extra gluon jets of the QCD radiations<sup>1</sup>. In both channels and all four regions the dominant source of hadronic-fake photons are the light quarks from  $W$  boson. However, in the non-isolated regions (region B and C) the percentage of hadronic-fake photons originating from  $b$  quarks are higher than in the isolated regions (region A and signal region).

---

<sup>1</sup> The number of gluon initiated jets per event is not known here, since this study is done only using a parton-level information, while the additional QCD radiations are simulated in later simulation levels.

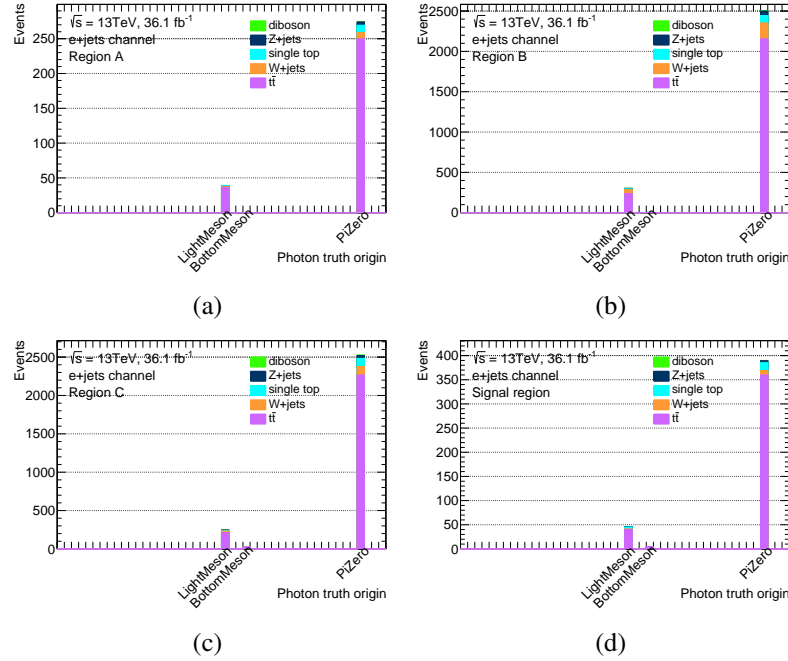


Figure B.1: Hadronic-fake photon truth origin according to the `MCTruthClassifier` package, in region (a) A, (b) B, (c) C and (d) signal region, in the  $e+jets$  channel.

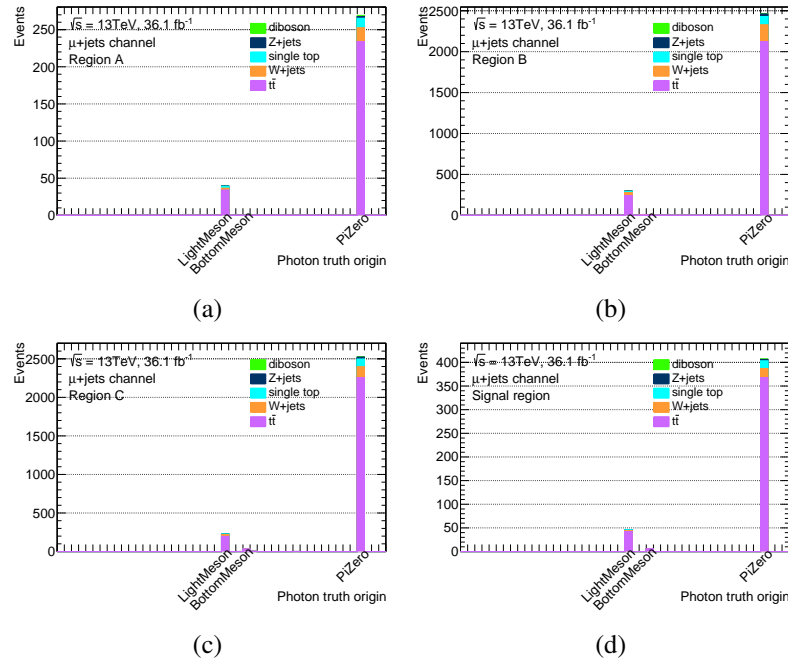


Figure B.2: Hadronic-fake photon truth origin according to the `MCTruthClassifier` package, in region (a) A, (b) B, (c) C and (d) signal region, in the  $\mu+jets$  channel.

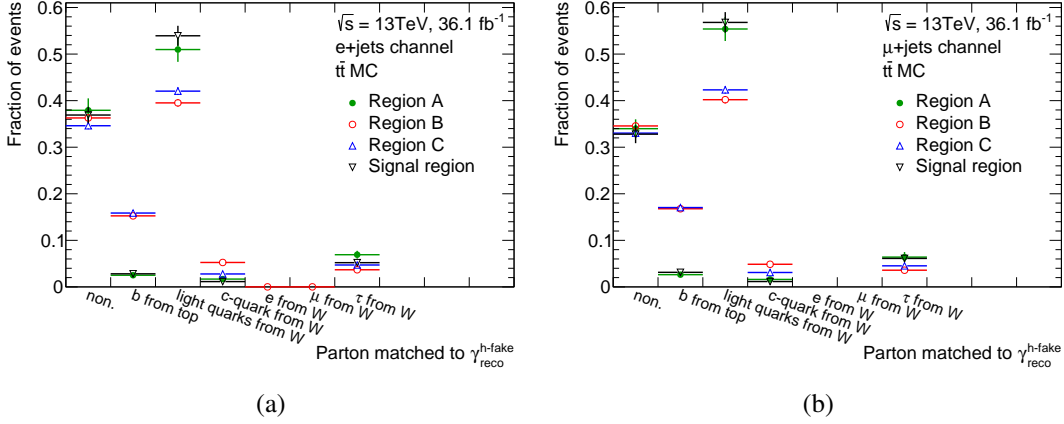
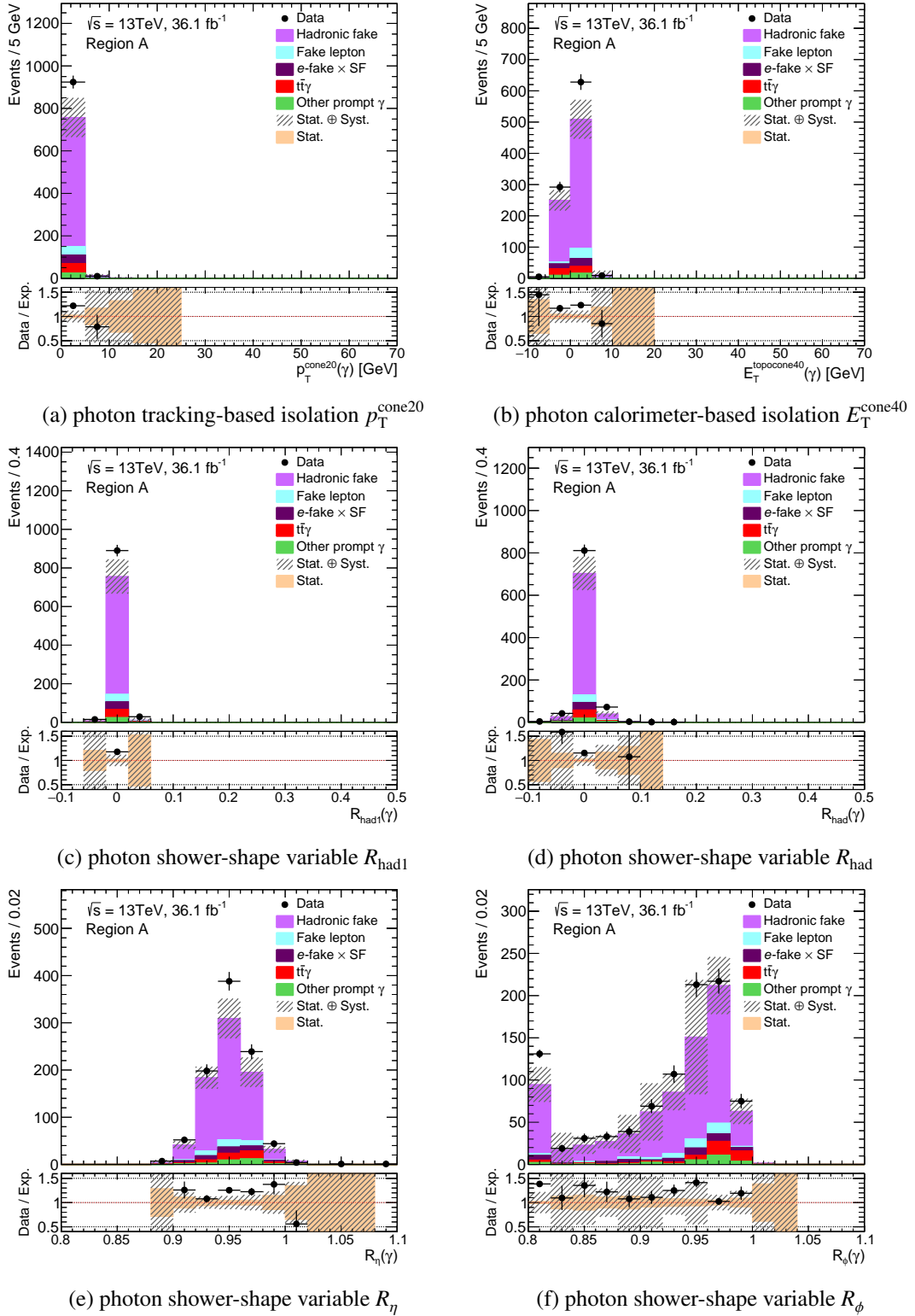
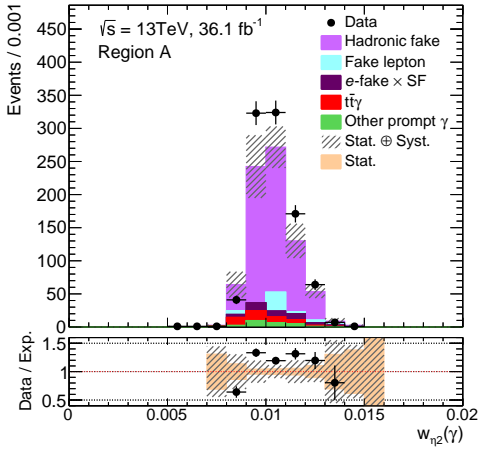
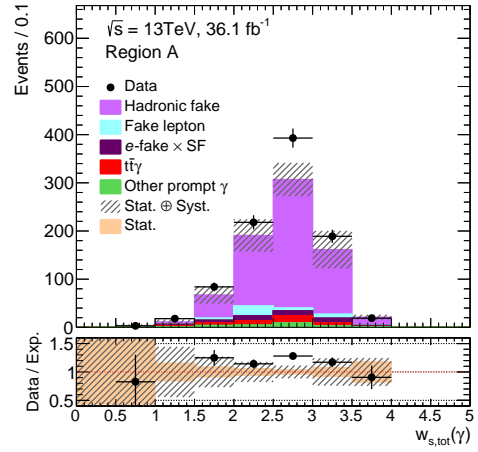
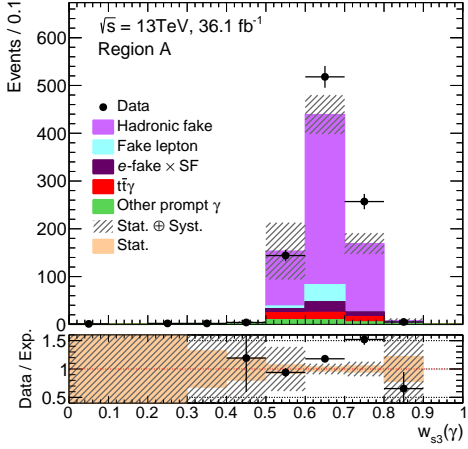
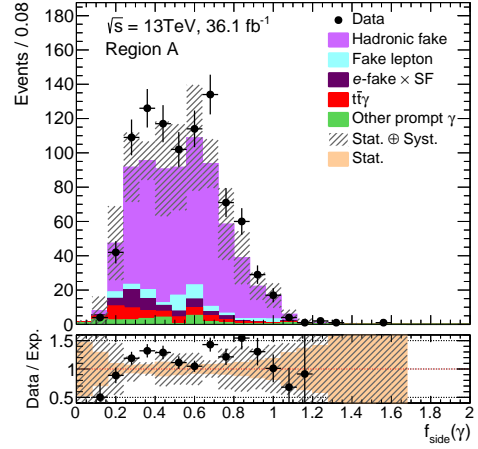
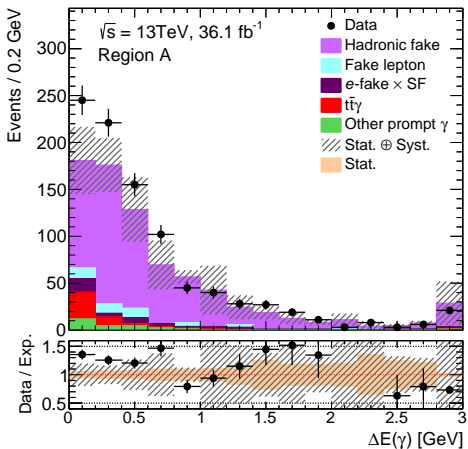
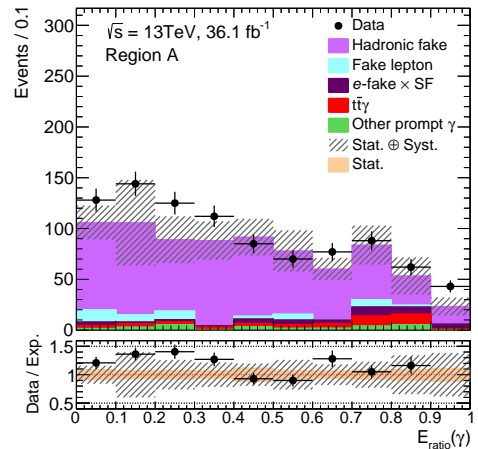


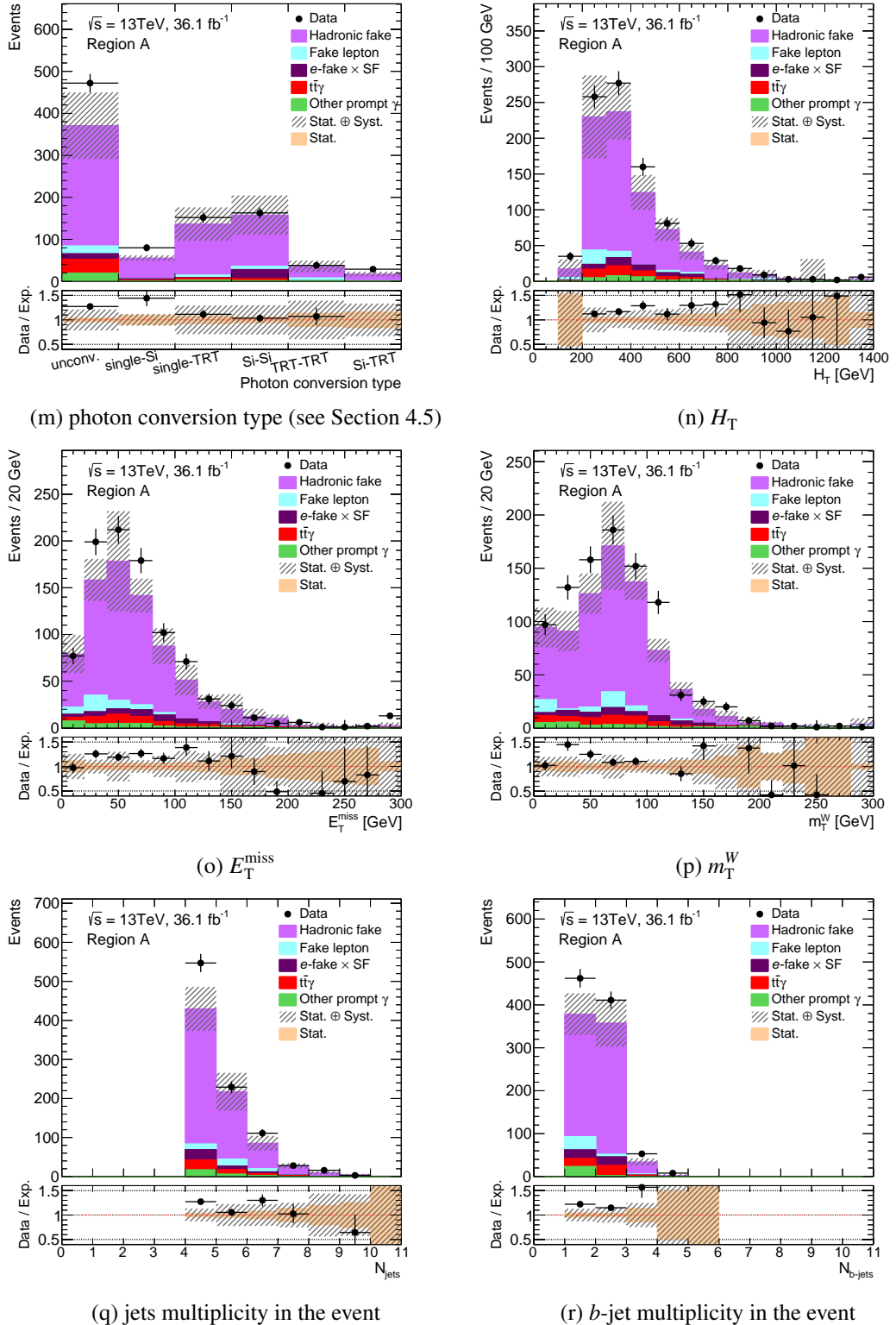
Figure B.3: Partons matched to a hadronic-fake photon in (a)  $e + \text{jets}$  and (b)  $\mu + \text{jets}$  channel, using  $t\bar{t}$  simulated sample. The first bin shows the fraction of events where no matched parton is found (within a  $\Delta R < 0.2$  distance), therefore it includes the events with hadronic-fake photons originated from extra jets.

## B.1.2 More Control Plots

In addition to Section 8.3.1.1, more control plots for regions A, B and C are shown in Figures B.4, B.5 and B.6, respectively.




 (g) photon shower-shape variable  $w_{\eta 2}$ 

 (h) photon shower-shape variable  $w_{s,\text{tot}}$ 

 (i) photon shower-shape variable  $w_{s3}$ 

 (j) photon shower-shape variable  $f_{\text{side}}$ 

 (k) photon shower-shape variable  $\Delta E$ 

 (l) photon shower-shape variable  $E_{\text{ratio}}$



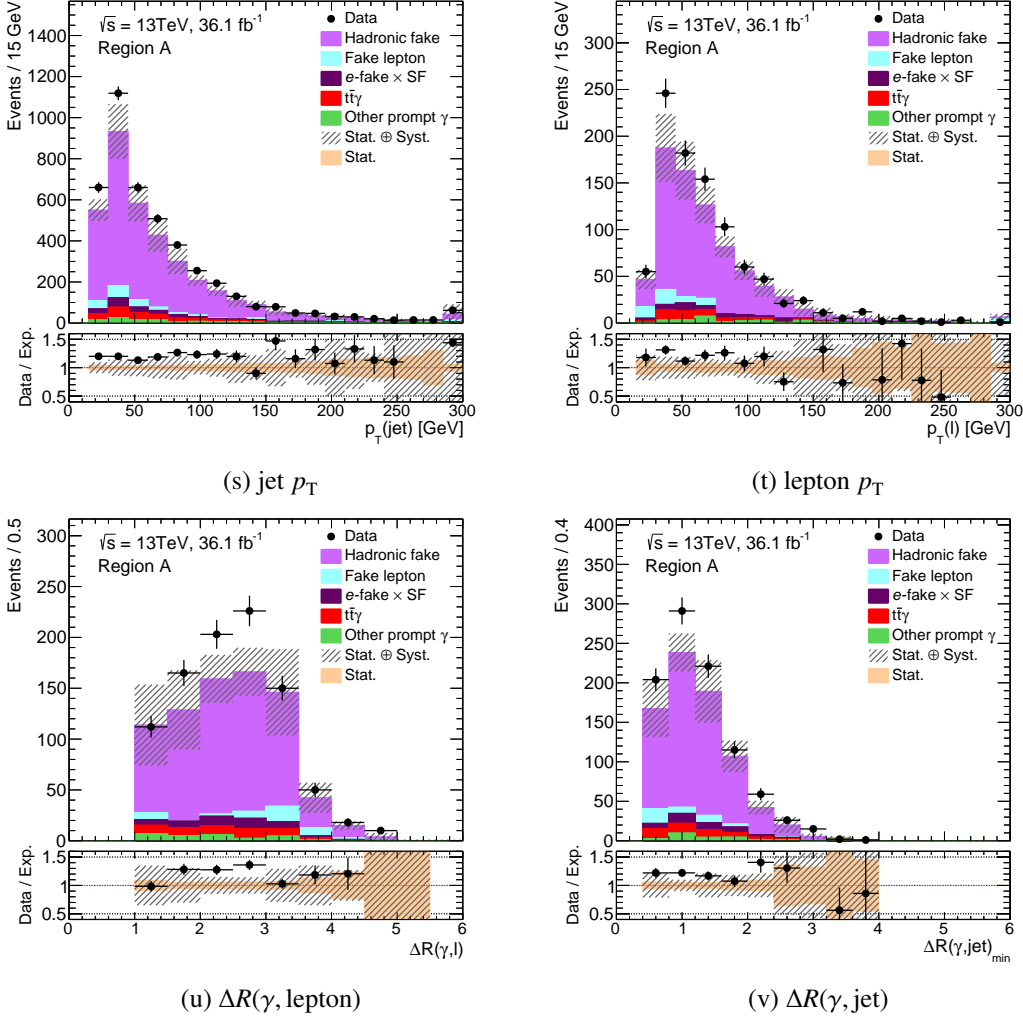
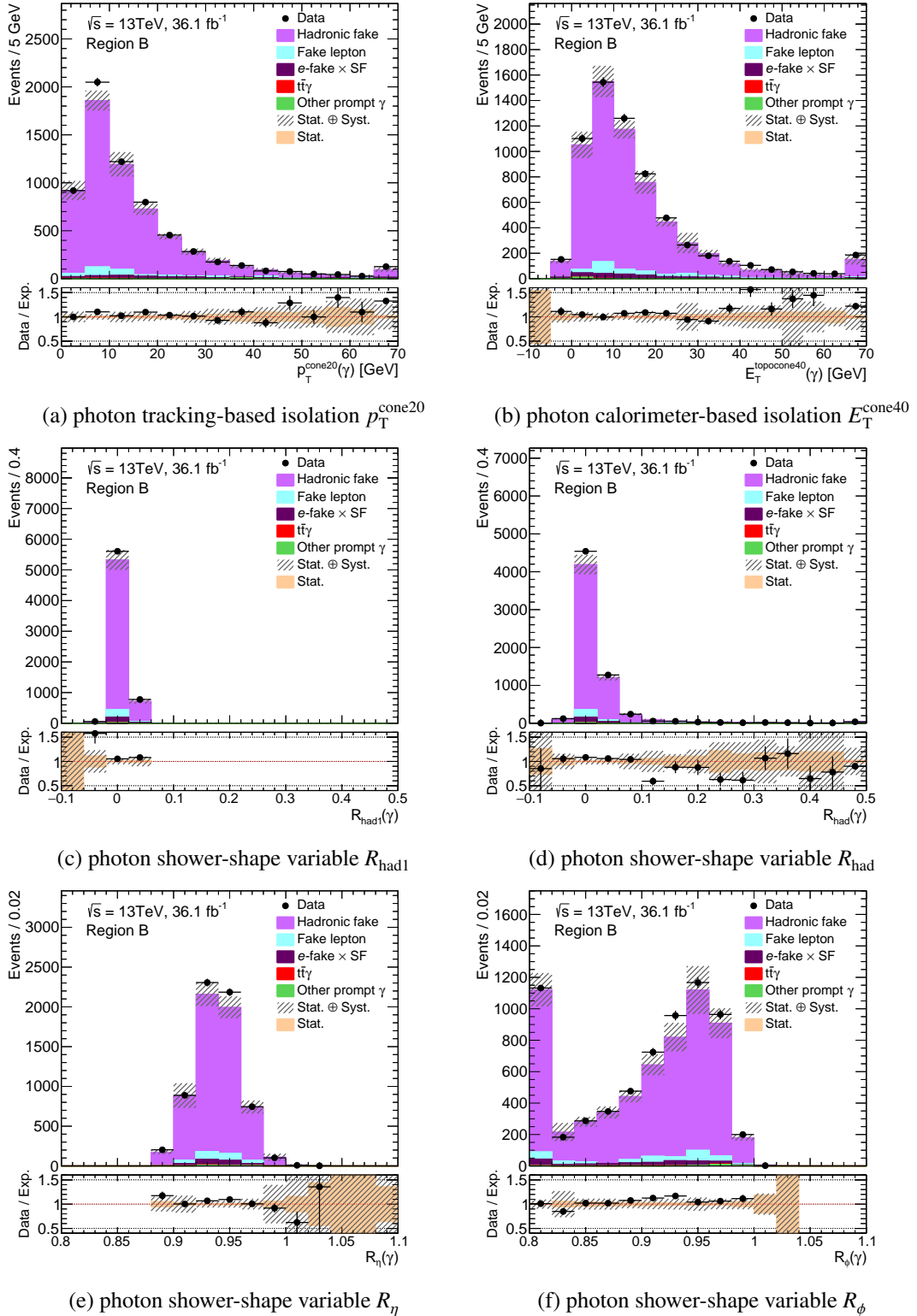
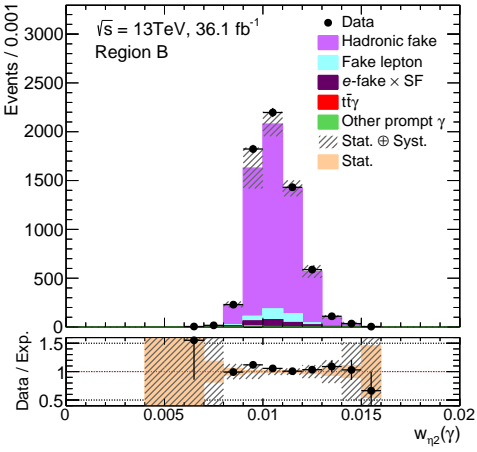
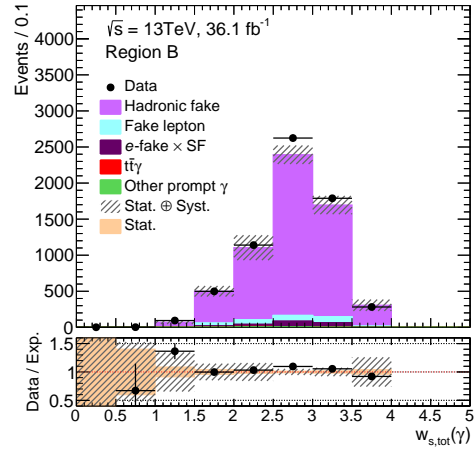
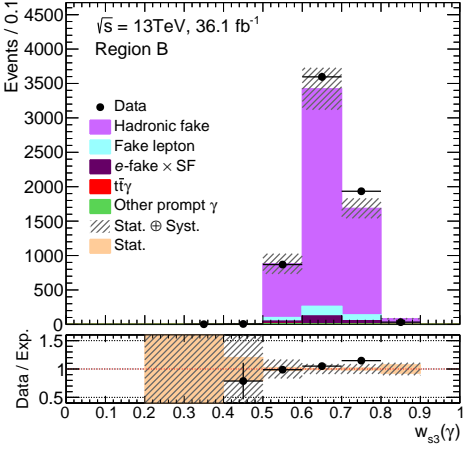
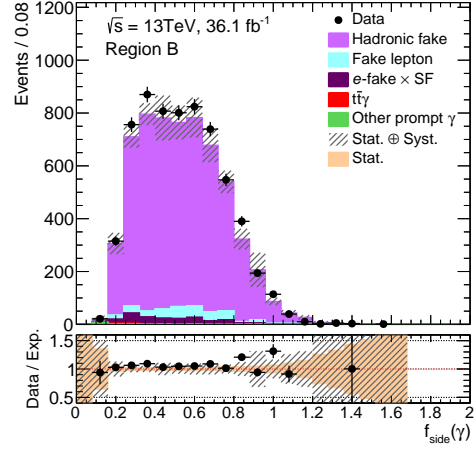
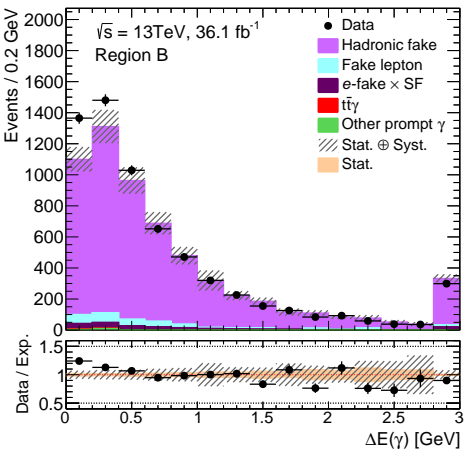
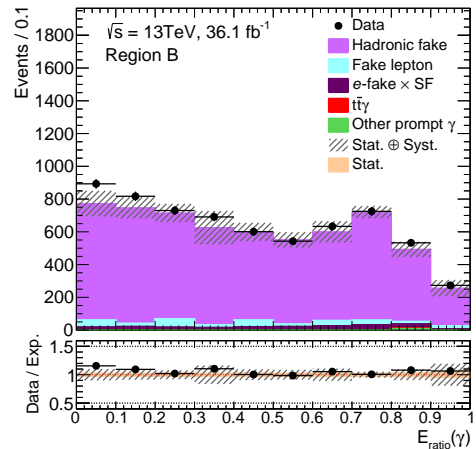
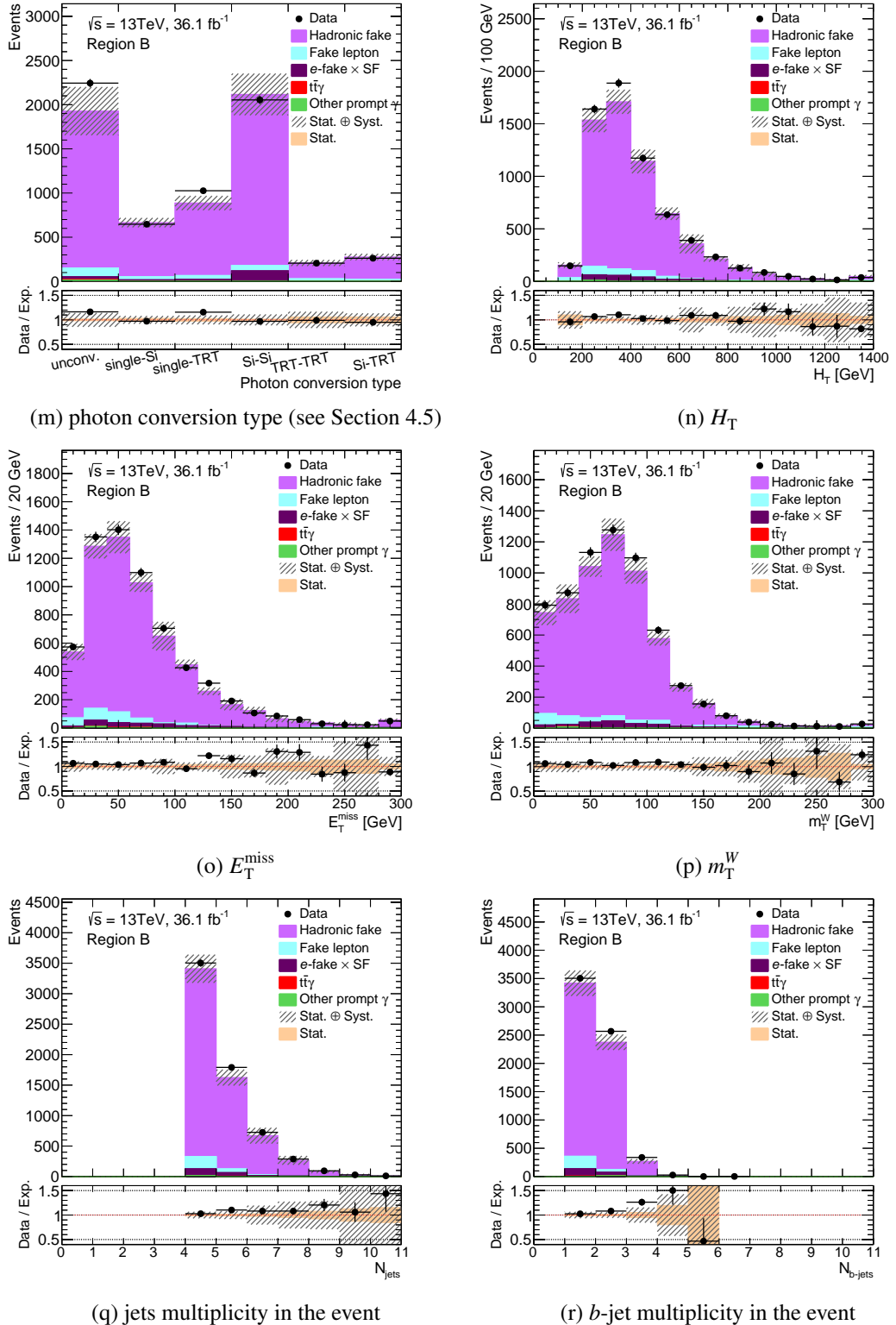


Figure B.4: More plots of region A in single-lepton channel, where photons are isolated and identified as fail-Tight. In each plot, the dashed area shows the total uncertainty of the total expectation while the solid band in the ratio panel shows the statistical uncertainty of the total expectation.




 (g) photon shower-shape variable  $w_{\eta 2}$ 

 (h) photon shower-shape variable  $w_{s,\text{tot}}$ 

 (i) photon shower-shape variable  $w_{s3}$ 

 (j) photon shower-shape variable  $f_{\text{side}}$ 

 (k) photon shower-shape variable  $\Delta E$ 

 (l) photon shower-shape variable  $E_{\text{ratio}}$



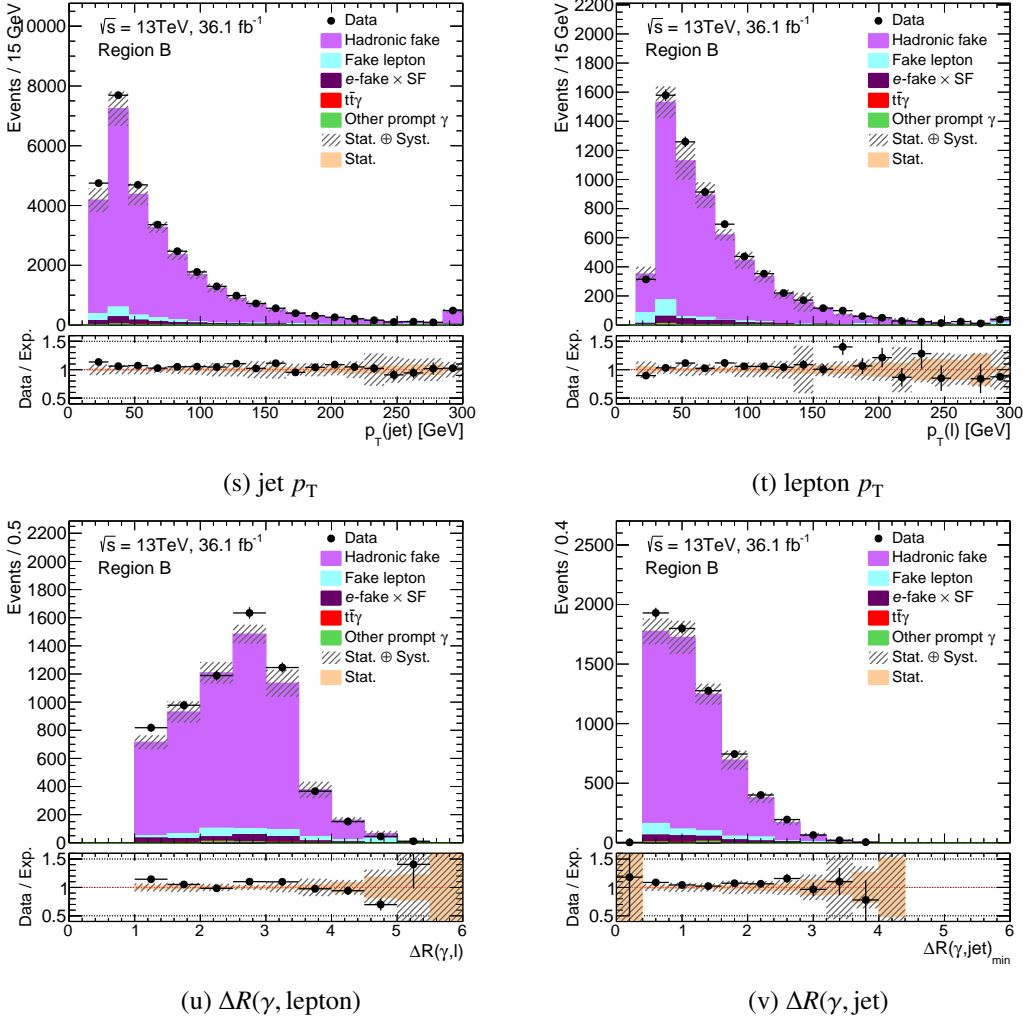
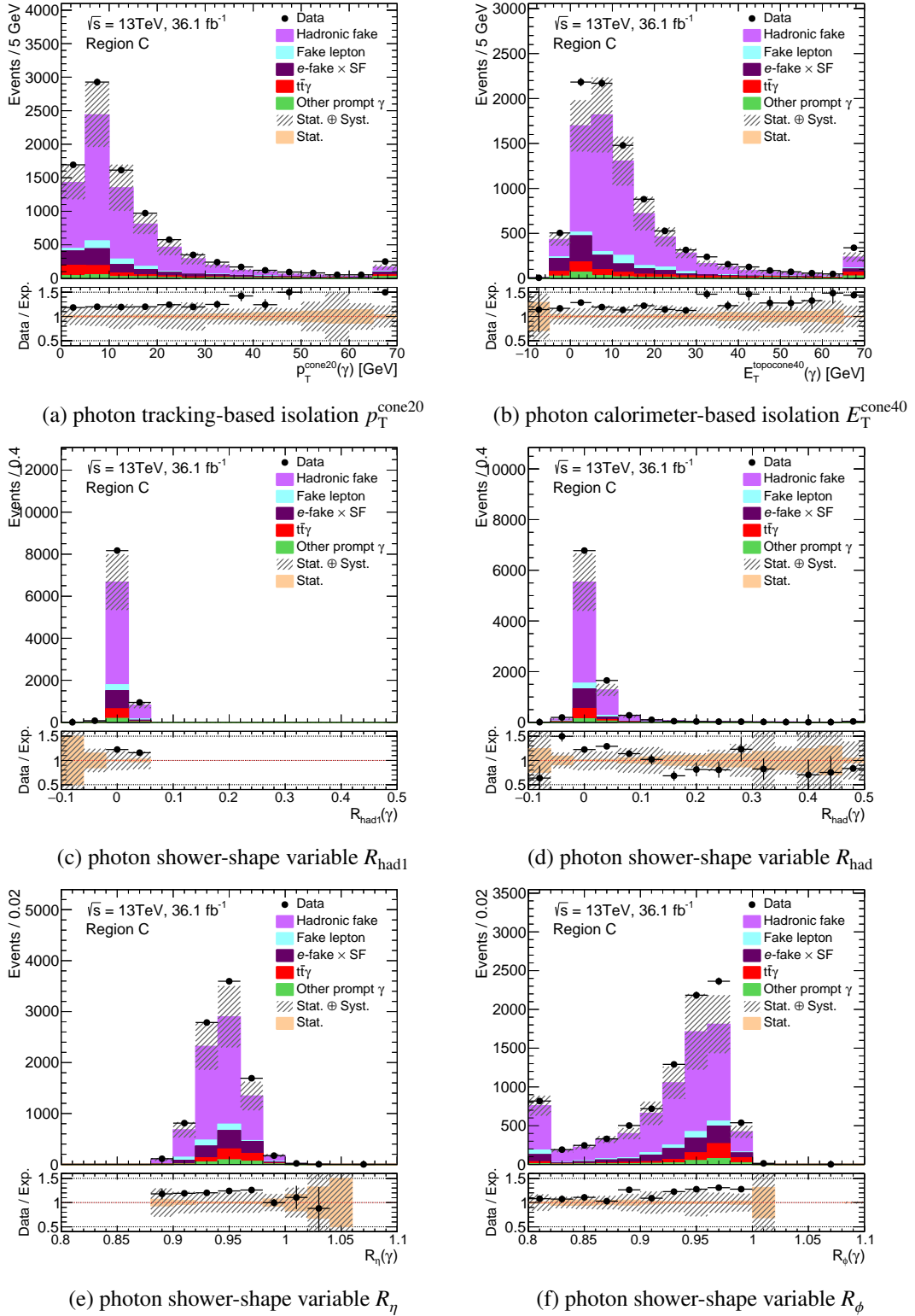
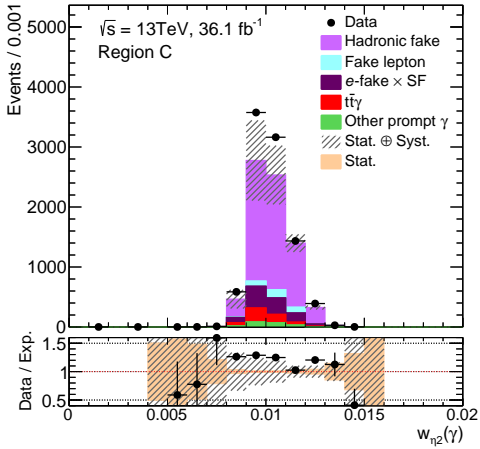
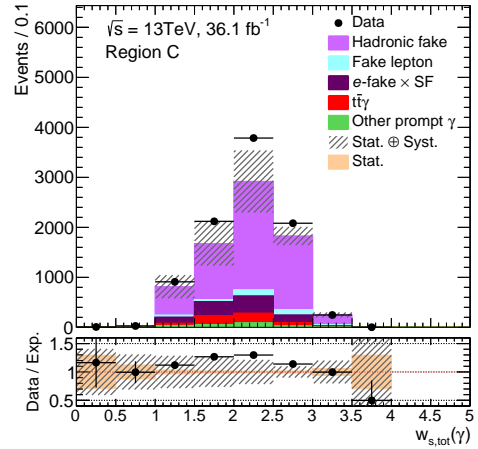
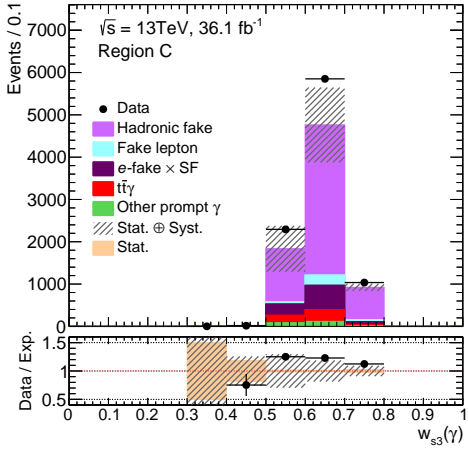
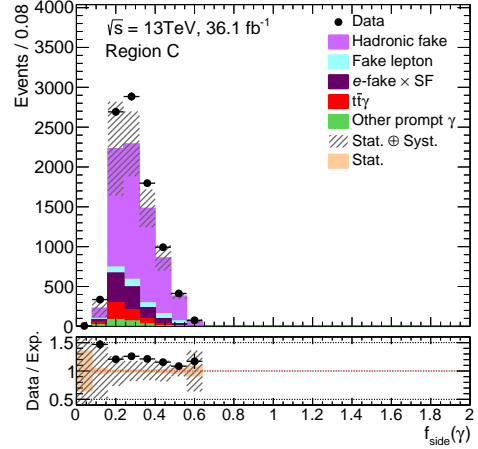
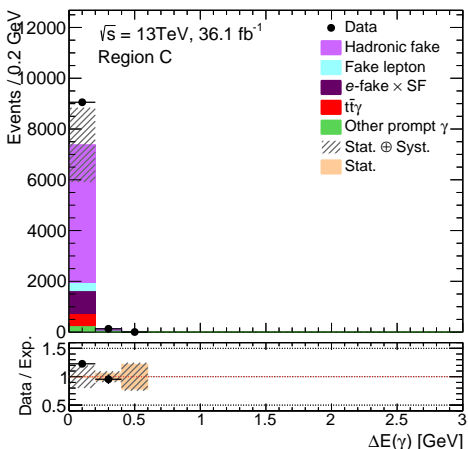
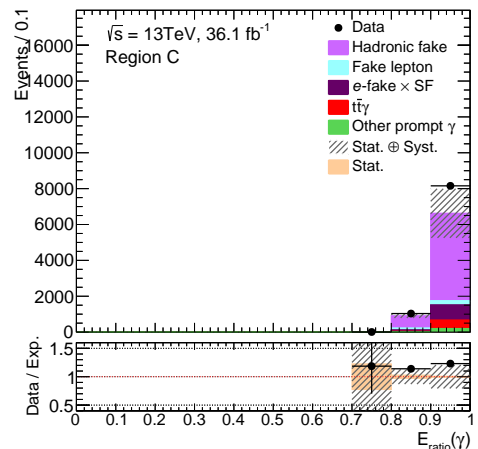
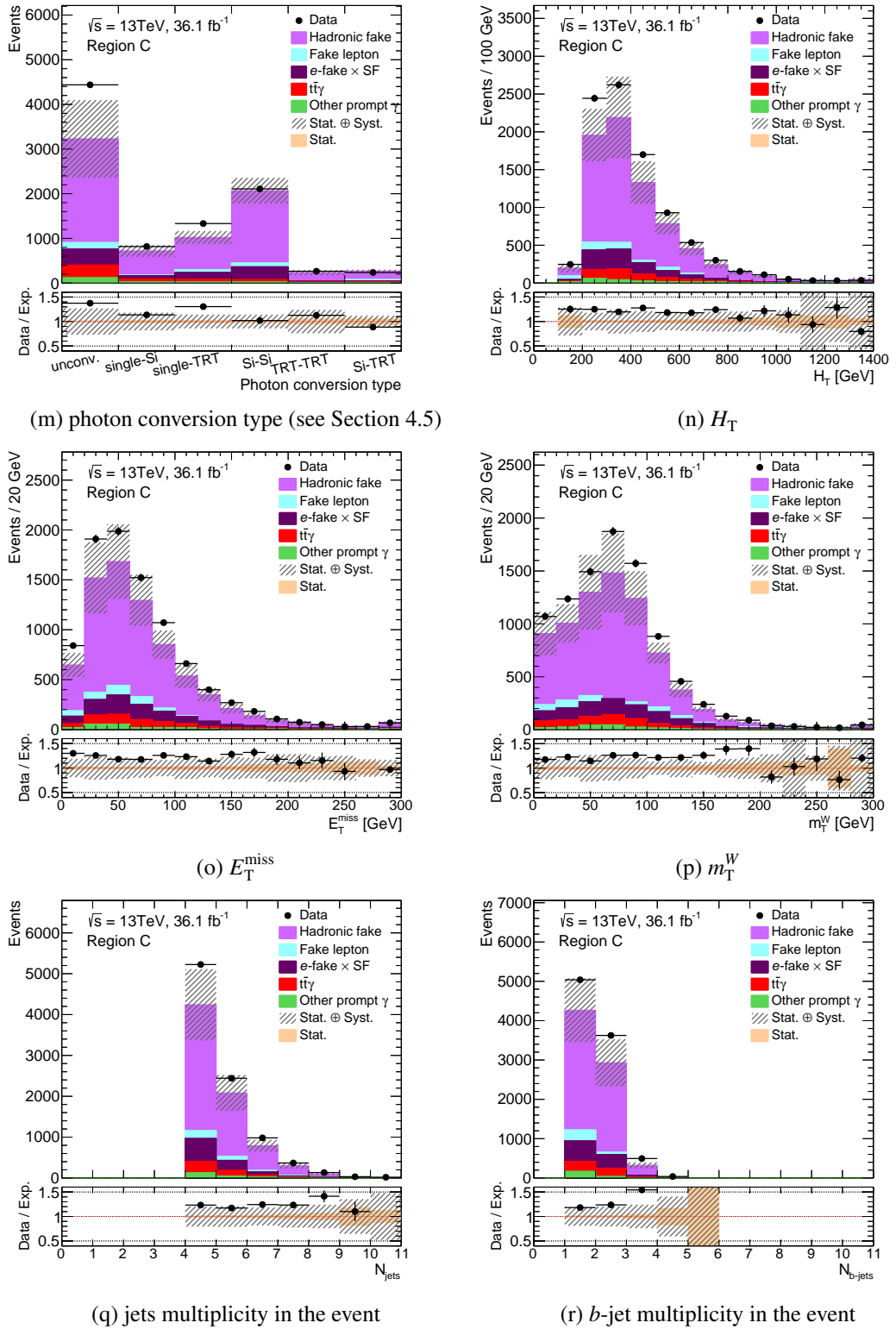


Figure B.5: More plots of region B in single-lepton channel, where photons are identified as fail-Tight as well being non-isolated. In each plot, the dashed area shows the total uncertainty of the total expectation while the solid band in the ratio panel shows the statistical uncertainty of the total expectation.




 (g) photon shower-shape variable  $w_{\eta 2}$ 

 (h) photon shower-shape variable  $w_{s,\text{tot}}$ 

 (i) photon shower-shape variable  $w_{s3}$ 

 (j) photon shower-shape variable  $f_{\text{side}}$ 

 (k) photon shower-shape variable  $\Delta E$ 

 (l) photon shower-shape variable  $E_{\text{ratio}}$



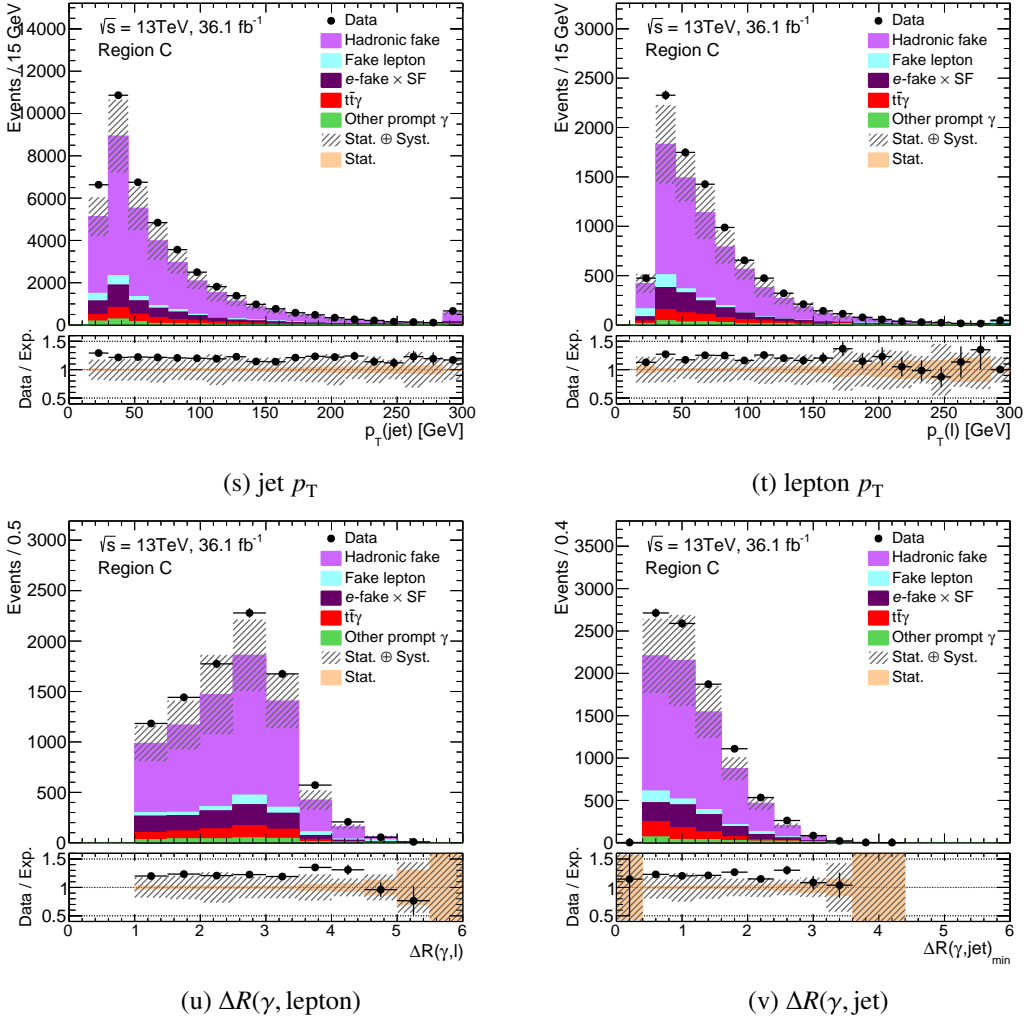


Figure B.6: More plots of region C in single-lepton channel, where photons are non-isolated and identified as Tight. In each plot, the dashed area shows the total uncertainty of the total expectation while the solid band in the ratio panel shows the statistical uncertainty of the total expectation.

### B.1.3 More on MC-based Double Ratio

The  $\theta_{\text{MC}}$  measured only as a function of photon  $p_{\text{T}}$  or photon  $\eta$  or photon conversion status are shown in Figure B.7. Figures B.8 and B.9 show the  $\theta_{\text{MC}}$  measured separately for the converted and unconverted photons, respectively, as a function of photon  $p_{\text{T}}$  or photon  $\eta$ . They are all also summarised in Table B.1, together with the inclusive measured  $\theta_{\text{MC}}$  for comparison.

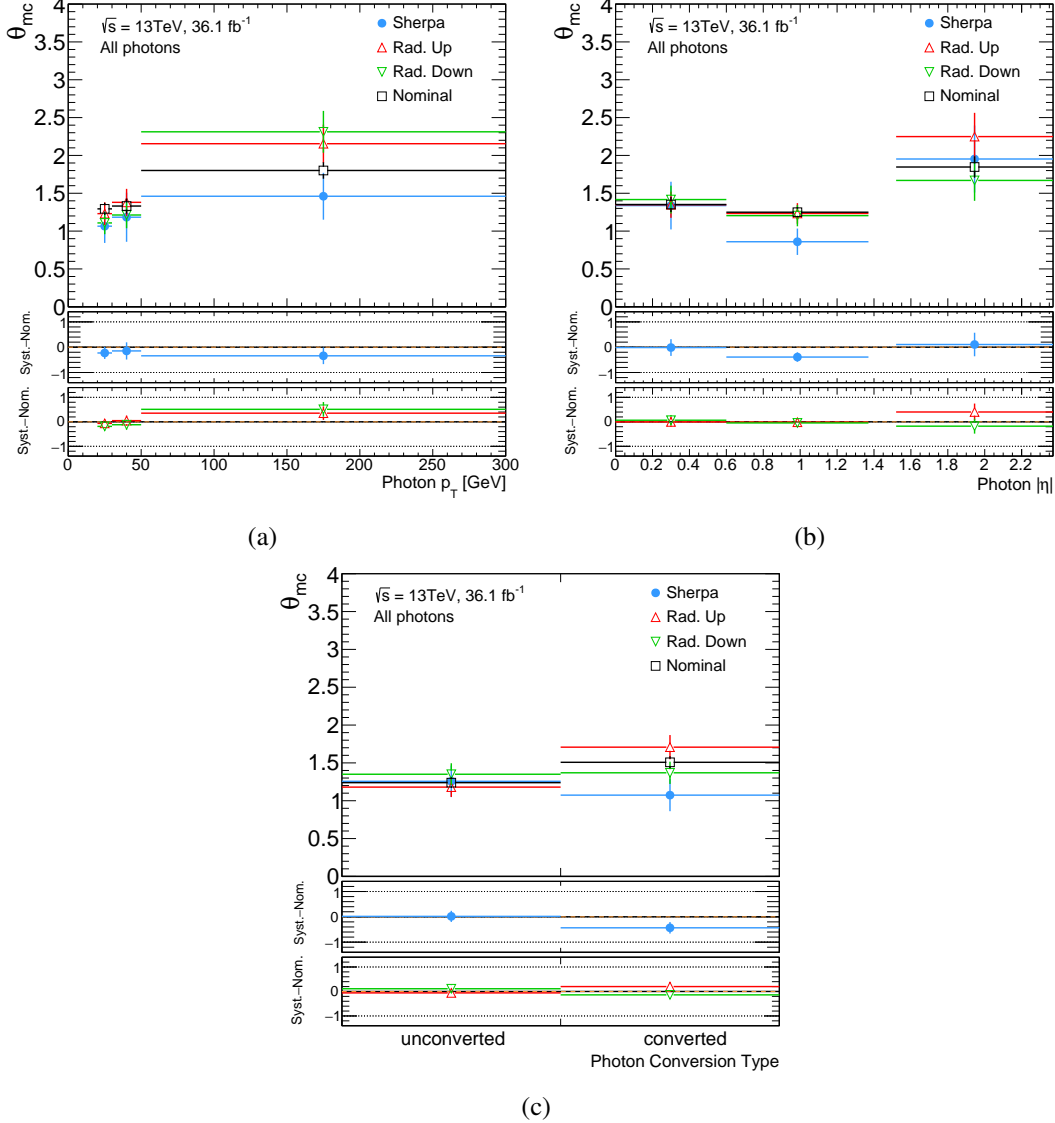


Figure B.7: The MC-based double ratio  $\theta_{\text{MC}}$  measured for all photons as function of (a) photon  $p_{\text{T}}$ , (b) photon  $\eta$  and (c) photon conversion status, from nominal MC and alternative MC samples that are used for systematic uncertainty evaluation. The error bars show the statistical uncertainties.

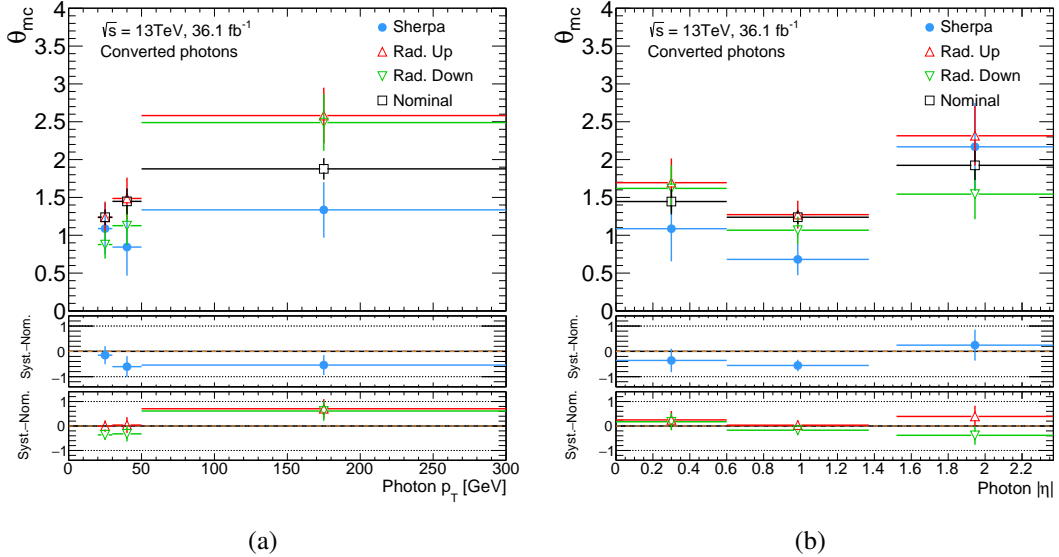


Figure B.8: The MC-based double ratio  $\theta_{MC}$  measured for converted photons as function of (a) photon  $p_T$  and (b) photon  $\eta$ , from nominal MC and alternative MC samples that are used for systematic uncertainty evaluation. The error bars show the statistical uncertainties.

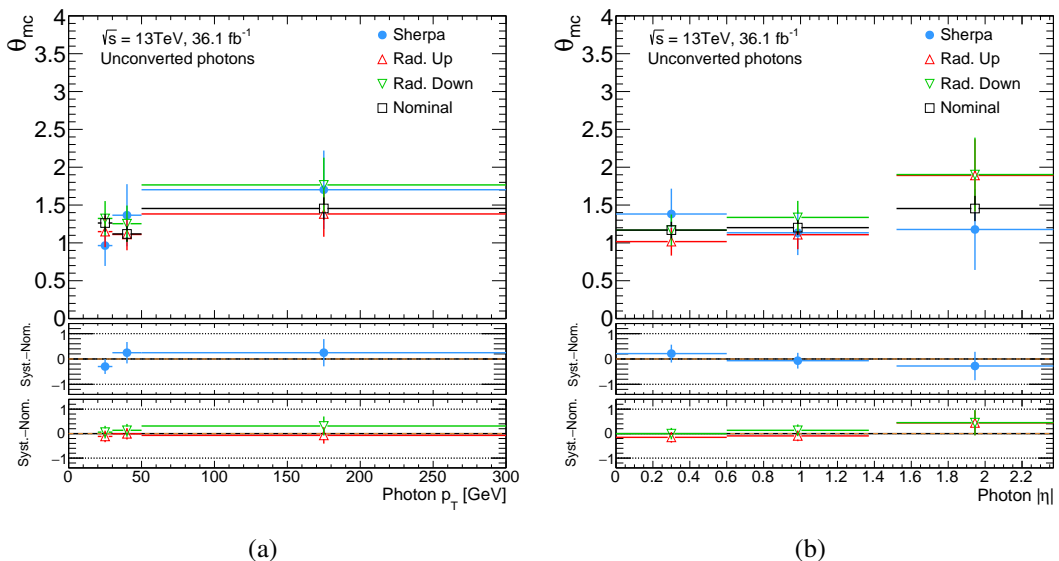


Figure B.9: The MC-based double ratio  $\theta_{MC}$  measured for unconverted photons as function of (a) photon  $p_T$  and (b) photon  $\eta$ , from nominal MC and alternative MC samples that are used for systematic uncertainty evaluation. The error bars show the statistical uncertainties.

Photon conversion status	Photon $p_T$ [GeV]	Photon $\eta$	$\theta_{MC} \pm$ Total uncertainty	Stat. uncertainty	Syst. uncertainty		
					rad.-up	rad.-down	Gen. & PS
All	Inclusive	Inclusive	$1.44 \pm 0.24$	$\pm 0.06$	$+0.08$	$-0.03$	$\pm 0.22$
	20 – 30	Inclusive	$1.29 \pm 0.31$	$\pm 0.08$	$-0.06$	$-0.19$	$\pm 0.23$
	30 – 50		$1.33 \pm 0.21$	$\pm 0.10$	$+0.05$	$-0.12$	$\pm 0.15$
	> 50		$1.80 \pm 0.62$	$\pm 0.11$	$+0.35$	$-0.51$	$\pm 0.34$
	Inclusive	$ \eta  < 0.60$	$1.35 \pm 0.12$	$\pm 0.10$	$+0.00$	$-0.07$	$\pm 0.01$
		$0.60 <  \eta  < 1.37$	$1.25 \pm 0.40$	$\pm 0.07$	$-0.02$	$-0.05$	$\pm 0.39$
		$1.52 <  \eta  < 2.37$	$1.85 \pm 0.44$	$\pm 0.14$	$+0.40$	$-0.18$	$\pm 0.11$
Converted	Inclusive	Inclusive	$1.51 \pm 0.48$	$\pm 0.08$	$+0.20$	$-0.14$	$\pm 0.43$
	20 – 30	Inclusive	$1.24 \pm 0.40$	$\pm 0.10$	$+0.00$	$-0.36$	$\pm 0.15$
	30 – 50		$1.45 \pm 0.71$	$\pm 0.17$	$+0.04$	$-0.32$	$\pm 0.60$
	> 50		$1.88 \pm 0.90$	$\pm 0.14$	$+0.70$	$-0.61$	$\pm 0.54$
	Inclusive	$ \eta  < 0.60$	$1.45 \pm 0.47$	$\pm 0.17$	$+0.25$	$-0.17$	$\pm 0.36$
		$0.60 <  \eta  < 1.37$	$1.34 \pm 0.57$	$\pm 0.08$	$+0.12$	$-0.06$	$\pm 0.55$
		$1.52 <  \eta  < 2.37$	$1.92 \pm 0.50$	$\pm 0.19$	$+0.39$	$-0.38$	$\pm 0.24$
Unconverted	Inclusive	Inclusive	$1.24 \pm 0.13$	$\pm 0.07$	$-0.06$	$-0.11$	$\pm 0.02$
	20 – 30	Inclusive	$1.26 \pm 0.34$	$\pm 0.12$	$-0.11$	$-0.06$	$\pm 0.30$
	30 – 50		$1.12 \pm 0.30$	$\pm 0.10$	$-0.01$	$-0.14$	$\pm 0.25$
	> 50		$1.45 \pm 0.42$	$\pm 0.15$	$-0.07$	$-0.31$	$\pm 0.25$
	Inclusive	$ \eta  < 0.60$	$1.17 \pm 0.28$	$\pm 0.11$	$-0.15$	$-0.00$	$\pm 0.21$
		$0.60 <  \eta  < 1.37$	$1.20 \pm 0.15$	$\pm 0.07$	$-0.12$	$-0.07$	$\pm 0.06$
		$1.52 <  \eta  < 2.37$	$1.45 \pm 0.55$	$\pm 0.17$	$+0.44$	$-0.45$	$\pm 0.28$

Table B.1: The MC-based double ratio  $\theta_{MC}$ , measured for inclusive, 1-dimensional and 2-dimensional bins of photon  $p_T$ ,  $\eta$  and conversion status, together with a break down of the uncertainties. The  $t\bar{t}$  modelling uncertainty on hard scattering and parton shower and hadronisation denoted by Gen. & PS. The uncertainty on  $t\bar{t}$  modelling due to scale choices and the modelling of ISR and FSR are denoted by rad.-up/-down. Note that inclusive  $p_T$  means  $p_T > 20$  and inclusive  $\eta$  is in fact  $|\eta| < 2.37$ .

### B.1.4 Data-Driven Double Ratio

If the double ratio in Equation 8.7 could be directly calculated from data, it will not be subject to modelling uncertainties as in the case of  $\theta_{MC}$ . Obviously one can not use the same A, B, C and D regions in data in Equation 8.7 to calculate the double ratio from data, as the number of hadronic-fakes in region D (i.e. signal region) in data is the unknown that is being estimated from the ABCD method itself. However, an equivalent double ratio,  $\theta'_{d.d.}$ , can be calculated from four new control regions in data, A', B', C' and D', corresponding to new definitions of isolated and non-isolated photons but same Tight and fail-Tight photon identification. These new regions are derived by splitting regions B and C, after reducing the isolation gap<sup>2</sup>. Figure B.10 illustrate the new A', B', C' and D' regions and the original A, B, C, and D regions.

Then, the data-driven double ratio is calculated as:

$$\theta'_{d.d.} = \frac{N_{D',\text{data}}^{\text{h-fake}} / N_{C',\text{data}}^{\text{h-fake}}}{N_{A',\text{data}}^{\text{h-fake}} / N_{B',\text{data}}^{\text{h-fake}}}, \quad (\text{B.1})$$

where the non-hadronic-fake and the fake lepton backgrounds are subtracted from data same as in Equation 8.6.

To define the new regions, the photon  $p_T^{\text{cone}20}$  distributions of regions B and C before applying the

<sup>2</sup> Isolation gap refers to the requirement  $p_T^{\text{cone}20} > 3$  GeV for the photons in control regions B and C, applied to reduce the contamination from prompt photons. See Section 8.3.1.

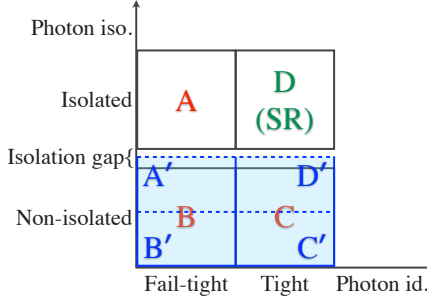


Figure B.10: An illustration of the regions  $A'$ ,  $B'$ ,  $C'$  and  $D'$  used for calculation of  $\theta'_{\text{d.d.}}$ , which are derived from dividing regions  $B$  and  $C$  after removal of the isolation gap.

isolation gap, shown in Figure 8.3, are used. Using these distributions, events are divided into low and high  $p_T^{\text{cone}20}$  regions, corresponding to new categories of isolated and non-isolated photons. Splitting the distribution in Figure 8.3(a) gives regions  $A'$  and  $B'$ , and the distribution in Figure 8.3(b) is used to obtain regions  $D'$  and  $C'$ .

Based on the photon  $p_T^{\text{cone}20}$  value at which the distributions are split, and how far the isolation gap is reduced, different boundaries defining the new regions are checked. The lower boundaries of region  $A'$  and region  $D'$  are varied by using three different requirement on minimum photon  $p_T^{\text{cone}20}$ , at 1, 2 and 3 GeV. The upper boundaries of region  $A'$  and region  $D'$ , which coincide with the lower boundaries of region  $B'$  and region  $C'$  respectively, are varied by placing nine different requirements on maximum  $p_T^{\text{cone}20}$ , at 7, 8, 9, 10, 11, 12, 13, 14 and 15 GeV. Regions  $B'$  and  $C'$  do not have an upper boundary.

The resulting  $\theta'_{\text{d.d.}}$  for these different choices of the control region  $p_T^{\text{cone}20}$  boundaries are shown in Figure B.11 for inclusive photons and as a function of photon conversion status, in Figures B.12 as a function of photon  $p_T$  and in Figure B.13 as a function of photon  $\eta$ . In all above figures the  $\theta'_{\text{d.d.}}$  is compared to the equivalent MC-based double ratio  $\theta'_{\text{MC}}$ , which is calculated from same  $A'$ ,  $B'$ ,  $C'$  and  $D'$  regions, only by replacing the data in Equation B.1 by MC. The comparison is shown separately for when only the statistical uncertainties are considered and with the total uncertainties (i.e. including systematic uncertainties). The systematic uncertainty of  $\theta'_{\text{d.d.}}$  is due to the subtraction of non-hadronic-fake and fake lepton backgrounds from data (see Section 8.3.1) and the systematic uncertainty of  $\theta'_{\text{MC}}$  comes from the  $t\bar{t}$  MC sample modelling (see Section 8.3.2.1). It can be seen that within the total uncertainties, the  $\theta'_{\text{d.d.}}$  and the equivalent  $\theta'_{\text{MC}}$  agree.

As can be seen from Figures B.11, B.12, and B.13, the measured  $\theta'_{\text{d.d.}}$  is not distributed flat against the different choices of boundaries for the control regions. The value of  $\theta'_{\text{d.d.}}$  which is supposed to quantify the photon isolation-identification correlation depends on the definition of the control regions used for its calculation. Therefore, the nominal  $\theta'_{\text{d.d.}}$  is calculated from  $1 < p_T^{\text{cone}20} < 12$  GeV as  $A'$  and  $D'$  boundaries and  $p_T^{\text{cone}20} > 12$  GeV as  $B'$  and  $C'$  boundaries, and then the difference of minimum and maximum of  $\theta'_{\text{d.d.}}$  in the 27 different choices of region definitions is taken as an extra systematic uncertainty.

As a cross check to the benchmark method of Equation 8.8, the number of hadronic-fake in signal region is estimated by using  $\theta'_{\text{d.d.}}$  as the correction factor:

$$N_{\text{est.}}^{\text{h-fake}} = \frac{N_{A,\text{data}}^{\text{h-fake}} \cdot N_{C,\text{data}}^{\text{h-fake}}}{N_{B,\text{data}}^{\text{h-fake}}} \times \theta'_{\text{d.d.}}. \quad (\text{B.2})$$

and then the  $\text{SF}^{\text{h-fake}}$  is calculated from Equation 8.9. The resulting  $\text{SF}^{\text{h-fake}}$  using  $\theta'_{\text{d.d.}}$  is compared

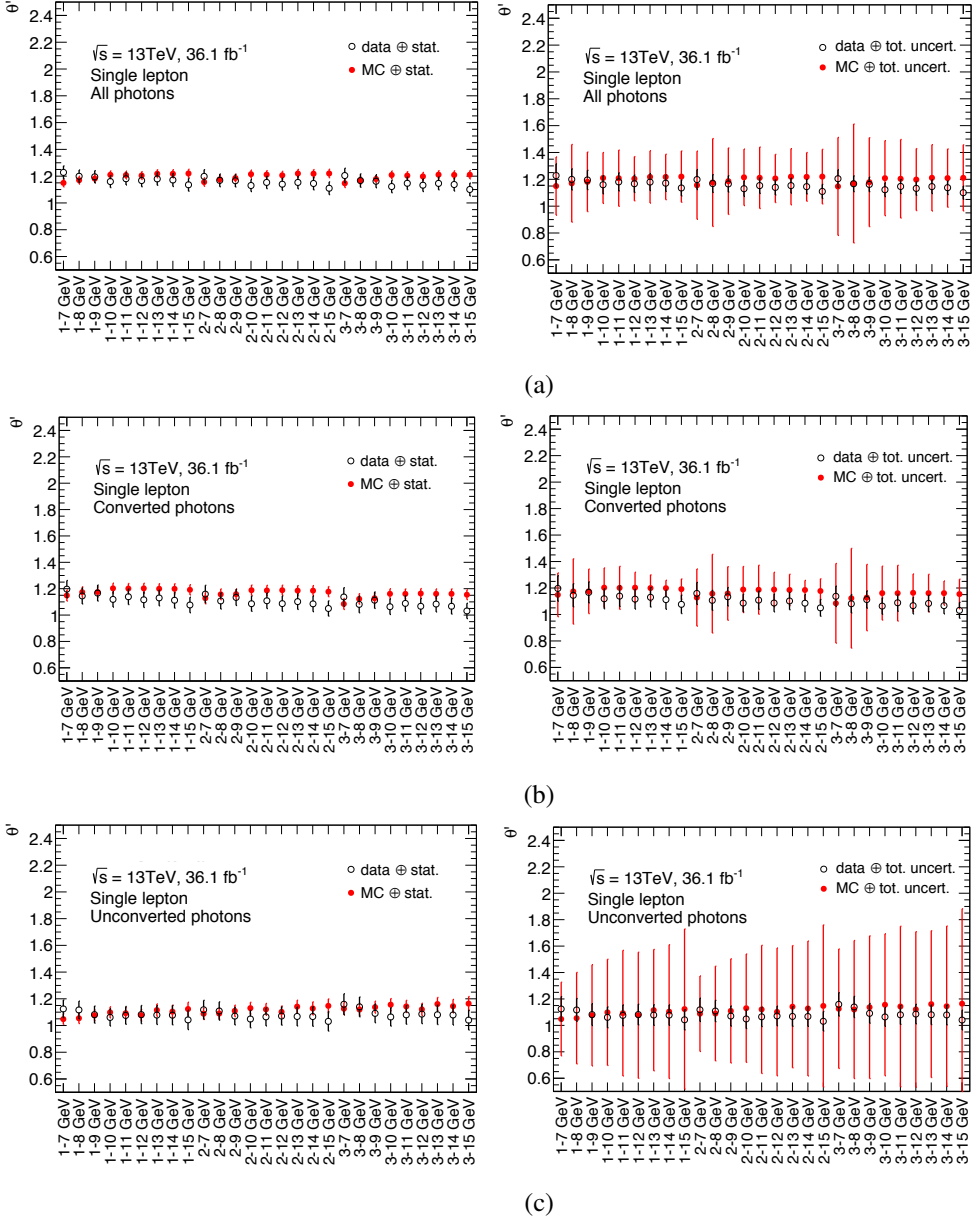


Figure B.11: The  $\theta'_{d,d}$  for different choices of  $A'$ ,  $B'$ ,  $C'$  and  $D'$  regions, for (a) all, (b) converted and (c) unconverted photons, compared to MC. The  $x$  axis shows the lower and upper  $p_T^{\text{cone}20}$  boundaries of regions  $A'$  and  $D'$  in GeV. The lower  $p_T^{\text{cone}20}$  boundaries of regions  $B'$  and  $C'$  coincide with the upper boundaries of regions  $A'$  and  $D'$  and they go up to infinity. The left column shows only the statistical uncertainties and the right column shows the total uncertainties.

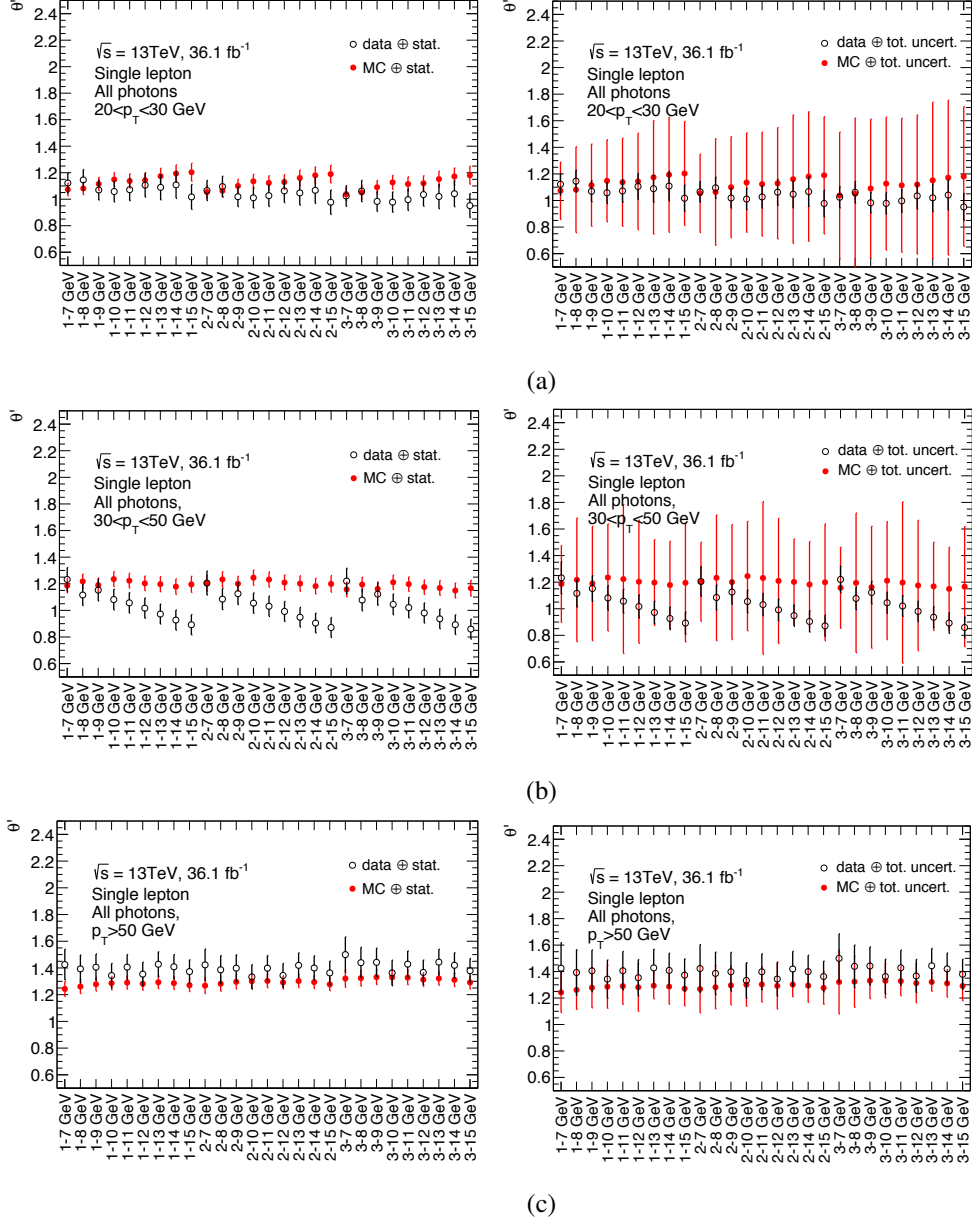


Figure B.12: The  $\theta'_{d,d}$  for different choices of  $A'$ ,  $B'$ ,  $C'$  and  $D'$  regions, in three different photon  $p_T$  slices, compared to MC. The  $x$  axis shows the lower and upper  $p_T^{cone20}$  boundaries of regions  $A'$  and  $D'$  in GeV. The lower  $p_T^{cone20}$  boundaries of regions  $B'$  and  $C'$  coincide with the upper boundaries of regions  $A'$  and  $D'$  and they go up to infinity. The left column shows only the statistical uncertainties and the right column shows the total uncertainties.

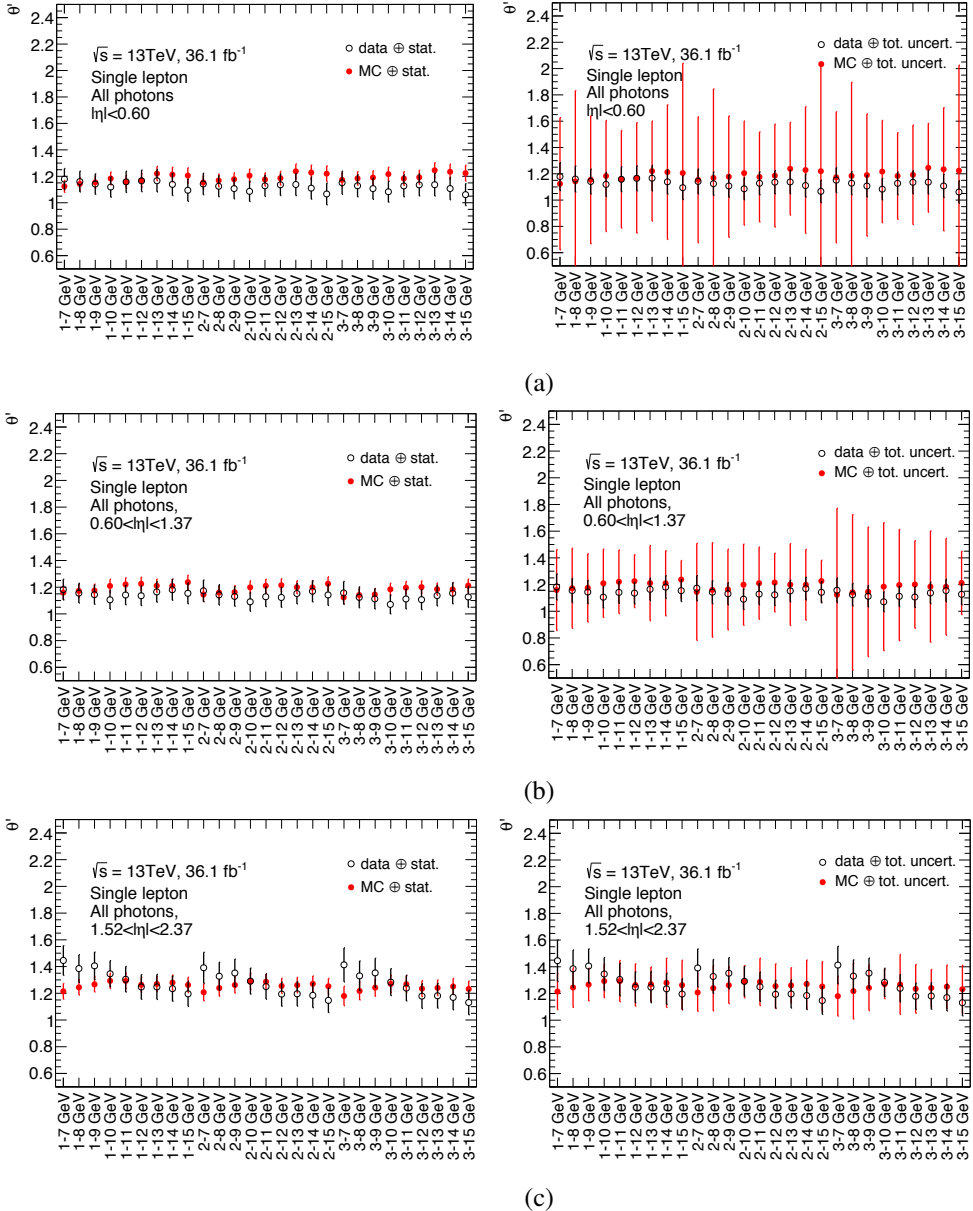


Figure B.13: The  $\theta'_{\text{d.d.}}$  for different choices of  $A'$ ,  $B'$ ,  $C'$  and  $D'$  regions, in three different photon  $\eta$  slices, compared to MC. The  $x$  axis shows the lower and upper  $p_T^{\text{cone}20}$  boundaries of regions  $A'$  and  $D'$  in GeV. The lower  $p_T^{\text{cone}20}$  boundaries of regions  $B'$  and  $C'$  coincide with the upper boundaries of regions  $A'$  and  $D'$  and they go up to infinity. The left column shows only the statistical uncertainties and the right column shows the total uncertainties.

with the calculated baseline  $SF^{h\text{-fake}}$  using  $\theta_{MC}$  in Figure B.14.

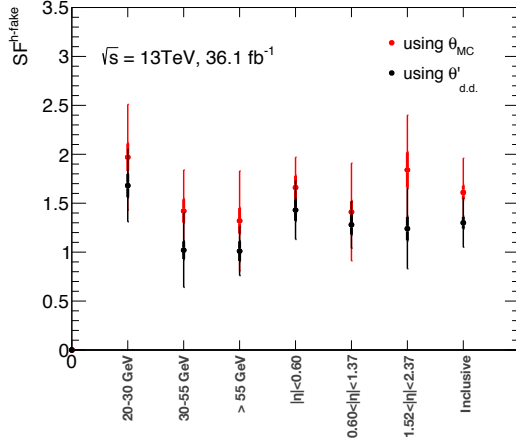


Figure B.14: The  $SF^{h\text{-fake}}$  calculated by using  $\theta'_{d.d.}$  (cross-check method) compared to  $SF^{h\text{-fake}}$  calculated by using  $\theta_{MC}$  (baseline method), in different photon  $p_T$  or photon  $\eta$  slices and inclusively. The thin error bars show the total uncertainty and the thick error bars show only the statistical uncertainty.

The result of two methods agree within the uncertainties. However, the  $\theta_{MC}$  is chosen as the baseline method, for several reasons: (1) Extending the  $A'$  and  $D'$  regions to the low isolation values ( $p_T^{\text{cone}20} > 1 \text{ GeV}$ ) is needed to make a fair extrapolation of isolated versus non-isolated regions ( $A'$  and  $D'$  versus  $B'$  and  $C'$ ) but in the other hand it introduces prompt photon contamination. (2) In the final fit the systematic uncertainties due to background subtraction in  $\theta'_{d.d.}$  and in  $N_{\text{est}}^{h\text{-fake}}$  must be correlated and this is technically difficult.



## APPENDIX C

---

# List of Monte Carlo Samples

---

In the tables that follow, DSID is the unique data-set identification number used internally in the ATLAS community.

## C.1 Monte Carlo Samples Used in the 8 TeV Analysis

### C.1.1 Nominal Samples

DSID	Description	ME gen. had. & part. show.	Settings	$\sigma_{\text{LO}}$ [pb]	NLO $k$ -factor
117478	$t\bar{t}\gamma$ non-all-had.	MADGRAPH5_aMC@NLO v2.1.0 PYTHIA v6.427	$\mu_R = \mu_F = 2m_{\text{top}}$ Perugia2011C CTEQ6L1(LO)	1.1907	1.895

Table C.1: Baseline  $t\bar{t}\gamma$  sample used in the 8 TeV analysis.

DSID	Description	ME gen. had. & part. show.	Settings
110404	$t\bar{t}$ non-all-had.	POWHEG-Box v1.0 PYTHIA v6.427	CT10(NLO) Perugia2011C CTEQ6L1(LO) $h_{\text{damp}} = m_{\text{top}}$

Table C.2: Baseline  $t\bar{t}$  samples used in the 8 TeV analysis.

DSID	Description	ME gen. had. & part. show.	Settings
110090	single-top ( $t$ -chan., top, lept.)	POWHEG-Box v1.0 PYTHIA v6.427	CT104fs Perugia2011C CTEQ6L1(LO)
110091	single-top ( $t$ -chan., antitop, lept.)	POWHEG-Box v1.0 PYTHIA v6.427	CT104fs Perugia2011C CTEQ6L1(LO)
110140	single-top ( $Wt$ -chan., incl.)	POWHEG-Box v1.0 PYTHIA v6.426	CT10(NLO) Perugia2011C CTEQ6L1(LO)
110119	single-top ( $s$ -chan., lept.)	POWHEG-Box v1.0 PYTHIA v6.427	CT10(NLO) Perugia2011C CTEQ6L1(LO)

Table C.3: Baseline single top samples used in the 8 TeV analysis.

DSID	Description	ME gen. had. & part. show.	Settings
126739	$e\gamma p_T^\gamma > 10 \text{ GeV}$	SHERPA v1.4.0	CT10(NLO)
126742	$\nu\mu\gamma p_T^\gamma > 10 \text{ GeV}$	SHERPA v1.4.0	CT10(NLO)
126856	$\tau\nu\gamma p_T^\gamma > 10 \text{ GeV}$	SHERPA v1.4.0	CT10(NLO)

Table C.4: Baseline  $W\gamma$  samples used in the 8 TeV analysis.

DSID	Description	ME gen. had. & part. show.	Settings
145161	$e\gamma\gamma p_T^\gamma > 10 \text{ GeV}$	SHERPA v1.4.0	CT10(NLO)
145162	$\mu\mu\gamma p_T^\gamma > 10 \text{ GeV}$	SHERPA v1.4.0	CT10(NLO)
126854	$\tau\tau\gamma p_T^\gamma > 10 \text{ GeV}$	SHERPA v1.4.0	CT10(NLO)

Table C.5: Baseline  $Z\gamma$  samples used in the 8 TeV analysis.

DSID	Description	ME gen. had. & part. show.	Settings
107100	$WW(l\nu l\nu) \text{ Np0}$	ALPGEN v2.14 HERWIG v6.520/JIMMY v4.31	CTEQ6L1 AUET2
107101	$WW(l\nu l\nu) \text{ Np1}$	ALPGEN v2.14 HERWIG v6.520/JIMMY v4.31	CTEQ6L1 AUET2
107102	$WW(l\nu l\nu) \text{ Np2}$	ALPGEN v2.14 HERWIG v6.520/JIMMY v4.31	CTEQ6L1 AUET2
107103	$WW(l\nu l\nu) \text{ Np3}$	ALPGEN v2.14 HERWIG v6.520/JIMMY v4.31	CTEQ6L1 AUET2
107104	$WZ(\text{incl. } ll) \text{ Np0}$	ALPGEN v2.14 HERWIG v6.520/JIMMY v4.31	CTEQ6L1 AUET2
107105	$WZ(\text{incl. } ll) \text{ Np1}$	ALPGEN v2.14 HERWIG v6.520/JIMMY v4.31	CTEQ6L1 AUET2
107106	$WZ(\text{incl. } ll) \text{ Np2}$	ALPGEN v2.14 HERWIG v6.520/JIMMY v4.31	CTEQ6L1 AUET2
107107	$WZ(\text{incl. } ll) \text{ Np3}$	ALPGEN v2.14 HERWIG v6.520/JIMMY v4.31	CTEQ6L1 AUET2
107108	$ZZ(\text{incl. } ll) \text{ Np0}$	ALPGEN v2.14 HERWIG v6.520/JIMMY v4.31	CTEQ6L1 AUET2
107109	$ZZ(\text{incl. } ll) \text{ Np1}$	ALPGEN v2.14 HERWIG v6.520/JIMMY v4.31	CTEQ6L1 AUET2
107110	$ZZ(\text{incl. } ll) \text{ Np2}$	ALPGEN v2.14 HERWIG v6.520/JIMMY v4.31	CTEQ6L1 AUET2
107111	$ZZ(\text{incl. } ll) \text{ Np3}$	ALPGEN v2.14 HERWIG v6.520/JIMMY v4.31	CTEQ6L1 AUET2

Table C.6: Baseline diboson samples used in the 8 TeV analysis.

### C.1.2 Samples for Estimation of Systematic Uncertainties

DSID	Description	ME gen. had. & part. show.	Settings
117980	$t\bar{t}\gamma$ scale variation	MADGRAPH5_aMC@NLO v2.1.0 PYTHIA v6.427	$\mu_R = \mu_F = m_{top}$ Perugia2011C CTEQ6L1(LO)
117981	$t\bar{t}\gamma$ scale variation	MADGRAPH5_aMC@NLO v2.1.0 PYTHIA v6.427	$\mu_R = \mu_F = 4m_{top}$ Perugia2011C CTEQ6L1(LO)
117480	$t\bar{t}\gamma$ ISR/FSR high	MADGRAPH5_aMC@NLO v2.1.0 PYTHIA v6.427	CTEQ6L1(LO) Perugia2011C radHi
117481	$t\bar{t}\gamma$ ISR/FSR low	MADGRAPH5_aMC@NLO v2.1.0 PYTHIA v6.427	CTEQ6L1(LO) Perugia2011C radLo
117482	$t\bar{t}\gamma$ had. & part. show. variation	MADGRAPH5_aMC@NLO v2.1.0 HERWIG v6.520	CTEQ6L1 Perugia2011C

 Table C.7: Alternative  $t\bar{t}\gamma$  samples used in the 8 TeV analysis for estimation of systematic uncertainties.

DSID	Description	ME gen. had. & part. show.	Settings
146430	$W\gamma$ Np0	ALPGEN v2.14 PYTHIA v6.426	CTEQ6L1 AUET2
146431	$W\gamma$ Np1	ALPGEN v2.14 PYTHIA v6.426	CTEQ6L1 AUET2
146432	$W\gamma$ Np2	ALPGEN v2.14 PYTHIA v6.426	CTEQ6L1 AUET2
146433	$W\gamma$ Np3	ALPGEN v2.14 PYTHIA v6.426	CTEQ6L1 AUET2
146434	$W\gamma$ Np4	ALPGEN v2.14 PYTHIA v6.426	CTEQ6L1 AUET2
146435	$W\gamma$ Np5	ALPGEN v2.14 PYTHIA v6.426	CTEQ6L1 AUET2

 Table C.8: Alternative  $W\gamma$  samples used in the 8 TeV analysis for estimation of systematic uncertainties.

### C.1.3 Other Samples

DSID	Description	ME gen. had. & part. show.	Settings
129160	di-jet $p_T(jet) > 17$ GeV	PYTHIA	CTEQ6L1 AU2

Table C.9: Di-jet sample used for study of prompt-photon contamination in hadronic-fake templates (Section 7.3.2.4) in the 8 TeV analysis.

## C.2 Monte Carlo Samples Used in the 13 TeV Analysis

### C.2.1 Nominal Samples

## Appendix C List of Monte Carlo Samples

---

DSID	Description	ME gen. had. & part. show.	Settings	$\sigma_{\text{LO}}$ [pb]	NLO $k$ -factor
410389	$t\bar{t}\gamma$ non-all-had.	MADGRAPH5_aMC@NLO v2.33 PYTHIA v8.212	dynamic $\mu_R$ and $\mu_F$ A14 NNPDF2.3LO	4.623	1.3

Table C.10: Baseline  $t\bar{t}\gamma$  sample used in the 13 TeV analysis.

DSID	Description	ME gen. had. & part. show.	Settings
410501	$t\bar{t}$ non-all-had.	POWHEG-Box v2 PYTHIA v8.210	NNPDF3.0NLO NNPDF2.3LO A14 $h_{\text{damp}} = 1.5m_{\text{top}}$

Table C.11: Baseline  $t\bar{t}$  samples used in the 13 TeV analysis.

DSID	Description	ME gen. had. & part. show.	Settings
410011	single-top ( $t$ -chan., top, lept.)	POWHEG-Box v1 PYTHIA v6.428	CT104fs Perugia2012 CTEQ6L1
410012	single-top ( $t$ -chan., antitop, lept.)	POWHEG-Box v1 PYTHIA v6.428	CT104fs Perugia2012 CTEQ6L1
410013	single-top ( $Wt$ -chan., top, incl.)	POWHEG-Box v1 PYTHIA v6.428	CT10(NLO) Perugia2012 CTEQ6L1
410014	single-top ( $Wt$ -chan., antitop, incl.)	POWHEG-Box v1 PYTHIA v6.428	CT10(NLO) Perugia2012 CTEQ6L1
410025	single-top ( $s$ -chan., top, non-all-had.)	POWHEG-Box v1 PYTHIA v6.428	CT10(NLO) Perugia2012 CTEQ6L1
410026	single-top ( $s$ -chan., antitop, non-all-had.)	POWHEG-Box v1 PYTHIA v6.428	CT10(NLO) Perugia2012 CTEQ6L1

Table C.12: Baseline single top samples used in the 13 TeV analysis.

DSID	Description	ME gen. had. & part. show.	Settings
361063	$ZZ(l l l l)$	SHERPA v2.1	CT10(NLO)
361064	$W^-Z(l^-\nu ll)$ same flavour leptons	SHERPA v2.1	CT10(NLO)
361065	$W^-Z(l^-\nu ll)$ different flavour leptons	SHERPA v2.1	CT10(NLO)
361066	$W^+Z(l^+\nu ll)$ same flavour leptons	SHERPA v2.1	CT10(NLO)
361067	$W^+Z(l^+\nu ll)$ different flavour leptons	SHERPA v2.1	CT10(NLO)
361068	$WW(l\nu l\nu)$	SHERPA v2.1	CT10(NLO)
361070	$WW(l\nu l\nu + jj)$ same sign leptons	SHERPA v2.1	CT10(NLO)
361071	$WW(l\nu l\nu + jj)$	SHERPA v2.1	CT10(NLO)
361072	$ZZ(l l l l + jj)$	SHERPA v2.1	CT10(NLO)
361077	$WW(gg \rightarrow l\nu l\nu)$	SHERPA v2.1	CT10(NLO)
361091	$WW(W^+ \rightarrow l^+\nu W^- \rightarrow qq)$	SHERPA v2.1	CT10(NLO)
361092	$WW(W^+ \rightarrow qq W^- \rightarrow l^-\nu)$	SHERPA v2.1	CT10(NLO)
361093	$WZ(l\nu qq)$	SHERPA v2.1	CT10(NLO)
361094	$WZ(qq ll)$	SHERPA v2.1	CT10(NLO)
361095	$WZ(qq \nu\nu)$	SHERPA v2.1	CT10(NLO)
361096	$ZZ(qq ll)$	SHERPA v2.1	CT10(NLO)
361097	$ZZ(qq \nu\nu)$	SHERPA v2.1	CT10(NLO)

Table C.13: Baseline diboson samples used in the 13 TeV analysis.

DSID	Description	ME gen. had. & part. show.	Settings
364500	$e\gamma$ $7 < p_T^\gamma < 15$ GeV	SHERPA v2.2.2	NNPDF3.0NLO
364501	$e\gamma$ $15 < p_T^\gamma < 35$ GeV	SHERPA v2.2.2	NNPDF3.0NLO
364502	$e\gamma$ $35 < p_T^\gamma < 70$ GeV	SHERPA v2.2.2	NNPDF3.0NLO
364503	$e\gamma$ $70 < p_T^\gamma < 140$ GeV	SHERPA v2.2.2	NNPDF3.0NLO
364504	$e\gamma$ $p_T^\gamma > 140$ GeV	SHERPA v2.2.2	NNPDF3.0NLO
364505	$\mu\gamma$ $7 < p_T^\gamma < 15$ GeV	SHERPA v2.2.2	NNPDF3.0NLO
364506	$\mu\gamma$ $15 < p_T^\gamma < 35$ GeV	SHERPA v2.2.2	NNPDF3.0NLO
364507	$\mu\gamma$ $35 < p_T^\gamma < 70$ GeV	SHERPA v2.2.2	NNPDF3.0NLO
364508	$\mu\gamma$ $70 < p_T^\gamma < 140$ GeV	SHERPA v2.2.2	NNPDF3.0NLO
364509	$\mu\gamma$ $p_T^\gamma > 140$ GeV	SHERPA v2.2.2	NNPDF3.0NLO
364510	$\tau\gamma$ $7 < p_T^\gamma < 15$ GeV	SHERPA v2.2.2	NNPDF3.0NLO
364511	$\tau\gamma$ $15 < p_T^\gamma < 35$ GeV	SHERPA v2.2.2	NNPDF3.0NLO
364512	$\tau\gamma$ $35 < p_T^\gamma < 70$ GeV	SHERPA v2.2.2	NNPDF3.0NLO
364514	$\tau\gamma$ $p_T^\gamma > 140$ GeV	SHERPA v2.2.2	NNPDF3.0NLO

 Table C.14: Baseline  $Z\gamma$  samples used in the 13 TeV analysis.

DSID	Description	ME gen. had. & part. show.	Settings
364521	$e\gamma$ $7 < p_T^\gamma < 15$ GeV	SHERPA v2.2.2	NNPDF3.0NLO
364522	$e\gamma$ $15 < p_T^\gamma < 35$ GeV	SHERPA v2.2.2	NNPDF3.0NLO
364523	$e\gamma$ $35 < p_T^\gamma < 70$ GeV	SHERPA v2.2.2	NNPDF3.0NLO
364524	$e\gamma$ $70 < p_T^\gamma < 140$ GeV	SHERPA v2.2.2	NNPDF3.0NLO
364525	$e\gamma$ $p_T^\gamma > 140$ GeV	SHERPA v2.2.2	NNPDF3.0NLO
364526	$\mu\gamma$ $7 < p_T^\gamma < 15$ GeV	SHERPA v2.2.2	NNPDF3.0NLO
364527	$\mu\gamma$ $15 < p_T^\gamma < 35$ GeV	SHERPA v2.2.2	NNPDF3.0NLO
364528	$\mu\gamma$ $35 < p_T^\gamma < 70$ GeV	SHERPA v2.2.2	NNPDF3.0NLO
364529	$\mu\gamma$ $70 < p_T^\gamma < 140$ GeV	SHERPA v2.2.2	NNPDF3.0NLO
364530	$\mu\gamma$ $p_T^\gamma > 140$ GeV	SHERPA v2.2.2	NNPDF3.0NLO
364531	$\tau\gamma$ $7 < p_T^\gamma < 15$ GeV	SHERPA v2.2.2	NNPDF3.0NLO
364532	$\tau\gamma$ $15 < p_T^\gamma < 35$ GeV	SHERPA v2.2.2	NNPDF3.0NLO
364533	$\tau\gamma$ $35 < p_T^\gamma < 70$ GeV	SHERPA v2.2.2	NNPDF3.0NLO
364534	$\tau\gamma$ $70 < p_T^\gamma < 140$ GeV	SHERPA v2.2.2	NNPDF3.0NLO
364535	$\tau\gamma$ $p_T^\gamma > 140$ GeV	SHERPA v2.2.2	NNPDF3.0NLO

 Table C.15: Baseline  $W\gamma$  samples used in the 13 TeV analysis.

## Appendix C List of Monte Carlo Samples

---

DSID	Description	ME gen. had. & part. show.	Settings
364100	$\mu\mu \max(H_T, p_T^Z) < 70$ GeV light-jet filter	SHERPA v2.2.1	NNPDF3.0NLO
364101	$\mu\mu \max(H_T, p_T^Z) < 70$ GeV c-jet filter	SHERPA v2.2.1	NNPDF3.0NLO
364102	$\mu\mu \max(H_T, p_T^Z) < 70$ GeV b-jet filter	SHERPA v2.2.1	NNPDF3.0NLO
364103	$\mu\mu 70 < \max(H_T, p_T^Z) < 140$ GeV light-jet filter	SHERPA v2.2.1	NNPDF3.0NLO
364104	$\mu\mu 70 < \max(H_T, p_T^Z) < 140$ GeV c-jet filter	SHERPA v2.2.1	NNPDF3.0NLO
364105	$\mu\mu 70 < \max(H_T, p_T^Z) < 140$ GeV b-jet filter	SHERPA v2.2.1	NNPDF3.0NLO
364106	$\mu\mu 140 < \max(H_T, p_T^Z) < 280$ GeV light-jet filter	SHERPA v2.2.1	NNPDF3.0NLO
364107	$\mu\mu 140 < \max(H_T, p_T^Z) < 280$ GeV c-jet filter	SHERPA v2.2.1	NNPDF3.0NLO
364108	$\mu\mu 140 < \max(H_T, p_T^Z) < 280$ GeV b-jet filter	SHERPA v2.2.1	NNPDF3.0NLO
364109	$\mu\mu 280 < \max(H_T, p_T^Z) < 500$ GeV light-jet filter	SHERPA v2.2.1	NNPDF3.0NLO
364110	$\mu\mu 280 < \max(H_T, p_T^Z) < 500$ GeV c-jet filter	SHERPA v2.2.1	NNPDF3.0NLO
364111	$\mu\mu 280 < \max(H_T, p_T^Z) < 500$ GeV b-jet filter	SHERPA v2.2.1	NNPDF3.0NLO
364112	$\mu\mu 500 < \max(H_T, p_T^Z) < 1000$ GeV light-jet filter	SHERPA v2.2.1	NNPDF3.0NLO
364113	$\mu\mu \max(H_T, p_T^Z) > 1000$ GeV light-jet filter	SHERPA v2.2.1	NNPDF3.0NLO
364114	$ee \max(H_T, p_T^Z) < 70$ GeV light-jet filter	SHERPA v2.2.1	NNPDF3.0NLO
364115	$ee \max(H_T, p_T^Z) < 70$ GeV c-jet filter	SHERPA v2.2.1	NNPDF3.0NLO
364116	$ee \max(H_T, p_T^Z) < 70$ GeV b-jet filter	SHERPA v2.2.1	NNPDF3.0NLO
364117	$ee 70 < \max(H_T, p_T^Z) < 140$ GeV light-jet filter	SHERPA v2.2.1	NNPDF3.0NLO
364118	$ee 70 < \max(H_T, p_T^Z) < 140$ GeV c-jet filter	SHERPA v2.2.1	NNPDF3.0NLO
364119	$ee 70 < \max(H_T, p_T^Z) < 140$ GeV b-jet filter	SHERPA v2.2.1	NNPDF3.0NLO
364120	$ee 140 < \max(H_T, p_T^Z) < 280$ GeV light-jet filter	SHERPA v2.2.1	NNPDF3.0NLO
364121	$ee 140 < \max(H_T, p_T^Z) < 280$ GeV c-jet filter	SHERPA v2.2.1	NNPDF3.0NLO
364122	$ee 140 < \max(H_T, p_T^Z) < 280$ GeV b-jet filter	SHERPA v2.2.1	NNPDF3.0NLO
364123	$ee 280 < \max(H_T, p_T^Z) < 500$ GeV light-jet filter	SHERPA v2.2.1	NNPDF3.0NLO
364124	$ee 280 < \max(H_T, p_T^Z) < 500$ GeV c-jet filter	SHERPA v2.2.1	NNPDF3.0NLO
364125	$ee 280 < \max(H_T, p_T^Z) < 500$ GeV b-jet filter	SHERPA v2.2.1	NNPDF3.0NLO
364126	$ee 500 < \max(H_T, p_T^Z) < 1000$ GeV light-jet filter	SHERPA v2.2.1	NNPDF3.0NLO
364127	$ee \max(H_T, p_T^Z) > 1000$ GeV light-jet filter	SHERPA v2.2.1	NNPDF3.0NLO
364128	$\tau\tau \max(H_T, p_T^Z) < 70$ GeV light-jet filter	SHERPA v2.2.1	NNPDF3.0NLO
364129	$\tau\tau \max(H_T, p_T^Z) < 70$ GeV c-jet filter	SHERPA v2.2.1	NNPDF3.0NLO
364130	$\tau\tau \max(H_T, p_T^Z) < 70$ GeV b-jet filter	SHERPA v2.2.1	NNPDF3.0NLO
364131	$\tau\tau 70 < \max(H_T, p_T^Z) < 140$ GeV light-jet filter	SHERPA v2.2.1	NNPDF3.0NLO
364132	$\tau\tau 70 < \max(H_T, p_T^Z) < 140$ GeV c-jet filter	SHERPA v2.2.1	NNPDF3.0NLO
364133	$\tau\tau 70 < \max(H_T, p_T^Z) < 140$ GeV b-jet filter	SHERPA v2.2.1	NNPDF3.0NLO
364134	$\tau\tau 140 < \max(H_T, p_T^Z) < 280$ GeV light-jet filter	SHERPA v2.2.1	NNPDF3.0NLO
364135	$\tau\tau 140 < \max(H_T, p_T^Z) < 280$ GeV c-jet filter	SHERPA v2.2.1	NNPDF3.0NLO
364136	$\tau\tau 140 < \max(H_T, p_T^Z) < 280$ GeV b-jet filter	SHERPA v2.2.1	NNPDF3.0NLO
364137	$\tau\tau 280 < \max(H_T, p_T^Z) < 500$ GeV light-jet filter	SHERPA v2.2.1	NNPDF3.0NLO
364138	$\tau\tau 280 < \max(H_T, p_T^Z) < 500$ GeV c-jet filter	SHERPA v2.2.1	NNPDF3.0NLO
364139	$\tau\tau 280 < \max(H_T, p_T^Z) < 500$ GeV b-jet filter	SHERPA v2.2.1	NNPDF3.0NLO
364140	$\tau\tau 500 < \max(H_T, p_T^Z) < 1000$ GeV light-jet filter	SHERPA v2.2.1	NNPDF3.0NLO
364141	$\tau\tau \max(H_T, p_T^Z) > 1000$ GeV light-jet filter	SHERPA v2.2.1	NNPDF3.0NLO

Table C.16: Baseline Z+jets samples used in the 13 TeV analysis.

DSID	Description	ME gen. had. & part. show.	Settings
364156	$\mu\nu \max(H_T, p_T^W) < 70$ GeV light-jet filter	SHERPA v2.2.1	NNPDF3.0NLO
364157	$\mu\nu \max(H_T, p_T^W) < 70$ GeV c-jet filter	SHERPA v2.2.1	NNPDF3.0NLO
364158	$\mu\nu \max(H_T, p_T^W) < 70$ GeV b-jet filter	SHERPA v2.2.1	NNPDF3.0NLO
364159	$\mu\nu 70 < \max(H_T, p_T^W) < 140$ GeV light-jet filter	SHERPA v2.2.1	NNPDF3.0NLO
364160	$\mu\nu 70 < \max(H_T, p_T^W) < 140$ GeV c-jet filter	SHERPA v2.2.1	NNPDF3.0NLO
364161	$\mu\nu 70 < \max(H_T, p_T^W) < 140$ GeV b-jet filter	SHERPA v2.2.1	NNPDF3.0NLO
364162	$\mu\nu 140 < \max(H_T, p_T^W) < 280$ GeV light-jet filter	SHERPA v2.2.1	NNPDF3.0NLO
364163	$\mu\nu 140 < \max(H_T, p_T^W) < 280$ GeV c-jet filter	SHERPA v2.2.1	NNPDF3.0NLO
364164	$\mu\nu 140 < \max(H_T, p_T^W) < 280$ GeV b-jet filter	SHERPA v2.2.1	NNPDF3.0NLO
364165	$\mu\nu 280 < \max(H_T, p_T^W) < 500$ GeV light-jet filter	SHERPA v2.2.1	NNPDF3.0NLO
364166	$\mu\nu 280 < \max(H_T, p_T^W) < 500$ GeV c-jet filter	SHERPA v2.2.1	NNPDF3.0NLO
364167	$\mu\nu 280 < \max(H_T, p_T^W) < 500$ GeV b-jet filter	SHERPA v2.2.1	NNPDF3.0NLO
364168	$\mu\nu 500 < \max(H_T, p_T^W) < 1000$ GeV light-jet filter	SHERPA v2.2.1	NNPDF3.0NLO
364169	$\mu\nu \max(H_T, p_T^W) > 1000$ GeV light-jet filter	SHERPA v2.2.1	NNPDF3.0NLO
364170	$ev \max(H_T, p_T^W) < 70$ GeV light-jet filter	SHERPA v2.2.1	NNPDF3.0NLO
364171	$ev \max(H_T, p_T^W) < 70$ GeV c-jet filter	SHERPA v2.2.1	NNPDF3.0NLO
364172	$ev \max(H_T, p_T^W) < 70$ GeV b-jet filter	SHERPA v2.2.1	NNPDF3.0NLO
364173	$ev 70 < \max(H_T, p_T^W) < 140$ GeV light-jet filter	SHERPA v2.2.1	NNPDF3.0NLO
364174	$ev 70 < \max(H_T, p_T^W) < 140$ GeV c-jet filter	SHERPA v2.2.1	NNPDF3.0NLO
364175	$ev 70 < \max(H_T, p_T^W) < 140$ GeV b-jet filter	SHERPA v2.2.1	NNPDF3.0NLO
364176	$ev 140 < \max(H_T, p_T^W) < 280$ GeV light-jet filter	SHERPA v2.2.1	NNPDF3.0NLO
364177	$ev 140 < \max(H_T, p_T^W) < 280$ GeV c-jet filter	SHERPA v2.2.1	NNPDF3.0NLO
364178	$ev 140 < \max(H_T, p_T^W) < 280$ GeV b-jet filter	SHERPA v2.2.1	NNPDF3.0NLO
364179	$ev 280 < \max(H_T, p_T^W) < 500$ GeV light-jet filter	SHERPA v2.2.1	NNPDF3.0NLO
364180	$ev 280 < \max(H_T, p_T^W) < 500$ GeV c-jet filter	SHERPA v2.2.1	NNPDF3.0NLO
364181	$ev 280 < \max(H_T, p_T^W) < 500$ GeV b-jet filter	SHERPA v2.2.1	NNPDF3.0NLO
364182	$ev 500 < \max(H_T, p_T^W) < 1000$ GeV light-jet filter	SHERPA v2.2.1	NNPDF3.0NLO
364183	$ev \max(H_T, p_T^W) > 1000$ GeV light-jet filter	SHERPA v2.2.1	NNPDF3.0NLO
364184	$\tau\nu \max(H_T, p_T^W) < 70$ GeV light-jet filter	SHERPA v2.2.1	NNPDF3.0NLO
364185	$\tau\nu \max(H_T, p_T^W) < 70$ GeV c-jet filter	SHERPA v2.2.1	NNPDF3.0NLO
364186	$\tau\nu \max(H_T, p_T^W) < 70$ GeV b-jet filter	SHERPA v2.2.1	NNPDF3.0NLO
364187	$\tau\nu 70 < \max(H_T, p_T^W) < 140$ GeV light-jet filter	SHERPA v2.2.1	NNPDF3.0NLO
364188	$\tau\nu 70 < \max(H_T, p_T^W) < 140$ GeV c-jet filter	SHERPA v2.2.1	NNPDF3.0NLO
364189	$\tau\nu 70 < \max(H_T, p_T^W) < 140$ GeV b-jet filter	SHERPA v2.2.1	NNPDF3.0NLO
364190	$\tau\nu 140 < \max(H_T, p_T^W) < 280$ GeV light-jet filter	SHERPA v2.2.1	NNPDF3.0NLO
364191	$\tau\nu 140 < \max(H_T, p_T^W) < 280$ GeV c-jet filter	SHERPA v2.2.1	NNPDF3.0NLO
364192	$\tau\nu 140 < \max(H_T, p_T^W) < 280$ GeV b-jet filter	SHERPA v2.2.1	NNPDF3.0NLO
364193	$\tau\nu 280 < \max(H_T, p_T^W) < 500$ GeV light-jet filter	SHERPA v2.2.1	NNPDF3.0NLO
364194	$\tau\nu 280 < \max(H_T, p_T^W) < 500$ GeV c-jet filter	SHERPA v2.2.1	NNPDF3.0NLO
364195	$\tau\nu 280 < \max(H_T, p_T^W) < 500$ GeV b-jet filter	SHERPA v2.2.1	NNPDF3.0NLO
364196	$\tau\nu 500 < \max(H_T, p_T^W) < 1000$ GeV light-jet filter	SHERPA v2.2.1	NNPDF3.0NLO
364197	$\tau\nu \max(H_T, p_T^W) > 1000$ GeV light-jet filter	SHERPA v2.2.1	NNPDF3.0NLO

 Table C.17: Baseline  $W$ +jets samples used in the 13 TeV analysis.

### C.2.2 Samples for Estimation of Systematic Uncertainties

DSID	Description	ME gen. had. & part. show.	Settings
410404	$t\bar{t}\gamma$ ISR/FSR up	MADGRAPH5_aMC@NLO v2.33 PYTHIA v8.212	A14 Var3c up NNPDF2.3LO
410405	$t\bar{t}\gamma$ ISR/FSR down	MADGRAPH5_aMC@NLO v2.33 PYTHIA v8.212	A14 Var3c down NNPDF2.3LO
410395	$t\bar{t}\gamma$ had. & part. show. variation	MADGRAPH5_aMC@NLO v2.33 HERWIG v7.0.1	NNPDF2.3LO

Table C.18: Alternative  $t\bar{t}\gamma$  samples used in the 13 TeV analysis for estimation of systematic uncertainties.

DSID	Description	ME gen. had. & part. show.	Settings
410250	$t\bar{t}$ single-lepton, $l^-$	SHERPA v2.2	NNPDF3.0NNLO
410251	$t\bar{t}$ single-lepton, $l^+$	SHERPA v2.2	NNPDF3.0NNLO
410252	$t\bar{t}$ dilepton	SHERPA v2.2	NNPDF3.0NNLO
410511	$t\bar{t}$ non-all-had.	POWHEG-BOX v2 PYTHIA v8.210	A14 Var3c up, $h_{damp} = 3m_{top}$ , QCD scales×0.5
410512	$t\bar{t}$ non-all-had.	POWHEG-BOX v2 PYTHIA v8.210	A14 Var3c down, $h_{damp} = 1.5m_{top}$ , QCD scales×2

Table C.19: Alternative  $t\bar{t}$  samples used in the 13 TeV analysis for estimation of systematic uncertainties.

# List of Abbreviations

---

**BDT** Boosted Decision Trees. 52

**CSC** Cathode-Strip Chamber. 41, 43, 49

**ELD** Event-level discriminator. 116–119, 121, 132–138, 141, 142

**EM** electromagnetic. 51

**EMCal** Electromagnetic Calorimeter. 39–41, 47, 48, 53–55, 74, 79, 80, 84, 114, 117

**FCal** Forward Calorimeter. 39, 41

**FSR** final state radiations. 20, 27, 60, 62–64, 128, 131, 174, 183, 188

**GSF** Gaussian Sum Filter. 47

**HCal** Hadron Calorimeter. 39, 41, 54, 55

**HT** high threshold. 38

**IBL** Insertable B-Layer. 37

**ID** Inner Detector. 35, 37, 39, 40, 46–50, 53, 54, 57, 74

**ISR** initial state radiations. 20, 27, 60, 62–64, 128, 131, 174, 183, 188

**JER** jet energy resolution. 107

**JES** jet energy scale. 52, 107

**JVF** Jet Vertex Fraction. 74, 107, 136

**JVT** Jet Vertex Tagger. 115, 136

**LCW** Local Cluster Weighting. 51

**LHC** Large Hadron Collider. 3, 17, 20, 24, 27, 29–33, 43, 59, 141

**LO** leading order. 19, 23, 24, 60–63, 83, 120, 181, 184

**LT** low threshold. 38

- MC** Monte Carlo. 47, 49, 50, 52, 55, 56, 59–63, 65–67, 75, 81, 83, 84, 86, 87, 92–94, 99, 104–109, 113, 115–117, 119–122, 124, 128–137, 139–141, 157, 172–178
- MDT** Monitored Drift Tube. 41, 43, 49
- ME** Matrix Element. 23, 60, 61, 63, 65, 181–188
- MS** Muon Spectrometer. 41, 43, 49, 50
- MVA** Multivariate Analysis. 47, 48, 52, 141
- NLO** next-to-leading order. 19, 23, 24, 60, 62, 63, 83, 110, 111, 120, 128, 137–139, 181, 184
- NN** Neural Network. 113, 114, 116, 141
- NNLO** next-to-next-to-leading order. 19, 23, 63
- PDF** Parton Distribution Function. 18, 19, 21, 22, 60–63, 83, 106, 120, 136
- PPT** Prompt-photon tagger. 116–118, 136, 137, 141, 142
- QCD** Quantum Chromodynamics. 8–13, 18–21, 23, 24, 60–63, 73, 83, 100, 106, 108, 110, 112, 117, 120, 128, 132, 135, 157, 188
- QED** Quantum Electrodynamics. 6, 8–14, 19, 21, 60, 63, 106
- QFT** Quantum Field Theory. 3, 15
- RPC** Resistive Plate Chamber. 43, 49
- SCT** Semi-Conductor Tracker. 35, 37, 46
- SM** Standard Model. 3–6, 10, 15, 17, 22, 24, 26, 28, 34, 71, 83, 110, 111, 137, 139, 142
- SSB** spontaneous symmetry breaking. 15
- TGC** Gap Chamber. 43, 49
- TRT** Transition Radiation Tracker. 35, 37, 38, 46–48, 53, 54, 101
- TST** Track Soft Term. 57